MACHINABILITY ENHANCEMENT OF STAINLESS STEELS THROUGH CONTROL OF BUILT-UP EDGE FORMATION

`

MACHINABILITY ENHANCEMENT OF STAINLESS STEELS THROUGH CONTROL OF BUILT-UP EDGE FORMATION

By YASSMIN SEID AHMED, M. SC., B. ENG.

A Thesis Submitted to the School of Graduate Studies in Partial Fulfillment of the Requirements for the Degree Doctor of Philosophy

McMaster University

©Copyright by Yassmin Seid Ahmed, March 2020

`

DOCTOR OF PHILOSOPHY (2020), McMaster University, Hamilton, Ontario (Mechanical Engineering)

TITLE: Machinability Enhancement of Stainless Steels Through Control of Built-Up Edge Formation

AUTHOR: Yassmin Seid Ahmed M. Sc., B. Eng., Mechanical Engineering

SUPERVISORS: Dr. Stephen C. Veldhuis

NUMBER OF PAGES: xxxiii, 269

`

Lay Abstract

Three main objectives are presented in this thesis. The first is a detailed investigation of the performance of stainless steel machining obtained by the use of different coated cutting tools and various cooling conditions. The goal of this research is to assess the reduction of tool service life, productivity, and part quality. The thesis also examines the causes of workpiece material adhesion to the cutting tool during the cutting test and to better explain its effects on tool wear and workpiece surface finish. This phenomenon is known as the "built-up edge" (BUE). Finally, different textures are applied on the cutting tool via a laser to stabilize the BUE formation on the cutting tool, thereby improving the quality of the part.

`

Abstract

Demand for parts made from stainless steel is rapidly increasing, especially in the oil and gas industries. Stainless steel provides a number of key advantages, such as high tensile strength, toughness, and excellent corrosion resistance. However, stainless steel cutting faces some serious difficulties. At low cutting speeds, workpiece material and the chips formed during machining tend to adhere to the cutting tool surface, forming a built-up edge (BUE). The BUE is an extremely deformed piece of material which intermittently sticks to the tool at the tool-chip interface throughout the cutting test, affecting tool life and surface integrity. Unstable BUE can cause tool failure and deterioration of the workpiece. However, stable BUE formation can protect the cutting tool from further wear, improving the productivity of stainless steel machining.

This thesis presents an in-depth study of machining performance using different coated tools and various coolant conditions to examine the nature of the different tool wear mechanisms present during the turning of stainless steels. Then, different textures are generated on the tool rake face to control the stability of BUE and reduce friction during the machining process.

Results show that the BUE can significantly improve the frictional conditions and workpiece surface integrity at low cutting speeds. Finally, square textures on tool rake face were found to control the stability of BUE and minimize the friction at the tool-chip interface. This reduces the average coefficient of friction by 20-24% and flank wear by 41-78% and increases surface finish by 54-68% in comparison to an untextured tool.

Keywords: Machining performance, Stainless steel, Built-up edge, Friction, Surface texturing.

`

Acknowledgment

It would not have been possible for me to accomplish this task on my own, and so it is with much gratitude that I acknowledge the support, encouragement, and contributions of several important people in my life.

First and foremost, I would like to express my sincere gratitude to my supervisor Prof. Stephen Veldhuis for all of his invaluable guidance, support, and encouragement in reaching the goals that I set out to achieve during my Ph.D. studies at McMaster University. It was a great privilege to join Dr.Veldhuis`s research group and work with him. I would like also to thank my committee members Dr. Eugene Ng and Dr. Neslihan Dogan for their encouragement and valuable suggestions. I would also express my gratitude to Prof. Igor Zhitomirsky for becoming the external examiner of my Ph.D. comprehensive exam and providing me with useful advice.

I would like to thank the co-authors and collaborators of this research project: Dr. Abul Arif and Dr. Jose Paiva. Without their kind help, it would have been difficult to make this research go as smoothly as it did. I also wish to express my gratitude to my colleagues at the McMaster Manufacturing Research Institute (MMRI) for their support in making the journey of pursuing a Ph.D. degree a joyful one for me.

I convey special acknowledgment and gratitude to the Natural Sciences and Engineering Research Council of Canada (NSERC) under the CANRIMT Strategic Research Network Grant NETGP 479639-15 for their financial support.

`

Lastly, but most importantly, I would like to express my heartful thanks and gratitude to my mother, my husband and my daughter for their continuous encouragement and endless help. You provided the greatest motivation for this Ph.D. thesis.

`

Declaration of Academic Achievement

This dissertation was used to fulfill the requirements of a Ph.D. degree. All the research was conducted from September 2016 to December 2019. The dissertation has been prepared in accordance with the regulations for a sandwich thesis format or as a compilation of research papers stipulated by the faculty of graduate studies at McMaster University. This dissertation has resulted in six appended publications. These papers are listed below:

Paper I

Yassmin Seid Ahmed, Jose Mario Paiva, Danielle Covelli, Stephen Clarence Veldhuis, "Investigation of Coated Cutting Tool Performance during Machining of Super Duplex Stainless Steels through 3D Wear Evaluations" Published in Coatings journal. Volume 7, 2017, pages 127–142, ISSN 0708-0127. https://doi.org/10.3390/coatings7080127.

Yassmin Seid Ahmed performed the cutting experiments as well as the metallographic, SEM, XRD and Alicona studies, and wrote the paper, Jose Mario Paiva planned experimental procedure, Danielle Covelli performed XPS studies, and Stephen Clarence Veldhuis was the supervisor of the research team.

Paper II

Yassmin Seid Ahmed, Jose Mario Paiva, Stephen Clarence Veldhuis, "Characterization and prediction of chip formation dynamics in machining austenitic stainless steel through supply of a high-pressure coolant" Published in The International Journal of Advanced Manufacturing Technology, Springer. Volume 102, 2019, pages 1671–1688, ISSN 0268-3768. https://doi.org/10.1007/s00170-018-03277-7.

`

Yassmin Seid Ahmed performed the cutting experiments and the metallographic, SEM, EBSD and Alicona studies, planned experimental procedures and wrote the paper. Jose Mario Paiva reviewed the manuscript. Stephen Clarence Veldhuis supervised the research team.

Paper III

Yassmin Seid Ahmed, Jose Mario Paiva, Bipasha Bose, Stephen Clarence Veldhuis, "New observations on built-up edge structures for improving machining performance during the cutting of superduplex stainless steel" Published in Tribology International, Elsevier. Volume 137, 2019, pages 212–227. https://doi.org/10.1016/j.triboint.2019.04.039.

Yassmin Seid Ahmed performed the cutting experiments and metallographic, SEM, EBSD, XRD analysis, nanohardness test, planned experimental procedures and wrote the paper. Jose Mario Paiva reviewed the manuscript. Bipasha Bose performed nanohardness maps of BUE samples. Stephen Clarence Veldhuis supervised the research team.

Paper IV

Yassmin Seid Ahmed, German Fox-Rabinovich, Jose Mario Paiva, Terry Wag, Stephen Clarence Veldhuis, "Effect of Built-Up Edge Formation during Stable State of Wear in AISI 304 Stainless Steel on Machining Performance and Surface Integrity of the Machined Part" Published in Materials Journal. Volume 10, pp 1230–1245. https://doi.org/10.3390/ma10111230.

Yassmin Seid Ahmed performed the cutting experiments as well as XRD, metallographic, SEM, and Alicona studies; and wrote the paper. German Fox-Rabinovich designed cutting experiments. Jose Mario Paiva reviewed the paper. Terry Wagg prepared the samples using the water jet machine. Stephen Clarence Veldhuis supervised the research team.

`

.

Paper V

Yassmin Seid Ahmed, Jose Paiva, Abdul Arif, Fred Amorim, Ricardo Torres, Stephen Clarence Veldhuis, “Effect of laser micro- scale textured tools on tool-chip interface performance and surface integrity during turning of austenitic stainless steel” Published in Applied Surface Science Journal. Volume 510. https://doi.org/10.1016/j.apsusc.2020.145455.

Yassmin Seid Ahmed performed the cutting experiments as well as FIB, metallographic, SEM, EBSD, XRD analyses, nanohardness test, planned experimental procedures and wrote the paper. Jose Mario Paiva and Abul Arif reviewed the manuscript. Fred Amorim and Ricardo Torres applied LST on the cutting tools. Stephen Clarence Veldhuis was the supervisor of the research team.

Paper VI

Yassmin Seid Ahmed, Stephen Clarence Veldhuis, “Effects of High pressure coolant on machining temperature and machinability of AISI 304 stainless steel”, Published in the Proceedings of The Canadian Society for Mechanical Engineering International Congress 2018, Toronto, Canada, 1-8, May 2018.

Yassmin Seid Ahmed performed the cutting experiments, metallographic, SEM, EBSD and Alicona studies, planned experimental procedures and wrote the paper. Stephen Clarence Veldhuis was the supervisor of the research team.

`

Table of Contents

Lay Abstract iii

Abstract...iv

Acknowledgment...v

Declaration of Academic Achievement..vii

Table of Contents x

List of Figures...xix

List of Tables..xxx

List of Abbreviations and Symbols xxxiii

Chapter 1 : Introduction 1

1.1 Background...1

1.1.1 Stainless Steels 2

1.1.2 Machining and Machinability..6

1.1.3 Machining Performance 9

1.1.4 Adhesion Mechanism 14

1.1.5 Control Built-Up Edge 20

`

1.2 Research Gaps 26

1.3 Motivation and Research Objectives...27

1.4 Thesis Organization..29

Chapter 1..30

Chapter 2:………. 30

Chapter 3:……… 31

Chapter 4:…………. 31

Chapter 5:………. 32

Chapter 6:……….. 33

Chapter 7:………. 34

Appendix A:……. 34

Appendix B:……..34

1.5 Note to the Reader 34

References 35

Chapter 2 : Investigation of Coated Cutting Tool Performance during Machining of Super Duplex Stainless Steels through 3D Wear Evaluations 45

Abstract...46

`

Keywords..47

2.1 Introduction 47

2.2 Experimental procedure..50

2.2.1 Workpiece Material 50

2.2.2 Cutting Tools and Cutting Fluid..51

2.2.3 Experimental Machine Techniques 52

2.3 Results and Discussion...54

2.3.1 Tool Life Measurements..54

2.3.2 Chip Characteristics..56

2.3.3 The Composition of Tribo Films and Frictional Conditions 59

2.3.4 Tool Wear Analysis...60

2.3.5 Machined Workpiece Characteristics..69

2.4 Conclusions 71

Acknowledgments 72

Author Contributions...73

References 73

`

Chapter 3 : Characterization and prediction of chip formation dynamics in machining austenitic stainless steel through supply of a high-pressure coolant.............................79

Abstract...80

Keywords...81

Nomenclatures...81

3.1 Introduction 83

3.2 Experimental procedure...85

3.2.1 High pressure coolant and machining system 85

3.2.2 Workpiece material characterization..88

3.2.3 Cutting tests..89

3.3 Experimental results and discussion..91

3.3.1 Chip morphology: effect of high pressure coolant...91

3.3.2 Chip morphology: effect of tool wear 98

3.4. Understanding the chip breaking process...105

3.4.1 Chip breaking theory 105

3.4.2 Chip upcurl radius measurement 107

3.5 Theoretical modelling of chip curling 108

`

3.5.1 Theory…………...109

3.5.2 Model assumptions...111

3.5.3 Derivation based on shear plane theory.......................................112

3.5.4 Derivation based on structural mechanics theory.........................115

3.5.5 Model validation..117

3.6 Conclusions...120

Acknowledgments...121

References..122

Chapter 4: New observations on built-up edge structures for improving machining performance during the cutting of superduplex stainless steel.................................129

Abstract...130

Keywords...130

4.1 Introduction...130

4.2 Experimental work..134

4.2.1 Workpiece material and cutting conditions..................................134

4.2.2 Cutting tests and characterization methods..................................136

4.3 Results and discussions...138

`

4.3.1 Investigation of BUE formation 138

4.3.2 In-detail evaluation of BUE structures 144

4.3.3 Inspection of machining outputs for existence of BUE.................................154

4.4 Conclusions 160

Acknowledgments 162

References 162

Chapter 5: Effect of Built-Up Edge Formation during Stable State of Wear in AISI 304 Stainless Steel on Machining Performance and Surface Integrity of the Machined Part169

Abstract..170

Keywords...171

5.1 Introduction 171

5.2. Experimental Procedures...175

5.2.1 Work material, Cutting Tool, and Cutting Parameters.....................................175

5.2.2 Experimental Machine Techniques 177

5.3 Results and discussion..179

5.3.1 Investigation of the BUE in the steady state zone...179

5.3.2 Effect of BUE formation on machined surface and chip undersurface.........184

`

5.3.3 Effect of BUE formation on residual stresses and peak half width..............186

5.3.4 Effect of BUE formation on cutting forces and chip formation....................189

5.4 Conclusions 191

Acknowledgments 192

Author Contributions...192

References 193

Chapter 6: Effect of laser micro- scale textured tools on tool-chip interface performance and surface integrity during turning of austenitic stainless steel 198

Abstract..198

Keywords..199

6.1 Introduction 199

6.2 Material and methods 203

6.2.1 Tool and workpiece material 203

6.2.2 Textured tools preparation...204

6.2.3 Testing and characterizations 208

6.3 Results and discussion...210

6.3.1 Cutting force components and average friction coefficients.........................210

`

6.3.2 Wear examination of textured tools 213

6.3.3 Chip formation...222

6.3.4 Influence of cutting tool state on Surface integrity 228

Conclusions 236

Acknowledgment..237

References 237

Chapter 7: Conclusions and Future Work 246

7.1 General Conclusions..246

7.2 Research Contributions 249

7.3 Recommendations for Future Research..251

Appendix A: Effect of HPC on tool life, BUE formation, and cutting forces 253

Preface 253

A.1 Cutting forces 253

A.2 Tool Life..255

A.3 BUE formation 256

A.4 Machined surface roughness 259

A.5 Remarks..260

`

References 260

Appendix B: Effect of laser micro- scale textured tools on the tool-chip interface performance during stainless steel machining under a dry condition 262

Preface 262

B.1 Flank wear resistance 262

B.2 Tool wear morphology 263

B.3 Remarks 268

References 269

`

List of Figures

Figure 1-1Classification of stainless steels 3

Figure 1-2 view of flank wear and crater wear 10

Figure 1-3 Typical stages in flank wear.. 10

Figure 1-4 tool wear mechanisms 11

Figure 1-5 Built-up edge (BUE) and Built-up layer (BUL) 15

Figure 1-6 Built-up edge (BUE) structure 16

Figure 1-7 Variation in BUE dimensions as a function of cutting speed, identifying the stable and unstable regimens and the critical cutting speed.. 18

Figure 1-8 Classification of different texture generation techniques... 23

Figure 2-1 Microstructure of the SDSS UNS S32750 showing the distribution of each phase (Ferrite is continuous phase with 36% while Austenite is second phase with 64%). Magnification is 200X…………………………………………………………………………………...51

Figure 2-2 Relation between flank wear and cutting length for uncoated and coated carbide inserts during machining SDSS. Additionally, the flank surface for each tool is presented at the end of tool life 55

Figure 2-3(a) General macrograph aspect of the chips, SEM images obtained with carbide inserts with (b) uncoated; (c) TiCN+Al2O3; and (d) AlTiN... 56

`

Figure 2-4 XPS data for tribo-films formed on the worn surface of AlTiN coating (a) XPS spot on the AlTiN tool rake face; (b) AlTiN XPS high resolution spectra line for Ti2p; (c) AlTiN XPS high resolution spectra line for AI2s; and (d) AlTiN XPS high resolution spectra line for O1s .. 58

Figure 2-5 Alicona 3D images of the cutting tools after machining of SDSS (a) before, and (b) after etching showing the details of the cutting tools with their major wear mechanisms 59

Figure 2-6 Comparison of total wear volume and BUE volume for uncoated and coated tools (a) before, and (b) after etching 62

Figure 2-7 SEM images of PVD AlTiN coated insert after machining SDSS. (a) cutting tool before etching; (b) cutting tool after etching; (c–e) cutting tool with different magnifications ... 64

Figure 2-8 SEM images of CVD TiCN + Al2O3 coated insert after machining SDSS. (a) cutting tool before etching; (b) cutting tool after etching; (c–f) cutting tool with different magnifications 66

Figure 2-9 SEM images of uncoated insert after machining SDSS. (a) Flank face after etching; (b) cutting tool before etching; and; (c) cutting tool with chipping 66

Figure 2-10 Three dimensional and SEM images of the machined surface obtained by (a) uncoated insert; (b) TiCN + Al2O3; (c) AlTiN insert and corresponding cutting forces and surface roughness values 71

Figure 3-1 The HPC tool holder; (b) direction of HPC on the cutting tool; (c) drawing of tool holder showing the geometry of nozzles [46] 86

`

Figure 3-2 The machining process used in the experimental work with the high pressure coolant supply 87

Figure 3-3 The microstructure of AISI 304 with an austenitic structure 89

Figure 3-4 Chip formation at different cutting conditions; (a) dry, (b) conventional coolant, (c) HPC (35 bar); HPC (70 bar) 92

Figure 3-5 Chip breaking under various cooling conditions, associated with chip undersurface obtained with (a) dry; (b) conventional coolant; (c) HPC of 35bar; and (d) HPC of 70 bar 93

Figure 3-6 SEM and BSE images of chip cross sections associated with orientations maps obtained under different cutting conditions (a-b) Dry; (c-d) Conventional coolant; (e-f) HPC of 35 bar; and (g-h) HPC of 70 bar 95

Figure 3-7(a) Parameters of chip serration, (b) the values of maximum and minimum chip thickness for different cooling conditions, (c-f) micrographs of serrated chip cross sections showing the average distance between segments at (c) dry; (d) conventional coolant; (e) HPC of 35 bar; and (f) HPC of 70 bar 96

Figure 3-8 Tool-chip contact length 98

Figure 3-9 Correlation between tool-wear degree and chip-segmentation degree associated with SEM of chips 100

`

Figure 3-10(a) Lamellae on the free surface of a continuous chip; (b) folds formed on the free surface of a continuous chip produced under the same conditions as the chip in a; (c) saw-tooth form chip under the same conditions as the chips in a and b... 102

Figure 3-11 Chip morphology obtained in (a) dry and (b) HPC; (A-D) and (F-I) images of free chip surface, generated with new tool and (E-J) with worn tool 104

Figure 3-12 (a-c) Parameters of chip curl radius; (a) chip up side radius; (b) Chip up curl radius; (c) twisting. [45], and (d) the formation of segmented chips under HPC supply [15] 106

Figure 3-13 Chip upcurl radius under different cooling conditions; (a) dry; (b) conventional coolant; (c) HPC of 35 bar; and (d) HPC of 70 bar 108

Figure 3-14(a) Graphical representation of shear plane model and (b) deformation axes for chip curling phase [42] 112

Figure 3-15 (a) The force model for HPC, hitting chip and (b) the free body diagram of chip curling 115

Figure 3-16 Comparison between the average values of theoretical and experimental chip curl radius with (a, b) HPC of 35 bar and (c, d) HPC of 70 bar.. 118

Figure 4-1 Microstructure of the SDSS UNS S32750 at 100× showing the distribution of each phase 135

`

Figure 4-2 (a) and (b) cutting tool cross section, c) the mounted tool showing the position of built-up edge, and (d) backscattered image of the cutting tool cross section 137

Figure 4-3 Flank face and rake face of the cutting tools for the cutting speeds of (a) 60 m/min, (b) 100 m/min, and (c) 150 m/min 139

Figure 4-4 (a) height and area measurements of the BUE at different cutting conditions, (b) and (c) Alicona images, showing the measurements of BUE height and area, respectively............ 140

Figure 4-5(a) relation between flank wear, cutting speed, and cutting length, (b-d) SEM images of the cutting tools after cutting length of 2000 m at different cutting speeds 141

Figure 4-6(a) setup of high speed camera, (b) and (c) micrographs of built-up edge obtained at 60 m/min and 150 m/min, respectively.. 142

Figure 4-7(a) profiles of cutting tool edge after cutting length of 1000 m at different cutting speeds, (b) flank and rake faces of the cutting tool after removing the adhesion layer, and (c) corresponding cutting edge profile after removing the a adhesion layer.................................. 144

Figure 4-8 Morphology of the BUE samples obtained at different cutting speeds 145

Figure 4-9 Temperature distribution on the tool and chip during machining SDSS at (a) 60 m/min and (b) 150 m/min 146

Figure 4-10 Backscattered images of the BUE cross section obtained at (a-e) 60 m/min and (f-i) 150 m/min, showing cracks formation... 148

`

Figure 4-11Nanohardness results of measurements done on the built-up edge cross sections after machining with different cutting speeds. (a, c) BUE sketch, showing the locations of the individual indents, and (b, d) nanohardness distribution maps.. 149

Figure 4-12 Phase maps of (a) built-up edge obtained at 60 m/min, (b) built-up edge obtained at 150 m/min, and (c) original material before the machining test.. 150

Figure 4-13 Microstructure of built-up cross sections obtained at different cutting speeds (a) and (b) orientation maps of BUE obtained at 60 m/min and 150 m/min, respectively, (c) and (e) are representative pole figures for ferrite phase and (d) and (f) are representative pole figures for austenite phase 153

Figure 4-14 (a) Relation between cutting force components and contact length for different cutting speeds, (b) and (c) cutting forces variations collected at 60 m/min and 150 m/min, respectively, and (d) and (e) thrust force variations collected at 60 m/min and150 m/min, respectively 155

Figure 4-15(a) General macrograph aspect of the chips, and chip undersurface obtained at (b) 60 m/min, (c) 100 m/min, and (d) 150 m/min 156

Figure 4-16 Chip microstructure obtained at (a) 60 m/min and (b) 150 m/min 157

Figure 4-17 Microhardness profile of the machined surface after machining (a) with different cutting speed and (b) high and low BUE 159

Figure 4-18 (a) Three dimensional and (b) SEM images of the machined surface obtained at different cutting speeds, associated with surface roughness values 160

`

Figure 5-1 The microstructure of AISI 304 with an austenitic structure 176

Figure 5-2 Method of sample preparation for XRD analysis 178

Figure 5-3 Relation between flank wear and cutting length for the uncoated carbide insert during machining AISI 304 stainless steel, combined with progressive SEM studies showing the BUE formation 181

Figure 5-4(a) Alicona 3D images of the cutting tool during steady state zone showing BUE propagation, combined with (b) BUE volume 182

Figure 5-5 Relation between BUE height and cutting length for uncoated insert during steady state zone. Additionally, the flank surface presented for some points in the steady state zone . 182

Figure 5-6 (a) SEM image of BUE region, (b) EDS spectrum analysis of the BUE zone on the rake face, (c) EDS spectrum analysis of the tool surface and (d) color map of the Fe and Cr elements on the BUE region 183

Figure 5-7 Relation between surface roughness and cutting length during steady state zone.... 185

Figure 5-8 Relation between surface residual stresses and cutting length during steady state zone in cutting and feed directions 187

Figure 5-9 In-depth residual stresses profiles for five selected points in the steady state zone in (a) cutting direction and (b) feed direction 188

`

Figure 5-10 (a)Relation between Peak Half width and cutting length during steady state zone and (b) In depth peak half width profiles in cutting and feed directions for the first point of steady state zone.. 189

Figure 5-11 (a) Relation between cutting force and cutting length during steady state zone combined with SEM image of chip formation, (b) Cutting force variations and (c) Chip undersurface for two selected points in Figure 5-11(a) 190

Figure 7-1(a) Different shapes of textures and an example of sectional-profile of textures, (b) rake face region for mechanical micro-texturing, and (c) fabricated rake face mechanical micro-too……………..…………………………………………………………………………...206

Figure 7-2 (a) SEM images of textured tools before machining, (b) the three-dimensional atomic force microscope image and (c) the corresponding two-dimensional profile of different textured tools with 5 ± 0.2 μm in width, 20 ± 0.3 μm in pitch, and 1.5±1 μm in depth…………….. …..207

Figure 7-3 Atomic force microscope images of surface topography of (a) square, (b) perpendicular (c) parallel, (d) untextured tools, and (e) the corresponding average surface roughness………………………………………………………………………………....208

Figure 7-4(a) cutting force variation with cutting speeds, (b) tool-chip contact length, (c) feed force variation with cutting speeds, and (d) coefficient of friction with cutting speeds for different tools…………………………………………………….………………...………..211

Figure 7-5 SEM images of (a) untextured, (b) perpendicular, (c) parallel, (d) and square textured tools after cutting length of 1000 m at cutting speed of 60 m/min and (e) SEM images of

`

untextured and textured tools at cutting speed of 150 m/min……………………………………………………………………………………. …..214

Figure 7-6 Relation between flank wear and cutting length for square textured and untextured tools under cutting speeds of 60 m/min and 150 m/min, associated with SEM images of the cutting tools at the end of tool life…………………………………………………………………..……………………….217

Figure 7-7 (a) 3D progressive study of untextured and square textured tool for cutting speeds of 60 m/min and 150 m/min, and (b) BUE height variation with cutting length at cutting speed of 60 m/min for untextured and square textured cutting tools……………………………………… …..218

Figure 7-8 Illustration of FIB-examinations of (a) square texture and (b) plain on the rake face with adhering workpiece material. (A) an overview of the rake face, (B) the location for FIB cross section, (C) surface bottom, and (D) region of worn surface…………………………...220

Figure 7-9 Angle between chip flow and (a) perpendicular, (b) parallel, and (c) square textured tools………………………………………………………………………………………..222

Figure 7-10 Back scatter electron (BSE) images of (a) chip free surfaces, (b) chip undersurfaces and (c) chip cross-sections obtained with (A) untextured, (B) perpendicular, (c) parallel, and (D) square textured tools……………………………………………………………………….. …225

Figure 7-11 (a, b) BSE images of the chip free surface obtained with the (a) square textured and (b) untextured tools, (c) an example of the geometrical feature of segmented chips, and (d)

`

variation of segmentation frequency and percentage of segmentation for different textured and untextured tools at various cutting speed………………………………………………… …..227

Figure 7-12 (a) Average surface roughness obtained at different cutting speeds for different textured and untextured tools and (b) SEM images of the machined surface obtained by square textured and untextured tool………………………………………………………….. …..229

Figure 7-13 Optical images of machined workpiece subsurface obtained with (a, b) untextured and (c, d) square textured tools at cutting speed of (a, c) 60 m/min and (b, d) 150 m/min……………………………………………………………………………………..231

Figure 7-14 (a) Typical pole figures obtained from EBSD analysis of the subsurface layers (square textured tool, new tool, vc = 60 m/min) and (b, c) texture index of the machined workpiece surfaces computed from pole figure analysis obtained with (b) new and (c) worn tools………………………………………………………………………………………232

Figure 7-15 Detailed EBSD orientation map and pole figure maps of the heat affected zone of the machined workpiece subsurface obtained with an untextured tool at 60 m/min………...……..233

Figure 7-16 Nanohardness distribution of the machined subsurface obtained with different textured and untextured tools at cutting speeds of 60 m/min and 150 m/min……………………. ……………………………………………………………..235

Figure A-1(a) Relation between cutting force and time at optimum cutting conditions and (b) associated cutting force variations for different cooling conditions…………………….. …..254

`

Figure A-2 Relation between flank wear and machining time during machining AISI 304. Additionally, SEM image for cooling condition is presented at the end of tool life (v = 60 m/min, a = 0.5mm, f = 0.1 mm/r)………………………………………………………………… 256

Figure A-3 Tool wear morphologies under different cooling conditions (v = 60 m/min, a_p = 0.5mm, f = 0.1 mm/r)…………………………………………………….. 258

Figure A-4 BUE height variations obtained with different cooling conditions (v = 60 m/min, a = 0.5mm, f = 0.1 mm/r)……………………………………………………………………...259

Figure A-5 Average surface roughness obtained at different cooling conditions……………... 259

Figure B-1 Relation between flank wear and cutting length for different textured and untextured tools at a cutting speed of 60 m/min…………………………………………………………263

Figure B-2 SEM images of untextured tools after cutting length of 1000 m at cutting speed of 60 m/min. 264

Figure B-3 SEM images of (a) parallel, (b) perpendicular and (c) square textured tools after cutting length of 1000 m at cutting speed of 60 m/min 266

Figure B-4 SEM images of (a) parallel, (b) perpendicular and (c) square textured tools after cutting length of 1000 m at cutting speed of 150 m/min 268

`

List of Tables

Table 1-1 Relative machinability ratings 8

Table 1-2 Mechanical properties of stainless steel and carbon steel 8

Table 2-1 Chemical composition and mechanical properties of S32750........50

Table 2-2 Characteristics of coating systems........ 52

Table 2-3 Cutting characteristics during the turning operation of SDSS [17]........ 57

Table 2-4 EDS analysis associated with cutting tools in Figures (2-7)–(2-9) 62

Table 2-5 A summary of the main causes and suggested solutions of different wear mechanisms observed for uncoated and coated tools 67

Table 3-1 Chemical composition and mechanical properties of AISI 304 stainless steel........88

Table 3-2 Cutting characteristics at various cooling conditions 98

Table 3-3 Chip characteristics at various cooling conditions and various flank wear values 101

Table 3-4 Validation of Experiment 119

Table 4-1 Chemical composition and mechanical properties of S32750 [36]........134

Table 4-2 Tool geometry and cutting parameters used in cutting experiments........ 135

`

Table 4-3 Average grain size values of BUE samples obtained at different cutting speeds in comparison with the original material 151

Table 4-4 Chip characteristics obtained at different cutting speeds 158

Table 5-1 Chemical composition and mechanical properties of AISI 304 [29]…………… …..175

Table 5-2 Parameters for X-ray residual stress analysis... 178

Table 5-3 EDS analysis of surface on the tool.. 184

Table 5-4 Machined surface and chip undersurface of five selected points in the steady state zone 185

Table 7-1 Mechanical properties of uncoated cemented carbide tool…………………………..…………………………………………………………….203

Table 7-2 Chemical composition, material properties and microstructure of AISI 304 stainless steel……………………………………………………………………………………… …..203

Table 7-3 Experimental setup and machining parameters used for laser system…………………………………………………………………….……………….205

Table 7-4 Tool geometry and cutting parameters used in cutting experiments……………………………………………………………………………………..209

Table 7-5 Chip up curl radius under different cutting conditions…………………………………………………………………………………223

`

Table B-1 EDS analysis related to Figures B-2 and B-3…………………………………………………………………………………………...266

`

List of Abbreviations and Symbols

BUE	Built-up edge
VB_B	Flank wear
SDSS	Superduplex stainless steel
HPC	High pressure coolant
AE	Acoustic emission
WT	Wavelet transform
ANN	Adaptive neuro-fuzzy inference system
ANFIS	Adaptive neuro-fuzzy inference system
LST	Laser surface technology
HAZ	Heat affected zone
SEM	Scanning electron microscope
EDS	Energy dispersive spectroscopy
EBSD	Electron backscatter diffraction
XRD	X-ray diffraction

`

Chapter 1 : Introduction

1.1 Background

Stainless steels are extensively used in different applications ranging from health appliances to automotive and chemical industries [1], [2] due to their outstanding corrosion resistance and high mechanical strength [3]. However, these materials are considered to be difficult to cut due to their high tensile strength, high work hardening rate, poor thermal conductivity and poor tribological performance. In addition, they also feature a high friction coefficient, cutting temperature and tendency of the workpiece material to adhere to the cutting tool, producing a built-up edge (BUE).

The developed BUE can lead to a change in the tool geometry and affect tool life and surface integrity [4]. Depending on its condition, the presence of a BUE may decrease or increase the cutting tool`s life. The structural stability of a BUE is low and its intermittent build up and breakage can cause cracking and damage on the tool surface [5]. At the same time, a thin and stable BUE can be used to protect the tool from wear by forming a thin protective film reducing the friction at the tool–chip and tool-workpiece interfaces[6]. Furthermore, a BUE can act as a burnishing tool, reducing the irregularity of the surface and enhancing the surface finish. However, since the BUE is generally not permanently attached to the cutting edge, it periodically becomes detached, sometimes adhering to the machined surface, and thus reducing the final surface quality for the produced part.

`

At the present stage, few research works have attempted to examine the BUE structures at different cutting speeds in any significant detail, particularly to assess the potential protective effect of BUE during stainless steel machining. Furthermore, no systematic study has been found to monitor and control the stability of the BUE to reduce friction during the machining process. Consequently, the current research strives to develop a means to monitor and control BUE formation during stainless steel machining to ensure high productivity and quality of the machined part. After demonstrating the utility of the BUE monitoring system, tools with different texture patterns will be generated on the tool rake face to control the adhesion and reduce the friction during the machining process. The performance of these tools will be compared to evaluate the advantage of different surface textures and to establish a guideline for selecting the most appropriate one.

1.1.1 Stainless Steels

Stainless steels do not constitute a single, well-defined material, but instead consist of several families of alloys with a characteristic microstructure, composition, and range of properties. The common feature of these alloys is the presence of about 11% Cr that provides high corrosion resistance, which is the chief characteristic of stainless steel [7]. They are called stainless, because, they develop a colorless, thin and hard adhesive chromium oxide Cr_2O_3 film in the presence of air (O_2) which retains the metal`s luster [8]. This film is self-healing since it is up again after the surface is scratched [7]. Several alloying elements such as Ni, Mn, Si, Mo, Cu, S, Se, P, etc., can be added to the Fe-Cr matrix to control its microstructure. There are well over 150 different types of stainless

`

steel, of which about 15 grades are the most commonly used [9]. Stainless steel is formed into coils, sheets, plates, bars, wire, and tubing. It is used in cookware, cutlery, surgical instruments, industrial equipment, automotive and aerospace structural alloy, and as a constructional material in large buildings [2].

Stainless steels can be divided into five families (Figure 1-1). Four of them are based on their characteristic microstructures: austenitic, ferrite, martensitic or duplex. The remaining family of precipitation-hardenable (PH) alloys are characterized according to the type of heat treatment used. All stainless steels have a high corrosion resistance, which becomes even better as the Cr content increases. The addition of Ni (and Mo) also improves corrosion resistance, making stainless steels suitable for more corrosive environments [10]. Based on these properties stainless steel is commonly used in marine applications, petrochemical plants, desalination plants, heat exchangers and papermaking. Two types of stainless steel are investigated in this thesis, austenitic and superduplex. Accordingly, the literature review will focus only on these two families of stainless steel.

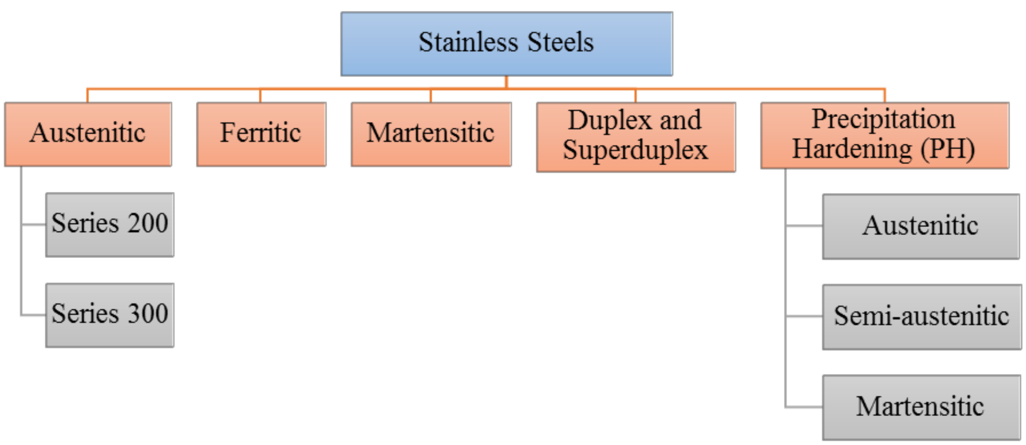

Figure 1-1Classification of stainless steels

`

Austenitic Stainless Steels

Carbon is usually kept at low levels ($C < 0.08\%$) in austenitic grades of steel. The chromium content ranges from 16-28% and nickel content from 3.5-32%. This chemical composition enables them to maintain an austenitic structure from cryogenic temperatures up to the melting point of the alloy. The key properties of these types of stainless steel include excellent corrosion resistance, ductility, and toughness [11]. The most commonly used austenitic stainless steels contain 18% chromium and 8% nickel. They have excellent corrosion resistance, weldability, formability, and ductility. In addition to excellent low-temperature properties, they are non-magnetic (if annealed) and hardenable by cold work only [8].

Higher chromium, nickel, molybdenum or copper may be added to improve corrosion and oxidation resistance (AISI-316, AISI-309, AISI-310, and 20Cb-3(N08020)). In 20Cb-3 stainless steel, Ni-level is high enough (38%Ni) to rate this type as a Ni-base alloy (serious 300). Titanium or Columbium (Cb) are also added to stabilize the carbon content and to prevent intergranular corrosion at high temperatures in alloys such as AISI-321 and AISI-347. Carbon levels are reduced in AISI-304L and AISI-316L to improve their weldability. Another category is the Mn-group (series 200), where a substantial quantity of Mn, usually in combination with high levels of Ni and in many cases N, is added. This group has lower cost and is deemed to have a somewhat lower quality as well [12].

`

Duplex Stainless Steels

In duplex stainless steels, carbon is kept at very low levels (C < 0.03%). They contain a relatively high chromium content, ranging from 21 to 26%, and a moderate amount of nickel, from 3.5 to 8% [3]. Since there is insufficient nickel to form a fully austenitic structure, the resulting combination of ferritic and austenitic structures is known as duplex. Most duplex stainless steels are composed of ferrite (50%) and austenite (50%) and contain molybdenum in the range of 2.5-4%. The original alloy of duplex stainless steel is AISI-329 (7-Mo) containing Cr, Mo, and sufficient Ni to provide the desired balance of both ferrite and austenite [9]. More recent versions such as 7-Mo Plus (S32950), Ferralium (S32550), and 2205 (S31803) alloys contain N and exhibit different ferrite/austenite balances [12]. Due to their microstructure, duplex stainless steels present a good combination of ferritic and austenitic steel properties: increased toughness, high mechanical strength, and high corrosion resistance in multiple environments, in addition to good weldability and formability. They are magnetic and have higher tensile and yield strengths than austenitic stainless steels [3].

SuperDuplex Stainless Steels

The term “SuperDuplex” was first used in the 1980’s to denote highly alloyed, high-performance Duplex steel with a pitting resistance equivalent of >40 (based on Cr% + 3.3Mo% + 16N%). With its high level of chromium, SuperDuplex steel provides outstanding resistance to acids, acid chlorides, caustic solutions and other environments in the chemical/petrochemical, pulp and paper industries, often replacing 300 series

`

stainless steel and nickel-based alloys. The chemical composition. consisting of high chromium, nickel and molybdenum content improves intergranular and pitting corrosion resistance. The addition of nitrogen promotes structural hardening by interstitial solid solution mechanism, which raises the yield strength and ultimate strength values without impairing toughness. Moreover, the two phase microstructure ensures higher resistance to pitting and stress corrosion cracking compared to conventional stainless steels.

1.1.2 Machining and Machinability

Machinability Concepts

The machinability of a material refers to how easily it can be machined using a cutting tool. Machinability is a term that has been suggested for the first time by Taylor [2] in the 1920s to describe the machining behavior of workpiece materials. Since that time, this term has been frequently used in literature, but seldom fully explained. It appears to have a variety of interpretations depending upon the viewpoint of the author using it. Mechanical and physical properties of the work material play an important role in the magnitude of energy consumption and temperature generated during cutting [13]. The effective mechanical properties such as tensile strength and ductility give some indication of the expected machinability characteristics, but cannot distinguish between the machinability of free cutting mild steel and austenitic stainless steel, since they have somewhat similar mechanical properties [12]. Material machinability is more or less dependent upon the selected machining process and its parameters. A material that is rated as having high machinability in one process may not be rated as machinable in

`

another. Moreover, a particular machining process may not be equally efficient for machining the same material under other cutting conditions [12].

From the previous discussion, the parameters affecting machinability are [12]:

- Work material preparation and its previous processing history.
- Tool material and geometry.
- Type of cutting process.
- Machining conditions.
- Type and quantity of cutting fluids.

Quantifying and Defining Criteria Which Make up Machinability

The common criteria for comparing material machinability include tool life, cutting forces generated and resulting surface integrity such as surface roughness [2]. An additional, frequently significant machinability criterion is the chip formation. Long thin ribbon chips, unless they can be subsequently broken up, can interfere with the tool and the workpiece leading to tool and workpiece damage as well as creating a hazardous area for workers [2]. This criterion is of vital importance in highly automated environments.

Since there is no unit of machinability, it is usually assessed by comparing one material with another taken as a reference. The American Iron and Steel Institute (AISI) determined machinability ratings for a wide variety of materials by comparing them to AISI-B1112, which has an assigned machinability rating of 100%. The machinability rating is determined by measuring the weighted averages of consumed power, surface finish and tool life for each material. A material with a machinability rating less than 100%

`

will be more difficult to machine than B1112 and one with a value greater than 100% would be easier to machine. Table 1-1 lists the relative machinability of some common alloys.

Table 1-1 Relative machinability ratings

Machinability rating	**Materials**
Excellent rating (200%-400%)	Al-alloys, Mg-alloys
Good rating (150%-250%)	Gray cast iron, brass, free cutting steel
Fair rating (~100%)	Low carbon steel, low alloy steel
Poor rating (50%-60%)	Free cutting 18-8 stainless steel
Very poor rating (20%-40%)	18-8 stainless steel, superalloys, Ti alloys

Adapted from [12]

Machining Challenges

Stainless steels are considered to be more difficult to machine than carbon steels due to their high tensile strength, high work-hardening rate, and low thermal conductivity (Table 1-2), which lead to a higher tool wear rate, difficulties with chip breakability, and poor surface finish [9].

Table 1-2 Mechanical properties of stainless steel and carbon steel

Material	**Grade**	**Tensile strength (MPa)**	**Elongation (%)**	**Thermal conductivity (W/mK)**
Austenite	S30400	516	40	16

`

Stainless Steel	S31600	485	40	16
Duplex	S32205	655	25	13
Stainless Steel	S32003	655	25	13
Carbon Steel	Grade 36	400	23	54
	Grade 50	450	21	58

Although stainless steels are relatively soft in the annealed condition and possess high ductility, they undergo extensive work hardening during machining [2]. For this reason, machining stainless steel alloys can result in excessive tool wear or breakage. The high ductility of these steels also presents an obstacle to efficient machining. Poor chip breakage can easily cause a built-up edge (BUE) to form on the cutting tool [15]. Additionally, the thermal conductivity of stainless steel is low, as shown in Table 1-2. Under these conditions, the heat can easily accumulate at the tool face [15]. Workpiece distortion and poor dimensional accuracy during machining can be affected by the high thermal expansion of these steels. The combination of these factors makes stainless steel difficult to machine [16].

1.1.3 Machining Performance

Tool Life and Wear Mechanisms

Tool wear is an important aspect of machining since it heavily influences manufacturing costs and product dimensional tolerance accuracy [15] and final part quality due to reduced surface integrity [2]. Tool wear is mainly concentrated in two regions of the

`

cutting tool: the flank face in relation to ‘flank wear’ and the rake face in relation to ‘crater wear’ [13], shown in Figure 1-2.

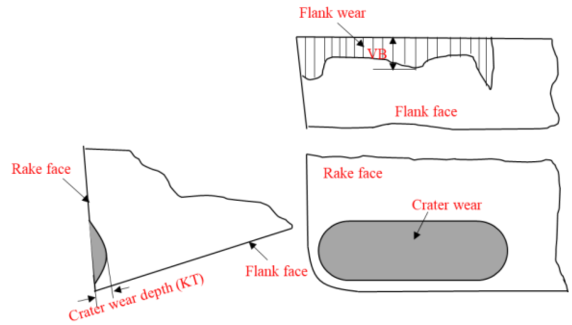

Figure 1-2 view of flank wear and crater wear

Flank wear occurs primarily due to abrasive wear mechanisms and it results in reduced dimensional accuracy and poor surface integrity of the machined part. According to ISO 3685:1993 and ISO 8688-2:1989, the tool life criterion is set to be VB_B=0.3 mm of flank wear. Figure 1-3 shows the characteristic tool wear curve. Crater wear decreases the strength of the cutting edge, enhancing the likelihood of tool breakage. Crater depth, KT, is most widely used to evaluate rake face wear, as shown in Figure 1-2.

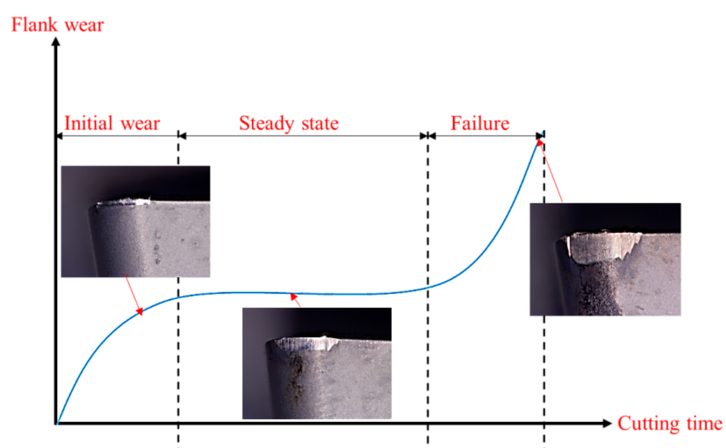

Figure 1-3 Typical stages in flank wear

`

The performance of a cutting tool is directly related to the condition of the flank and rake surfaces. Extensive flank or crater wear will result in either tool failure or poor surface integrity [17]. The mechanisms that cause either wear or damage to the cutting tool include adhesion, abrasion, diffusion, and oxidation (Figure 1-4).

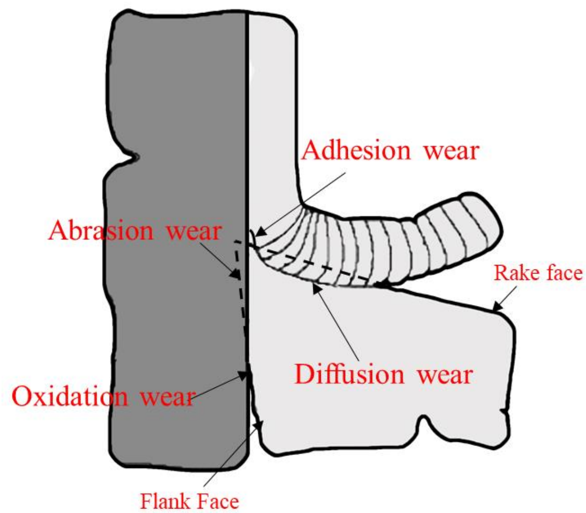

Figure 1-4 tool wear mechanisms

Adhesion develops when a built-up edge (BUE) or irregular material flow is present and microscopic debris are pulled out from the tool surface and dragged alongside the flow of the workpiece material, leaving small cavities on the surface of the tool. The areas worn by adhesion have a rough appearance. Abrasion is caused by friction between the hard particles of the workpiece material and the tool. The region of the tool worn by abrasion generally displays scratches parallel to the cutting direction. Diffusion involves the transfer of atoms from one material to another and is strongly dependent on the temperature and the chemical affinity between the materials of the workpiece and the tool in the region of the chip/tool/workpiece interface. The areas worn by diffusion have a

`

smooth appearance. Oxidation is often encountered on the tool during the development of notch wear at the end of the depth of cut region [15].

Many researchers have studied the wear mechanisms associated with the machining of different types of stainless steel using different coated and uncoated tools. Sobiyi et al. [18] studied the wear mechanisms of mixed ceramic and CBN tools during the hard turning of AISI 440B martensitic stainless steel (40-44 HRC). Abrasive wear was the dominant wear mechanism on the ceramic tools and abrasion and adhesion on the CBN tools. Corrêa et al. [19] conducted turning tests on martensitic S41000 and super martensitic S4142 steel using CVD TiC/TiCN/TiN tools. The main wear mechanisms were found to be diffusion and abrasion, although adhesion and abrasion were generally predominant as well. Krolczyk et al. [20] also studied duplex S31803 stainless steel machining with TiCN/Al_2O_3/TiN and found abrasion to be the most common wear mechanism. Selvaraj and Chandramohan [21] performed cutting tests on duplex S32205 stainless steel at different cutting speeds. The authors discovered that the main wear mechanism was abrasion at low cutting speeds and oxidation and diffusion at high cutting speeds. Junior et al. [22] studied different tool wear and wear mechanisms during UNS S32750 duplex stainless steel machining using PVD TiAlN tools. The authors noted that there was a high amount of adhered material on the cutting tool and that notch wear was responsible for tool failure. Junior and Eduardo [23] also performed experimental tests on precipitation hardened martensitic stainless steels using a milling process and TiAlN coated tools. The authors reported that adhesion was the most dominant wear mechanism

`

under a range of conditions including dry machining, minimum quantity level coolant and use of conventional flood coolant. They found there was less adhesion of workpiece material to the tool under a minimum quantity level coolant, which enhanced tool life.

Surface Integrity

The surface integrity of a machined workpiece can be described by three main parameters: residual stress, surface roughness, and work hardening in the surface zone. Residual stress is present in an elastic body after all external loads are removed. Machining generally involves a large amount of plastic deformation with extremely high magnitude and rate of strain [15]. Residual stress is induced in the surface layer by three things: the mechanical effect leading to severe plastic deformation, the thermal effect that causes thermal plastic flow and phase transformation. In most machining processes, the temperature does not exceed the phase transformation point, so the latter can be isolated [15]. High mechanical properties and severe work hardening of stainless steels, combined with low thermal conductivity, generate high cutting forces alongside high localized interfacial temperatures and adhesion in the cutting zone, which end up being the main reasons for poor surface integrity [1].

Few studies were performed on the surface integrity during stainless steels machining. Xavior et al. [24] reported that high work-hardening rate, high built-up edge tendency, and low thermal conductivity of stainless steels are responsible for poor surface finish of 304 austenitic stainless steel. Wang et al. [25] reported that BUE was mainly responsible for surface roughness deterioration during the cutting of 316L austenitic stainless steel.

`

Krolczyket al. [26] analyzed the microhardness of S322750 duplex stainless steel under dry and wet machining conditions. It was observed that wet machining of stainless steel reduces the surface integrity hardening depth. Also, Krolczyk et al. [27] investigated surface integrity under different cutting parameters during the dry turning process of 321 austenitic stainless steel. It was observed that an increase in cutting speed led to a corresponding increase of surface integrity hardening depth.

In summary, there are many wear mechanisms associated with machining stainless steel. However, based on the literature review, it can be concluded that the most dominant wear mechanism is adhesion. Adhesive wear is responsible for tool failure since BUE is inherently unstable. It breaks off upon reaching a certain size, causing catastrophic failure over time. In addition, sometimes the broken BUE welds on to the machined surface, affecting surface integrity.

1.1.4 Adhesion Mechanism

Adhesion on the cutting tool is caused by the high tool-chip interface temperature and high pressure [15]. Adhesive material formed during cutting is fundamentally important in machining processes because it affects the surface integrity, tool wear, dimensional tolerances, cutting forces, and chip formation. The workpiece material adheres to the rake face of the cutting tool in two different shapes, as shown in Figure 1-5. The first shape is known as a built-up edge (BUE), which is the adhesion of the workpiece to the cutting edge. The second is called a built-up layer (BUL), where the material adheres over wide areas of the tool`s rake face.

`

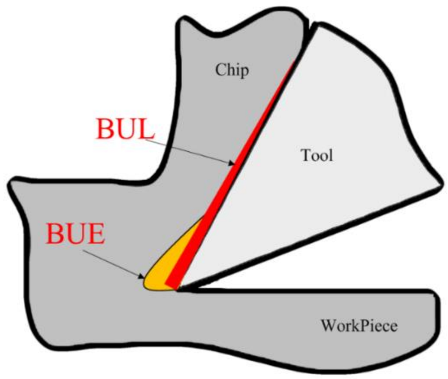

Figure 1-5 Built-up edge (BUE) and Built-up layer (BUL)

Built-Up Edge Structure

The extremely deformed material of the BUE that firmly sticks to the tool surface throughout the cutting test, is shown in Figure 1-6 [19]. Compressive stresses are so high during machining, that the bonds between the BUE and the tool are strong enough to block the material from sliding above the cutting tool. Trent and Wright [28] describe the BUE phenomenon: at the beginning of the cut, the material strongly adheres to the tool through atomic bonds that increase yield strength. At this stage, the shear stresses are not large enough to overcome these bonds. As the strains continue to rise, another layer of the workpiece material is formed. The repetition of this process generates a fully developed BUE. As the BUE evolves, its yield point also gradually increases until the shear stresses become insufficient to break these bonds [15]. Whenever shear stresses exceed the bond force of the BUE, the latter breaks off and becomes carried away by the chip or the workpiece. A new BUE then emerges, and the process is repeated. This phenomenon may also cause the emergence of some microcracks which then contribute to cutting tool failure. The hardness of the BUE is about two or three times higher than that of the metal

`

being machined. As a result, it can cut a layer of metal from the workpiece. Since it can be seen as an extension of the tool, the BUE also alters the tool geometry. Consequently, as it travels together with the tool, the BUE affects tool wear, forces acting on the tool and the ensuing surface finish [25].

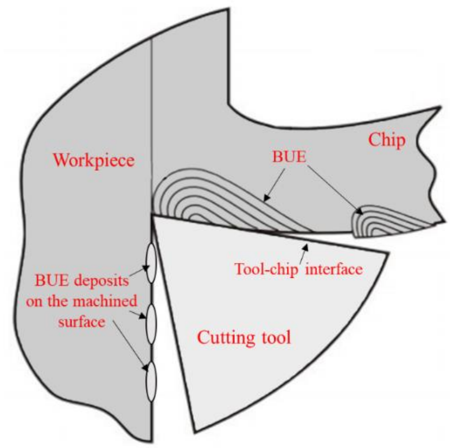

Figure 1-6 Built-up edge (BUE) structure

Factors Affecting Built-Up Edge Formation

Effect of adhesion:

The adhesion between the tool and the workpiece material is one of the most important factors, affecting the formation of a BUE. The mechanical aspect of adhesion is related to the development of large areas of intensive contact between the work material and the tool. The work material in the cutting zone, particularly near the cutting edge, is subjected to a high temperature and pressure [15]. Measurements of the tool forces indicate that the compressive stress on the face surface of the tool is highest at the contact area. It was also reported that a typical value of the mean compressive stress is around 3 GPa [15]. when a BUE is present, the cutting steel temperature at the tool-chip interface may reach 600^{o}C-

`

800^{o}C. Due to this extreme pressure and relatively high temperature, the workpiece material will plastically deform and create a continuous contact with both "hills and valleys" on the tool surface. This mechanical interlocking of asperities can certainly be a significant factor in adhesion. It has been demonstrated that higher roughness of the contact surfaces can promote material transfer or adhesion [25].

Effect of work material properties:

Number of researchers has indicated the importance of work hardening on the BUE formation. Medina-Clavijoa et al. [29] reported that strain hardening of the workpiece material could promote the growth of a BUE. However, Williams and Rollason, [30] show that work-hardening is not a sufficient explanation for the generation and growth of the built-up material. From a large number of cutting tests, they observed that pure metals and single-phase alloys do not normally form built-up edges, regardless of how high their work-hardening rates are. The authors showed that built-up material is only formed when cutting alloys have more than one phase. The absence of built-up material during the cutting of pure metals and single-phase alloys may possibly cause a separation between the chip and the tool within the cutting zone due to the homogenous nature of such materials. This boundary condition in metal cutting is usually interpreted as sliding.

Effect of temperature and cutting speed:

No matter how the BUE process is considered, cutting temperature remains a major factor [15]. The emergence and disappearance of the BUE are caused by the variations of the cutting temperatures at the tool-chip interface [31]. In practice, the formation and

`

disappearance of BUE is detected from the results of the variations of the cutting conditions, such as cutting speed and feed rate. As the cutting speed of the cutting process changes, so does the temperature of the cutting zone, tool and the workpiece. The literature review indicates that the BUE does not form at very low and high cutting speeds [5]. Figure 1-7 shows the variations in BUE dimensions along with the cutting speed.

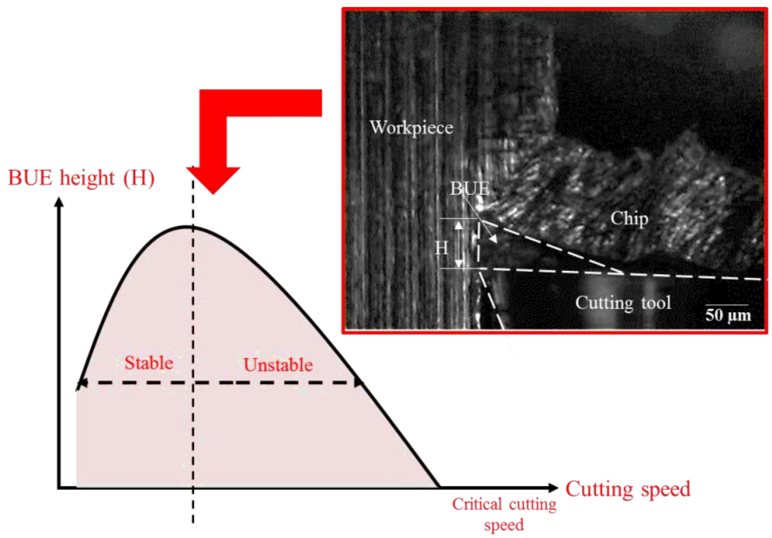

Figure 1-7 Variation in BUE dimensions as a function of cutting speed, identifying the stable and unstable regimens and the critical cutting speed

Effect of tool geometry, tool material, and cutting fluid:

A number of other parameters can also affect the formation of BUE, such as tool geometry, tool material, cutting fluid, etc. [32]. Tool geometry such as that of edge radius and rake angle, has a strong influence on the frictional conditions and consequently, on the BUE formation. A tool with a greater edge radius has a higher tendency to form a BUE [29]. This can be attributed to the fact that as the cutting edge radius is increased, so will the volume of stationary work material, the deformation zone and friction at the

`

cutting edge. Also, an increase of rake angle will reduce the cutting force and compressive stress on the rake face, which in turn will reduce BUE formation [31]. The thermal conductivity of the tool material also influences BUE formation. Decreasing conductivity increases the tool-chip interface temperature and provides favorable conditions for BUE to emerge [15]. Furthermore, Rahim and Sasahara [33] compared dry and lubricant machining and concluded that lubrication reduces work material adherence on the cutting tool to a greater degree than under the dry condition. Hence, lubrication is another parameter that decreases work material adhesion and the subsequent BUE formation.

Effect of the Built-Up Edge on Machining Performance

The influence of BUE formation on machining performance during the cutting process was the subject of several studies. Sukvitfayawong et al. [34] and Oliaei et al. [35] concluded that larger BUE sizes increase cutting force components and improve the workpiece quality. However, Sivaiah et al. [36] reported that the growth of BUE worsens the machined surface finish. The bad surface quality can be due to the instability of the BUE effectively changing the tool geometry during the machining process. In addition, upon breaking off, some of the BUE particles stick to the machined surface, further reducing the surface quality. Also, Kümmel et al. [37] observed that the development of BUE has a significant effect on the residual stresses of the machined workpiece. A noticeable increase in tensile residual stress was noticed with the rise of BUE height.

`

Furthermore, the instability of BUE has a significant effect on tool wear behavior; sometimes decreasing the tool life and sometimes enhancing it. Kumar et al. [38] noticed that high temperature generation during dry turning might intensify the formation of an unstable BUE on the cutting tool, which decreases tool life. Conversely, Niknam [39] observed that flank wear decreased when the expected BUE develops on the cutting edges during machining. BUE influences friction behavior at the tool–chip zone where it behaves as a new edge, preventing the chip from directly contacting the tool, thereby increasing cutting edge life.

1.1.5 Control Built-Up Edge

As discussed earlier, continuous appearance and disappearance of the BUE have a significant effect on machining performance. Thus, methods of controlling its size (to render it smaller and more stable) during the machining process were thoroughly investigated over the years. The different methods used to control the BUE formation are discussed in detail below.

Cutting Conditions

Nalbant et al. [49] investigated the effects of different cutting speeds on BUL and BUE during the machining of an aluminum alloy. They concluded that increasing the cutting speed decreased BUL and BUE formation but did not entirely control them. Bilgin [50] also found a minimum presence of BUE at higher speeds for AISI 310 austenitic stainless steel at a cutting speed range from 50 to 150 m/min. This phenomenon can be attributed

`

to the substantial reduction of the cutting time needed to dissipate the cutting temperature, thereby causing the latter to substantially rise. Zhou et al. [51] investigated the effect of feed rate on BUE formation during the high-speed turning of Inconel 718. The authors found that the BUE has a lower tendency to form at a low feed rate than at a higher feed rate due to an increase in the size of the plastic-deformation area at the interface of the tool and the workpiece. Chattopadhyay et al. [52] studied the effect of different coated tools on BUE formation during machining an aluminum alloy. They observed that a large BUE was formed on the uncoated and all the coated carbide inserts, excluding the diamond tool. The BUE height was lowest in the diamond-coated carbide tool.

High Pressure Coolant

Coolants play a significant role in improving lubrication as well as minimizing temperature at the tool–chip and tool-workpiece interfaces, which as a consequence, minimizes the formation of built-up during machining. Flood cooling is not effective in lowering the cutting temperature when machining stainless steel. The coolant does not readily access the tool-workpiece and tool–chip interfaces that are under seizure. Application of a high pressure coolant (HPC) jet has emerged as an effective liquid-based coolant technology for the machining of difficult-to-cut materials such as stainless steel. This system not only provides adequate cooling at the tool-workpiece interface but also effectively removes chips from the cutting area. The coolant jet under high-pressure is capable of creating a hydraulic wedge between the tool and the chip, deeply penetrating the interface at a speed exceeding even that of very high-speed machining. The

`

penetration of the high energy jet at the tool–chip interface reduces the temperature gradient and minimizes the seizure effect, offering adequate lubrication at the tool–chip interface with a significant reduction in friction and adhesion [53].

Several studies concluded that this technique improves machining performance compared to the use of a conventional coolant. Naves et al. [54] investigated the wear mechanism of coated cemented carbide tools during the turning operation of AISI 316 stainless steel. Cutting fluid was applied at various pressures (10, 15, and 20 MPa) between the chip and the tool at the rake face. It was observed that the lowest values of flank wear land and BUE height were obtained at a cutting fluid concentration of 10% and pressure of 10 MPa. Application of a HPC jet is recommended over dry machining during the turning of investigated stainless steel. Habak and Lebrun [55] also reported some results regarding the role of HPC on tool wear during the machining of AISI 316L stainless steel. Their study illustrated that in HPC assisted machining process of stainless steel, adhesive chips were not observed while in the dry machining process.

Surface Texturing

Various methods have been used to reduce BUE, including cutting conditions, tool materials, tool geometry, tool coatings, and HPC. However, cutting conditions can affect tool wear and surface integrity and the use of new tool materials is limited by their inherent characteristics, such as low impact toughness. Modifications of tool geometries can also affect the strength of the cutting tools. Moreover, the development of new coating materials usually requires a very long time to pass from the research to

`

application stages. In addition, many of the devices used to apply HPC are expensive and difficult to operate. Surface texturing of the cutting tool can be an efficient solution to address these issues [59].

Researchers have investigated nano/microtextures on rake faces of cutting tools. They found that by changing the topography of the tool surface, surface textures significantly affect the cutting mechanisms, reducing cutting forces, minimizing friction and increasing anti-adhesive properties and wear resistance. Applying a textured tool can reduce energy consumption, extend tool life, and improve surface finish.

Methods and classification:

Surface textures can be obtained using different techniques such as abrasive blasting, laser surface texturing (LST), micro-cutting, micro-electrical discharge machining, (EDM), micro electrochemical machining (ECM), and etc. [59]. Different techniques that can be used to generate a texture are summarized in Figure 1-11.

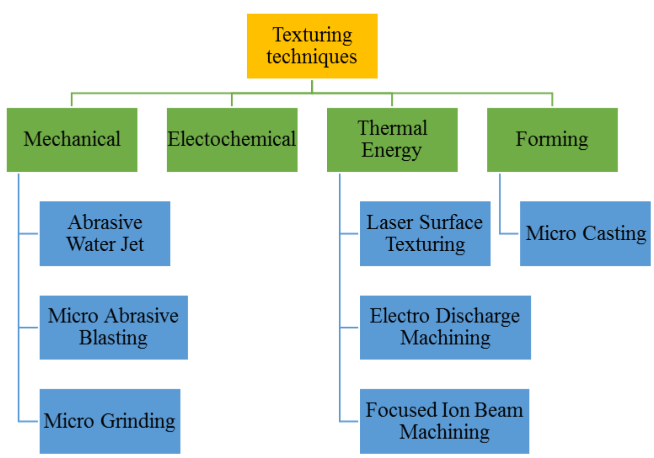

Figure 1-8 Classification of different texture generation techniques

`

LST is the most common method of applying surface textures. This method uses an ultra-high frequency impulse laser with high instantaneous power, such as a femtosecond laser, that can focus on a small area a few micrometers in size. Wet etching is widely used to obtain a nanostructure using photosensitive material to produce desired 2D shapes. The structure is then etched in a solution to trace the 2D shape. In micro-EDM and micro-ECM, the material is eroded by an electrical discharge or electrochemical reaction in an electrolyte. Micro cutting normally uses micro tools to micro mill textures on the surface of the material. Micro and nano-sized dimples and grooves are used in tool texturing to form different textures and different geometric shapes depending on how they are arranged. Some surface texture application methods, such as abrasive blasting and micro-EDM, do not result in a specific geometric shape [60].

Effects on adhesion and friction:

In recent years, surface texturing technology has been introduced to cutting tools with the goal of minimizing the friction during metal removal processes. The presence of microtextures on the tool surface can reduce the contact length of the chip sliding over the tool, which in turn reduces the friction. Reduction in contact length also favors lesser material adhesion, thereby improving tool life [61].

Kümmel et al. [62] found that micro-grooved tools improved the antiadhesion properties and machined surface finish during the cutting of AISI 1045. They reported that textures on the cutting tool stabilize BUE formation over the course of the machining process, leading to a better surface finish. Ling et al. [63] created rectangular shape surface

`

textures on the drill margins to machine a Ti6Al4V plate. The authors observed that texturing facilitates the removal of adhered chips, thus extending tool life. Rahim et al. [33] inspected the effects of textures on wear resistance of milling cutters. The cited study concluded that the micro-grooved tool exhibited the smallest flank wear compared to conventional cutting tools. The reduction in flank wear takes place in the micro-textured tool due to less adhesion between the tool and work material in comparison with the conventional milling tool. Ze et al. [64] reported that the coefficient of friction tended to decrease with the growth of cutting speed during the dry turning of Ti6Al4V alloy. It was observed that the coefficient of friction on the rake face of the textured tool decreased to a greater extent than at the flank face of a conventional tool. Niketh and Samuel [56] used micro-textured surfaces to minimize the friction between the contacts during the machining of a Ti6Al4V alloy. A micro-textured drilling tool was found to have a 16.33% lower friction coefficient than the conventional tool. Thomas and Kalaichelvan [65] observed an improvement in the machined surface quality during the turning of Aluminium (AA 6351) and mild steel (EN3B) with the textured tool. The enhancement in the surface finish was due to lower adhesion tendency during the machining process where a 23% and 16% reduction in surface roughness was observed following the machining of the mild steel and aluminum alloy.

Mechanism of better performance:

Various authors stated that there are basically two mechanisms involved in the improvement of the tribological properties between the chip and textured cutting tool

`

interface during machining. Under dry cutting conditions, the texture can reduce the tool-chip contact area and serve as a wear debris trap, which reduces friction. Under lubricated conditions, the texture enhances the effectiveness of the lubricant, which reduces friction and improves the anti-adhesive and wear resistance properties of the cutting tool. Several mechanisms contribute to minimizing friction under lubricated conditions. First, the texture serves as a storage for the lubricant, reduces the chance of lubricant leakage and releases the lubricant during the cutting process to minimize friction. Second, similar to dry cutting, wear debris can become trapped within the surface patterns, preventing wear debris from scratching and inducing plastic deformation [66].

1.2 Research Gaps

A literature review exposes the following three important gaps:

- There is minimal literature on understanding the machining performance during stainless steel machining. This will help to investigate the different wear mechanisms associated with machining stainless steels.
- Very few studies have been made regarding the mechanism of BUE formation during the machining process. The possible protective effect of BUE at various cutting speeds is not fully examined and the connection between BUE formation, tool wear, and machining outputs needs to be studied in more detail.
- No explanation as of yet has been provided in the literature that accounts for the BUE reduction achieved by surface texturing. Although, LST is a commonly

`

recommended method of reducing the size of a BUE, a solid explanation of this phenomenon is yet to be provided in the literature. Also, no studies so far described how surface texturing can be used to stabilize (control) the BUE formation and reduce friction during the machining process.

1.3 Motivation and Research Objectives

Stainless steels are commonly used in a large number of applications that range from health care to the automotive and chemical industries. Due to their chemical composition and microstructure, which provide high mechanical strength and thermal resistance as well as high ductility, the machinability of these alloys is generally poor, resulting in long production cycles and high tooling costs. A primary long-established issue with the machining of stainless steel alloys is they have a high tendency to generate BUE, an undesired phenomenon that describes the workpiece material adhering to the cutting tool during machining. Unstable BUE can cause machining issues such as poor machined surface finish, wider dimensional tolerancing and more importantly, accelerated tool wear. However, stable BUE formation can protect the cutting tool from further wear, improving the productivity of stainless steel machining. Thus, to maintain high productivity and quality of the machined part, it is necessary to control the BUE formation during stainless steel machining.

Motivated by the discussion above, the main objective of this research is to enhance the machinability of stainless steel by controlling the friction and adhesion mechanisms

`

during the machining process. Considering the gaps found in the literature review, the main research objectives are:

1. An in-depth understanding of machining performance during stainless steel machining.

- The tool life and wear mechanisms of uncoated and coated carbide tools are investigated during stainless steel turning. In addition, tribological performance is evaluated by studying chip characteristics such as thickness, compression ratio, shear angle, and undersurface morphology. The surface integrity of the machined surface is also investigated to measure surface roughness and to reveal the surface distortions created during the cutting process. **(Chapter 2)**
- The use of a high-pressure coolant supply (HPC) can lead to a considerable improvement in machining performance and process stability during the cutting of difficult materials such as stainless steel. For this reason, the chip morphology of stainless steel following the application of HPC directed at the tool–chip interface is compared to conventional coolant and dry conditions during the cutting tests. The influence of tool wear on the chip shape and type of chip segmentation is also investigated. **(Chapter 3)**

2. Investigation of the role of adhesion mechanisms on tool failure and surface integrity.

- Continuous appearance and disappearance of built-up edge (BUE) have a significant effect on tool wear behavior and surface integrity. For that reason, BUE patterns are studied when stainless steels are machined at different cutting speeds to assess the potential protective effect of BUE. In addition, microcrack

`

formation is analyzed to understand the mechanisms of BUE formation. The effect of cutting speeds and BUE formation on machining performance and machined surface quality are explained in further detail. **(Chapter 4)**

- The relationship between BUE formation and surface integrity during stainless steel machining is investigated in this study. Residual stresses, cutting forces and chip formation in the stable state of wear are studied to evaluate the effects of BUE formation on the machined workpiece surface. **(Chapter 5)**

3. Evaluation of the impact of surface texturing on controlling the friction and adhesion mechanisms.

- Surface textured tools can partially improve cutting performance by decreasing the cutting forces, contract length, and BUE formation. Therefore, a comprehensive study of the influence of different rake face textures (square, parallel and perpendicular) on the tool-chip interface performance is presented. In addition, BUE formation during the continuous turning process is investigated in-depth to account for the BUE stabilizations. **(Chapter 6)**

1.4 Thesis Organization

In compliance with the regulations of McMaster University, the main body of this dissertation is assembled in a sandwich thesis format composed of seven journal articles addressing the objectives outlined above. The structure of the thesis chapters and appendices is arranged as follows:

`

Chapter 1:

This chapter introduces the research area along with the motivation and relevant background information to frame the scope of work of this thesis.

Chapter 2:

This chapter consists of a journal article that was published in Coatings [67]:

Yassmin Seid Ahmed, et al. "Investigation of Coated Cutting Tool Performance during Machining of Super Duplex Stainless Steels through 3D Wear Evaluations" Coatings journal. Volume 7, 2017, pages 127–142, ISSN 0708-0127. https://doi.org/10.3390/coatings7080127.

Preface: This chapter presents a comprehensive description of the machining performance experienced during stainless steel machining. Tool life, wear mechanisms and tribological performance of different coated and uncoated cemented carbide inserts were compared and discussed during the turning of stainless steel. The performance of these cutting tools was evaluated in terms of tool life, chip formation, surface integrity and cutting forces. This research helps to understand the main reasons for different wear mechanisms acting during turning of stainless steels with different coated and uncoated tools.

`

Chapter 3:

This chapter consists of a journal article that was published in The International Journal of Advanced Manufacturing Technology [68]:

Yassmin Seid Ahmed, et al. “Characterization and prediction of chip formation dynamics in machining austenitic stainless steel through supply of a high-pressure coolant” The International Journal of Advanced Manufacturing Technology, Springer. Volume 102, 2019, pages 1671–1688, ISSN 0268-3768. https://doi.org/10.1007/s00170-018-03277-7.

Preface: This chapter analysed the chip forming mechanism and chip breakability of stainless steel with a supply of high pressure coolant (HPC) directed at the tool–chip interface. The experiments were conducted under different cooling conditions including: a dry condition, conventional coolant supply and two pressures of HPC. The chip formation mechanism, based on the microscopic images of the chip’s form, was evaluated in terms of chip characteristics, segmentation, and free surface. The second part of this chapter includes a three-dimensional (3D) theoretical model of chip curl during metal cutting, which evaluated the effect of HPC supply on chip geometry. The model was then validated with experimental results.

Chapter 4:

This chapter consists of a journal article that was published in Tribology International [69] :

`

Yassmin Seid Ahmed, et al. “New observations on built-up edge structures for improving machining performance during the cutting of superduplex stainless steel” Tribology International, Elsevier. Volume 137, 2019, pages 212–227. https://doi.org/10.1016/j.triboint.2019.04.039.

Preface: This chapter features an in-depth examination of the built-up edge (BUE) structures at different cutting speeds. This was done to evaluate the potential protective effect of a BUE. Also, a comprehensive investigation of the mechanism of BUE and microcrack formation was conducted using electron backscatter diffraction (EBSD) and nanoindentation methods. The effect of cutting speeds and BUE formation on machining performance and machined surface quality was also studied.

Chapter 5:

This chapter consists of a journal article that was published in Materials [6]:

Yassmin Seid Ahmed, et al. “Effect of Built-Up Edge Formation during Stable State of Wear in AISI 304 Stainless Steel on Machining Performance and Surface Integrity of the Machined Part” Materials Journal. Volume 10, pp 1230–1245. https://doi.org/10.3390/ma10111230.

Preface: This chapter discusses the close link between the BUE formation, surface integrity, and cutting forces during the stable state of wear for uncoated cutting tools. In this study, an X-ray diffraction (XRD) method was used for measuring superficial residual stresses on the machined surface through the stable state of wear in the cutting

`

and feed directions. In addition, surface roughness of the machined surface was investigated to reveal the surface distortions created during the cutting process. This was combined with chip undersurface analyses to better understand friction and adhesion.

Chapter 6:

This chapter consists of a journal article that was published in Applied Surface Science [70]:

Yassmin Seid Ahmed, et al. " The effect of laser micro-scale textured tools on the tool-chip interface performance and surface integrity during austenitic stainless-steel turning" Applied Surface Science Journal. Volume 510. https://doi.org/10.1016/j.apsusc.2020.145455.

Preface: This chapter considered the potential of using laser surface texturing (LST) to control the stability of a BUE and to reduce the friction during the machining process. In this chapter, LST was used to apply different texture shapes on the rake face of the cutting tool to mitigate the BUE`s tendency to adhere to the cutting tool. A comprehensive study of the influence of different rake faces on the tool-chip interface performance was also investigated. Furthermore, deformation characteristics and the mechanical state of machined workpiece subsurface layers following machining with textured and untextured tools under different cutting speeds are discussed in this research.

`

Chapter 7:

This chapter presents the summary and conclusions drawn from the current research studies, along with some suggestions for future work.

Appendix A:

Chapter 3 analyses the chip forming mechanism and chip breakability of stainless steel with a supply of HPC. Appendix A consists of an unpublished section on the effect of HPC on tool life, BUE formation and cutting forces which are not discussed in Chapter 3.

Appendix B:

Chapter 8 discusses the influence of different surface features on the rake face on the tool-chip interface performance during wet machining of stainless steels. Appendix B consists of an unpublished section on the effect of laser micro-scale textured tools on tool-chip interface performance during machining stainless steel under dry conditions.

1.5 Note to the Reader

Since this thesis consists of a series of journal articles, the repetition of certain material might be found during reading. In particular, there is some overlap in the introduction section of some chapters. In addition, the sections describing experimental instruments and measurement methodology in some of the chapters contain significant repetition since the same facilities were used for all experiments. However, the background section of each chapter provides more specific references related to the study presented in each paper.

`

References

1. S. Bagherifard, S. Slawik, I. Fernández-Pariente, C. Pauly, F. Mücklich, and M. Guagliano, "Nanoscale surface modification of AISI 316L stainless steel by severe shot peening," *Mater. Des.*, vol. 102, pp. 68–77, 2016.
2. H. A. Youssef, "Types and Classifications of Stainless Steels," in Machining of Stainless Steels and Super Alloys, John Wiley & Sons, Ltd, 2016, pp. 11–26.
3. J. O. Nilsson, "Overview superduplex stainless steels, " Mater. Sci. Technol. vol. 8, pp.685–700, 1992.
4. S. N. B. Oliaei and Y. Karpat, "Built-up edge effects on process outputs of titanium alloy micro milling," Precis. Eng., vol. 49, pp. 305–315, 2017.
5. S. N. B. Oliaei and Y. Karpat, "Investigating the influence of built-up edge on forces and surface roughness in micro scale orthogonal machining of titanium alloy Ti6Al4V," J. Mater. Process. Technol., vol. 235, pp. 28–40, 2016.
6. Y. S. Ahmed, G. Fox-Rabinovich, J. M. Paiva, T. Wagg, and S. C. Veldhuis, "Effect of built-up edge formation during stable state of wear in AISI 304 stainless steel on machining performance and surface integrity of the machined part," Materials (Basel)., vol. 10, no. 11, pp. 1–15, 2017.
7. H. S. Khatak and B. Raj, Corrosion of Austenitic Stainless Steels - Mechanism, Mitigation and Monitoring. Woodhead Publishing Limited, 2002.
8. S. Bruschi, L. Pezzato, A. Ghiotti, M. Dabalà, and R. Bertolini, "Effectiveness of using low-temperature coolants in machining to enhance durability of AISI 316L

stainless steel for reusable biomedical devices," J. Manuf. Process., vol. 39, no. March, pp. 295–304, 2019.

9. D. Peckner and I. M. (Irving M. Bernstein, Handbook of stainless steels. McGraw-Hill, 1977.
10. G. Karafyllias, A. Galloway and E. Humphries, " The effect of low pH in erosion-corrosion resistance of high chromium cast irons and stainless steels, " Wear, vol. 420–421, pp. 79-86, 2019.
11. ASMI, "Chapter 6: Austenitic Stainless Steels," Stainl. Steels Des. Eng., pp. 69–78, 2008.
12. H. A. Youssef, Machining of Stainless Steels and Super Alloys: Traditional and Nontraditional Techniques. wiley, 2015.
13. I. Rosenthal, E. Tiferet, M. Ganor, and A. Stern, "Post-processing of AM-SLM AlSi10Mg specimens: Mechanical properties and fracture behaviour," Ann. "Dunarea Jos" Univ. Galati, Fascicle XII, Weld. Equip. Technol., vol. 26, pp. 33–38, 2015.
14. O. Unal and R. Varol, "Almen intensity effect on microstructure and mechanical properties of low carbon steel subjected to severe shot peening," Appl. Surf. Sci., vol. 290, pp. 40–47, 2014.
15. M. C. Shaw, "The Theory of Metal Cutting," in Proceedings of the Twenty-Fifth International Machine Tool Design and Research Conference, S. A. Tobias, Ed. London: Macmillan Education UK, 1985, pp. 33–36.
16. H. Zheng and K. Liu, "Machinability of Engineering Materials," Handbook of

Manufacturing Engineering and Technology, pp.1–34, 2013.

17. M. Rizal, J. A. Ghani, M. Z. Nuawi, and C. H. C. Haron, "Cutting tool wear classification and detection using multi-sensor signals and Mahalanobis-Taguchi System," Wear, vol. 376–377, pp. 1759–1765, 2017.

18. K. Sobiyi, I. Sigalas, G. Akdogan, and Y. Turan, "Performance of mixed ceramics and CBN tools during hard turning of martensitic stainless steel," Int. J. Adv. Manuf. Technol., vol. 77, no. 5–8, pp. 861–871, 2015.

19. J. G. Corrêa, R. B. Schroeter, and Á. R. Machado, "Tool life and wear mechanism analysis of carbide tools used in the machining of martensitic and supermartensitic stainless steels," Tribol. Int., vol. 105, pp. 102–117, Jan. 2017.

20. G. M. Krolczyk, P. Nieslony, R. W. Maruda, and S. Wojciechowski, "Dry cutting effect in turning of a duplex stainless steel as a key factor in clean production," J. Clean. Prod., vol. 142, pp. 3343–3354, 2017.

21. D. P. Selvaraj and P. Chandramohan, "Optimization of Surface Roughness of AISI 304 Austenitic Stainless Steel in Dry Turning Operation using Taguchi Design Method," J. Eng. Sci. Technol., vol. 5, no. 3, pp. 293–301, 2010.

22. C. A. De Oliveira Junior, A. E. Diniz, and R. Bertazzoli, "Correlating tool wear, surface roughness and corrosion resistance in the turning process of super duplex stainless steel," J. Brazilian Soc. Mech. Sci. Eng., vol. 36, no. 4, pp. 775–785, 2014.

23. A. B. Junior and A. Eduardo, "Tool Wear and Tool Life in End Milling of 15-5 PH Stainless Steel under different cooling and lubrication conditions," Int J Adv

`

Manuf Technol, vol.43, pp. 756–764, 2009.

24. M. A. Xavior, "Evaluating the machinability of AISI 304 stainless steel using alumina inserts," J. Achiev. Mater. Manuf. Eng., vol. 55, no. 2, pp. 841–847, 2012.
25. Z. Wang, V. Kovvuri, A. Araujo, M. Bacci, W. N. P. Hung, and S. T. S. Bukkapatnam, "Built-up-edge effects on surface deterioration in micromilling processes," J. Manuf. Process., vol. 24, pp. 321–327, 2016.
26. G. M. Krolczyk, R. W. Maruda, P. Nieslony, and M. Wieczorowski, "Surface morphology analysis of Duplex Stainless Steel (DSS) in Clean Production using the Power Spectral Density," Measurement, vol. 94, pp. 464–470, 2016.
27. G. M. Krolczyk, P. Nieslony, and S. Legutko, "Science Direct Determination of tool life and research wear during duplex stainless steel turning," Arch. Civ. Mech. Eng., vol. 15, no. 2, pp. 347–354, 2014.
28. Trent, E.; Wright, P. Metal Cutting, 4th ed.; Butterworth–Heinemann: London, UK, 2000; p. 464.
29. B. Medina-Clavijo, M. Saez-de-Buruaga, C. Motz, D. Soler, A. Chuvilin, and P. J. Arrazola, "Microstructural aspects of the transition between two regimes in orthogonal cutting of AISI 1045 steel," J. Mater. Process. Technol., vol. 260, no. May, pp. 87–96, 2018.
30. Williams, J. E., Rollason, C. E., (1970), Metallurgical and Practical Machining Parameters Affecting Built-up Edge Formation in Metal cutting. Journal of the Institute of Metals, Vol. 95: 144-153.
31. E. M. Trent, "Metal cutting and the tribology of seizure: II movement of work

`

material over the tool in metal cutting," Wear, vol. 128, no. 1, pp. 47–64, 1988.

32. J. Nomani, A. Pramanik, T. Hilditch, and G. Littlefair, "Investigation on the Behavior of Austenite and Ferrite Phases at Stagnation Region in the Turning of Duplex Stainless Steel Alloys," Metall. Mater. Trans. A Phys. Metall. Mater. Sci., vol. 47, no. 6, pp. 3165–3177, 2016.
33. E. A. Rahim and H. Sasahara, "A study of the effect of palm oil as MQL lubricant on high speed drilling of titanium alloys," Tribol. Int., vol. 44, no. 3, pp. 309–317, Mar. 2011.
34. S. Sukvittayawong and I. Inasaki, "Detection of built-up in turning process," Int.J.Mach.Tools Manufact.vol. 34, no. 6, pp. 829–840, 1994.
35. S. N. B. Oliaei and Y. Karpat, "Investigating the influence of built-up edge on forces and surface roughness in micro scale orthogonal machining of titanium alloy Ti6Al4V," J. Mater. Process. Technol., vol. 235, pp. 28–40, 2016.
36. P. Sivaiah and D. Chakradhar, "Performance improvement of cryogenic turning process during machining of 17-4 PH stainless steel using multi objective optimization techniques," Meas. J. Int. Meas. Confed., vol. 136, pp. 326–336, 2019.
37. J. Kümmel, J. Gibmeier, V. Schulze, and A. Wanner, "Effect of built-up edge formation on residual stresses induced by dry cutting of normalized steel," vol. 996, pp. 603–608, 2014.
38. V. Kumar and V. Ganta, "Optimization of process parameters in drilling of GFRP composite using Taguchi method," Integr. Med. Res., vol. 3, no. 1, pp. 35–41,

`

2013.

39. S. A. Niknam, J. Kouam, V. Songmene, and M. Balazinski, “Dry and semi-dry turning of titanium metal matrix composites (Ti-MMCs),” Procedia CIRP, vol. 77, no. Hpc, pp. 62–65, 2018.

40. A. Hase, M. Wada, T. Koga, and H. Mishina, “The relationship between acoustic emission signals and cutting phenomena in turning process,” Int. J. Adv. Manuf. Technol., vol. 70, no. 5–8, pp. 947–955, 2014.

41. C. Zhang, X. Yao, J. Zhang, and H. Jin, “Tool condition monitoring and remaining useful life prognostic based on awireless sensor in dry milling operations,” Sensors (Switzerland), vol. 16, no. 6, 2016.

42. N. Mokhtar, M. A. Gebremariam, H. Zohari, and A. Azhari, “Analysis of acoustic emission during abrasive waterjet machining of sheet metals,” IOP Conf. Ser. Mater. Sci. Eng., vol. 342, no. 1, 2018.

43. D. E. Lee, I. Hwang, C. M. O. Valente, J. F. G. Oliveira, and D. A. Dornfeld, “Precision Manufacturing Process Monitoring with Acoustic Emission,” in Condition Monitoring and Control for Intelligent Manufacturing, L. Wang and R. X. Gao, Eds. London: Springer London, 2006, pp. 33–54.

44. E. Liu, R. Han, G. Tan, and Z. Li, “Analysis of chip breaking prediction in cutting aluminum alloys,” Mater. Sci. Forum, vol. v 532-533, no. 1, pp. 213–216, 2006.

45. A. V. Filippov, V. E. Rubtsov, S. Y. Tarasov, O. A. Podgornykh, and N. N. Shamarin, “Detecting transition to chatter mode in peakless tool turning by monitoring vibration and acoustic emission signals,” Int. J. Adv. Manuf. Technol.,

`

vol. 95, no. 1–4, pp. 157–169, 2018.

46. K. Ramasubramanian, N. Arunachalam, and M. S. R. Rao, “A Study on CVD Diamond Coated Cutting Tools Wear Performance using Vibration and Acoustic Emission Signals,” Procedia CIRP, vol. 72, pp. 1415–1420, 2018.
47. A. Hase, H. Mishina, and M. Wada, “Correlation between features of acoustic emission signals and mechanical wear mechanisms,” Wear, vol. 292–293, pp. 144–150, Jul. 2012.
48. Hutton DV, Yu Q (1990) On the effects of a built-up edge on acoustic emission in metal cutting. Trans ASME 112:184–189
49. M. Nalbant, H. Gökkaya, I. Toktaş, and G. Sur, “The experimental investigation of the effects of uncoated, PVD- and CVD-coated cemented carbide inserts and cutting parameters on surface roughness in CNC turning and its prediction using artificial neural networks,” Robot. Comput. Integr. Manuf., vol. 25, no. 1, pp. 211–223, Feb. 2009.
50. M. B. Bilgin, "Investigating the effects of cutting parameters on the built-up-layer and built-up-edge formation during the machining of AISI 310 austenitic stainless Steels,"Mater. Tehnol., vol 49, pp.779–84, 2015.
51. J. Zhou, V. Bushlya, R. L. Peng, Z. Chen, S. Johansson, and J. E. Stahl, “Analysis of subsurface microstructure and residual stresses in machined Inconel 718 with PCBN and Al2O3-SiCw tools,” in Procedia CIRP, 2014, vol. 13, pp. 150–155.
52. A. K. Chattopadhyay, P. Roy, A. Ghosh, and S. K. Sarangi, “Wettability and machinability study of pure aluminium towards uncoated and coated carbide

`

cutting tool inserts," Surf. Coatings Technol., vol. 203, no. 8, pp. 941–951, Jan. 2009.

53. M. Mia and N. R. Dhar, "Effects of duplex jets high-pressure coolant on machining temperature and machinability of Ti-6Al-4V superalloy," J. Mater. Process. Technol., vol. 252, pp. 688–696, 2018.
54. V. T. G. Naves, M. B. Da Silva, and F. J. Da Silva, "Evaluation of the effect of application of cutting fluid at high pressure on tool wear during turning operation of AISI 316," Wear, vol. 302, pp. 1201-1208, 2013.
55. M. Habak and J. Lou Lebrun, "An experimental study of the effect of high-pressure water jet assisted turning (HPWJAT) on the surface integrity," International Journal of Machine Tools and Manufacture, vol. 51, no. 9. Elsevier Ltd, pp. 661–669, 2011.
56. S. Niketh and G. L. Samuel, "Surface texturing for tribology enhancement and its application on drill tool for the sustainable machining of titanium alloy," J. Clean. Prod., vol. 167, pp. 253–270, Nov. 2017.
57. N. Kawasegi, T. Kawashima, N. Morita, K. Nishimura, M. Yamaguchi, and N. Takano, "Effect of texture shape on machining performance of textured diamond cutting tool," Precis. Eng., vol. 60, pp. 21–27, Nov. 2019.
58. S. Niketh and G. L. Samuel, "Drilling performance of micro textured tools under dry, wet and MQL condition," J. Manuf. Process., vol. 32, pp. 254–268, 2018.
59. C. S. Kumar and S. K. Patel, "Application of surface modification techniques during hard turning: Present work and future prospects," Int. J. Refract. Met. Hard

`

Mater., vol. 76, pp. 112–127, 2018.

60. T. Vijaya Babu and J. S. Soni, “Investigation of process parameters optimization in die-sinking and wire cut EDM to improve process performance using taguchi technique,” in Materials Today: Proceedings, 2018, vol. 5, no. 13, pp. 27088–27093.

61. D. Vasumathy and A. Meena, “Influence of micro scale textured tools on tribological properties at tool-chip interface in turning AISI 316 austenitic stainless steel,” Wear, vol. 376–377, pp. 1747–1758, 2017.

62. J. Kümmel et al., “Study on micro texturing of uncoated cemented carbide cutting tools for wear improvement and built-up edge stabilisation,” J. Mater. Process. Technol., vol. 215, pp. 62–70, 2015.

63. E. J. Y. Ling, J. Saïd, N. Brodusch, R. Gauvin, P. Servio, and A.-M. Kietzig, “Investigating and understanding the effects of multiple femtosecond laser scans on the surface topography of stainless steel 304 and titanium,” Appl. Surf. Sci., vol. 353, pp. 512–521, Oct. 2015.

64. W. Ze, D. Jianxin, C. Yang, X. Youqiang, and Z. Jun, “Performance of the self-lubricating textured tools in dry cutting of Ti-6Al-4V,” Int. J. Adv. Manuf. Technol., vol. 62, no. 9–12, pp. 943–951, Oct. 2012.

65. S. Jesudass Thomas and K. Kalaichelvan, “Comparative study of the effect of surface texturing on cutting tool in dry cutting,” Mater. Manuf. Process., vol. 33, no. 6, pp. 683–694, Apr. 2018.

66. Y. L. Zhang, X. G. Zhang, and G. Matsoukas, “Numerical study of surface

`

texturing for improving tribological properties of ultra-high molecular weight polyethylene," Biosurface and Biotribology, vol. 1, no. 4, pp. 270–277, 2015.

67. Y. Seid Ahmed, J. M. Paiva, D. Covelli, S. C. Veldhuis, "Investigation of Coated Cutting Tool Performance during Machining of Super Duplex Stainless Steels through 3D Wear Evaluations", Coatings, vol. 7, pp. 127–142, 2017.
68. Y. Seid Ahmed, J. M. Paiva, and S. C. Veldhuis, "Characterization and prediction of chip formation dynamics in machining austenitic stainless steel through supply of a high-pressure coolant," Int. J. Adv. Manuf. Technol., vol. 102, no. 5–8, pp. 1671–1688, 2019.
69. Y. S. Ahmed, J. M. Paiva, B. Bose, and S. C. Veldhuis, "New observations on built-up edge structures for improving machining performance during the cutting of superduplex stainless steel," Tribol. Int., vol. 137, no. April, pp. 212–227, 2019.
70. Ahmed YS, Paiva JM, Arif AFM, Amorim FL, Torres RD, Veldhuis SC. The effect of laser micro-scale textured tools on the tool-chip interface performance and surface integrity during austenitic stainless-steel turning. Applied surface science 2020;510:779–84. https://doi.org/10.1016/j.apsusc.2020.145455.

`

Chapter 2 : Investigation of Coated Cutting Tool Performance during Machining of Super Duplex Stainless Steels through 3D Wear Evaluations

Yassmin Seid Ahmed [1, 2, *], Jose Mario Paiva [1, 3], Danielle Covelli [4], and Stephen Clarence Veldhuis [1]

[1] McMaster Manufacturing Research Institute (MMRI), Department of Mechanical Engineering, McMaster University, 1280 Main Street West, Hamilton, ON L8S4L7, Canada; Paivajj@mcmaster.ca (J.M.P.); covelld@mcmaster.ca (D.C.); veldhu@mcmaster.ca (S.C.V)

[2] Production Engineering Department, Alexandria University, Alexandria, 21544, Egypt

[3] Department of Mechanical and Materials Science, Catholic University of Santa Catarina, Rua Visconde de Taunay, 427-Centro, Joinville-SC 89203-005, Brazil

[4] Biointerfaces Institute, McMaster University, ETB 422, 1280 Main Street West, Hamilton, ON L8S 0A3, Canada

* **Correspondence:** seidahmy@mcmaster.ca; Tel.: +1-365-888-1186

`

This paper is published in Coating journal. Volume 7, 2017, pages 127–142, ISSN 0708-0127. https://doi.org/10.3390/coatings7080127. This paper is republished here with permission.

Abstract

In this study, the wear mechanisms and tribological performance of uncoated and coated carbide tools were investigated during the turning of super duplex stainless Steel - Grade UNS S32750, known commercially as SAF 2507. The tool wear was evaluated throughout the tests and the wear mechanisms were investigated using an Alicona Infinite Focus microscope and a scanning electron microscope (SEM) equipped with energy dispersive spectroscopy (EDS). Tribo-film formation on the worn rake surface of the tool was analyzed using X-Ray Photoelectron Spectroscopy (XPS). In addition, tribological performance was evaluated by studying chip characteristics such as thickness, compression ratio, shear angle, and undersurface morphology. Finally, surface integrity of the machined surface was investigated using the Alicona microscope to measure surface roughness and SEM to reveal the surface distortions created during the cutting process. The results obtained showed that the predominant wear mechanism is adhesion for all tools investigated and that the AlTiN coating system exhibited better performance in all aspects when compared with the other tools; in particular, built-up edge formation was significantly reduced.

`

Keywords

super duplex stainless steel; tool wear mechanisms; tribo-films; chip characteristics; surface integrity

2.1 Introduction

Super duplex stainless steels (SDSS) are a specific type of stainless steel alloys that have a biphasic microstructure, consisting of approximately 50 % ferrite and 50 % austenite by volume. SDSS has a favorable combination of chromium, nickel and molybdenum [1] which provides an attractive combination of mechanical and corrosion properties and is thus widely applied in aggressive corrosion environments such as chemical, petrochemical, and gas and oil industries. These materials are considered difficult to machine because they have low thermal conductivity combined with high tensile strength and high shear strength and during machining they show a high tendency to work-hardening [2-4]. These characteristics make SDSS more difficult to machine than standard austenitic stainless steels [5]. The work hardening increases the friction forces during the contact between the work piece and cutting tool edge, which increases the temperature, causing oxidation [6]. In addition, the high ductility of the stainless steel leads to the formation of long continuous chips and to the intensive sticking of the workpiece material to the cutting tool surface, which results in an adhesive wear enhancement [7]. These conditions promote built-up edge (BUE) formation and tearing off during cutting, which results in cutting edge chipping and cutting force

`

instability. This response to the machining process results in severe surface damage to the machined part and chipping of the tool cutting edge [8]. Several papers have suggested the application of PVD coatings on the cutting tools as a way to reduce friction conditions during the cutting process, by reducing heat generation [9]. For applications where the cutting process is characterized by high temperatures in the cutting zone, for instance, in machining of materials with low thermal conductivity, the use of cemented carbide tools coated with self-adaptive PVD coatings is strongly recommended. During machining, these coatings form protective, nano-scale tribo-films on the tool rake surface, which reduce friction and result in a reduction of the degree of BUE formation, leading to wear performance improvement [10, 11].

Many researchers have studied the wear mechanisms associated with the machining of different types of stainless steels using CVD and PVD coated tools. Corrêa studied the machinability of two stainless steels, martensitic S41000 and super martensitic S41426, during turning with CVD TiC–TiCN–TiN coated tools. The authors found that abrasion and diffusion were the main wear mechanisms in the machining of martensitic stainless steel, while for the super martensitic stainless steel, attrition and abrasion were dominant [6]. Krolczyk et al. predicted surface roughness in machining of duplex stainless steel (AISI S31803) with Ti (C/N)/Al_2O_3/TiN coated tools. The authors determined that the main wear mechanism is abrasion [12]. Selvaraj et al. also investigated machining of two types of duplex stainless steel and found that the wear mechanisms changed depending on the cutting speed. At low cutting speed, the main wear mechanism was abrasion, while diffusion and oxidation wear were predominant at high cutting speed

`

[13]. Carlos et al. performed turning experiments with a super duplex stainless steel alloy (S32750) using a PVD multi-coated (TiAlN and TiN layers) cemented carbide tool. The authors noted that notch wear at the end of depth of cut was the responsible for the end of tool life and that a large amount of the material adhered to the tool wear area [14]. Jawaid et al. used CVD Ti(C/N)/TiC/ Al_2O_3 and PVD TiN coated inserts. The authors reported that attrition was the principal wear mechanism at lower speed conditions, while abrasion and diffusion wear mechanisms were the failure modes at higher speed conditions. They also found that CVD coated inserts exhibited the worst performance, owing to the greater effects of thermo-mechanical loads, coarse grain size, and higher Co-content (18% Co) of the carbide substrate. In contrast, the PVD coated insert gave better performance because of the thermal stability of the alumina coating [15].

The objective of this investigation is to compare the tool life, wear mechanisms and tribological performance of coated (PVD AlTiN, CVD TiCN+Al_2O_3) and uncoated inserts during turning of super duplex stainless steel - Grade UNS S32750. The performance of these cutting tools will be evaluated in terms of tool life, chip formation, surface integrity, and cutting forces. This research will increase understanding of the main reasons for different wear mechanisms acting during the cutting process and suggest a way to increase tool life for industry.

2.2 Experimental procedure

2.2.1 Workpiece Material

In this work, cylindrical tubes of super duplex stainless steel - UNS S32750 were investigated during turning (roughing operations). The chemical composition and mechanical properties of the material are shown in Table 2-1. To reveal the workpiece microstructure, samples of the super duplex stainless steel were prepared, polished and etched with Beraha's solution (100 ml H_2O + 20 ml hydrochloric Acid (HCl) + 0.3–0.6 g of potassium metabisulfite). The microstructure of the SDSS workpiece generated during the cutting process was characterized using a Nikon ECLIPSE IV 100 microscope equipped with UC30 camera. The microstructure and phase distribution of the material were analyzed using NIS Elements imaging software (see Figure 2-1).

Table 2-1 Chemical composition and mechanical properties of S32750

Chemical Composition %								
C	**Si**	**Mn**	**P**	**S**	**Cr**	**Ni**	**Mo**	**N**
0.03	0.80	1.2	0.035	0.02	25	7	4	0.24

Proof Strength (0.2% yield) MPa	**Tensile Strength MPa**	**Elongation**	**Hardness HRC**
550	800-1000	15	32

`

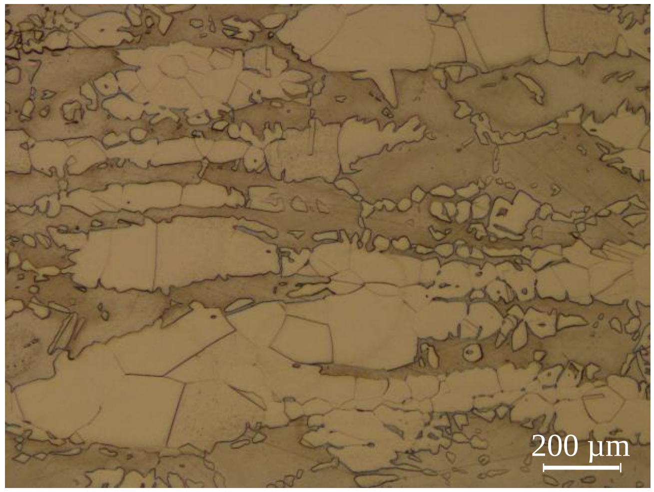

Figure 2-1 Microstructure of the SDSS UNS S32750 showing the distribution of each phase (Ferrite is continuous phase with 36% while Austenite is second phase with 64%). Magnification is 200X

2.2.2 Cutting Tools and Cutting Fluid

Cemented carbide inserts coated with PVD AlTiN and CVD TiCN + Al_2O_3 coatings were compared during cutting tests to determine tool life. The coating characteristics are shown in Table 2-2. The cemented carbide is WC/6%Co and the ISO code for the cutting inserts is CNMG432-SM with the following geometry characteristics: back rake angle, λ0 = 9; clearance angle, α0 = 5°; wedge angle, β=76°; edge radius, r=24 µm and nose radius, Rε = 0.8 mm. The inserts were manufactured by Sandvik and the tool-holder was an ISO PCLNL 45165 12HP, supplied by Kennametal. The machining experiments were carried out on an OKUMA CNC Crown L1060 lathe with 15 kW of power and an OKUMA OSP-U10L controller. The turning tests were conducted for roughing operations with a cutting speed of 120 m/min, feed rate of 0.3 mm/rev, and depth of cut of 1 mm, under wet

`

conditions. The cutting fluid was applied at a flow rate of 11 L/min via a nozzle positioned directly above the cutting tool and directed toward the tool tip. The cutting fluid chosen was semi-synthetic coolant-CommCool ™ 8800, manufactured by the Wallover Company, at a concentration of 7 %, typically used with stainless steel alloys.

Table 2-2 Characteristics of coating systems

Coating	Process	Layer	Structure	Residual Stresses (MPa)	Hardness (GPa)	Thickness (µm)	Roughness – Ra (µm)
AlTiN	PVD	Monolayer	Columnar nano-crystalline	293±88	35 [17]	1.8	0.039
$TiCN+Al_2O_3$	CVD	Bi layer	Columnar micro-crystalline	439±20	31 [17]	Sublayer 5, Toplayer 3	0.038

2.2.3 Experimental Machine Techniques

During the machining tests, the cutting force measurements were performed with a 3D component tool holder Kistler dynamometer type 9121 with a data acquisition system. The signals of the forces from the dynamometer were transmitted to a Kistler 5010 type amplifier, and then recorded on a computer using LABVIEW software. The acquisition rate was 300 data points per second, scale was 20 MU/volt and sensitivity was 3.85 mV/MU. The tool flank wear was measured using a KEYENCE – VHX 5000 digital

`

microscope, equipped with a CCD camera and image analyzer software. The tool life criterion was set to a flank wear of 0.3 mm to follow the recommendation of the ISO 3685 Standard [16]. After the tests, the cutting tools were analyzed by SEM, using a Vega 3-TESCAN, coupled to EDS. The new and worn inserts were also analyzed using an Alicona Infinite Focus G5 microscope, which works by focus variation, to generate real 3D surface images. This microscope allows for the capture of images with a lateral resolution down to 400 nm and a vertical resolution down to 10 nm. In order to measure the wear volume and BUE volume of a cutting edge, first a 3D model of a new edge of the original insert was measured and then the edge was measured a second time after cutting (0.3 mm flank wear). The software used the 3D image of the new edge as a reference and compared it with a 3D image of a worn edge. Following these measurements, all the inserts were etched using an HCl solution to remove all adhered material on the cutting tool to reveal the wear mechanisms.

The chip compression ratio, the shear angle and the friction coefficient at the tool-chip interface were determined using standard methods [17]. The surface roughness of the machined workpiece was evaluated by means of an Alicona Infinite Focus which conforms to EN ISO standard 25178 [18]. Roughness measurements were taken with a cut-off wavelength of 800 μm, a vertical resolution of 100 nm and lateral resolution of 2 μm.

The structural and phase transformation at the cutting tool/workpiece interface, as well as the chemical nature of the tribo-films formed were determined by X-ray photoelectron spectroscopy (XPS) on a Physical Electronics (PHI) Quantera II. The XPS spectrometer

`

was equipped with a hemispherical energy analyzer and an Al anode source for X-ray generation and a quartz crystal monochromator for focusing the generated X-rays. A monochromatic Al K-α X-ray (1486.7 eV) source was operated at 50W–15 kV. The system base pressure was as low as 1.33×10^{-7} Pa with an operating pressure that did not exceed 2.66×10^{-6} Pa. Before any spectra were collected, the samples were sputter-cleaned for 4 min using a 4-kVAr+ beam. A 200-μm beam was used for all data collected on the samples. A pass energy of 280 eV was used to obtain all survey spectra, while a pass energy of 69 eV was used to collect all high resolution data. All spectra were obtained at a 45° take off angle. A dual beam charge compensation system was also utilized to ensure neutralization of all samples. The instrument was calibrated using a freshly cleaned Ag reference foil, where the Ag 3d5/2 peak was set to 368 eV. All data analysis was performed using PHI Multipak version 9.4.0.7 software.

2.3 Results and Discussion

2.3.1 Tool Life Measurements

Figure 2-2 shows the plot of flank wear versus cutting length for the uncoated and coated cutting inserts tested during machining of SDSS. A significant improvement in machining productivity was obtained when machining with a cutting insert coated with PVD AlTiN.

The results show that the PVD AlTiN coated cutting insert has a cutting length almost two times greater than the CVD TiCN+Al_2O_3 coated cutting insert. The PVD AlTiN coating shows the ability to improve the friction at the cutting interface which leads to the rapid flow of the chip on the rake surface (Figure 2-3). This happens because the AlTiN

`

coating has the ability to adapt to external stimuli, i.e. to self-organize. During the cutting process, a part of the cutting energy is spent on self-organization of the coating layer to form a thermal barrier/lubricating tribo-film [11, 19] which reduces the friction at the cutting zone and increases the tool life. The tool life obtained by CVD coated cutting inserts is shorter due to the intense friction conditions experienced in the cutting zone.

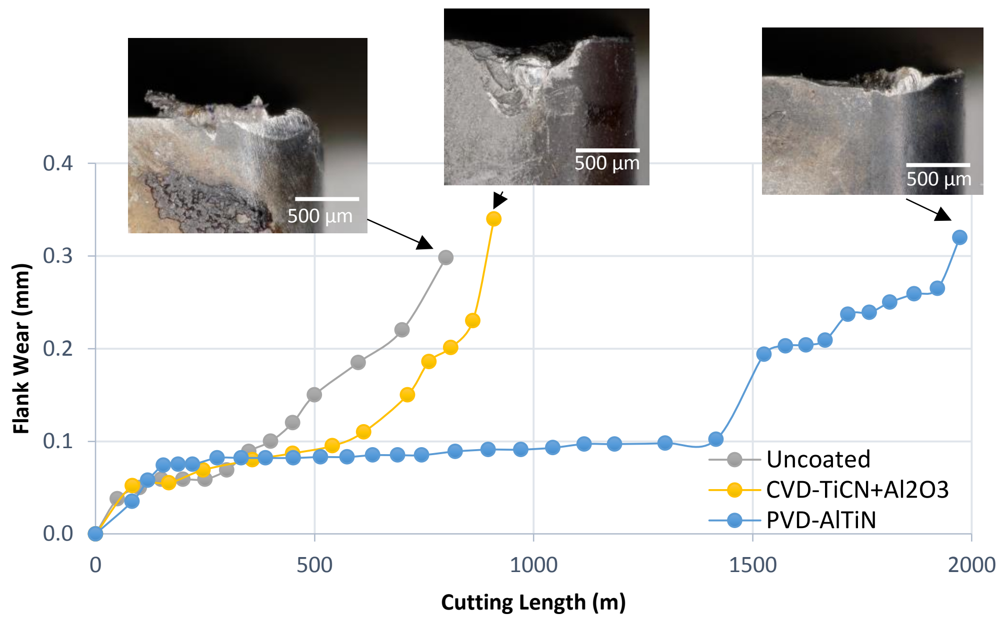

Figure 2-2 Relation between flank wear and cutting length for uncoated and coated carbide inserts during machining SDSS. Additionally, the flank surface for each tool is presented at the end of tool life

Images of the chip undersurface collected during machining experiments show high intensity flow (Figure 2-3). The high friction conditions at the chip–tool interface reduce the chip speeds during the chip flow, increasing area of contact between tool and chip on the rake face surface and, therefore, contributing to increase the temperature in the cutting

`

zone. High temperature due to high friction at the cutting zone results in reduced tool life for $TiCN+Al_2O_3$ coated inserts.

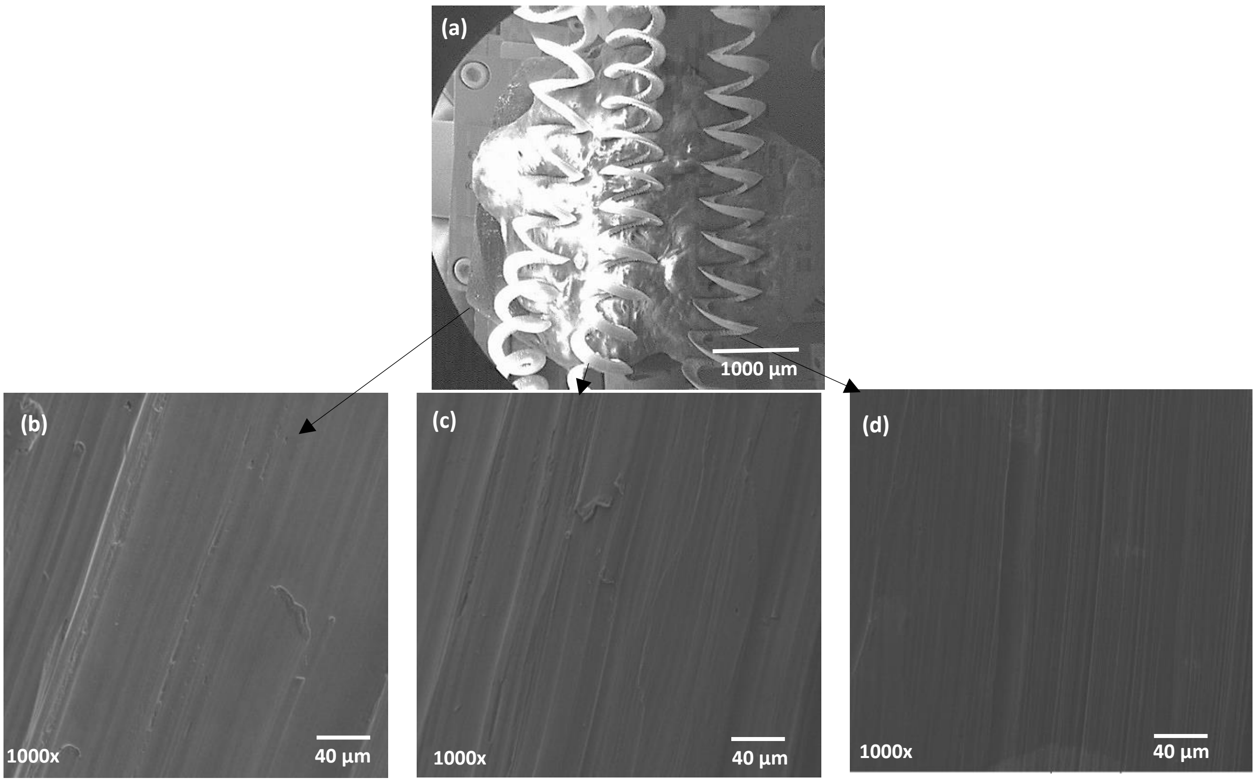

Figure 2-3(a) General macrograph aspect of the chips, SEM images obtained with carbide inserts with (b) uncoated; (c) $TiCN+Al_2O_3$; and (d) AlTiN

2.3.2 Chip Characteristics

Following machining, chip types and morphology were determined for each combination of workpiece and cutting tool. Figure 2-3 shows SEM images of the chips for the uncoated and coated tools; the chips have similar curling for both coatings. However, the chip undersurface morphology is better for the PVD AlTiN cutting insert. Usually, the type of chip and the undersurface morphology is a direct indicator of frictional conditions

`

at the tool/chip interface [17]. In this case, it is evident from chip characteristic studies that the friction conditions in the cutting zone (chip-tool interface) were more favorable for the AlTiN coating. The measured values of chip thickness and calculated values of the chip compression ratio, shear angle, and coefficient of friction are tabulated in Table 2-3. The chip thickness, chip compression ratio, and shear angle are better for the AlTiN coated tool compared to the other tools (Table 2-3). These characteristics confirm the AlTiN coated tool has lower friction between the chip and tool leading to lower wear of the cutting tool.

Table 2-3 Cutting characteristics during the turning operation of SDSS [17]

Type of coating	Chip thickness (mm)	Chip compression ratio	Shear angle (°)	Coefficient of friction	Tool chip contact length (mm)
AlTiN	0.433	0.69	36	0.267	0.682
$TiCN+Al_2O_3$	0.560	0.54	29	0.404	0.797
Uncoated	0.653	0.46	27	0.445	0.903

A possible explanation of the observed improvement on the metal flow in the case of the AlTiN coated insert versus the CVD TiCN + Al_2O_3 coated and uncoated tools is the formation of tribo-films on the rake surface during friction [23]. Smoother morphology of the chips (Figure 2-3d) during machining of SDSS using cutting tools with the AlTiN coated tool corresponds to better thermo-frictional conditions during cutting. In this case, a beneficial heat flow redistribution is taking place: The majority of the heat generated

`

during cutting goes into the chips and dissipates with chip removal [24]. The tribo-films generated on the surface of PVD coated tool can change the wear behavior substantially: They provide surface protection, some lubricity and improve frictional and wear performance, resulting in very beneficial heat flow redistribution at the tool-chip interface. The presence of these tribofilms was confirmed by XPS investigation. This analysis was performed on the cutting tool (Rake face). Figure 2-4a shows the location selected for XPS studies.

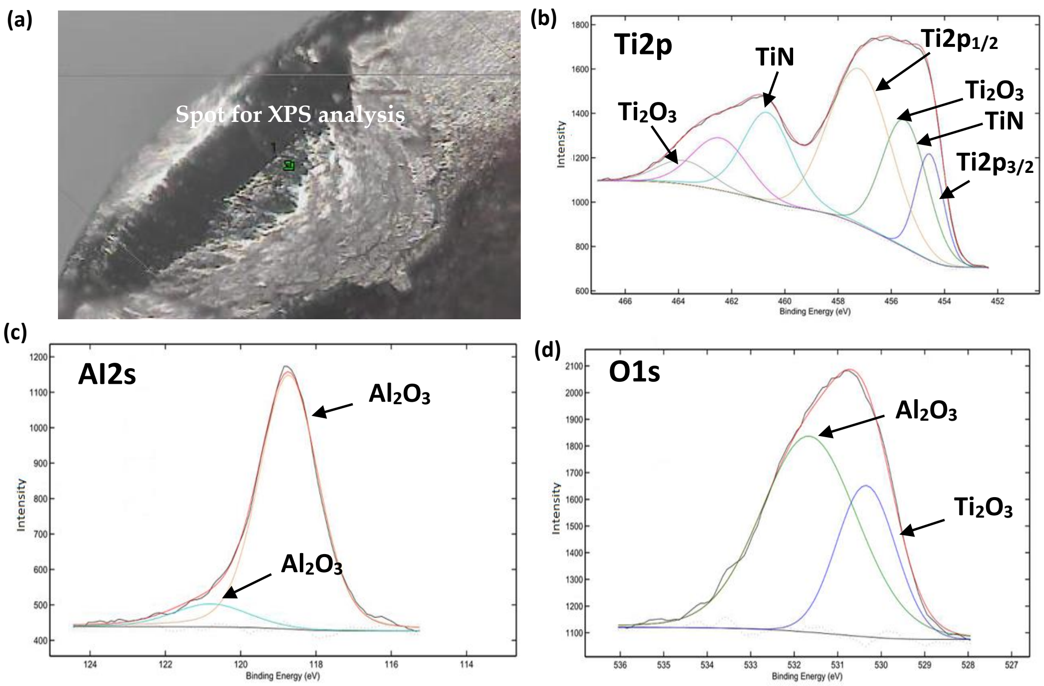

Figure 2-4 XPS data for tribo-films formed on the worn surface of AlTiN coating (a) XPS spot on the AlTiN tool rake face; (b) AlTiN XPS high resolution spectra line for Ti2p; (c) AlTiN XPS high resolution spectra line for AI2s; and (d) AlTiN XPS high resolution spectra line for O1s

`

2.3.3 The Composition of Tribo Films and Frictional Conditions

Figure 2-4(b–d) shows respectively the XPS Ti2p, Al2s and O1s spectra obtained from the rake surface of AlTiN coated cutting tool. The rake face was chosen for the analysis because of the elevated temperatures typically caused by tool-chip contact on this surface. The presence of Al_2O_3 shows that a partial chemical transformation of aluminum, in the AlTiN coating, takes place during cutting (Figure 2-4(c)). The spectra also indicate the formation of an amorphous-like structure of the alumina-based tribo-films [25, 26]. Titanium in the AlTiN coating (Figure 4(b, d)) forms non-stoichiometric titanium tribo-oxide and rutile TiO_2 (peaks 530.4, 457.4 and 463.8 eV). The formation of these tribo-films with high chemical stability reduces the adherence of the workpiece material to the cutting tool surface (Figure 2-5).

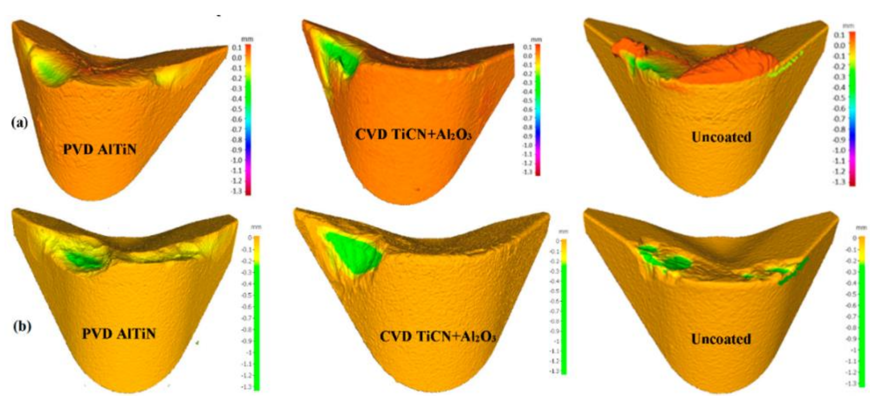

Figure 2-5 Alicona 3D images of the cutting tools after machining of SDSS (a) before, and (b) after etching showing the details of the cutting tools with their major wear mechanisms

`

In this way, the reduction of adhered material on the rake surface results in constant material flow, which leads to lower heat generation at the tool/workpiece interface. Due to the improved lubricity of this oxide under elevated cutting temperatures [27], the characteristics of the chips formed change critically (Figure 2-3) and the chip flow along the chip undersurface is also improved, which improves the chip compression ratio (Table 2-3). These phenomena serve to enhance the adaptability of the coatings, which thus results in a better tool life (Figure 2-2). For this reason, formation of these nano-scale tribofilms is very beneficial on the surface of PVD coating in contrast to the microns thick alumina layer on the CVD coated tools. To understand further why the PVD AlTiN coated tool has a better performance than CVD TiCN + Al_2O_3 coated tool, the residual stresses of new PVD AlTiN and CVD TiCN + Al_2O_3 coated tools were measured and listed in Table 2-2. It was found that the tensile residual stress in CVD TiCN + Al_2O_3 is much higher (439 MPa) as compared to PVD AlTiN coated insert (293 MPa). The reason for that is the CVD coating process occurs under much higher temperature typically ranging from 200–1600°C compared to lower than 500°C in case of the PVD AlTiN coating [28]. High tensile residual stress in CVD coating induces internal stresses, which increase thermal loads and reduce thermal stability.

2.3.4 Tool Wear Analysis

As discussed previously, the main focus of this research is to compare different wear mechanisms of coated and uncoated inserts. For this reason, real 3D images of the worn tools were studied by means of an Alicona microscope, see Figure 2-5(a). All the tools

`

showed intense chipping, adhesion and flank wear during machining tests, which results in reduced tool life. The main reason for these behaviors is the instability in the chip formation temperature, combined with strong adhesion at the tool-chip interface resulting in high compressive stress; these phenomena are associated with low thermal conductivity of SDSS, which leads to high cutting temperature and accelerates the wear formation. The presence of test material adhered onto the tools was observed in all tests. In order to analyze the wear mechanisms, it was necessary to remove the adhered layers of the cutting tools through chemical attack with HCl, see Figure 2-5(b). It can be seen that there is no BUE on the surface of the tools, which means that all the adhered material was removed, allowing differentiation between wear mechanisms acting on the tools.

Each tool studied, total wear volume and the volume of BUE before and after etching were measured using the Alicona microscope. These results are presented in Figure 2-6. It is noted that the PVD AlTiN coated insert has the lowest total wear and BUE volume compared with the CVD TiCN + Al_2O_3 coated and uncoated inserts, indicating that AlTiN coating exhibits good performance during machining of SDSS. This conclusion agrees with the results obtained from the XPS studies (Figure 2-4), where it is observed that the AlTiN coating has the capacity to adapt to external stimuli, i.e., to self-organize. In this way, the tribo-film formation can enhance the process of cutting, which provides benefits such as reducing the friction conditions in the cutting zone, which leads to smoother chip undersurface (Figure 2-3(d)), reduction in BUE formation and increase in tool life (Figure 2-2) [11].

`

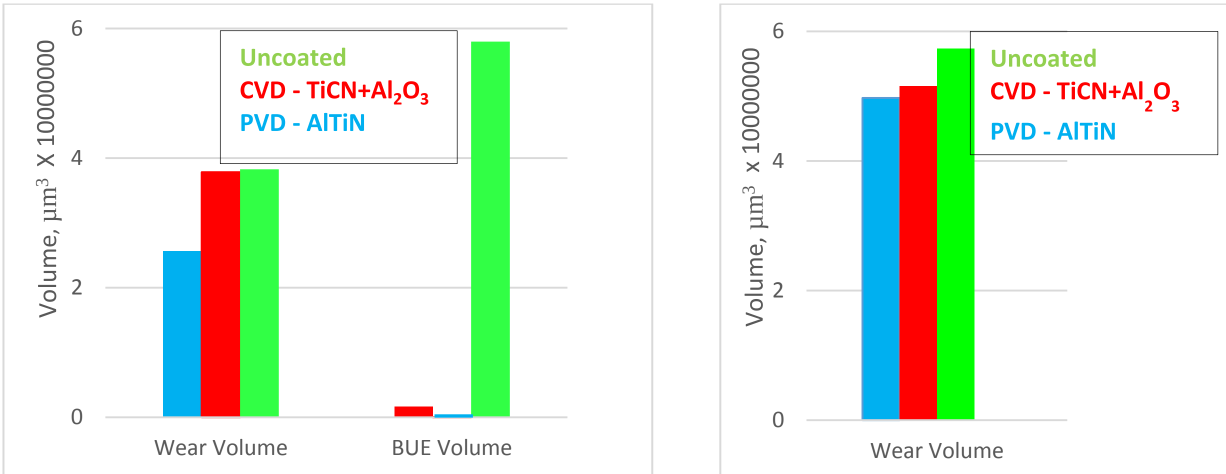

Figure 2-6 Comparison of total wear volume and BUE volume for uncoated and coated tools (a) before, and (b) after etching

Different wear mechanisms commonly associated with the machining of SDSS were observed during the wear tests, flank wear and chipping being the most significant modes. Also, material adhesion was observed in all cutting tools. As was explained in the previous paragraph, adhesive wear is the main wear mechanism during the machining of stainless steel. However, after etching and at high magnifications, different wear mechanisms were observed. In the following paragraphs, the different modes of wear are discussed, and associated EDS analysis is summarized in Table 2-4.

Table 2-4 EDS analysis associated with cutting tools in Figures (2-7)–(2-9)

	Chemical Composition %								
EDS	**Fe**	**W**	**O**	**Cr**	**Ni**	**C**	**Ti**	**N**	**Al**
1	26.3	7.55	30.37	16.04	4.25	23.49	0.54	–	1.41
2	0.11	2.10	20.2	1.20	0.30	14.00	2.54	12.50	49.20

`

3	34.06	1.37	13.12	15.9	3.92	24.95	3.00	–	0.75
4	0.11	0.92	54.45	–	0.10	28.7	0.56	–	29.13
5	0.11	66.4	13.00	1.13	-	23.00	0.1	–	0.50
6	44.2	0.8	15.00	18.0	8415	18.2	0.48	–	0.42

Figure 2-7 shows in detail the wear mechanisms of the PVD AlTiN coated insert. Figure 2-7(a) shows the tool before etching where the presence of adhered workpiece material was confirmed by EDS 1 (high percentage of Fe and Cr). Figure 2-7(b–e) show the same tool after etching, where there is no adhered material on the tool, see EDS 2. Figure 2-7(a) shows areas with a rough aspect on the cutting edge, which is characteristic of the adhesive (or attrition) wear mechanism [30]. This mechanism frequently occurs when there is chemical affinity between the tool and the workpiece material, and adhesion leads to the formation of BUE at the coated tool-chip interface. Another relevant phenomenon, which can be related to the tribological system behavior is the high tool-chip interface temperature: machining at a speed of 120 m/min generates high temperatures at the tool-chip interface that can generate adhesion on the tool rake and flank face as evidenced by plastic flow of the workpiece material (stick-slip, followed by plucking action). Similar results were reported by Corrêa et al. [6] and Junior et al. [31]. Figure 2-7(c) shows a high magnification of tool-adhered layer interface where a large crack is observed running perpendicular to the flank face. This crack could have been caused by one or a combination of the following wear mechanisms [32]: Diffusion, adhesion, abrasion and oxidation. These wear mechanisms lead to a continual loss or dislocation of material. Also, BUE formation can lead to mass loss or mass dislocation as it grows throughout the cutting process and periodically breaks off, creating cracks on the tool surface and break-out the cutting edge [11]. Figure 2-7(d) shows intensive chipping developed on the cutting edge, which indicates that mechanical fatigue caused by BUE formation caused damage to the cutting tool [32]. Above the cutting edge in Figure 2-7(e), there is a smooth surface, which is associated with diffusion wear. Diffusion wear is a mechanism that involves transport of the atoms from high concentration (cutting tool) to low concentration (chip) [**Error! Reference source not found.**], which depends mainly on the cutting temperature, contact time and the solubility of the elements in the secondary shear zone [34]. This process takes place in a very narrow area at the interface between the cutting tool and chip and causes a weakening of the cutting tool.

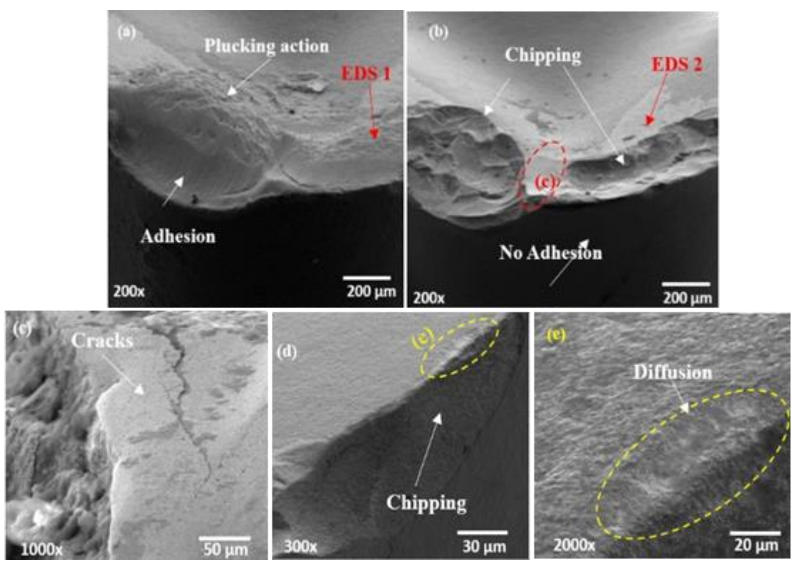

Figure 2-7 SEM images of PVD AlTiN coated insert after machining SDSS. (a) cutting tool before etching; (b) cutting tool after etching; (c–e) cutting tool with different magnifications

`

Figure 2-8 shows the wear mechanisms of the CVD TiCN + Al_2O_3 coated insert. Figure 2-8(a) shows the insert before etching and Figure 2-8(b–f) shows the insert after etching, see EDS 3 and 4 in Table 2-4. Figure 2-8(c) shows the rake face of the tool where the coating was removed from the cutting tool. EDS 5 and 6 results identify two strips of the coating (EDS 4) on the substrate of the tool (EDS 5). The coating was exposed along the cutting edge, and severe chipping and micro-chipping developed (see Figure 2-8(d)). These mechanisms confirm the previous results obtained by X-ray stress analysis (Table 2-2). Due to high coating temperature, internal stress is induced, increases thermal loads and reduces thermal stability, leading to intensive chipping on the cutting edge. Figure 2-8(e) shows a very smooth surface, which is clearly seen at high magnification, suggesting that a diffusion wear mechanism prevailed on the rake face [32]. Figure 2-8(f) shows parallel lines in the direction of sliding action, which indicate abrasive wear. The ASTM International tool wear standard explains that abrasive wear occurs as a result of hard particles forced against and moved along a solid surface [34], which is in this case BUE fragments. Selvaraj et al. [13] explained that abrasion wear mechanism is caused by grains broken off during the turning process, which become restricted between the chip and the tool, creating scratches on the flank face of the tool. The same explanation was also suggested by Krolczyk et al. [2] and Jawaid et al. [15].

`

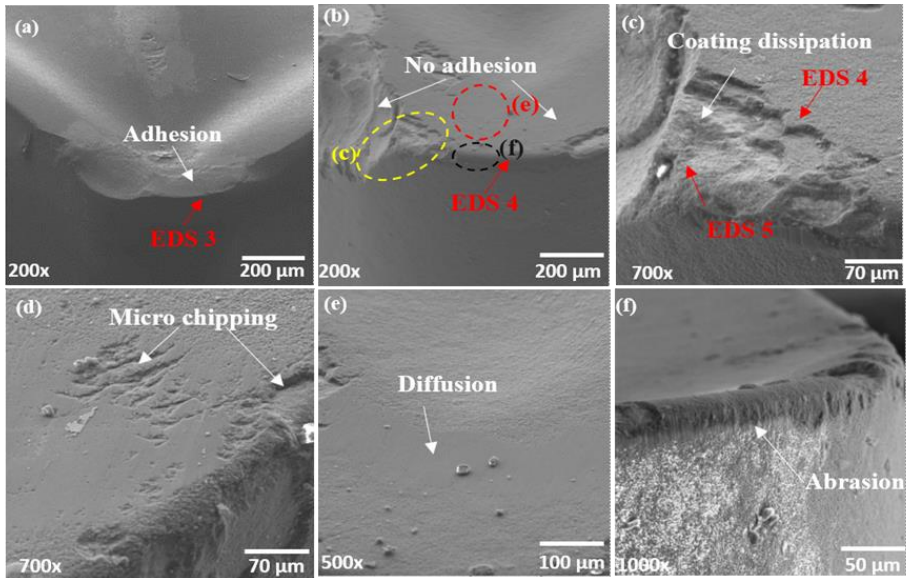

Figure 2-8 SEM images of CVD TiCN + Al2O3 coated insert after machining SDSS. (a) cutting tool before etching; (b) cutting tool after etching; (c–f) cutting tool with different magnifications

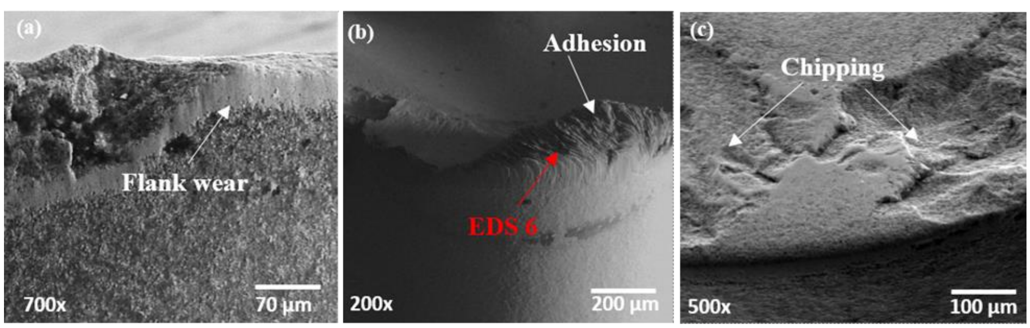

Figure 2-9 SEM images of uncoated insert after machining SDSS. (a) Flank face after etching; (b) cutting tool before etching; and; (c) cutting tool with chipping

Figure 2-9 shows the different wear mechanisms on the surface of the uncoated insert before and after etching. Figure 2-9(a) shows the flank face of the tool after chemical etching, where a view of the regular flank wear is shown. Figure 2-9(b) shows the tool before etching where a large BUE is seen on the tool as indicated in EDS 6. After etching (Figure 2-9(c)), all the adhered material was removed revealing that severe chipping has occurred on the cutting edge.

In summary, after the turning of SDSS with different cutting tools, it is possible to see that, due to the low machinability of SDSS, the tools are easily affected, leading to excessive tool wear during machining operations. To ensure good results with SDSS, it is necessary to understand how the cutting tool behaves during cutting. Under the cutting conditions tested, the cutting tools showed wear from various mechanisms: Adhesion, abrasion, and diffusion. It is important for the industry to understand the main reasons for these mechanisms in order to reduce its effect on tool life. A summary of the main causes of wear observed during cutting SDSS through this research and suggested solutions is given in Table 2-5.

Table 2-5 A summary of the main causes and suggested solutions of different wear mechanisms observed for uncoated and coated tools

Cutting Tool	Wear Mechanism	Main Causes	Suggested Solutions
PVD AlTiN	Adhesive wear (Attrition)	High strain hardening High ductility	Use very low or very high cutting speeds to decrease the formation of BUE [**Error! Reference source not found.**].
	Chipping	BUE formation	
	Diffusion	High cutting temperature	Increase the flow and pressure of the coolant

`

			to reduce the cutting temperature.
CVD TiCN + Al_2O_3	Cracks	BUE formation	Use very low or very high cutting speeds to decrease the formation of BUE [**Error! Reference source not found.**].
	Abrasive wear	BUE fragments	
	Adhesive wear (Attrition)	High strain hardening High ductility	
	Coating dissipation	High tensile residual stresses	Use PVD coated tools.
	Chipping	Coating dissipation	
	Diffusion	High cutting temperature	Increase the flow and pressure of the coolant to reduce the cutting temperature.
Uncoated	Adhesive wear (Attrition)	High strain hardening High ductility	Use very low or very high cutting speeds to decrease the formation of BUE [**Error! Reference source not found.**].
	Chipping	Chip jamming	Use a cutting tool with a proper chip breaker to be able to break chips [36]

`

2.3.5 Machined Workpiece Characteristics

Surface integrity plays an important role in many areas and has great importance in the evaluation of machining accuracy. Many factors affect the surface conditions of machined parts, one of them being the cutting tool, which has a significant influence on the surface roughness. Stainless steel is a material generally used for applications requiring the greatest reliability, and therefore, and any damage to the subsurface layers must be controlled [37].

For this reason, small pieces of the machined workpiece were cut off to be analyzed using the SEM to reveal the surface distortions created during the cutting process and Alicona microscope to measure the surface roughness. Figure 2-10 shows three-dimensional and SEM images of the machined workpiece along with cutting force data collected at the beginning of the turning process and the values of surface roughness measured after the cutting tests. In Figure 2-10(a, b) the machined surfaces obtained with uncoated and CVD TiCN + Al_2O_3 coated inserts show cracks and distortions. It can be seen that minor cracks were found and bad surface finish with low distortion was accomplished. As a result of intensive BUE formed on the uncoated insert (Figure 2-5(a)) and high friction generated during cutting, some of the chips welded onto the surface of the workpiece (227 μm). Zhou et al. [38] and Alabdullah et al. [39] observed the same phenomenon during machining of difficult-to-cut materials.

Chip sticking on the machined workpiece is consistent with the high cutting forces measured during cutting. In addition, there is a high variation of the values of cutting

`

forces for the uncoated insert (Figure 2-10(a)), which indicates that high frictions conditions in the cutting zone were generated during the cutting process with the uncoated insert. This phenomenon is strongly diminished for the coated tools: The variations of cutting forces are smaller, surface roughness is lower and there is no chip sticking on the machined surfaces (Figure 2-10(b, c)), which is a significant improvement.

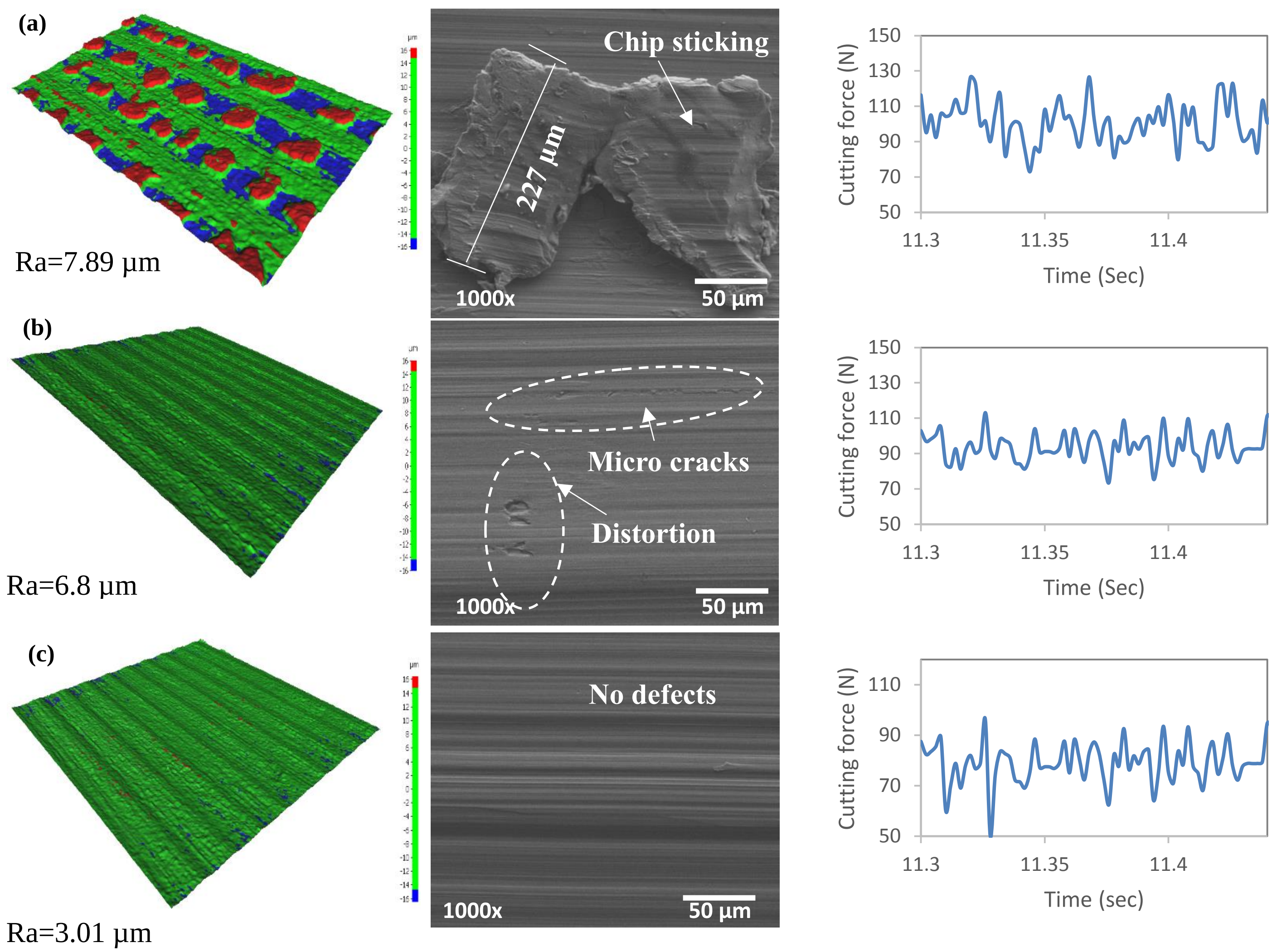

`

Figure 2-10 Three dimensional and SEM images of the machined surface obtained by (a) uncoated insert; (b) TiCN + Al2O3; (c) AlTiN insert and corresponding cutting forces and surface roughness values

2.4 Conclusions

The tool life results, analysis of wear mechanisms and tribological performance of different coated and uncoated tools during the turning of SDSS allowed the following conclusions to be drawn:

- Substantial improvement in tool life was achieved with the AlTiN coated insert: Tool life was approximately twice that of the CVD TiCN + Al_2O_3 coated insert and three times than uncoated insert.
- The chip thickness, chip compression ratio and shear angle values are better for the AlTiN coated tool, compared to the CVD TiCN + Al_2O_3 coated and uncoated tools, and the chip undersurface is smoother without any defects, indicating lower friction between the chip and tool rake face, which results in a constant chip flow over the tool rake surface.
- XPS analysis revealed that the underlying cause of the high performance of the AlTiN coating is the formation of aluminum oxide tribo-films at the tool-chip interface.

- The AlTiN coated tool had the lowest value for both BUE and total wear volume compared with the CVD TiCN + Al_2O_3 coated and uncoated tools, indicating that PVD AlTiN coated tool performs very well with SDSS**.**
- Adhesion wear and chipping are the predominant wear mechanism for all the cutting tools studied. When turning with the PVD AlTiN coated tool, adhesion and diffusion were present in different places on the worn area of the tools. Machining with the CVD TiCN + Al_2O_3 coated tool shows diffusion, abrasion, chipping and adhesion wear mechanisms while sever adhesion wear and chipping were the main wear mechanism with the uncoated insert.
- The machined surface obtained using the AlTiN coated tool had the lowest surface roughness value. The machined surfaces obtained with the CVD TiCN + Al_2O_3 coated and uncoated inserts show minor cracks and distortions, and there is some chip sticking on the machined workpiece obtained by the uncoated insert, as a result of intensive BUE formation and high friction generated during cutting. Spikes in cutting forces at the beginning of the cutting process were highest for the uncoated cutting tool, which is directly related to chip sticking on the surface of the workpiece.

Acknowledgments

The authors would like to gratefully acknowledge the financial supported from the Natural Sciences and Engineering Research Council of Canada's (NSERC) Strategic Canadian Network for Research and Innovation in Machining Technology (CANRIMT).

`

Author Contributions

Yassmin Seid Ahmed performed the cutting experiments, performed metallographic, SEM, XRD and Alicona studies, and wrote the paper, Jose Mario Paiva planned experimental procedure, Danielle Covelli performed XPS studies, and Stephen Clarence Veldhuis is the supervisor of the research team. All authors have read and approved the final manuscript.

References

1. Bordinassi, E.C.; Stipkovic, M.F.; Batalha, G.F.; Delijaicov, S.; Lima, N.B. Superficial integrity analysis in a super-duplex stainless steel after turning. J. Achiev. Mater. Manuf. Eng.2006, 18, 335–338.
2. Biksa, A.; Yamamoto, K.; Dosbaeva, G.; Veldhuis, S.C.; Fox-rabinovich, G.S.; Elfizy, A.; Wagg, T.; Shuster, L.S. Wear behavior of adaptive nano-multilayered AlTiN/Me_xN PVD coatings during machining of aerospace alloys. Tribol. Int. 2010, 43, 1491–1499.
3. Paro, J.; Hänninen, H.; Kauppinen, V. Tool wear and machinability of HIPed P/M and conventional cast duplex stainless steels. Wear 2001, 249, 279–284.
4. Nilsson, J.O.; Kangas, P.; Karlsson, T. Wilson Mechanical properties, microstructural stability and kinetics of σ phase formation in 29Cr–6Ni–2Mo–0.38N in super duplex stainless steel. Metall. Mater. Trans. 2000, 31, 35–45.

`

5. Nilsson, J.-O. Overview superduplex stainless steels. Mater. Sci. Technol. 1992, 8, 685–700.
6. Corrêa, J.G.; Schroeterb, R.B.; Machadoa, A.R. Tool life and wear mechanism analysis of carbide tools used in the machining of martensitic and supermartensitic stainless steels. Tribol. Int. 2017, 105, 102–117.
7. Paiva, J.M.; Torres, R.D.; Amorim, F.L.; Covelli, D.; Tauhiduzzaman, M.; Veldhuis, S.C.; Dosbaeva, G.; Fox-Rabinovich, G. Frictional and wear performance of hard coatings during machining of superduplex stainless steel. Int. J. Adv. Manuf. Technol. 2017, 24, 1–10.
8. Endrino, J.L.; Fox-rabinovich, G.S.; Gey, C.; Hard AlTiN-AlCrN PVD coatings for machining of austenitic stainless steel. Surf. Coat. Technol. 2006, 200, 6840–6845.
9. Ciftci, I. Machining of austenitic stainless steels using CVD multi-layer coated cemented carbide tools. Tribol. Int. 2006, 39, 565–569.
10. Sik, I.; Amanov, A.; Kim, J.D. The effects of AlCrN coating, surface modification and their combination on the tribological properties of high speed steel under dry conditions. Tribol. Int. 2015, 81, 61–72.
11. Fox-Rabinovich, G.S.; Paiva, J.M; Gershman, I.; Aramesh, M.; Cavelli, D.; Yamamoto, K.; Dosbaeva, G.; Veldhuis, S.C. Control of self-organized criticality through adaptive behavior of nano-structured thin film coatings. Entropy 2016, 18, 290.

`

12. Krolczyk, G.; Legutko, S.; Gajek, M. Predicting the surface roughness in the dry machining of duplex stainless steel DSS. Metalurgija 2013, 52, 259–262.

13. Selvaraj, P.D.; Chandramohan, P.; Mohanraj, M. Optimization of surface roughness, cutting force and tool wear of nitrogen alloyed duplex stainless steel in a dry turning process using Taguchi method. Measurement 2014, 49, 205–215.

14. Carlos, O.J.; Anaelmo, E.D.; Rodnei, B. Correlating tool wear, surface roughness and corrosion resistance in the turning process of super duplex stainless steel. J. Braz. Soc. Mech. Sci. Eng. 2014, 36, 775–785.

15. Jawaid, A.; Olajire, K.; Ezugwu, O. Machining of martensitic stainless steels (JETHETE) with coated carbides. Proc. Inst. Mech. Eng. Part B J. Eng. Manuf. 2001, 215, 769–779.

16. ISO 3685–Tool Life Testing with Single-Point Turning Tools, 2nd ed.; International Organization for Standardization: Geneva, Switzerland, 1993. (Revised in 2017).

17. Shaw, M. Metal Cutting Principles, 2nd ed.; Oxford University Press: New York, NY, USA, 2005.

18. ISO 25178–2–Geometrical Product Specifications (GPS)—Surface Texture: Areal Part 2: Terms, Definitions and Surface Texture Parameters; International Organization for Standardization: Geneva, Switzerland, 2012.

19. Dobrzański, L.A; Pakuła, D.; Křiž, A. Tribological properties of the PVD and CVD coatings put down onto the nitride tool ceramics. In Proceedings of the 12th

`

International Scientific Conference: Achievements in Mechanical& Materials Engineering, Podgorica, Montenegro, 2–5 April 2003; pp. 267–270.

20. ISO 3685–Tool Life Testing with Single-Point Turning Tools, 2nd ed.; International Organization for Standardization: Geneva, Switzerland, 1993. (Revised in 2017).
21. ISO 25178–2–Geometrical Product Specifications (GPS)—Surface Texture: Areal Part 2: Terms, Definitions and Surface Texture Parameters; International Organization for Standardization: Geneva, Switzerland, 2012.
22. Fox-Rabinovich, G.; Totten, G.E. Self-Organization during Friction: Advanced Surface-Engineered Materials and Systems Design; CRC Press: Boca Raton, FL, USA, 2006.
23. Jacobson, S.; Hogmark, S. Tribofilms—On the crucial importance of tribologically induced surface modification. In Recent Developments in Wear Prevention, Friction and Lubrication; Nikas, G.K., Ed.; Research Signpost; Kerala, India, 2010.
24. Fox-Rabinovich, G.; Kovalev, A.; Veldhuis, S.; Yamamoto, K.; Endrino, J.L.; Gershman, I.S.; Rashkovskiy, A.; Aguirre, M.H.; Wainstein, D.L. Spatio-temporal behaviour of atomic-scale tribo-ceramic films in adaptive surface engineered nano-materials. Sci. Rep. 2015, 5, 8780.
25. Kalss, W.; Reiter, A.; Derflinger, V.; Gey, C.; EndrinoInt, J.L. Study of PVD AlCrN coating for reducing carbide cutting tool deterioration in the machining of titanium alloys. J. Refract. Metal. Hard Mater. 2006, 24, 399.

`

26. Bershadsky, B.I.; Kostetsky, L. I. The general concept in tribology. Russian Friction and Wear 1993, Trenie I Iznos, 14, 6–18.
27. Takago, S., Gotoh, M., Sasaki, T. Hirose, Y. The residual stress measurements of TiCN PVD films. Adv. X-ray Anal. 2002, 45, 365–370.
28. Ho, W.Y.; Huang, D.H.; Hsu, C.H.; Wang, D.Y. Corrosion behaviors of Cr(N,O)/CrN double-layered coatings by cathodic arc deposition. Surf. Coat. Technol. 2004, 172, 177–178.
29. Joseph, R.D. ASM Specialty Handbook: Tool Material-Technology and Engineering; ASM International: Almere, Netherlands, 1 January 1995; pp. 67–77.
30. Noordin, M.Y.; Venkatesh, V.C.; Sharif, S. Dry turning of tempered martensitic stainless tool steel using coated cermet and coated carbide tools. J. Mater. Proc. Technol. 2007, 185, 83–90.
31. Junior, A.B.; Diniz, A.E.; Teixeira Filho, F. Tool wear and tool life in end milling of 15–5 PH stainless steel under different cooling and lubrication conditions. Int. J. Adv. Manuf. Technol. 2009, 43, 756–764.
32. Trent, E.; Wright, P. Metal Cutting, 4th ed.; Butterworth–Heinemann: London, UK, 2000; p. 464.
33. Melo, A.C.; Milan, J.C.G.; Silva, M.B.; Machado, A.R. Some observations on wear and damage in cemented carbide tools. J. Braz. Soc. Mech. Sci. Eng. 2006, 28, 269–277.

`

34. Diniz, A.E.; Marcondes, F.C.; Coppini, N.L. The performance evaluation of ceramic and carbide cutting tools in machining of stainless steels. In Tecnologia da Usinagem dos Materiais, 5th ed.; Artliber Editora: São Paulo, Brazil, 2006.
35. ASTM G40-15, Standard Terminology Relating to Wear and Erosion; ASTM: West Conshohocken, PA, USA, 1987; Volume 03.02, pp. 243–250.
36. Choi, J.P.; Lee, S.L. Efficient chip breaker design by predicting the chip breaking performance. Int. J. Adv. Manuf. Technol. 2001, 17, 489–497.
37. Fahrion, M.E.; Brown, J.C.; Hassell, J.C. Technical Basis for Improved Reliability Of 347H Stainless Steel Heavy Wall Piping in Hydrogen Service; NACE International: San Diego, CA, USA, 2003.
38. Zhou, J.; Bushlya, V.; Avdovic, P.; Stahl, J.E. Study of surface quality in high speed turning of Inconel 718 with uncoated and coated CBN tools. Int. J. Adv. Manuf. Technol. 2012, 58, 141–151.
39. Alabdullah, M.; Polishetty, A.; Littlefair, G. Microstructural and surface texture analysis due to machining in super austenitic stainless steel. J. Metall. 2016, 2, 1–8.

`

Chapter 3 : Characterization and prediction of chip formation dynamics in machining austenitic stainless steel through supply of a high-pressure coolant

Yassmin Seid Ahmed [1, 2, *], Jose Mario Paiva [1, 3], and Stephen Clarence Veldhuis [1]

[1] McMaster Manufacturing Research Institute (MMRI), Department of Mechanical Engineering, McMaster University, 1280 Main Street West, Hamilton, ON L8S4L7, Canada; paivajj@mcmaster.ca (J.M.P.); veldhu@mcmaster.ca (S.C.V.)

[2] Production Engineering Department, Alexandria University, Alexandria, 21544, Egypt

[3] Department of Mechanical and Materials Science, Catholic University of Santa Catarina, Rua Visconde de Taunay, 427-Centro, Joinville-SC 89203-005, Brazil

[*] **Correspondence**: seidahmy@mcmaster.ca; Tel.: +1-365-888-1186

This paper is published in The International Journal of Advanced Manufacturing Technology. Volume 102, 2019, pages 1671–1688, ISSN 0268-3768. https://doi.org/10.1007/s00170-018-03277-7. *This paper is republished here with permission.*

`

Abstract

Use of a high pressure coolant supply (HPC) can lead to a considerable improvement in machining performance and process stability during the cutting of difficult materials such as stainless steels. Due to the high pressure of coolant jet, a hydraulic wedge was formed at the tool–chip interface and thus reduced tool–chip contact length and friction behavior. Moreover, the cutting stability can be enhanced as a result of efficient chip breakability. The goal of this work is to evaluate how chip morphology is influenced by three thin jets of pressurized coolant directed into the tool–chip interface during machining of AISI 304 austenitic stainless steel and compare the resulting performance of the tool with dry and conventional coolant conditions. Furthermore, this research evaluates the influence of tool wear on the chip forming mechanism during the turning process. An analysis of the chip generated under machining emphasizes the hypothesis that variations in the cutting tool wear directly affect the chip shape and type of chip segmentation. Finally, a theoretical model was developed to predict chip upcurl radius under HPC machining. This model is based on shear plane and structural mechanical theories which evaluate plastic strain and the bending moments along the length of the curled chip. The chip upcurl radius values from the developed theoretical model were found to be in good agreement with those measured in the machining tests.

`

Keywords

Chip morphology, High pressure coolant supply, Stainless steel machining, Theoretical model

Nomenclatures

HPC	High pressure coolant
f	Feed rate
r	Chip thickness ratio
t_c	Chip thickness
t	Undeformed chip thickness
μ	Coefficient of friction
R_n	Natural chip upcurl radius
R_i	Initial chip upcurl radius
R_f	Final chip upcurl radius
L_c	Tool–chip contact length
VB_B	Average flank wear
ASB	Adiabatic shear band

`

$h_{1,} h_2$	Maximum and minimum chip thickness, respectively
w	Distance between chip segments
G_s	Degree of chip segmentation
ε	Plastic strain
ε_{fr}	Fracture strain
ε_{chip}	Chip strain
ε_{up}	Chip upcurl strain
ϕ	Shear angle
γ	Rake angle
εx, εy, εz	Normal strain in X, Y, Z directions, respectively
γ_{xy},γ_{yz}, γ_{xz}	Shear strain in X, Y, Z directions, respectively
$\varepsilon_{a,}$ ε_b	Normal strain components in ab coordinate system
γ_{ab}	Shear strain in ab coordinate system
ψ	Rotation angle around the third axis
θ	Rotation angle in XYZ system

`

δ	Spiral angle
I_1, I_2, I_3	Stress invariants
R_1	HPC force
R_2, R_3	Reaction forces acting on chip body
ω_1, ω_2	Angle between vertical line and R_1 and R_2, respectively
σ	Angle between R_3 and horizontal line
F_3, F_{n3}	HPC force components
M	Bending moment

3.1 Introduction

Machining of austenitic stainless steel are considered as a difficult-to cut materials due to high strain hardening, high ductility, and low thermal conductivity. These properties promote high cutting temperature and continuous chips which can cause serious problems during machining [1]. In this context, High Pressure Coolant (HPC) is a modern technology that has significant potential to improve the process which satisfy the industry's demand [2]. HPC system delivers sufficient cooling at the tool–workpiece interface and effective chip evacuation from the cutting area [3]. The adequate penetration of HPC into the tool–chip interface reduces the machining temperature and consequently the seizure effect which minimizes the friction at the cutting zone [4]. In

`

addition, the coolant jet is able to create a coolant wedge under high pressure, which forms between the cutting tool and the chip to bend upwards, thus enhancing chip formation process and chip control [5].

Several studies have concluded that this machining technique improves chip characteristics compared to conventional coolant. Furthermore, HPC can be used to break apart chips during machining [6]. Kubala et al. [7] used a high pressure water jet in their investigation to study its effect on the machining performance. The authors found that the chip thickness and chip compression ratio were decreased, consequently improving machining performance. Kaminski and Alvelid [6] investigated the impact of HPC and the conventional coolant system on chip shape and friction behavior during turning process. The authors showed that conventional coolants are ineffective due to their low-pressure at the interface, which contributes to extreme friction conditions at the cutting zone. Moreover, Courbon et al. [8] and Palanisamy et al. [9] compared the effect of both conventional coolant and HPC on tribological performance. Their investigation showed that HPC was able to reduce chip thickness and increase shear angle compared to the larger chip thickness and smaller shear angle under a conventional coolant.

Despite a high number HPC application studies, few papers discuss the advantages of HPC for chip control during stainless steel machining, and there is no study on the prediction of chip breakability under HPC. Chip control during machining of stainless steel is gaining wide attention due to its vital role in increasing machining productivity [10]. Due to the lack of theoretical methods which can quantify HPC chip breakability, it

`

becomes difficult to control chip breakability with a good level of accuracy [11, 12]. Henriksen [13] and Okushima et al. [14] reported that the undeformed chip thickness and the chip upcurl radius affect the chip breakability. It was concluded that the chip fracture increased either in reverse relation to the chip upcurl radius or with an increase in the undeformed chip thickness.

Considering the gaps in the literature review, this research aims to investigate the chip forming mechanism and chip breakability of AISI 304 stainless steel with a supply of HPC directed to the tool–chip interface. The experiments were conducted at different cooling conditions: dry condition, conventional coolant supply, and two pressures of HPC. The chip formation mechanism, based on the microscopic images of the chip's form, is evaluated in terms of chip characteristics, segmentation, and free surface. The second part of this study includes a three-dimensional (3D) theoretical model of chip curling during metal cutting, which evaluates the effect of HPC supply on chip geometry. Finally, the experimental results are used to validate the theoretical model.

3.2 Experimental procedure

3.2.1 High pressure coolant and machining system

Experimental trials were performed on a CNC lathe model using a Nakamura-Tome Sc-450. The cutting fluid used in the cutting processes was a semi-synthetic coolant at a concentration of 6% that was employed by conventional coolant system at a pressure of 0.7 bar and flow rate of 2.7 L min^{-1}. Uncoated cemented carbide tools (WC 6%Co) were

`

used for the experiments and the ISO code for the cutting inserts is WNMG 06 04 08-SM 1105. These inserts are recommended by the manufacturer [15] and Koyee, et al. [16] for machining stainless steels. The cutting tool holder has ISO specification PWLNR 16-4DHP, supplied by Sandvik. This tool holder is specially designed for use with HPC. The tool holder has three cooling nozzles (1.5 mm in diameter) to deliver HPC very close to the cutting zone, as shown in Figure 3-1.

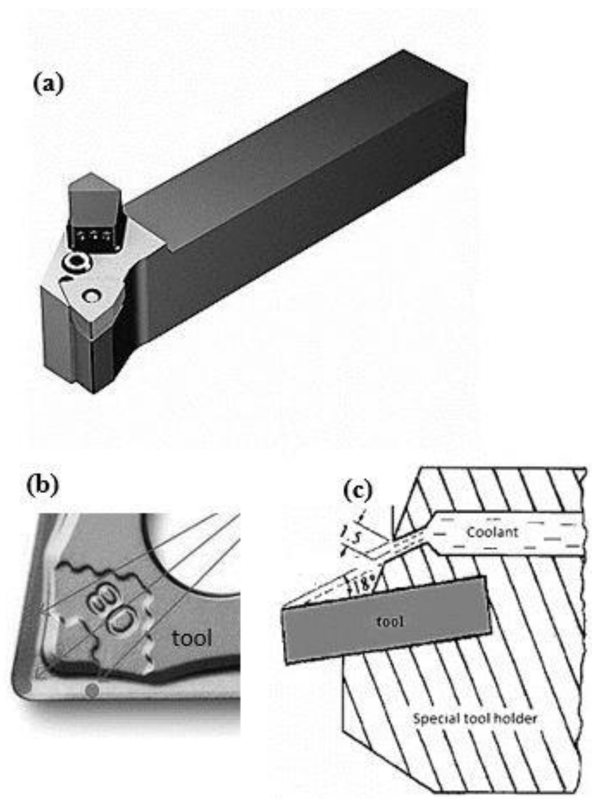

Figure 3-1 The HPC tool holder; (b) direction of HPC on the cutting tool; (c) drawing of tool holder showing the geometry of nozzles [46]

The nozzles make an 18° angle with the rake face and the distance between the nozzles and the tooltip is around 25 mm which helps reach the proximity of the tool–chip contact

`

zone and eliminate the possible interference between the nozzle and the removed chips. Figure 3-2 presents the machining system including an external high pressure pump and workpiece/cutting tool setup system. The pump is able to provide a coolant with pressures from 0.1 bar to 70 bar and flow rate of 90 L min^{-1}. Four trials were performed: (a) using HPC (with 35 and 70 bar); (b) using conventional coolant system, and (c) dry condition. The choice of 35 and 70 bar is based on the output pressure limit of the HPC supply system.

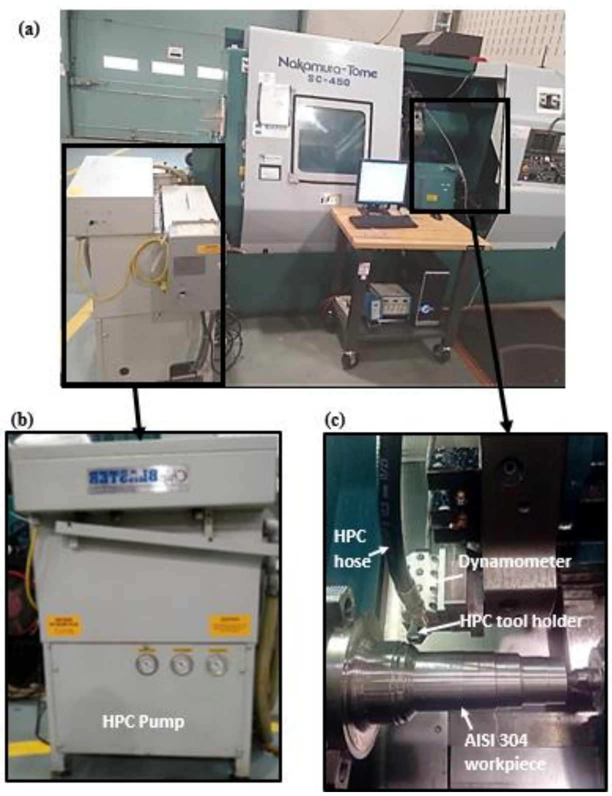

Figure 3-2 The machining process used in the experimental work with the high pressure coolant supply

`

3.2.2 Workpiece material characterization

The workpiece was an AISI 304 austenitic stainless steel round bar with a length of 500 mm and a diameter of 120 mm. Table 3-1 shows the mechanical and chemical compositions of the AISI 304 as provided by the material manufacturer. A sample of the AISI 304 was cut from the round bar and then cold mounted and polished. Glycergia solution (20 mL HNO3 + 1 mL Glycerol + 20 mL hydrochloric Acid (HCl)) served as etching fluid to show the microstructure, and the microstructure observation was conducted using a Nikon ECLIPSE IV 100 microscope, equipped with a UC30 camera. On Figure 3-3, it is possible to see the microstructure of the material.

Table 3-1 Chemical composition and mechanical properties of AISI 304 stainless steel

Chemical composition %							
C	**SI**	**Mn**	**P**	**S**	**Cr**	**Ni**	**N**
0.08	0.75	2.0	0.045	0.03	20.0	0.50	0.10
Proof Strength (0.2% yield) MPa	**Tensile Strength MPa**	**Elongation %**	**Modulus of Elasticity GPa**	**Shear Modulus GPa**		**Hardness HRC**	
215	505	70	200	86		70	

`

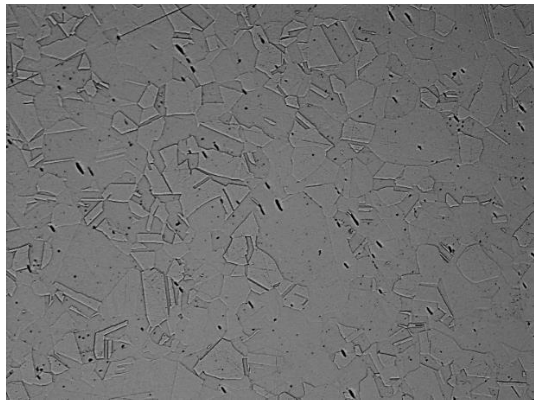

Figure 3-3 The microstructure of AISI 304 with an austenitic structure

3.2.3 Cutting tests

According to the recommendations of the manufacturer [15], the cutting conditions were formed with a feed rate of 0.1 mm/rev, depth of cut of 0.5 mm, and cutting speed of 60 m/min. These parameters are commonly applied in industry for machining austenitic stainless steel. During the experiments, average tool flank wear (VB_B) was measured with an optical microscope (KEYENCE – VHX 5000). Each test was repeated at least three times. The tool failure criteria can be estimated by a maximum VB_B of 0.3 mm [17]. Moreover, the cutting tools were investigated with a scanning electron microscope (SEM) facility (Vega 3-TESCAN).

The chips obtained after machining with the new and worn tools (VB_B =0.1, 0.2, and 0.3 mm) at different cooling conditions (Dry, Conventional coolant, HPC (35 and 70 bar)) were mounted with epoxy so that the chip cross section could be seen. After appropriate preparation, the cross sections were observed with SEM and EBSD to analyze chip morphology and to conduct an adiabatic study of the shear bands and cracks formation.

`

No etching treatment was used on the samples for EBSD analysis. The SEM images were acquired under high current, 10 mm working distance, and 60 µm aperture operating at 20 kV accelerating voltage. EBSD scans were performed in a JEOL 6610LV high-resolution scanning electron microscope (JEOL solutions for innovation, Peabody, Massachusetts, USA), operating at 20 kV and 60 µm aperture size. A CCD detector was used at a 176 mm insertion distance. The sample was positioned at a 70 degrees tilt angle and working distances ranged between 8 and 12 mm. The BUE cross sections were phase-mapped using Tango-Maps software (Oxford Instruments HKL, Hobro, Denmark) and processed using Chanel 5HKL

Average chip thickness and chip upcurl radius, obtained with different cooling conditions and flank wear values, were measured. Next, the chip thickness ratio, the friction coefficient and the shear angle at the tool–chip interface were calculated according to M.Shaw [18]. The chip free surface and chip undersurface under the same conditions mentioned above were also analyzed using SEM to understand the chip forming mechanism and the friction behavior at the tool–chip interface. The average surface roughness of the chip undersurface was evaluated using white light interferometry (Alicona Infinite Focus) [19].

`

3.3 Experimental results and discussion

3.3.1 Chip morphology: effect of high pressure coolant

3.3.1.1 Chip form and segmentation

The chips produced throughout the turning experiments were collected to investigate their morphology (shapes, structures, geometry) and to provide an in-depth study of chip formation under HPC use. Figure 3-4 gives an overview of the resultant chip types depending on the coolant conditions. It can be shown that the turning of stainless steel under dry and conventional coolant produced continuous chips, whereas HPC produced smaller segmented chips. HPC conditions help to break up chips, producing shorter segmented chips [20]. In contrast, dry and conventional coolant did not show the distinct effect on chip formation. Under dry and conventional coolant, chip fracture occurs because of the force generated by an obstruction-type chip breaker [10, 13, 21-23]. However, enhanced chip breaking occurring under HPC, is a consequence of the high force created by the HPC system [24]. The 35 and 70 bar coolant pressures are large enough to break the chip, before it comes in contact with an obstruction [21].

`

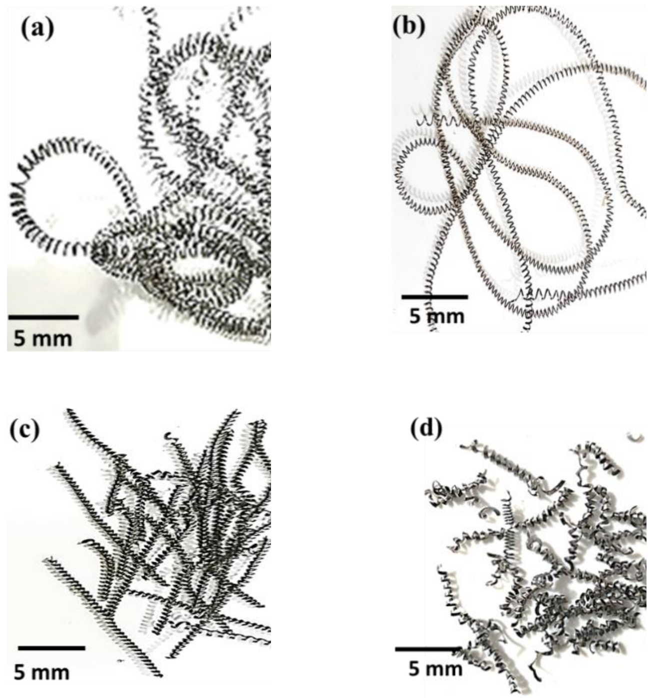

Figure 3-4 Chip formation at different cutting conditions; (a) dry, (b) conventional coolant, (c) HPC (35 bar); HPC (70 bar)

Furthermore, the HPC supply can remove the chips beyond the deformation zone, reducing the tool–chip contact area and improving the friction conditions at the interface [22] which helps to enhance chip undersurface morphology as well as chip fragmentation [25]. To confirm this behavior, the chip undersurface morphology showing the chip flow and the surface roughness is presented in Figure 3-5. A substantial difference in chip undersurface morphology is evident: HPC application results in smoother chip undersurface (Ra=0.54 μm) compared to dry cutting, (Ra=0.89 μm) where a clear stick-slip phenomenon is present. This means that the application of HPC improves tribological conditions as a consequence of the smaller contact area [26].

`

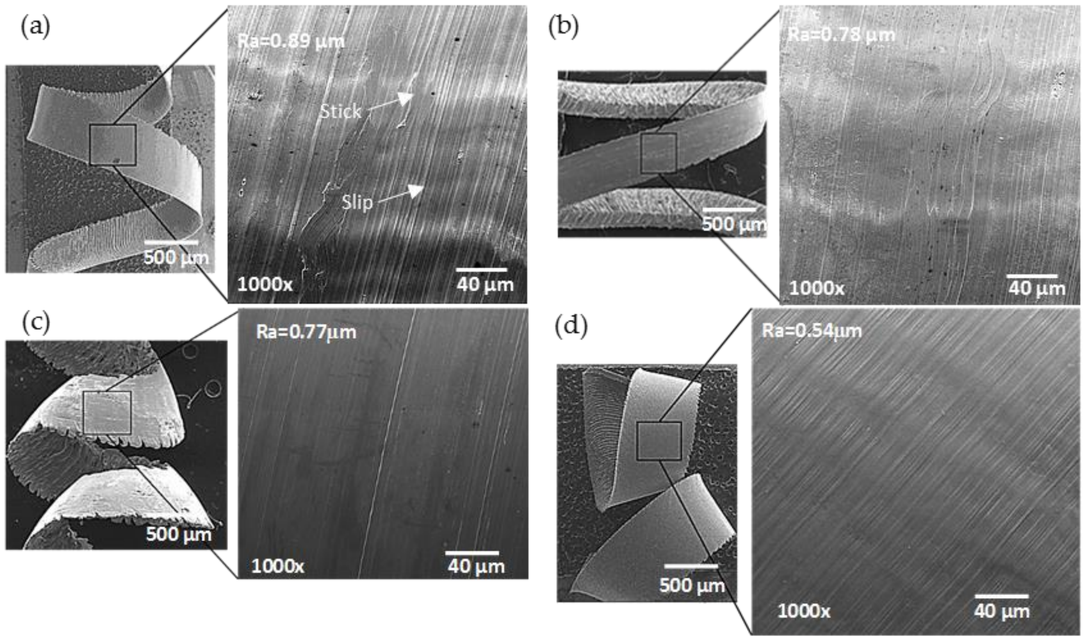

Figure 3-5 Chip breaking under various cooling conditions, associated with chip undersurface obtained with (a) dry; (b) conventional coolant; (c) HPC of 35bar; and (d) HPC of 70 bar

To investigate the role of the HPC system on chip form, the chip cross sections were analyzed using SEM and EBSD analysis, and their data presented in Figure 3-6. As shown, continuous chips obtained with dry and conventional coolants were compared to serrated chips with a supply of HPC, where periodic adiabatic shear bands (ASBs) and cracks were observed. Adiabatic shear bands result from thermo-mechanical instability, which increases shear deformations in small areas [27]. This high localized strain leads to a considerable increase in temperature, and in turn, ASBs [23]. It is commonly known that materials with low strain rates do not show ASBs because heat expansion creates a uniform temperature in the workpiece [28]. Under HPC, the high positive bending

`

moment contributes to the growth of ASBs`frequency, which leads to an increase of the plastic strain in the formed chip (Figures 3-6(c) and 3-6(d)) [29]. Once the chip strain exceeds the chip breaking strain, cracks develop on the ASBs that separate the adjacent segments [30]. As indicated in Figure 3-6, under HPC conditions, the degree of serration in the chip as well as the crack size (the crack depth is around 20 μm) depend on the strength of the shearing action caused by HPC. Also, although no segmentation can be seen in the dry and conventional coolant (Figures 3-6(a) and 3-6(c)), very well-defined segmented chips are generated under HPC conditions (Figures 3-6(e) and 3-6(g)). In order to examine the shear bands differences in greater detail, EBSD analysis was used to investigate the highly deformed shear regions within each chip. The resulting orientations maps of the regions taken from the chips in Figures 3-6(a), 3-6(c), 3-6(e), 3-6(g) are shown in Figures 3-6(b), 3-6(d), 3-6(f), and 3-6(h), respectively. As shown, it can be observed that the grains are more elongated in case of HPC conditions which conforms the sever plastic deformation caused by HPC application. Here, the shear bands formed by dry and conventional coolant have very equiaxed grains (∼1 μm) compared with a mixture of equiaxed grains (∼3 μm) and very elongated grains.

`

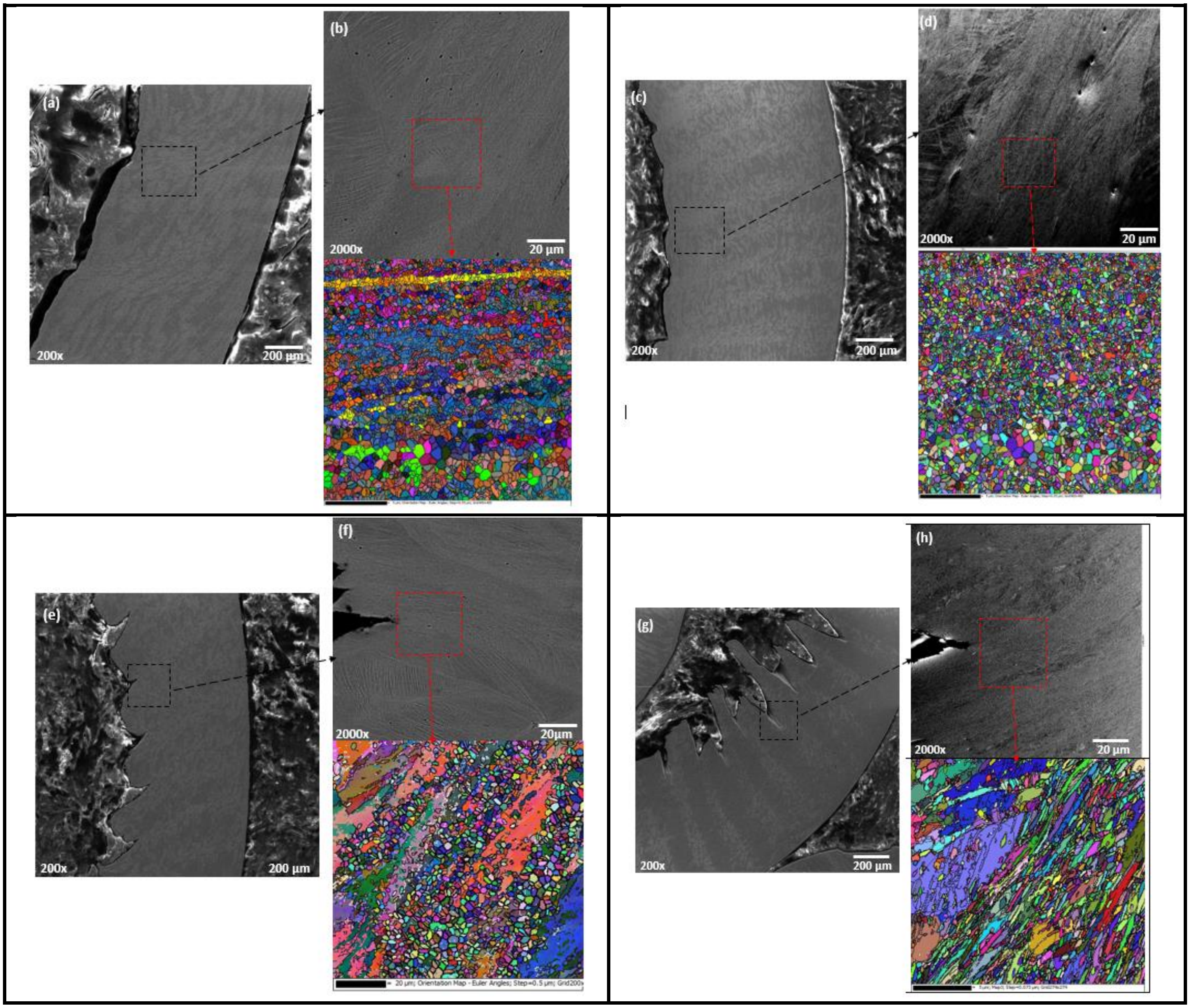

Figure 3-6 SEM and BSE images of chip cross sections associated with orientations maps obtained under different cutting conditions (a-b) Dry; (c-d) Conventional coolant; (e-f) HPC of 35 bar; and (g-h) HPC of 70 bar

`

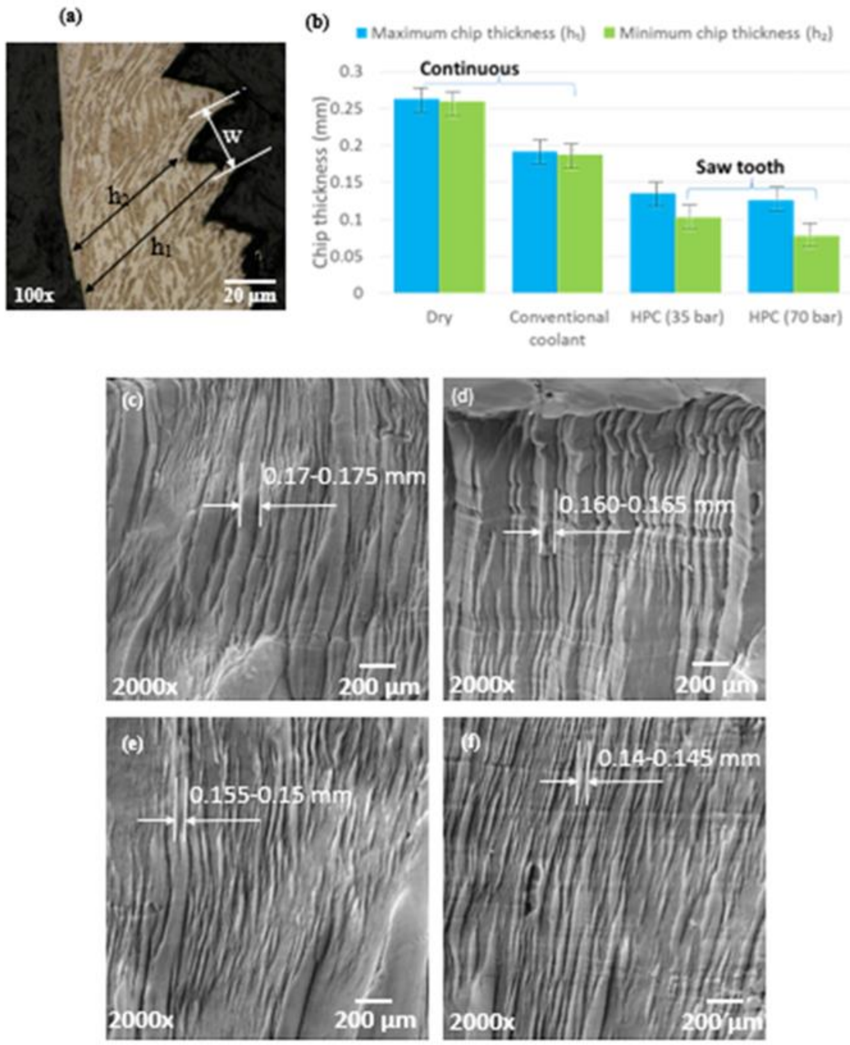

Figure 3-7(a) Parameters of chip serration, (b) the values of maximum and minimum chip thickness for different cooling conditions, (c-f) micrographs of serrated chip cross sections showing the average distance between segments at (c) dry; (d) conventional coolant; (e) HPC of 35 bar; and (f) HPC of 70 bar

In addition, the chip thickness was also evaluated. The data that characterize chip serration are presented in Figure 3-7a. In this figure, h_1 and h_2 represent, respectively, the highest and lowest chip thickness, and w represents the distance between segments. The

`

values of h_1 and h_2 at distinct cooling conditions were measured, and the results are presented in Figure 3-7b. The difference between h_1 and h_2 is observed, and the values decrease under the supply of HPC.

This also agrees with the previous conclusion that the HPC can enhance chip segmentation during the machining process. On the other hand, there is no noticeable difference between the values of h_1 and h_2 in case of dry and conventional coolant; these results confirm the previous conclusion that no segmentation can be observed under the use of dry and conventional coolant.

Furthermore, the distance between segments (w) was measured and presented in Figure 3-7(c-f). The distance between segments is 0.15–0.155 mm and 0.140–0.145 mm for 35 and 70 bar, respectively (Figure 3-7 (e, f)) compared with 0.17–0.175 mm and 0.160–0.165 mm for dry condition and conventional coolant, respectively, as shown in Figure 3-7 (c, d). The distance between segments was found to decrease under HPC, which promotes greater shear formation during the turning process of stainless steel [25].

3.3.1.2 Chip characteristics

The thickness of the chips (t_c) and the tool–chip contact length (L_c) were measured according to the different cutting conditions proposed in this work. An example of measured tool chip contact length is shown in Figure 3-8.

`

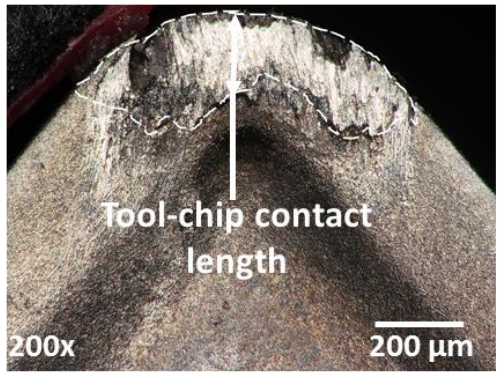

Figure 3-8 Tool-chip contact length

Table 3-2 Cutting characteristics at various cooling conditions

Cooling condition	Chip thickness (mm)	Chip-tool contact length (mm)	Chip thickness ratio	Shear angle (°)	Theoretical Coefficient of friction
Dry	0.263	0.33	0.38	20.8	0.56
Conventional coolant	0.192	0.27	0.52	27.4	0.416
HPC (35 bar)	0.135	0.22	0.74	36.2	0.234
HPC (70 bar)	0.126	0.21	0.79	38.3	0.206

From the chip characteristic results illustrated in Table 3-2, it is possible to see that there is an apparent difference in shear angle and coefficient of friction values for both the dry coolant and HPC. In this case, the chips obtained by HPC produced larger shear angles and a lower coefficient of friction. This phenomenon is a response to the effect of HPC

`

jets directed onto the cutting zone. As a consequence of better fluid access into the cutting zone, the tool–chip contact length is improved, resulting in lower chip thickness compared to dry and conventional conditions. Therefore, machining of AISI 304 under an HPC system produces a short shear area, which leads to thinner chips [8-11, 31] and lower cutting forces and friction coefficient [32].

3.3.2 Chip morphology: effect of tool wear

3.3.2.1 Chip segmentation frequency

The degree of chip deformation was obtained for five different continuous chip segments and the mean value was used. Based on the measured parameters shown in Figure 3-7a, the degrees of chip segmentation can be calculated from Equation 1.

$$G_s = \frac{h_1 - h_2}{h_2} \tag{1}$$

The graph in Figure 3-9 presents the relation between the degree of tool wear and chip segmentation. The measurements show that during the initial phase (new cutting tool insert), a continuous chip is generated in dry condition. Once a particular tool wear degree is reached (F_w=0.2 mm), the chip forming mechanism switches to produce a saw–tooth chip form. On the other hand, no clear variation was found in the degree of segmentation at different flank wears under HPC conditions, which indicates that flank wear did not affect the chip segmentation when HPC is used.

`

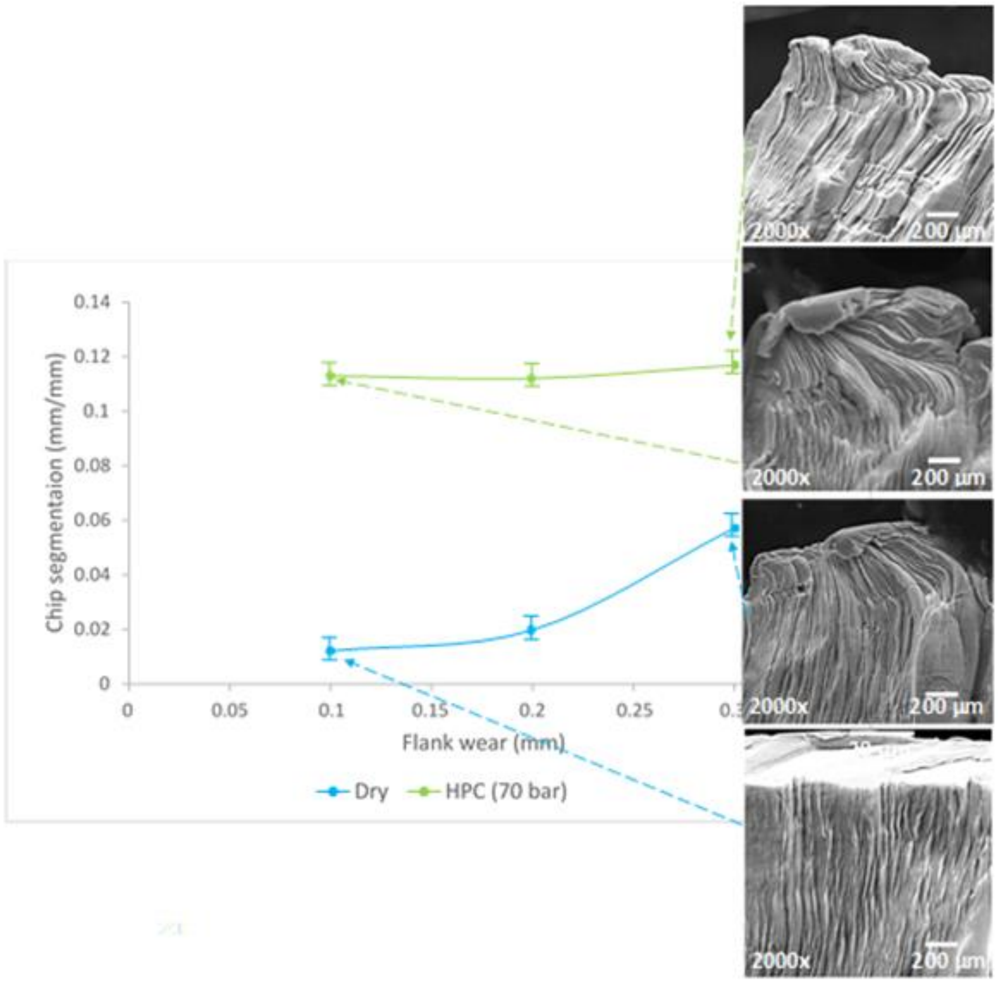

Figure 3-9 Correlation between tool-wear degree and chip-segmentation degree associated with SEM of chips

Also, the variations in segmented chip features under increasing flank wear for dry conditions and HPC are summarized in Table 3-3. As in the dry condition, h_1 and h_2 significantly increased along with the flank wear: these results confirm the previous conclusion that the chip's structure is changed from continuous to saw-tooth form. In contrast, no significant difference in h_1 and h_2 values was found upon an increase in flank wear in the case of HPC due to high plastic deformation generated by HPC during the

`

cutting process. Furthermore, a slight increase of the chip width was observed around the flank wear in both conditions: dry and HPC. This condition is related to high wear and results in an unsharpened cutting tool, which consequently leads to a rough chip edge formation.

Table 3-3 Chip characteristics at various cooling conditions and various flank wear value

Cooling condition	Flank wear (mm)	Maximum chip thickness (mm)	Minimum chip thickness (mm)	Distance between segments (mm)
Dry	0.1	0.251	0.248	0.175
	0.2	0.255	0.253	0.185
	0.3	0.259	0.251	0.198
Conventional Coolant	0.1	0.185	0.183	0.165
	0.2	0.189	0.185	0.173
	0.3	0.191	0.189	0.185
HPC (35 bar)	0.1	0.137	0.122	0.160
	0.2	0.137	0.122	0.168
	0.3	0.138	0.122	0.172
HPC (70 bar)	0.1	0.128	0.115	0.150
	0.2	0.129	0.117	0.163
	0.3	0.129	0.116	0.178

`

As discussed, the transformation from continuous chip to saw-tooth chip under dry and conventional coolant is accompanied by an increase in flank wear. Investigation of the chips' free surface obtained under dry condition reveals two distinct structures, the most frequently observed of which is the lamellar structure (Figure 3-10(a)). A difference in the chips' free surface geometry was investigated just prior to the formation of chip segments caused by an increase in flank wear. These new geometries, shown in Figure 3-10(b), have been termed as folds. Further increase in flank wear leads to more deformation, which in turn can enhance the formation of saw-tooth chips (Figure 3-10(c)).

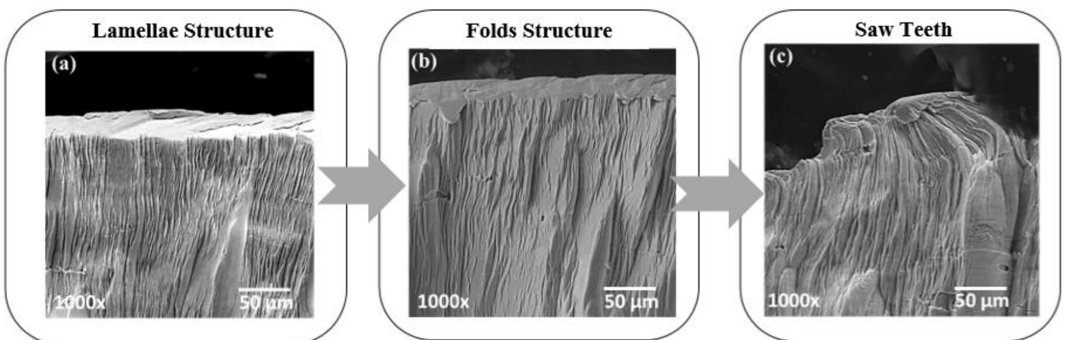

Figure 3-10(a) Lamellae on the free surface of a continuous chip; (b) folds formed on the free surface of a continuous chip produced under the same conditions as the chip in a; (c) saw-tooth form chip under the same conditions as the chips in a and b

3.3.2.2 Free surface of chips

Figure 3-11(a, b) shows the free surface of typical chips obtained with new and worn tools under dry and HPC conditions. A lamellar structure is evident on the underside of the chips obtained under dry conditions and HPC (Figures 3-11(B, G)). At high magnification, it is observed that each segment of the free surface has slipping and

`

undeformed surfaces, (Figures 10(a-C, b-C)). With the new tool, the slipping surface features a high number of dimples (Figures 3-11(C, H)), as a result of high plastic deformation during chip segmentation. As shown, the incidence of dimples in case of HPC is greater compared to the dry condition, which confirms that HPC is capable of increasing the plastic deformation during cutting and consequently, the fracture mechanism. On the other side, it can be seen that there are sliding lines on the undeformed surface, as described in Figures 3-11(C, H), which were produced by high friction between the cutting tool and the chip (the frequency of sliding lines is less in HPC, since the tool–chip contact length is lower (Table 3-3)).

When the cutting tool reaches its maximum wear (F_w=0.3 mm) under the dry condition, the frequency of undeformed surfaces is greater than that of the new tool because the chips are transformed from continuous into segmented types, as described in Figure 3-9. Also, the deformation on the slipping surface shows an obvious viscous behavior (Figure 3-11(a-E)), which indicates that the cutting temperature is much higher at tool failure compared to that of a fresh tool. In contrast, at the end of tool life with HPC, no viscous behavior is observed (Figure 3-11(b-E)), which indicates that the HPC is capable of significantly decreasing the cutting temperature even at a greater flank wear.

`

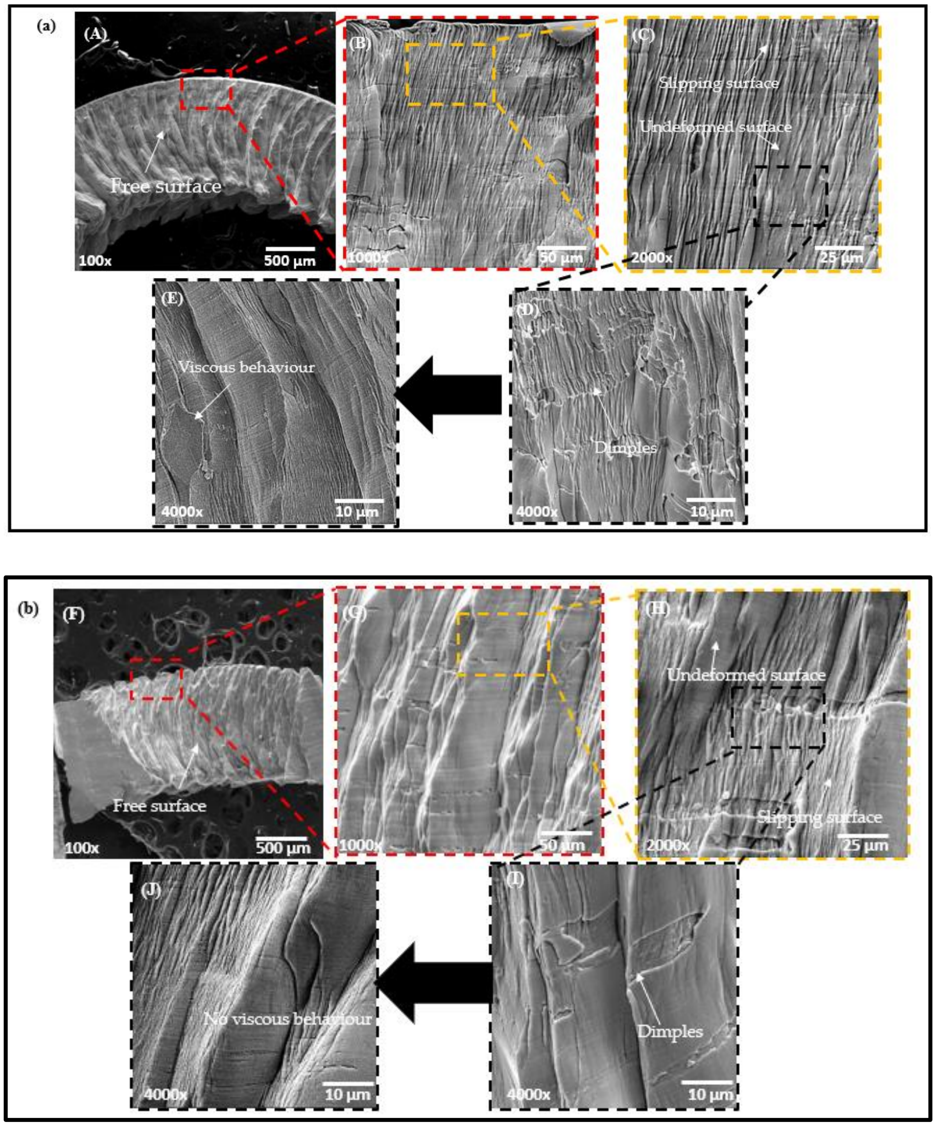

Figure 3-11 Chip morphology obtained in (a) dry and (b) HPC; (A-D) and (F-I) images of free chip surface, generated with new tool and (E-J) with worn tool

`

3.4. Understanding the chip breaking process

During the machining operation, the penetration of the coolant at the tool–chip interface affects the chip formation and its removal from the cutting area [33]. Since machining involves a great deal of chip formation processes, their breaking mechanisms have been studied for many years [5, 7, 17, 18]. The mechanisms of chip breaking are found to be affected by different parameters, such as machining conditions, workpiece material, tool insert geometry, cutting fluid and pressure level [6, 9]. In this section, the theory of chip breaking will be discussed in general and then the influence of HPC on chip breakability will be investigated. Following the chip breaking theory, the chip upcurl radius will be measured at different cooling conditions to study the impact of different cooling conditions on the chip curling behavior.

3.4.1 Chip breaking theory

Chip curling mainly depends on the direction of chip flow [23]. The chip curl geometry is defined by three parameters, side curling, upcurling, and twisting [34] (Figure 3-12(a-c)). The chip upcurl radius (R_f) has an important influence on chip breakability where upcurl is dominant [11]. The chip breaking process occurs when strain on chip body exceeds the maximum strain of chip material which is mainly the result of forces generated by HPC [36]. These contact forces will generate a moment leading up to chip fracture [35], and this is expressed as:

`

$$\varepsilon_{chip} = \frac{t_c}{2}\left[\frac{1}{R_f} - \frac{1}{R_n}\right] \geq \varepsilon_{fr} \quad 2)$$

Where t_c is the chip thickness, R_n is the natural chip radius, and ε_{fr} is the breaking strain.

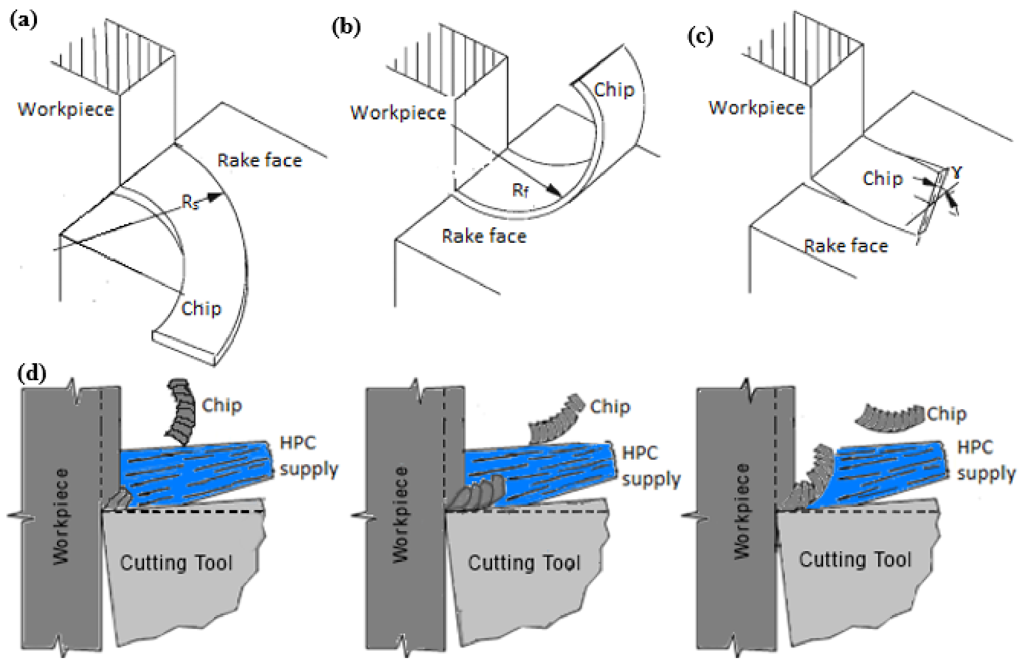

Figure 3-12 (a-c) Parameters of chip curl radius; (a) chip up side radius; (b) Chip up curl radius; (c) twisting. [45], and (d) the formation of segmented chips under HPC supply [15]

Mathematical equations utilizing the above formula were characterized by Nakayama et al. [37]. The formulations of chip curl are qualitatively defined, and they have been used for many years to predict the chip breaking behavior. However, these equations miss the linkage between HPC and chip curling. Thus, understanding the role of HPC on the chip upcurl radius is necessary to predict chip breakability during machining.

`

To understand the relation between HPC and chip curling, Figure 3-12 (d) illustrates how HPC can affect the chip curling process. As shown, the mechanism of chip curling through the HPC system is a continuous process. After deformation occurs at the primary shear plane, the chip starts to grow and curl due to the high pressure of the HPC system [38]. Then, due to high force of the HPC, the chip further grows until it reaches the limit of chip material strain [5]. The most probable point of breakage is where the HPC is at its maximum strength, forcing the chip away from the cutting tool [12]. Meantime, a new chip is formed, and the process repeats itself [39].

3.4.2 Chip upcurl radius measurement

The final chip upcurl radius was measured to quantify the above observations and relate them to the cutting conditions. The main part of this study focuses on the capability to employ chip upcurling as a method to verify the theoretical model of chip breaking in the machining operation.

After each test, the chips were collected and scanned using SEM to measure the chip upcurl radius. The variation of chip radius with respect to the cooling conditions is shown in Figure 3-13. It seems that the final chip upcurl radius depends on the coolant conditions. Firstly, under dry and conventional coolant, the chips showed a large radius which corresponds to the shape of the chip space of the cutting tool [5]. The larger tool-chip contact length, results in a greater tendency of material sticking on the cutting tool,

`

restraining further chip movement [22]. In contrast, under HPC conditions, the chips become smaller, reducing chip length as well as the final chip upcurl radius [40].

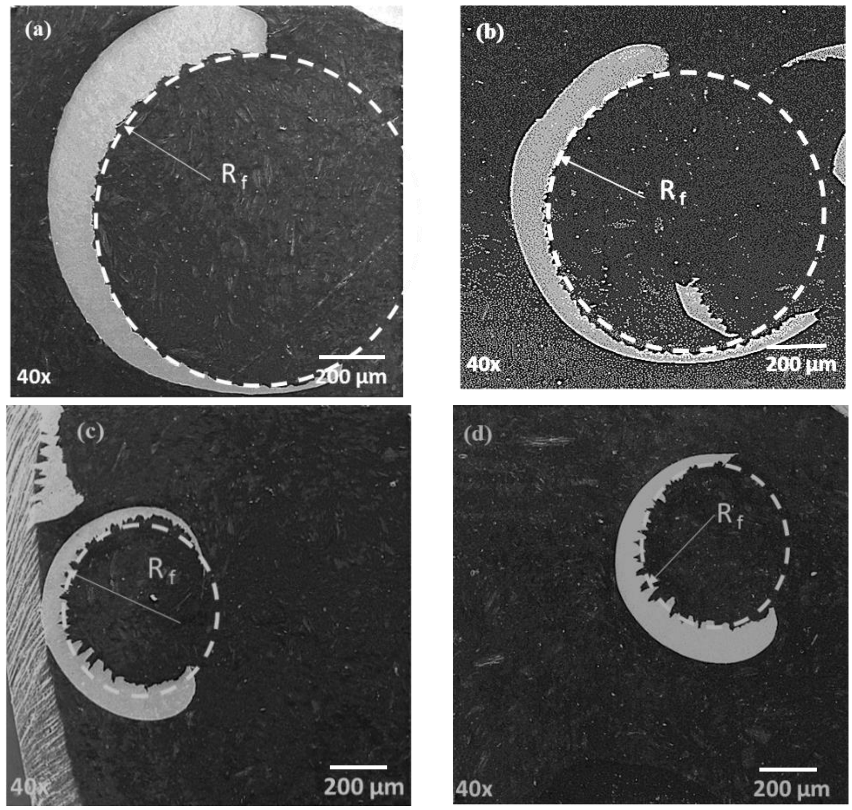

Figure 3-13 Chip upcurl radius under different cooling conditions; (a) dry; (b) conventional coolant; (c) HPC of 35 bar; and (d) HPC of 70 bar

3.5 Theoretical modelling of chip curling

In this section, a 3D theoretical model will be developed to predict chip upcurl radius under HPC. To derive the model, the effect of plastic strain on chip free surfaces will be derived individually in section 5.3. Next, the effect of HPC on the chip body will be investigated in section 5.4. The model is based on the shear plane and structural

`

mechanical theories involving plastic strain and bending moments along the length of the curled chip caused by HPC.

3.5.1 Theory

In the theoretical model, it is assumed that the cutting tool is rigid with rake angle (γ) and the undeformed and formed chip thicknesses are denoted t and t_c, respectively. Merchant [41] applied the shear plane theory (Figure 3-14(a)) to derive an expression for the plastic strain as:

$$\varepsilon = \frac{cos\gamma}{cos(\Phi - \gamma)sin\Phi} \qquad 3)$$

Where Φ is shear angle

Astakhov and Shevets [42] modified Equation 3 and used a von Mises yield criteria to derive the plastic strain on the chip free surface during 3D chip formation and the derived equation is as follows:

$$\varepsilon = \frac{\sqrt{2}}{3}\left[\left(\varepsilon_x - \varepsilon_y\right)^2 + \left(\varepsilon_y - \varepsilon_z\right)^2 + (\varepsilon_z - \varepsilon_x)^2 + 6\left(\gamma_{xy}^2 + \gamma_{yz}^2 + \gamma_{zx}^2\right)\right]^{0.5} \qquad (4)$$

Where ε_x, ε_y, ε_z, γ_{xy}, γ_{xz}, γ_{yz} are the strain components of the strain tensor.

From literature, there are many authors who used the plastic chip strain as a method for predicting the chip breaking process. They showed that by decreasing the chip upcurl

`

radius, the tendency of chip failure increases by enhancing the chip plastic strain [5.7]. Nakamura [37] presented a relation of the plastic chip strain, which developed from the initial chip upcurl radius to the final chip upcurl radius (Equation 2).

However, there are many researches in this field, the scarcity of basic theory for 3D plastic flow and study the effect of HPC on chip breakability make it difficult to develop a 3D oblique cutting model. Here, the objective of introducing these parameters to make the model simpler to develop. A 3D oblique process can be treated as a modification of a 2D orthogonal cutting process. Therefore, the fracture mechanism of 3D process can be described by the 2D bending of a curved beam. The only difference here between Nakamura equation and Equation 5 is that the used parameters should be replaced by their corresponding parameters, i.e:

$$\varepsilon_{up} = \frac{t_c}{2R_f} \tag{5}$$

Where t_c is the maximum chip thickness, R_f is the radius of chip fracture, and $\varepsilon_{up}$is the chip strain.

However, few authors derived theoretical models that show the effect of plastic strain on chip curling. A clear understanding of the mechanism of chip breakability under HPC use is yet to be found. The bending moment and forces acting on the chip body through HPC play a key role in the chip curling and breaking process [38]. The chip's formation out of the cutting tool edge's meeting point with the workpiece is considered to be a plastic

`

deformation process [45]. After this process occurs, the material of the chip shows obvious strain hardening. Thus, it is assumed that the chip generated after HPC has no further plastic deformation [38]. The chip is presumed to move with an angular speed as a static structure. By understanding how the forces and bending moments affect the chip body, the chip breakability will be investigated.

In summary, chip upcurling plays a vital role on chip breakability. The impact of HPC on chip upcurling behavior still merits further investigation, which may help to develop a more effective system with favorable chip breaking properties.

3.5.2 Model assumptions

The machining operation is a sophisticated process; thus, several assumptions were made to predict the chip upcurl radius. The theoretical model thus assumes the following holds true:

(1) Tool edge radius is neglected;

(2) Chip formation is continuous;

(3) Volume is constant;

(4) No material separation;

(5) The chip forming after the application of HPC has no further plastic deformation;

`

(6) The cutting tool and the machining system are rigid during the cutting operation.

3.5.3 Derivation based on shear plane theory

As discussed in the previous section, the chip plastic strain (ε_{up}) is a function of both t_c and R_f (Figure 3-14a). ε_{up} is proportional to the t_c and inversely proportional to R_f (Equations 5). To predict the value of R_f, it is necessary to predict the values of ε_{up} and t_c. t_c can be calculated from Equation 6.

$$t_c = \frac{t}{r} \tag{6}$$

Where thickness ratio, r, is assumed to be 0.05 [42]. Thus, t_c can be assumed to be 0.05t. t can also be calculated from Equation 7.

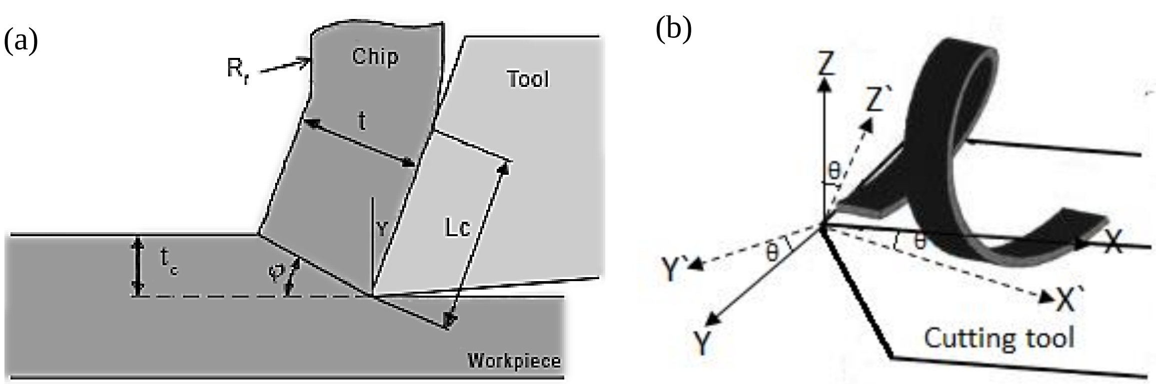

Figure 3-14(a) Graphical representation of shear plane model and (b) deformation axes for chip curling phase [42]

$$t = f cos\Phi \tag{7}$$

To be able to define the tensor of the chip strain, the tensor is conducted around the rotation angle (θ) (Figure 3-14(b)). This tensor can be described using Mohr's circle

`

relationship. Equation 8 relates the transformation of a strain tensor from the unrotated ab-coordinate system. Here, the tensor is assumed to be rotated around the third axis (ψ).

$$\varepsilon_{up} = \begin{bmatrix} \varepsilon_a & \gamma_{ab} \\ \gamma_{ba} & \varepsilon_b \end{bmatrix} \tag{8}$$

Considering the deformation axes and volume constancy, ε_a, ε_b, and $\gamma_{ab}=\gamma_{ba}$ can be calculated as follows:

$$\varepsilon_{ax} = \frac{\varepsilon_{xx} + \varepsilon_{zx}}{2} + \frac{\varepsilon_{xx} - \varepsilon_{zx}}{2} cos(2\psi) + \gamma_{xz} sin(2\psi) \tag{9}$$

$$\varepsilon_{ay} = \frac{\varepsilon_{xy} + \varepsilon_{zy}}{2} + \frac{\varepsilon_{xy} - \varepsilon_{zy}}{2} cos(2\psi) - \gamma_{xz} sin(2\psi) \tag{10}$$

$$\varepsilon_{bx} = \frac{\varepsilon_{xx} + \varepsilon_{zx}}{2} + \frac{\varepsilon_{xx} - \varepsilon_{zx}}{2} cos(2\psi) + \gamma_{xz} sin(2\psi) \tag{11}$$

$$\varepsilon_{by} = \frac{\varepsilon_{xy} + \varepsilon_{zy}}{2} + \frac{\varepsilon_{xy} - \varepsilon_{zy}}{2} cos(2\psi) - \gamma_{xz} sin(2\psi) \tag{12}$$

$$R = \frac{-\varepsilon_a - \varepsilon_b}{2} sin(2\psi) + \gamma_{ab} cos(2\psi) \tag{13}$$

$$\varepsilon_a = \frac{\varepsilon_{ax} + \varepsilon_{ay}}{2} \tag{14}$$

$$\varepsilon_b = \frac{\varepsilon_{bx} + \varepsilon_{by}}{2} \tag{15}$$

$$\varepsilon_a = \frac{\varepsilon_x + \varepsilon_z}{2} + \frac{\varepsilon_x - \varepsilon_z}{2} cos(2\psi) \tag{16}$$

`

$$\varepsilon_b = \frac{\varepsilon_a + \varepsilon_b}{2} - \frac{\varepsilon_a - \varepsilon_b}{2} cos(2\psi) \tag{17}$$

$$\gamma_{dc} = \frac{-\varepsilon_a - \varepsilon_b}{2} sin(2\psi) \tag{18}$$

Thus, the chip upcurl strain tensor can be expressed in the XYZ coordinate system as follows:

$$\varepsilon_{up} = \begin{bmatrix} \frac{\varepsilon_x + \varepsilon_z}{2} + \frac{\varepsilon_x - \varepsilon_z}{2} cos(2\psi) + \gamma_{ab} sin(2\psi) & 0 & \frac{-\varepsilon_x - \varepsilon_z}{2} sin(2\psi) + \gamma_{ab} cos(2\psi) \\ 0 & \varepsilon_y = \varepsilon_z & 0 \\ \frac{-\varepsilon_x - \varepsilon_z}{2} sin(2\psi) + \gamma_{ab} cos(2\psi) & 0 & \frac{\varepsilon_x + \varepsilon_z}{2} - \frac{\varepsilon_x - \varepsilon_z}{2} cos(2\psi) - \gamma_{ab} sin(2\psi)) \end{bmatrix} \tag{19}$$

To solve the tensor, I_1, I_2 and I_3 can be calculated as follows:

$$-\varepsilon^3 + I_1\varepsilon^2 - I_2\varepsilon + I_3 = 0 \tag{20}$$

$$I_1 = \varepsilon_x + \varepsilon_y + \varepsilon_z \tag{21}$$

$$I_2 = \varepsilon_X\varepsilon_y + \varepsilon_y\varepsilon_z + \varepsilon_x\varepsilon_z - \gamma_{xy}^2 - \gamma_{xz}^2 - \gamma_{yz}^2 \tag{22}$$

$$I_3 = \varepsilon_x\varepsilon_y\varepsilon_z + 2\varepsilon_{xy}\varepsilon_{xz}\varepsilon_{yz} - \varepsilon_{xy}^2\varepsilon_z - \varepsilon_{xz}^2\varepsilon_y - \varepsilon_{yz}^2\varepsilon_{zx} \tag{23}$$

By knowing the values of I_1, I_2 and I_3, ε_{up} can be obtained from Equation 19 and R_f from Equation 5.

3.5.4 Derivation based on structural mechanics theory

HPC used with continuous chip production may strike the chip, creating a reactive force on it, causing a bending moment to act along the chip body, which in turn, bends the chip [46]. In this case, the curved chip can be considered to be a statically d'eterminant curved beam as shown in Figure 3-15(a). To analyze the force system on the curled chip, the chip may be regarded as a free body held in static equilibrium and the force system acting on it (Figure 3-15(b)) [47].

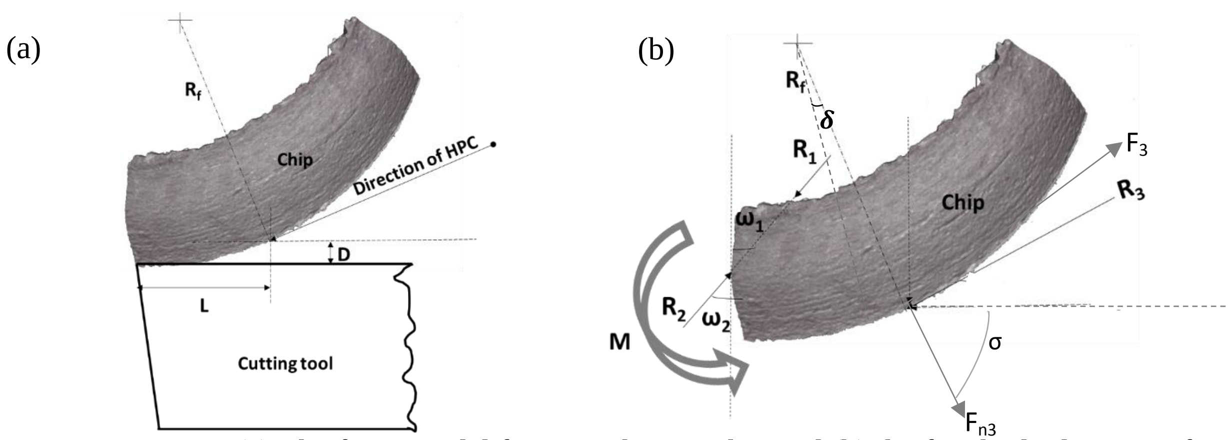

Figure 3-15 (a) The force model for HPC, hitting chip and (b) the free body diagram of chip curling

$$R_1 + R_2 + R_3 = 0 \tag{24}$$

By using the vector equilibrium relationship of forces (Equation 24), the equation can be expressed as follows:

$$-R_1 sin\omega_1 + R_2 sin\omega_2 + F_{n3} Cos\sigma + F_3 cos(90 - \sigma) = 0 \tag{25}$$

`

$$R_1 cos\omega_1 - R_2 cos\omega_2 - F_{n3} Sin\sigma - F_3 sin(90 - \sigma) = 0 \qquad (26)$$

The friction force (F_3) can be expressed as $F_3 = \mu F_{n3}$, where μ is the friction coefficient, thus μ can be expressed by:

$$\mu = \frac{F_3}{F_{n3}} \qquad (27)$$

From Equations 25, 26 and 27, R_2 can be expressed as follows:

$$R_2 = \frac{F_{n3}}{sin\omega_2}(cos\sigma + \mu \sin\sigma) + \frac{R_1 \sin\omega_1}{sin\omega_2} \qquad (28)$$

Substitution of Equation 27 into Equation 28, F_3 and F_{n3} can be expressed as follows:

$$F_{n3} = \frac{R_1(cos\omega_1 sin\omega_2 - cos\omega_2 sin\omega_1)}{cos\omega_2 Cos\sigma - sin\omega_2 Sin\sigma + \mu(sin\omega_2 cos\sigma + cos\omega_2 Sin\sigma)} \qquad (29)$$

$$F_3 = \frac{\mu R_1(cos\omega_1 sin\omega_2 - cos\omega_2 sin\omega_1)}{cos\omega_2 Cos\sigma - sin\omega_2 Sin\sigma + \mu(sin\omega_2 cos\sigma + cos\omega_2 Sin\sigma)} \qquad (30)$$

Therefore, based on the force equilibrium principle, the bending moment M at any cross section along the curved chip length located at the spiral angle δ, can be determined from the following:

$$M = F_3 R_f (1 - Cos\delta) - F_{n3} R_f Sin\delta \qquad (31)$$

Or, $M = F_{n3} R_f (\mu - \mu Cos\delta - Sin\delta)$ (32)

`

From the values of F_{n3}, M, μ, and spiral angle (σ), final chip upcurl radius can be calculated:

$$R_f = \frac{M}{F_{n3}(\mu - \mu cos\delta - sin\delta)} \tag{33}$$

From Equations 5, 19, and 33, final chip upcurl radius obtained by HPC is:

$$R_{fHPC} = \left|\frac{t_c}{2\varepsilon_{up}} - \frac{M}{F_{n3}(\mu - \mu cos\delta - sin\delta)}\right| \tag{34}$$

Where, t_c, ε_{up}, and μ, F_{n3}, M are determined by Equations 5, 19, 27, 29, and 32, respectively.

3.5.5 Model validation

The theoretical model established above to predict the resultant chip upcurl radius was evaluated for its credibility. The experimental values of chip upcurl radius were compared to the predicted values obtained from the theoretical models (Figure 3-16). Figure 3-16(a) and 3-16(b) show the average prediction errors at different feed rates for HPC (35 bar) and HPC (70 bar), respectively. As shown, the resultant chip upcurl radius values generated by the model gave results very close to the experimental values of the resultant chip upcurl radius with an error of 5 – 6 %.

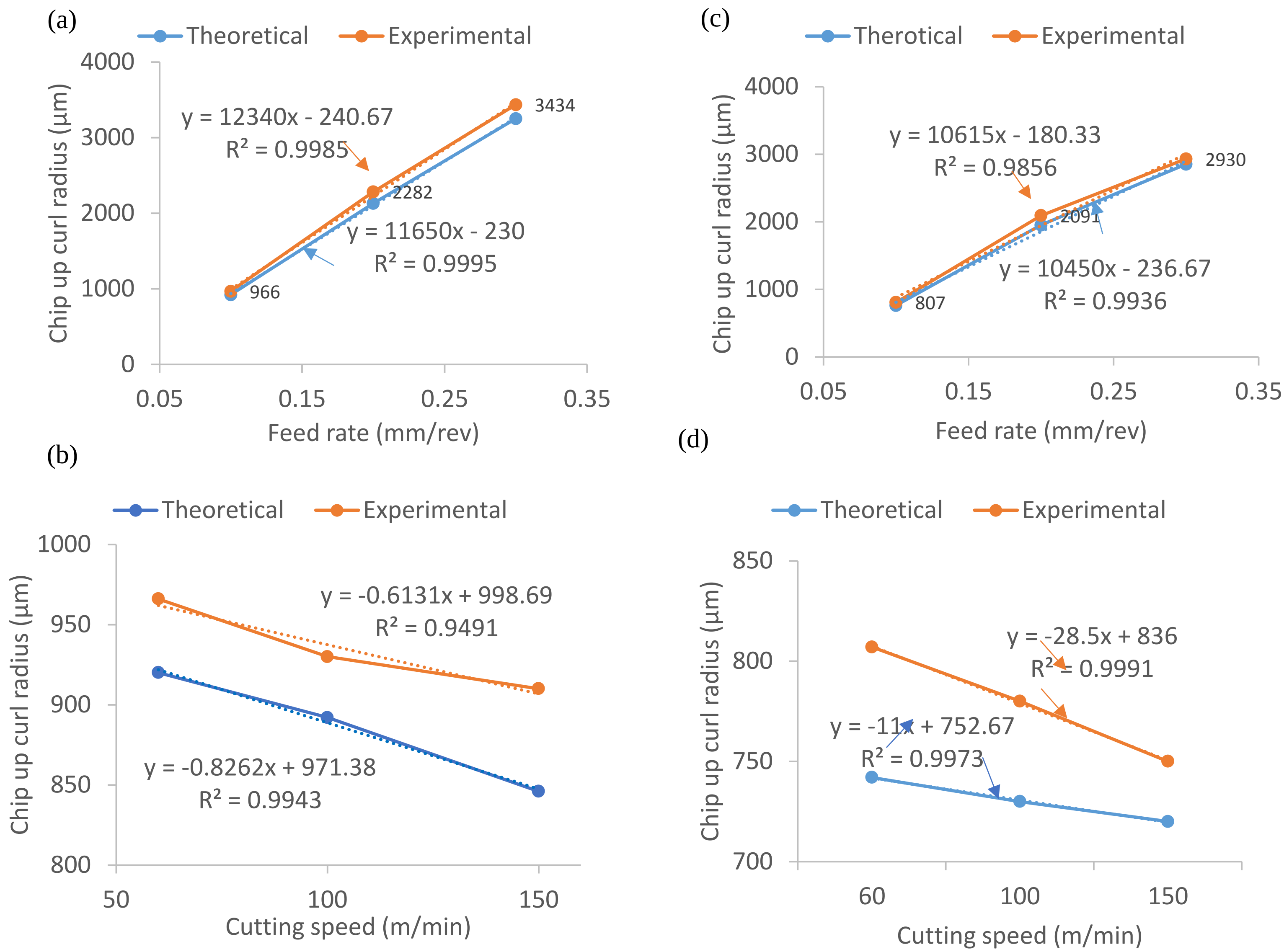

Figure 3-16 Comparison between the average values of theoretical and experimental chip curl radius with (a, b) HPC of 35 bar and (c, d) HPC of 70 bar

In addition, in Figure 3-16(c) and 3-16(d), the average prediction errors at different cutting speeds are 8% and 9% for HPC (35 bar) and HPC (70 bar), respectively. This indicates that the proposed model is reliably able to predict the chip upcurl radius even at

`

different cutting speeds. From these comparisons, it can be concluded that the theoretical model can make a very good predictions for chip upcurl radius at different HPC conditions as well as at different cutting conditions.

Table 3-4 Validation of Experiment

HPC	Cutting speed (m/min)	Feed rate (mm/rev)	Average experimental value (μm)	Average theoretical value (μm)	Error %
35 bar	**60**	0.1	920	966	5
		0.2	2130	2282	7
		0.3	3250	3434	5.6
	100	0.1	950	912	4
		0.2	2250	2115	6
		0.3	3122	2915	6.6
	150	0.1	910	846	7
		0.2	2232	2101	5.9
		0.3	3015	2880	4.5
70 bar	**60**	0.1	807	742	8
		0.2	2091	1950	6.7
		0.3	2930	2850	2.7
	100	0.1	790	740	2
		0.2	1998	1820	6.3
		0.3	2710	2513	7.2
	150	0.1	720	665	7.6
		0.2	1807	1730	4.2
		0.3	2520	2320	7.9

(b)

`

Table 3-4 shows the exact percentage of error between the results obtained from experimental and theoretical model values for the two different HPC conditions at different cutting conditions. This shows that the theoretical model can be used in the future to monitor chip breakability under HPC supply at different cutting conditions.

3.6 Conclusions

In this research, multiple experiments were conducted to investigate the chip morphology and the chip forming mechanism during machining of AISI 304 stainless steel with an HPC system, and to compare the results with those of dry and conventional coolant. From the experimental results and theoretical model, the specific conclusions can be drawn:

1. HPC conditions help to break up chips, producing shorter segmented chips, which in turn enhance the process efficiency. However, dry and conventional coolant did not show a distinct effect on chip breakability.
2. HPC conditions produce more regular serration in the chips, compared with absent segmentation observed in dry and conventional coolant.
3. Tribological performance was improved with HPC. Lower chip thickness and higher shear angle are obtained under HPC conditions, compared to dry and conventional coolant, which in turn leads to decrease cutting forces and increase chip curl to improve chip control.

4. The chip undersurface is smooth and has no observable defects under HPC conditions, indicating low tool-chip contact length and consequently lower friction between the chip and the cutting tool.
5. The variation of flank wear affects the chip forming mechanism and its segmentation. Machining with new tool inserts under dry and conventional coolant, generated continuous chips, and upon increasing flank wear, the type of generated chip transitions from continuous to saw-tooth. This is due to high friction between the worn cutting edge and chip, leading to significant shear on the machined surface in the chip.
6. No significant difference was found in the degree of segmentation in the case of HPC at different flank wears, which indicates that the flank wear did not affect the chip segmentation whenever HPC is used. This is due to sever plastic deformation caused by HPC application.
7. Lastly, a 3D theoretical model was developed to predict chip upcurl radius under HPC machining and the results were found to be in good agreement with actual measurements taken from a machining experiment with AISI 304 stainless steel.

Acknowledgments

This research was supported by Natural Sciences and Engineering Research Council of Canada (NSERC) under the CANRIMT Strategic Research Network Grant NETGP 479639-15.

`

References

1. Xavior MA (2012) Evaluating the machinability of AISI 304 stain- less steel using alumina inserts. J Achiev Mater Manuf Eng 55:841– 847
2. Gariani S, Shyha I, Inam F, Huo D (2017) Evaluation of a novel controlled cutting fluid impinging supply system when machining titanium alloys. Appl Sc 7:560
3. Rahman M, Senthil Kumar A, Choudhury MR (2000) Identification of effective zones for high pressure coolant in milling. CIRP Ann Manuf Technol 49:47–52
4. Mia M, Dhar NR (2018) Effects of duplex jets high-pressure cool- ant on machining temperature and machinability ofTi-6Al-4V super alloy. J Mater Process Technol 252:688–696
5. Liu E, Han R, Tan G, Li Z (2006) Analysis of chip breaking pre- diction in cutting aluminum alloys. Mater Sci Forum 532:213–216
6. Kaminski J, Alvelid B (2000) Temperature reduction in the cutting zone in water-jet assisted turning. J Mater Process Technol 106:68–73
7. Kubala Z (1989) Metal machining with high- pressure water-jet cooling assistance—a new possibility. J Eng Ind 111:7–12
8. Courbon C, Sajn V, Kramar D, Rech J, Kosel F, Kopac J (2011) Investigation of machining performance in high pressure jet assisted turning of Inconel 718: an experimental study. J Mater Process Technol 211:1834–1851
9. Palanisamy S, Townsend D, Scherrer M,Andrews R, Dargusch MS (2009) High pressure coolant application in milling titanium. Mater Sci Forum 618:89–92

`

10. Machado AR, Wallbank J, Pashby IR, Ezugwu EO (1998) Tool performance and chip control when machining Ti6A14V and Inconel 901 using high pressure coolant supply. Mach Sci Technol 2:1–12

11. slip-line field theory with adhesion friction at chip / tool. J Mater Process Technol 170(1):509–515

12. Joshi SS, Ramakrishnan N, Ramakrishnan P (1999) Analysis of chip breaking during orthogonal machining of Al/SiCp composites. J Mater Process Technol 88(1):90–96

13. Henriksen Ek (1954) Chip breaker studies I: design and performance of ground chip breakers, Engineering Reprint Series Reprint Number 12 The University of Missouri Bulletin, Missouri

14. Okushima K, Minato K (1959) On the behaviour of chip in steel cutting. Bulletin JSME 2(5):58–64

15. Sandvik Coromant (2017) Turning tools, Switzerland 16. Koyee RD, Schmauder S, Heisel U, Eisseler R (2015) Numerical modeling and optimization of machining duplex stainless steels. Prod ManufRes 3:36–83

16. Koyee RD, Schmauder S, Heisel U, Eisseler R (2015) Numerical modeling and optimization of machining duplex stainless steels. Prod Manuf Res 3:36–83

17. Panda A, Duplák J, Vasilko K (2012) Analysis of cutting tools durability compared with standard ISO 3685. Int J Comput Theory Eng 4(4):621–624

18. Shaw M (2005) Metal cutting principles, 2nd edn. Oxford University Press, New York

`

19. ISO (2000) ISO 5436-1:2000 (en): Geometrical product specifications (GPS)—surface texture: profile method, Measurement standards–part1, Geneva, Switzerland
20. Shivpuri R, Hua J, Mittal P, Srivastava AK, Lahoti GD (2002) Microstructure-mechanics interactions in modeling chip segmentation during titanium machining. CIRP Ann 51(1):71–74
21. Mia M, Dhar NR (2015) Effect of high pressure coolant jet on cutting temperature, tool wear and surface finish in turning hardened (Hrc 48) steel. J Mech Eng 45(1):1–16
22. Abukhshim NA, Mativenga PT, Sheikh MA (2004) An investigation of the tool-chip contact length and wear in high-speed turning of EN19 steel. Proc Inst Mech Eng B J Eng Manuf 218(8):889–903
23. Wan ZP, Zhu YE, Liu HW, Tang Y (2012) Microstructure evolution of adiabatic shear bands and mechanisms of saw-tooth chip formation in machining Ti6Al4V. Mater Sci Eng A 531(1):155–163
24. Habak M, Lou Lebrun J (2011) An experimental study of the effect of high-pressure water jet assisted turning (HPWJAT) on the surface integrity. Int J Mach Tools Manuf 51(9):661–669
25. Haddag B, Makich H, Nouari M, Dhers J (2015) Characterization and modelling of the rough turning process of large-scale parts: tribological behavior and tool wear analyses. Procedia CIRP 31(1):293–298

`

26. Bi XF, Sutter G, List G, Liu YX (2009) Influence of chip curl on tool-chip contact length in high speed machining. Mater Sci Forum 626(1):71–74
27. Molinari A, Musquar C, Sutter G (2002) Adiabatic shear banding in high speed machining ofTi-6Al-4V: experiments and modeling. Int J Plast 18(1):443–459
28. Miguèlez MH, Soldani X, Molinari A (2013) Analysis of adiabatic shear banding in orthogonal cutting of Ti alloy. Int J Mech Sci 75(1):212–222
29. Barry J, Byrne G (2002) The mechanisms of chip formation in machining hardened steels. J Manuf Sci Eng 124(3):528–545
30. Sima M, Özel T (2010) Modified material constitutive models for serrated chip formation simulations and experimental validation in machining of titanium alloy Ti-6Al-4V. Int J Mach Tools Manuf 50(11):943–960
31. Da Silva RB, MacHado AR, Ezugwu EO, Bonney J, Sales WF (2013) Tool life and wear mechanisms in high speed machining ofTi-6Al-4Valloy with PCD tools under various coolant pressures. J Mater Process Technol 213(8):1459–1464
32. Gajrani KK, Sankar MR (2017) ScienceDirect state of the art on micro to nano textured cutting tools. Mater Today Proc 4(2):3776– 3785
33. Khan MA (2015) Effect of high pressure coolant jets in turning Ti-6al-4v alloy with specialized designed nozzle. Dissertation, Bangladesh University of Engineering & Technology Dhaka
34. Jawahir IS (1990) On the controllability of chip breaking cycles and modes of chip breaking in metal machining. CIRP Ann Manuf Technol 39(1):47–51

`

35. Wang B, Liu Z (2016) Evaluation on fracture locus of serrated chip generation with stress triaxiality in high speed machining of Ti6Al4V. Mater Des 98(1):68–78

36. Skrzypek J, Ganczarski A (1999) Modeling of material damage and failure of structures. Theory and Applications, London

37. NakayamaK, Arai M,Kanda T (2011) Machining characteristics of hard materials. Mach Hard Mater 37(1):1–21

38. Zhou L (2011) Machining chip-breaking prediction with grooved inserts in steel turning, dissertation, Worcester Polytechnic Institute

39. Buchkremer S, Schoop J (2016) A mechanics-based predictive model for chip breaking in metal machining and its validation. CIRP Ann Manuf Technol 65(1):69–72

40. Devotta A, Beno T, Löf R, Espes E (2015) Quantitative characterization of chip morphology using computed tomography in orthogonal turning process. Procedia CIRP 33(1):299–304

41. Merchant ME (1945) Mechanics of the metal cutting process. II. Plasticity conditions in orthogonal cutting. J Appl Phys 16(1):318– 324

42. Astakhov VP, Shvets SV, Osman MOM (1997) Chip structure classification based on mechanics of its formation. J Mater Process Technol 71(2):247–257

43. Buchkremer S, Klocke F, Lung D (2015) Finite-element-analysis of the relationship between chip geometry and stress triaxiality distribution in the chip

`

breakage location of metal cutting operations. Simul Model Pract Theory 55(1):10–26

44. Buchkremer S, Klocke F, Lung D (2014) Analytical study on the relationship between chip geometry and equivalent strain distribution on the free surface of chips in metal cutting. Int J Mech Sci 85: 88–103
45. Nomani J, Pramanik A, Hilditch T, Little fair G (2017) Stagnation zone during the turning of Duplex SAF 2205 stainless steels alloy. Mater Manuf Process 32(13):1486–1489
46. Klocke F, Sangermann H, Krämer A, Lung D (2011) Influence of a high-pressure lubricoolant supply on thermo-mechanical tool load and tool wear behavior in the turning of aerospace materials. Proc Inst Mech Eng B J Eng Manuf 225(1):52–61
47. Çolak O (2012) Investigation on machining performance of Inconel 718 under high pressure cooling conditions. Stroj Vestn-J Mech Eng 58(11):683–690
48. Kamruzzaman M, Dhar NR (2008) The effect of applying high- pressure coolant (HPC) jet in machining of 42crmo4 steel by un- coated carbide inserts. J Mech Eng 39(2):71–77
49. Ezugwu EO, Bonney J (2004) Effect of high-pressure coolant sup- ply when machining nickel-base, Inconel 718, alloy with coated carbide tools. J Mater Process Technol 153(1):1045–1050
50. Zhou L, Rong Y, Li Z, Yang JA (2003) Development of web-based machining chip breaking prediction systems. Int J Adv Manuf Technol 22(5):336–343

`

51. Zhang YZ, Peklenik J (1980) Chip curl, chip breaking and chip control of the difficult-to-cut materials. CIRP Ann Manuf Technol 29(1):79–83

`

Chapter 4: New observations on built-up edge structures for improving machining performance during the cutting of superduplex stainless steel

Yassmin Seid Ahmed [1, 2, *], Jose Mario Paiva [1], Bipasha Bose[1], and Stephen Clarence Veldhuis [1]

[1] McMaster Manufacturing Research Institute (MMRI), Department of Mechanical Engineering, McMaster University, 1280 Main Street West, Hamilton, ON L8S4L7, Canada; paivajj@mcmaster.ca (J.M.P.); boseb@mcmaster.ca (B.B); veldhu@mcmaster.ca (S.C.V.)

[2] Production Engineering Department, Alexandria University, Alexandria, 21544, Egypt

[*] **Correspondence**: seidahmy@mcmaster.ca; Tel.: +1-365-888-1186

This paper is published in Tribology International, Elsevier. Volume 137, 2019, pages 212–227. https://doi.org/10.1016/j.triboint.2019.04.039. This paper is republished here with permission.

`

Abstract

This work features a comprehensive investigation of built-up edge (BUE) formation during machining of superduplex stainless steel (SDSS), grade UNS S32750. To visually investigate BUE formation during the machining test, a detailed examination of BUE structures obtained at different cutting speeds was performed. The BUE geometries were determined by scanning electron microscope (SEM) and 3D white light interferometry. In addition, various BUE adhesion patterns were analyzed through electron backscatter diffraction (EBSD) and nano-indentation methods. The examined BUE revealed a high level of grain refinement and elongation for both ferrite and austenite structures, as well as a tool protection effect at specific cutting speeds. Finally, the influence of BUE on the machining process in terms of chip formation and surface integrity was studied in detail. Considerable improvements could be made to the frictional conditions and workpiece surface integrity at low cutting speeds.

Keywords

built-up edge, machining of SDSS, tool wear, surface integrity, friction condition

4.1 Introduction

A phenomenon known as a built-up edge (BUE) may happen in the cutting zone during machining of dual phase materials such as super duplex stainless steel (SDSS) [1]. The

`

BUE is an extremely deformed material which firmly sticks at the tool-chip interface throughout the cutting test [2]. Compressive stresses are so high during machining which make the bonds between the BUE and the tool are strong enough to block the material from sliding above the cutting tool [3, 4]. Trend and wrights [5] describes the BUE phenomenon: at the beginning of cut, the material strongly adheres to the tool through atomic bonds which increases yield strength. Therefore, the shear stresses are not large enough to overcome these bonds. As the strains continue to rise, another layer of workpiece material is formed. The repetition of this process generates a fully developed BUE. As BUE evolves, its yield point also gradually increases until the shear stresses are not high enough to break these bonds [6]. Whenever the shear stresses exceed the bond force of the BUE, the latter breaks off and becomes carried away by the chip or the workpiece [7, 8]. A new BUE then emerges, and the process is repeated. This phenomenon may also develop some microcracks which may contribute to cutting tool failure [2, 9].

The highly deformed material on the cutting tool may cause a variation in cutting edge geometry and affect process outputs, especially surface quality [9]. Oliaei et al. [10] concluded that larger BUE sizes lead to higher cutting force components and better workpiece quality. However, Sivaiah et al. [11], Wika et al. [12], and Medeoss et al. [13] reported that the growth of BUE causes a reduction in machined surface finish. The bad surface quality can be due to the instability of BUE during the machining process, and, when it breaks off, some particles of BUE stick on the machined surface, reduce the surface quality. Also, Ahmed et al. [9] observed that the development of BUE has a

`

significant effect on the machined workpiece residual stresses, where a noticeable increase in tensile residual stress was noticed with a rise in BUE height. Furthermore, continuous appearance and disappearance of BUE have a significant effect on tool wear behavior; sometimes decreasing the tool life and sometimes enhancing it [14]. Kumar et al. [15] noticed that the high temperature generation due to dry turning might cause higher and unstable BUE formation on the cutting tool, resulting in a decrease in tool life. While Niknam [16] and Kümmel et al. [17] observed that tool life improves when intended BUE develops on the cutting edges during machining. BUE influences friction behavior at the tool–chip zone where it behaves as a new edge, preventing the chip from directly contacting the cutting tool, which increases cutting edge life [18]. In our earlier investigation [9], the positive impact of BUE on tool wear was investigated during the cutting of AISI 304 material. It was found that sometimes the BUE is capable of minimizing friction at the tool-chip interface, reducing the cutting tool wear. However, upon reaching a particular size, the BUE tears off completely, damaging the tool surface.

It is well known from the literature that various significant factors affect BUE formation, such as machining temperature, cutting speeds, work hardening, etc. [19]. The relation between these parameters is independent and predicting their influence on BUE evolution is exceedingly tricky. Medina-Clavijoa [20] reported that strain hardening of the workpiece material could promote the growth of a BUE; however, it's not necessary to expect every material with high strain hardening to form BUE because BUE does not exist under all cutting conditions [4,6]. Bilgin [21] studied BUE behavior at different cutting conditions, and the author found that cutting speed has a more significant effect

`

on BUE size than feed rate and depth of cut. In an earlier study, Trent [22] reported the change in BUE formation at different cutting conditions for a particular workpiece material. Charts were drawn in this investigation, from which conditions for BUE emergence could be predicted. Although this type of data is beneficial for industry, there are still many parameters that can affect the formation of BUE, making prediction difficult.

Most recent machining studies related to BUE [14, 21, 23] concentrated only on the study of BUE formation at different machining conditions. However, few research studies [14, 24] were conducted to examine the structure of the BUE itself during the machining process. In the current work, an in-depth study of BUE structure was performed to understand the mechanism of BUE and microcrack formation. The protective effect of BUE is anticipated in this study, therefore the tool wear will be inspected at different cutting lengths throughout the machining process. According to the discussed litrature, this research addresses the following aspects:

(i) Examination of BUE structures at different cutting speeds and study of the potential protective effect of BUE,

(ii) Understanding the mechanisms of BUE through an in-depth investigation of microcrack formation and EBSD analysis,

(iii) Ascertaining the effect of cutting speeds and BUE formation upon machining performance and machined surface quality.

4.2 Experimental work

4.2.1 Workpiece material and cutting conditions

In this study, turning experiments were implemented on SDSS—type UNS S32750. cylindrical pipes. The chemical composition and the mechanical properties of the workpiece are presented in Table 4-1.

Table 4-1 Chemical composition and mechanical properties of S32750 [36]

Chemical Composition %								
C	**Si**	**Mn**	**P**	**S**	**Cr**	**Ni**	**Mo**	**N**
0.03	0.80	1.2	0.035	0.02	25	7	4	0.24
Proof Strength (0.2% yield) MPa			**Tensile Strength MPa**			**Elongation %**	**Hardness HRC**	
550			800–1000			15	32	

SDSS samples were cut, cold mounted and polished. A Beraha etching solution (50 mL H_2O + 20 mL hydrochloric acid + 0.4 g of potassium metabisulfite) was used to reveal the microstructure. The microstructure of the SDSS sample was captured using a Nikon ECLIPSE LV 100 microscope. Figure 4-1 presents the phase distribution of each phase of the workpiece material, where ferrite content is 36% and austenite 64%.

`

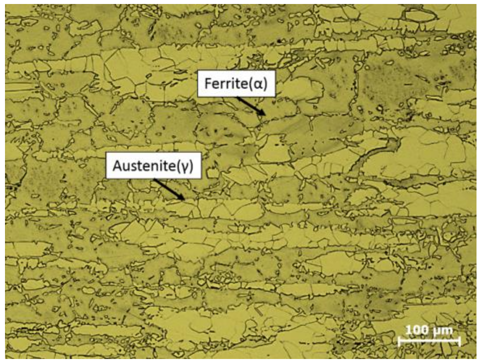

Figure 4-1 Microstructure of the SDSS UNS S32750 at 100× showing the distribution of each phase

The cutting experiments were performed on a CNC lathe machine (OKUMA Crown L1060), under wet conditions, using a semi-synthetic cutting coolant CommCool™ 8800. As suggested by [6], a coolant flow rate of 12 L min^{-1} with a concentration of 6% was selected in the cutting tests. Uncoated carbide tools manufactured by Sandvik (CNMG432-SM) were chosed to perform the cutting experiments. The tool geometry data and cutting parameters used in cutting trials are summarized in Table 4-2.

Table 4-2 Tool geometry and cutting parameters used in cutting experiments

Tool geometry	
Rake angle (°)	9
Clearance angle (°)	5
Wedge angle (°)	76
Nose radius (mm)	0.8
Edge radius (µm)	24
Cutting parameters	
Cutting speeds (m/min)	60, 110, 150
Feed rate (mm/rev)	0.3 mm/rev
Depth of cut (mm)	0.5 mm

`

4.2.2 Cutting tests and characterization methods

Average flank wear (VB_B) was measured during the machining tests using an optical microscope with each experiment conducted thrice. The cutting tests were stopped at VB_B of 0.3 mm, as recommended by the ISO 3685 Standard [25]. Comprehensive characterization of the cutting tool was performed at different cutting lengths and flank wear values using a scanning electron microscope (SEM), model- Vega 3-TESCAN. Also, the height of BUE and its area were measured during the cutting process using a white light interferometry microscope (Alicona Infinite Focus). This investigation was conducted with a 50X magnification and the measurements were performed three times for each cutting tool.

For a more detailed investigation of the mechanism of BUE formation, a wire EDM was used to separate the BUE samples into sections. The reason for choosing wire EDM technique is the ability to cut hard materials like stainless steels very smoothly without any burrs on the surface [26]. The region from which the samples were prepared is shown in Figure 4-2. BUE samples were polished using MD-Mol pads down to 0.025 μm and no etching solution was applied for the Electron Backscatter Diffraction (EBSD) analysis. EBSD analysis was carried out on a JEOL 6610LV scanning electron microscope with the sample being placed at a 70 degrees tilt. The phase and orientation mapping was performed by Tango-Maps software and processed with Chanel 5HKL. Also, nano-indentation tests were conducted in a Micro Materials NanoTest indentation testing platform to measure the hardness differences in the BUE samples obtained at various cutting speeds. All the measurements were done at room temperature using a diamond

`

Berkovich indenter, with the indentation load of 100 mN being applied at a constant rate throughout the test.

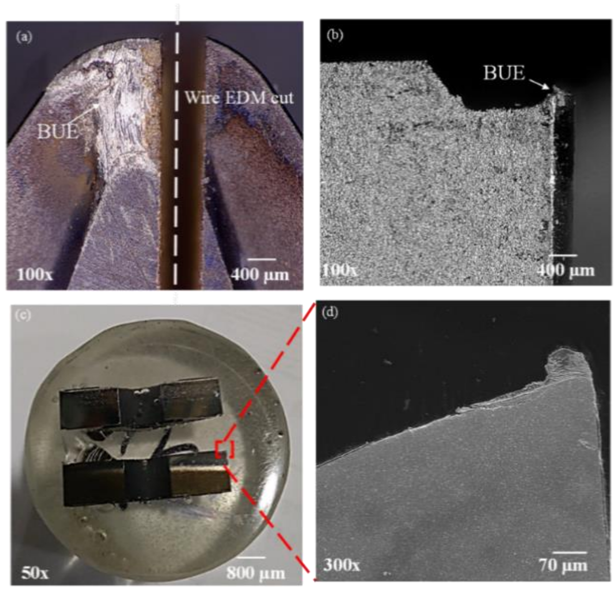

Figure 4-2 (a) and (b) cutting tool cross section, c) the mounted tool showing the position of built-up edge, and (d) backscattered image of the cutting tool cross section

To understand the impact of BUE size on machining outputs, a tool holder dynamometer (Kistler–-type 9121) was used to measure cutting forces during the machining process. Next, chip thicknesses obtained at different cutting speeds were measured at least three times with the average value being taken. Then, according to M.Shaw [27], both the chip thickness ratio and the shear angle were calculated. The chip undersurface was also analyzed using SEM to examine the friction condition in the cutting zone at varied machining parameters. Average surface roughness (Ra) of the chip undersurface and the machined workpiece were studied using an Alicona microscope with a profile roughness module [28]. Finally, the microhardness of the workpiece was determined after the

`

machining test. The measurements were performed using a microhardness tester with an applied load of 0.05 kgf for 20 s.

4.3 Results and discussions

4.3.1 Investigation of BUE formation

4.3.1.1 Variations in BUE dimensions

In the first section of the results, BUE produced on the new cutting tools (after a short pass) at different cutting speeds is investigated. Figure 4-3 presents the flank and rake faces of the cutting tools obtained at 60, 100, and 150 m/min, respectively. As shown, the most significant BUE height and area can be seen at 60 m/min on the flank and rake faces (Figure 4-3(a)). However, the height and area of BUE diminish (Figure 4-3(b, c)), as cutting speed is increased (100 and 150 m/min). It is also evident from the rake face images that only adhesion is present at all investigated cutting speeds; here the BUE has a different distribution on the cutting tools. Most BUE material generates quite close to the tool edge (Figure 4-3(c)) at high cutting speeds, whereas BUE (Figure 4-3(a, b)) covers a large area at lower cutting speeds.

`

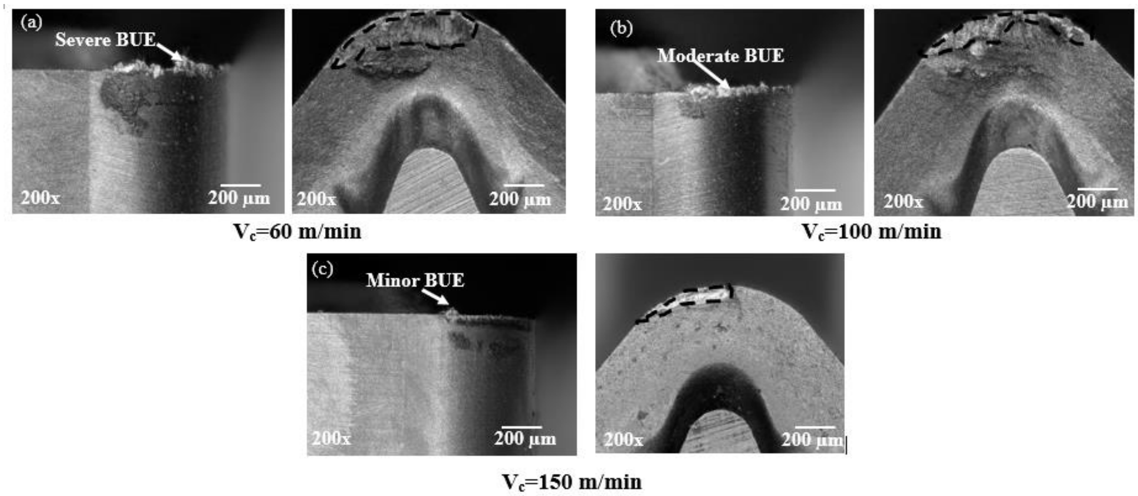

Figure 4-3 Flank face and rake face of the cutting tools for the cutting speeds of (a) 60 m/min, (b) 100 m/min, and (c) 150 m/min

Figure 4-4 (a) reports the BUE height and area measurements for various cutting speeds and Figure 4-4 (b, c) shows examples of BUE height and area measurements. It can be clearly seen in Figure 4-4 that BUE height and area diminished as cutting speed increased (BUE height reduced from 70 µm to 35 µm for v_c=60 m/min and v_c=150 m/min, respectively whereas the BUE area decreased from 325000 µm² to 215000 µm² for v_c=60 m/min and v_c=150 m/min, respectively). These results entirely agree with those obtained by Bilgin [21] for AISI 310 austenitic stainless steel at v_c= (50–150) m/min. The author also found no presence of BUE at higher speeds. This can be attributed to the reduction of the time it takes for temperature to be dissipated, causing a significant increase in the cutting temperature [29, 30].

`

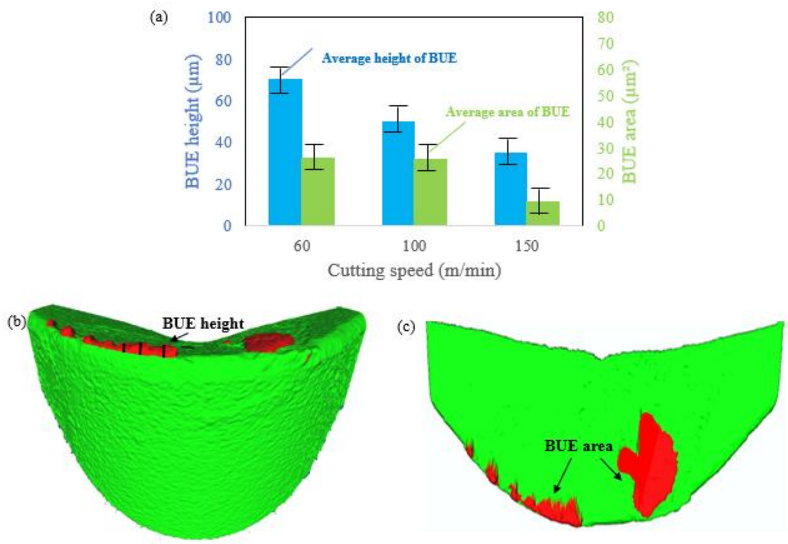

Figure 4-4 (a) height and area measurements of the BUE at different cutting conditions, (b) and (c) Alicona images, showing the measurements of BUE height and area, respectively

4.3.1.2 Positive influence of BUE

Different wear experiments were performed to understand the potential protective impact of BUE on the edge life. The cutting process was paused every 200 m and the cutting tool was observed with optical microscopes and SEM. Figure 4-5a presents the flank wear variation with cutting speed and length. Figure 4-5(b-d) shows SEM images of the cutting edges obtained at various cutting speeds (60-150 m/min) and after cutting 2000 m. The results shown in Figure 4-5 clarify that as cutting speed increases, flank wear on the cutting tools correspondingly increases as well. Low flank wear is present (Figure 4-5(b)) at a 60 m/min cutting speed, compared with high flank wear at 150 m/min (Figure 4-5(d)). Also, it is evident that chipping and crater wear are the main wear types present at a high cutting speed (150 m/min). No evidence of crater wear or chipping can be seen at lower cutting speeds (60 and 100 m/min), which indicates that BUE could benefit tool life by preventing the tool from chipping and catastrophic failure. In general, the high cutting pressure and force during machining tends to cause cracks and chipping on the tools [31, 32]. As shown, the BUE formed at lower cutting speeds (Figure 4-5(b, c)) covers a larger area of the rake face compared to the higher cutting speed (Figure 4-5(d)). This gives the BUE a greater chance to protect the cutting tool from wear, since the new chip forms above the cutting edge that is altered by the adhering BUE (Figure 4-5(b, c)). Thus, the cutting tool featured lower wear at a lower cutting speed compared to the higher cutting speeds.

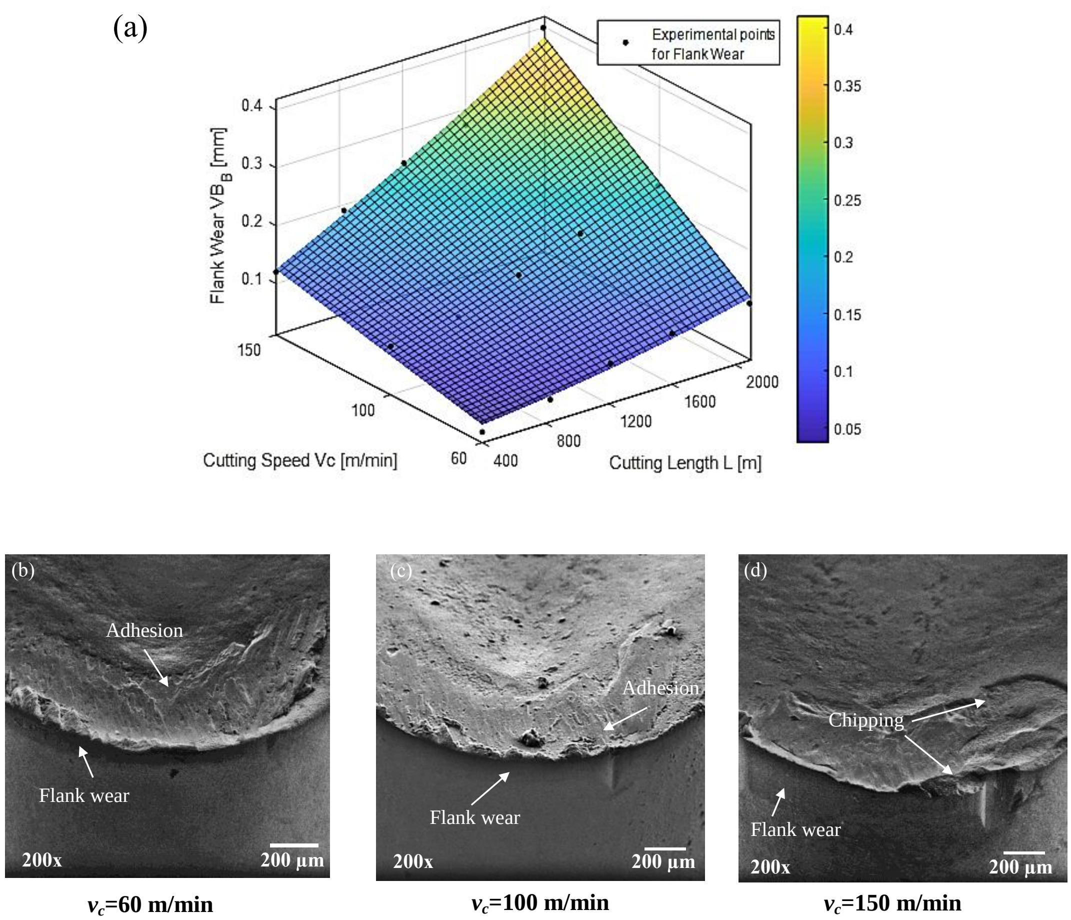

Figure 4-5(a) relation between flank wear, cutting speed, and cutting length, (b-d) SEM images of the cutting tools after cutting length of 2000 m at different cutting speeds

To validate this explanation, real-time monitoring of BUE formation was performed using a high speed camera (HSC) during the cutting process. It is worth mentioning that the experimental setup of HSC is shown in Figure 4-6(a).

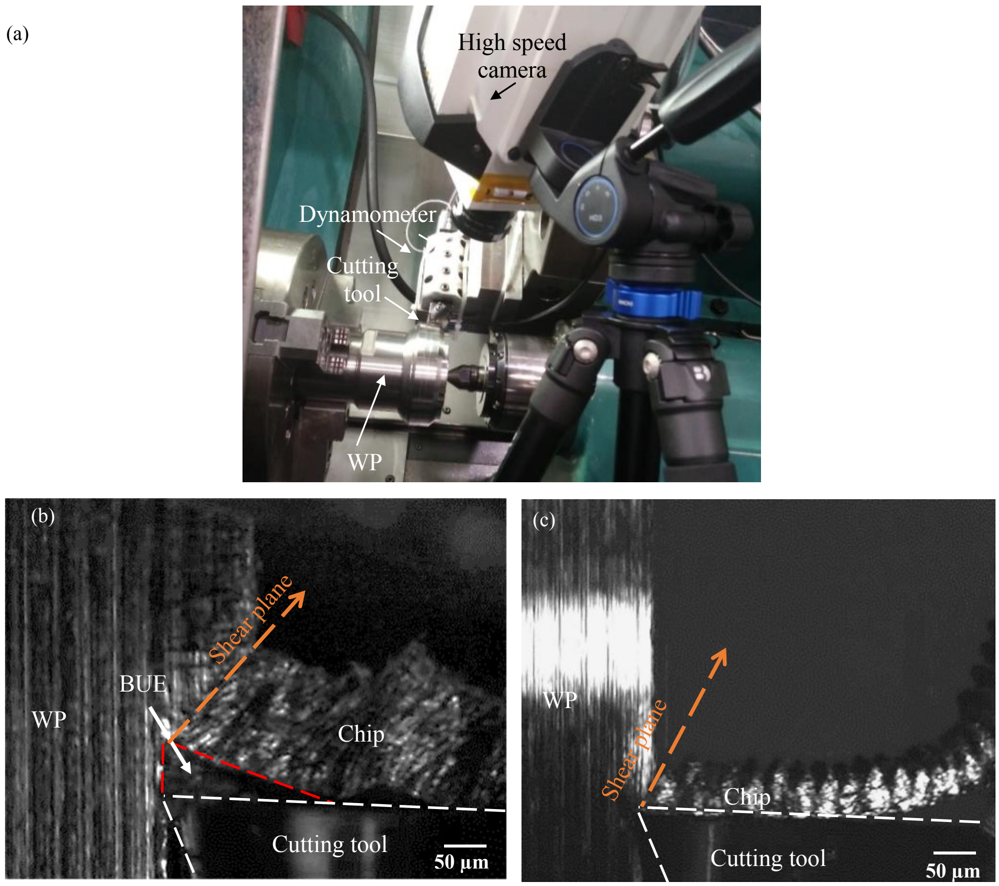

Figure 4-6(a) setup of high speed camera, (b) and (c) micrographs of built-up edge obtained at 60 m/min and 150 m/min, respectively

The HSC captured the cutting temperature at a frame rate of 20000 fps and 8ms time. Figures 4-6(b, c) illustrate representative examples of the BUE image captured at the lowest and highest cutting speeds (60 m/min and 150 m/min), respectively. As can be seen at a lower cutting speed, the BUE situated between the cutting tool and the chip, protects the cutting tool from direct contact with the chip. However, no BUE can be

`

noticed at 150 m/min, causing intense friction during the chip formation process and consequent increase in flank wear. Identical conclusions were drawn by Kümmel et al. [17], Ikuta et al. [33] and Armendia et al. [34]. They noticed that tool wear increased quickly at high cutting speeds as a result of the removal of the protective layer.

In addition, the reduced cutting tool edge may also reduce the stability of the BUE throughout the machining test and increase the possibility of the protective layer becoming removed at higher speeds. This phenomenon can be clearly observed in Figure 4-7(a), where the geometry of the cutting tools was analyzed using the 3D Alicona microscope. In Figure 4-7(a), the profiles of the cutting tool edge after cutting 1000 m with different cutting speeds are investigated to understand the influence of tool wear on the cutting edge. As flank wear increases (due to increase in cutting speed), cutting edge radius is reduced from 37.36 μm at v_c=60 m/min (VB_B=0.06 mm) to 35.22 μm, to 34.13 μm at 100 m/min (VB_B=0.13 mm) and to 150 m/min (VB_B=0.21 mm), respectively. In this case, cutting edge radius decreases with the growth in cutting tool wear, contributing to BUE instability. To further emphasize the protective effect of BUE, the cutting tool obtained at 60 m/min (Figure 4-7(a)), was etched with HCL for more than six hours to remove the adhesion layer. Figure 4-7(b) shows the flank and rake faces after etching. Low flank wear and no sign of crater wear was observed, which emphasizes the protective impact of BUE. Also, Figure 4-7(c) illustrates the profile of the cutting edge after the BUE was removed, where a reduction in cutting edge radius can be seen (edge radius of 37.36 μm before etching and 37.006 μm after etching:). This phenomenon confirms that BUE may increase the edge radius of the cutting tool, also increasing the

`

cutting forces during the machining process (which will be discussed further in section 3.3). The results presented in this section are in agreement with those of Gómez-Parra et al. [35] and Kummel et al. [17].

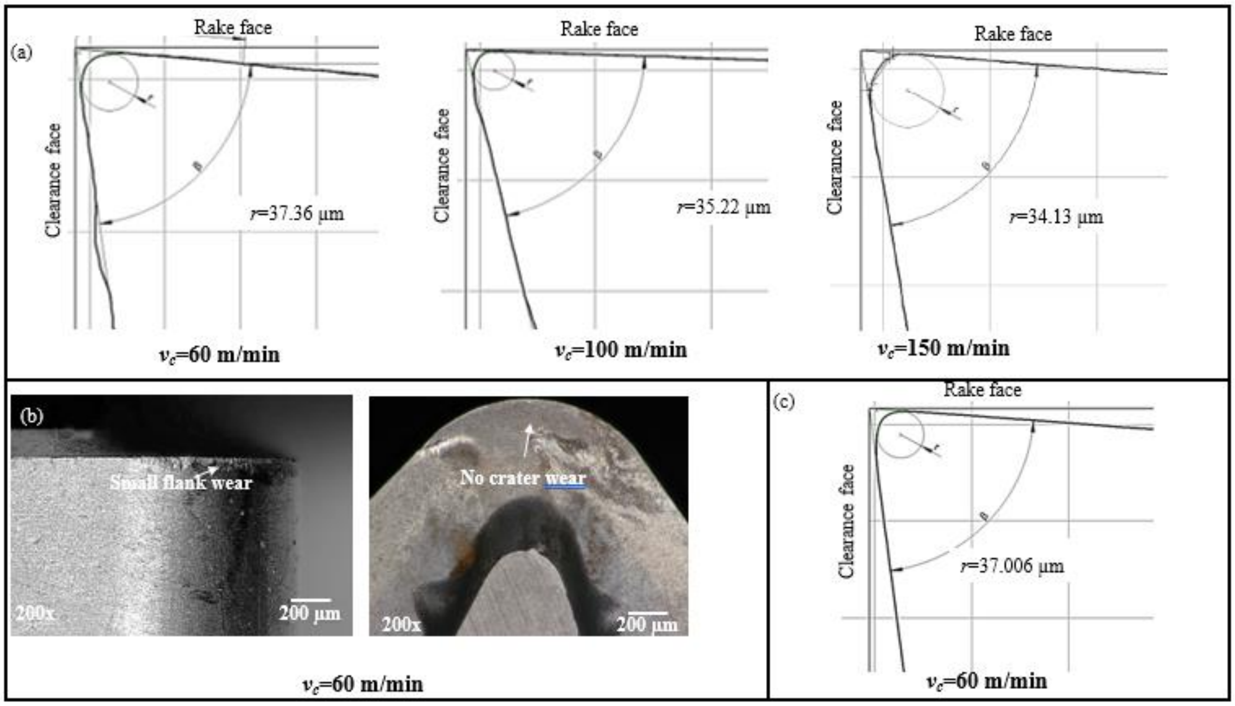

Figure 4-7(a) profiles of cutting tool edge after cutting length of 1000 m at different cutting speeds, (b) flank and rake faces of the cutting tool after removing the adhesion layer, and (c) corresponding cutting edge profile after removing the a adhesion layer

4.3.2 In-detail evaluation of BUE structures

4.3.2.1 BUE morphology and microcrack formation

Study of BUE morphology requires its structure to be examined in detail. Figure 4-8 shows the structure of a BUE obtained with 60 m/min and 150 m/min, respectively. The BUE was found to consist of shear lamellae in both cases (Figure 4-8 (a, b)). Accumulation of the shear lamellae was caused by slipping mechanisms, shearing, and fracturing behavior throughout the cutting process. However, the adhesive wear caused by BUE formation may lead to flank wear and chipping as the machining process progresses, since the BUE particles are unstable and can easily break off during the cutting experiments [31, 36]. Also, by comparing the lamellae structure at low and high speeds (Figure 4-8 (a, b)), the structure obtained at the higher speed is rougher than the structure obtained at the lower speed which is due to the elevated cutting temperatures present in the machining process, according to Refs. [17, 37].

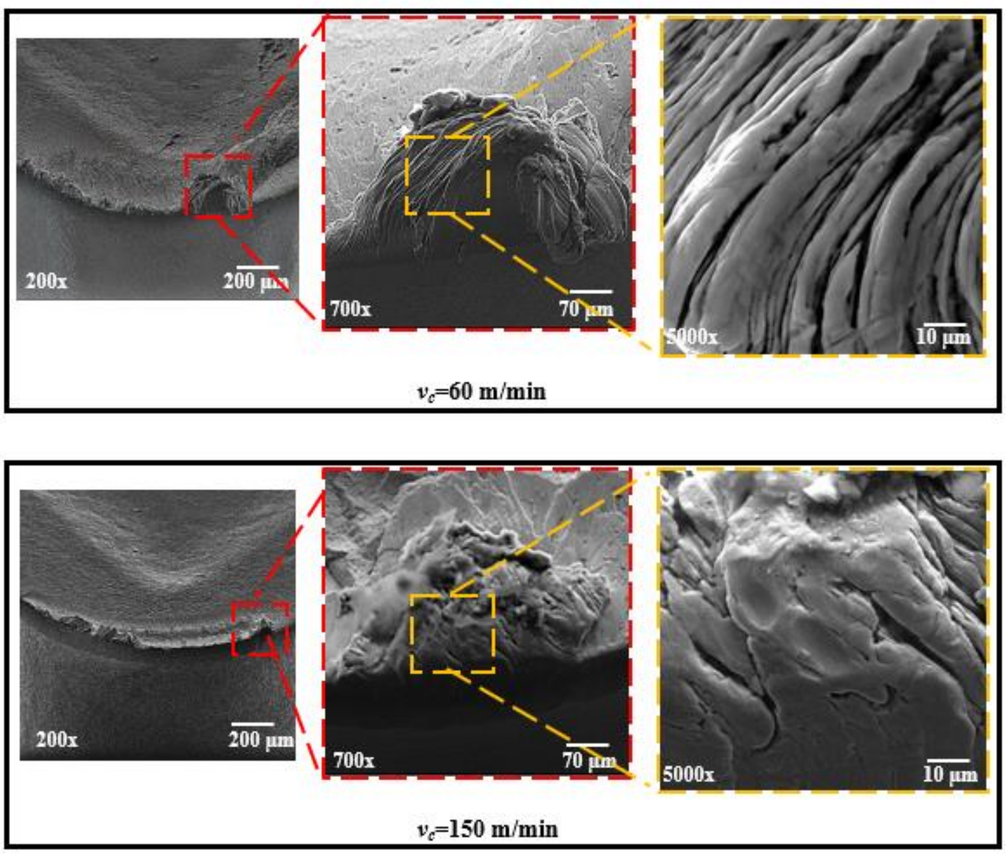

Figure 4-8 Morphology of the BUE samples obtained at different cutting speeds

`

In general, a high cutting temperature between 500°C-800°C can be present in the cutting zone [32.38]. In this investigation, the cutting temperatures are 520°C at 60 m/min and 700°C at 150 m/min, which are high enough to generate BUE on the cutting tool. The images of the cutting temperature profile during cutting at 60 m/min and 150 m/min are captured with an infrared camera and presented in Figures 4-9(a) and 4-9(b), respectively.

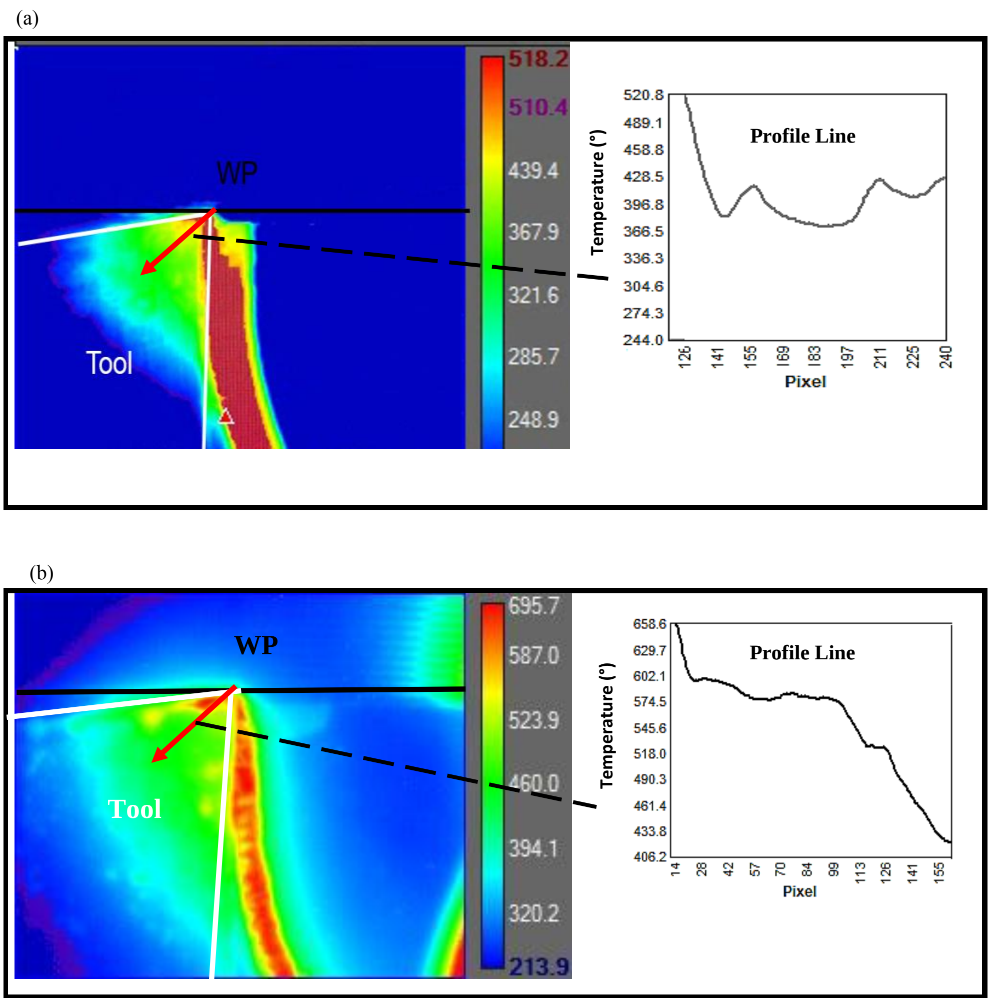

Figure 4-9 Temperature distribution on the tool and chip during machining SDSS at (a) 60 m/min and (b) 150 m/min

`

The BUE cross sections obtained at various cutting speeds were also studied in detail using the backscatter detector (Figure 4-10). In Figure 4-10(a-e), two types of crack formation can be observed at 60 m/min. One type is formed inside the BUE and develops in the direction of the shear deformation zone (Figure 4-10(b)) whereas the other emerges on the rake face of the cutting edge (Figure 4-10(c)). The second crack occurs due to strong adhesion in the cutting zone, restricting the material flow. As a result, a high amount of shearing occurs between the tool and BUE, producing a crack away from the cutting edge at a distance of around 15 µm (Figure 4-10(c)). Another possible cause of these cracks are high compressive stresses along the cutting edge, which decrease with distance from it [17]. Furthermore, Figure 4-10(d) shows the microscopic cutting tool particles adhered on the edge of the formed BUE. EDS analysis of these tool particles was confirmed in Figure 4-10(e), where tungsten could be clearly observed in the EDS map. These small particles separated from the substrate and adhered to the formed BUE. When the chip flows against the cutting tool, the adhered particles cause cratering on the tool through abrasion [9].

Moreover, Figure 4-10(f-i) shows the BUE cross section obtained at 150 m/min. As shown, compared with the BUE cross section obtained at 60 m/min, only one type of cracks is observed inside the BUE (Figure 4-10(h, i)). There is no sign of microcracks on the rake face of the tool (Figure 4-10(g)), which means that the adhesion at the tool-chip interface is not strong enough to produce cracks during machining [39]. Moreover, the normal stress along the rake face is not as high as that generated at a low cutting speed. Thus, no big difference in normal stresses can be observed at a distance from the cutting edge during machining with high cutting speed. This behavior was also reported to Ref.

`

[27]. To prove this explanation, cutting forces were measured at both 60 m/min and 150 m/min at the same cutting conditions listed in Figure 4-10. It is found that the forces at 60 m/min (100 N) are twice greater than those obtained at 150 m/min (50 N), which indicates that normal forces captured at higher speeds are lower than those obtained at low speeds.

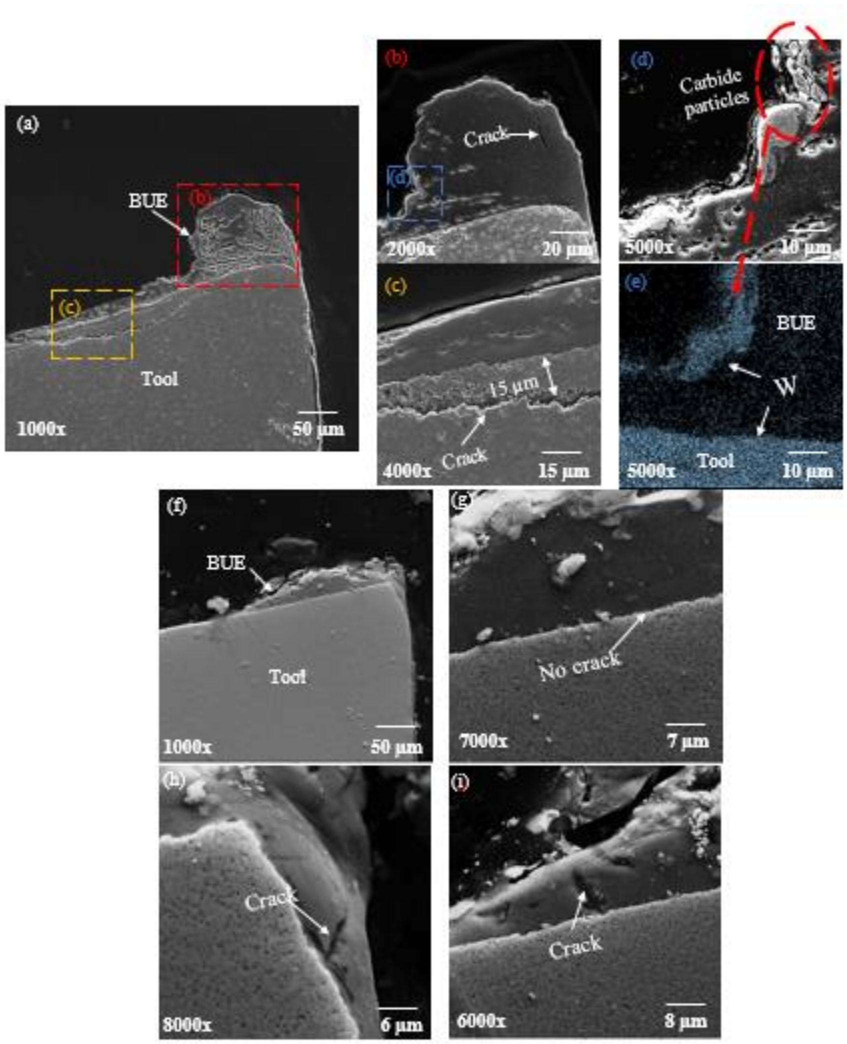

Figure 4-10 Backscattered images of the BUE cross section obtained at (a-e) 60 m/min and (f-i) 150 m/min, showing cracks formation

In addition to that, nanoindentation tests were carried out to examine the nanohardness of the BUE cross sections. Figure 4-11(a, c) illustrates the locations of the individual indents

`

and the resulting nanohardness maps for the BUE formed at 60 m/min and 150 m/min, are demonstrated in Figure 4-11(b, d), respectively. As shown, the range of obtained nanohardness is between 2–8 GPa which is twice higher than the received material (microhardness of ferrite 4.28 ± 0.26 GPa, microhardness of austenite: 4.75 ± 0.25 GPa). These conclusions agree with the results obtained in Ref. [17]. Here, hardness measurements of the BUE samples consist of 64 values, whereas hardness values of austenite and ferrite phases are taken from 80–100 measurements on the received material.

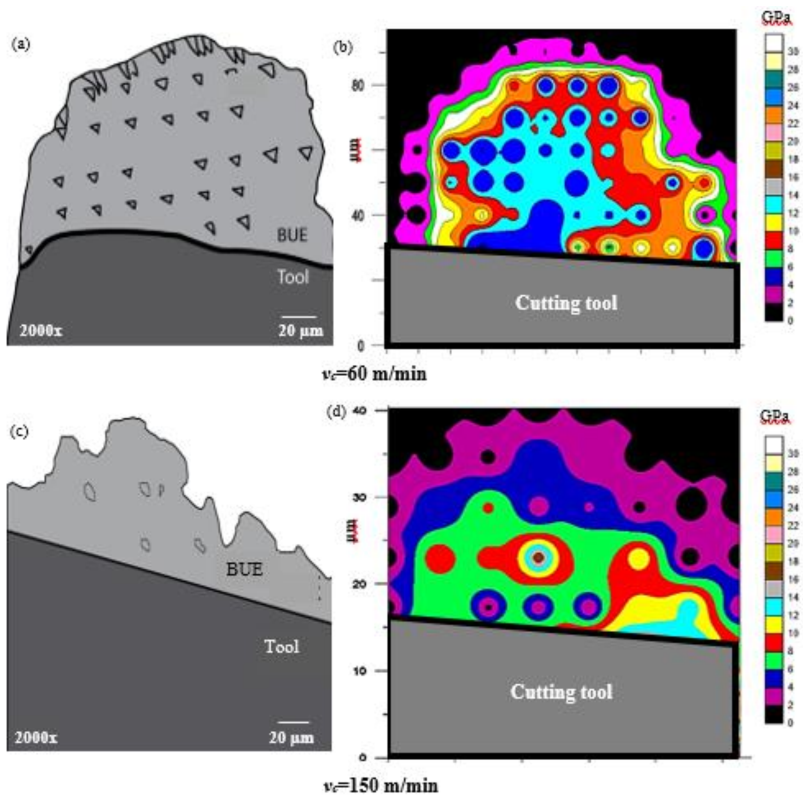

Figure 4-11Nanohardness results of measurements done on the built-up edge cross sections after machining with different cutting speeds. (a, c) BUE sketch, showing the locations of the individual indents, and (b, d) nanohardness distribution maps

4.3.2.2 Phase characterization

To explore the main reasons for BUE structural differences at low and high cutting speeds, the BUE cross-section specimens shown in Figure 4-10 were prepared for EBSD analysis. The scans were captured with a step size of 100 nm and included an area of 50 × 50 μm. The resulting EBSD phase mapping images of the regions taken from the BUE cross sections are shown in Figure 4-12(a, b) where both ferrite (red) and austenite (blue) phases can be seen for both cutting speeds.

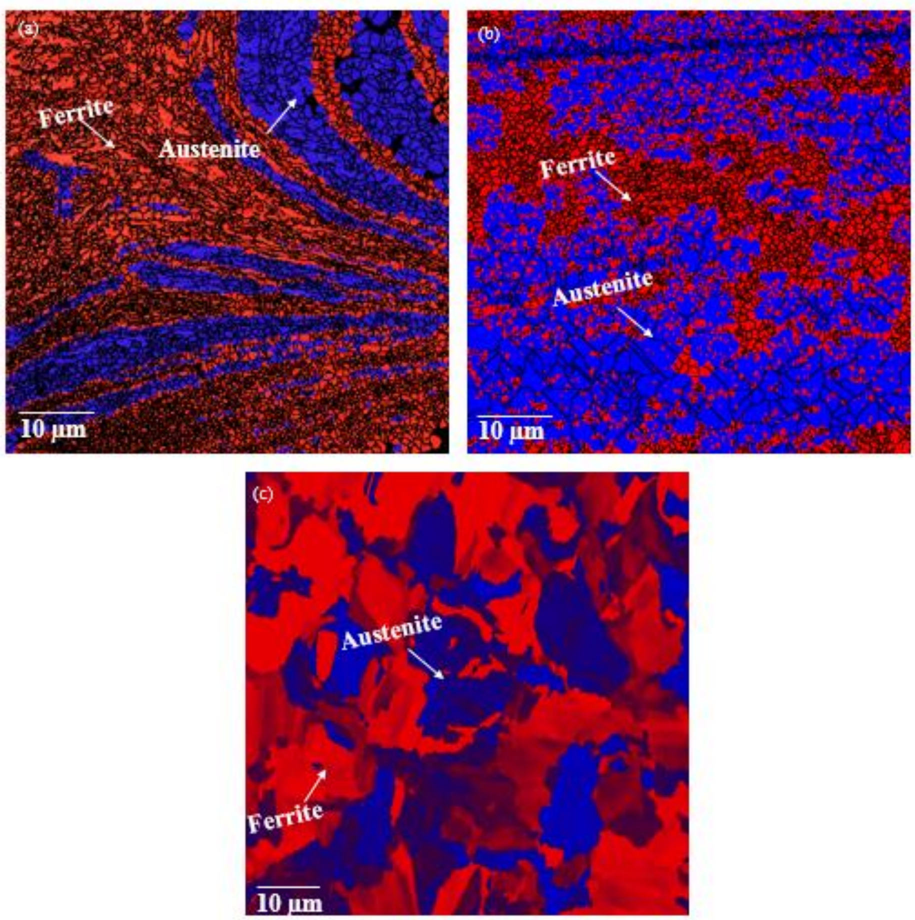

Figure 4-12 Phase maps of (a) built-up edge obtained at 60 m/min, (b) built-up edge obtained at 150 m/min, and (c) original material before the machining test

`

The average grain size of the BUE samples shown in Figure 4-12(a, b), generated by Channel 5 HKL software grain size Statistics-Tango-maps software, is presented in Table 4-3. Here, ASTM standard E112 was used to determine the average grain sizes [40]. Accordingly, the strain values for each phase of the BUE samples at different cutting speeds were measured by comparing the BUE sample grain size to the grain size of the original material (Figure 4-12(c)). In Figure 4-12 and Table 4-3, it can be generally observed that the BUE sample grains are remarkably refined compared to the raw material used in the present paper. In addition, ferrite possessed higher strain levels at both cutting speeds compared to austenite which may be because the ferrite phase is considerably softer [24].

Table 4-3 Average grain size values of BUE samples obtained at different cutting speeds in comparison with the original material

Phase	**Original**	**BUE obtained at 60 m/min**		**Average strain**	**BUE obtained at 150 m/min**		**Average strain**
	Average grain size (µm²)	**Phase count**	**Average grain size (µm²)**		**Phase count**	**Average grain size (µm²)**	
Ferrite	10.365	25320/68784	0.076	4.915	53191/68784	0.0945	4.697
Austenite	6.243	9836/68784	4.025	0.438	15623/67874	0.0774	4.390

`

By comparing the strain values at various cutting speeds, it can be noted that austenite maintains an almost constantly high strain at an increasing speed, whereas the ferrite strain grows along with cutting speed, reducing the strain difference between these two phases. As reported, the austenite strain value was found to be very close to the value of the ferrite strain at higher cutting speeds (v_c =150 m/min). Therefore, low plastic strain recovery at high speeds corresponds to the low BUE formation [14, 24, 41]. These conclusions are consistent with the results obtained in section 3.1.

Microstructure and texture evolutions of BUE samples were examined by EBSD which detects both the orientations and structure of the grains. Figure 4-13 presents the orientation maps as well as the pole figures maps of the BUE obtained at various cutting conditions. In general, the overall grains were significantly refined (Figure 4-13 (a, b)) when compared to the initial workpiece (Figure 4-12(c)), especially for the BUE sample collected at high cutting speed (Figure 4-13(b)). As the cutting speed decreased to 60 m/min, the grains became remarkably coarser, as shown in Figure 13a. These conclusions agree with data obtained in Table 4-3. Meanwhile, the majority of grains within the ferrite phase in the BUE obtained at 60 m/min, exhibit a Cube {1 1 1} (001) texture (Figure 4-13(c)), while the grains within the austenite phase mainly show a Goss {1 1 0} (001) texture (Figure 4-13(d)). Most of the grains obtained at 150 m/min (ferrite and austenite) possess an orientation close to the Cube {1 0 0} (001) texture as shown in Figure 4-13(e, f). Yang et al. [42] showed that the plasticity of the Cube texture is higher than that of the Goss texture. The authors observed that the cube texture is more liable to deformation compared to other textures, since it contains more slip systems and as such, better

`

plasticity. Accordingly, there is low plastic strain recovery at high cutting speeds because both ferrite and austenite phases feature cube textures compared to two different textures (Cube texture for ferrite phase and Goss texture for austenite one) obtained at a low cutting speed. This conclusion agrees with the calculated strain values (Table 4-3).

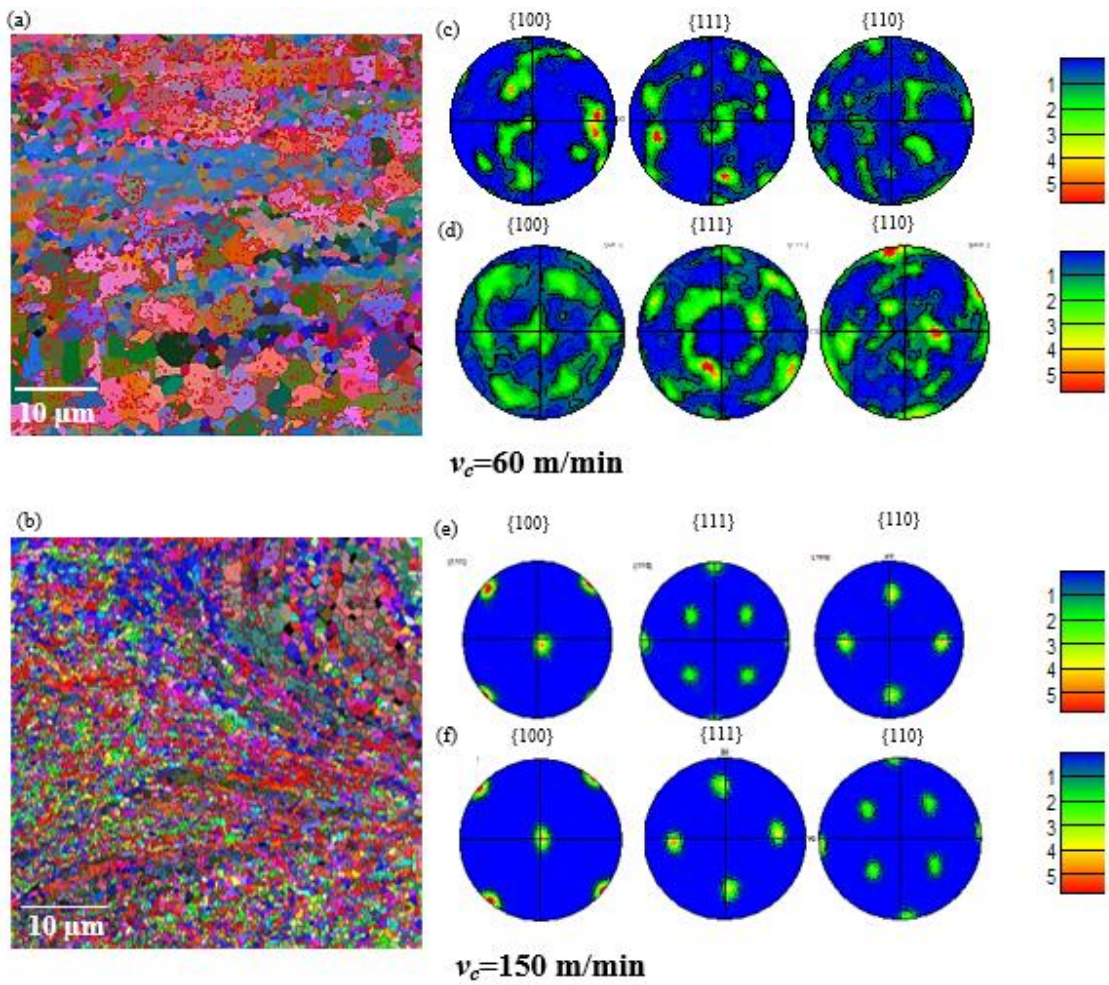

Figure 4-13 Microstructure of built-up cross sections obtained at different cutting speeds (a) and (b) orientation maps of BUE obtained at 60 m/min and 150 m/min, respectively, (c) and (e) are representative pole figures for ferrite phase and (d) and (f) are representative pole figures for austenite phase

`

4.3.3 Inspection of machining outputs for existence of BUE

In the previous sections, an in-depth consideration of the BUE mechanism was studied alongside the possible protective effect of BUE. However, further study is needed to examine the impact of BUE formation on process outputs such as cutting force components, chip characteristics, and surface integrity.

4.3.3.1 Cutting force measurements

Figure 4-14(a) shows force component measurements at different cutting speeds during SDSS machining until tool failure (VB_B=0.3 mm). At the beginning of the cutting process, the cutting force components sharply increased due to the rapid increase in flank wear [43], demonstrating a change in the friction conditions between the cutting edge and BUE. Furthermore, the rise in cutting forces values along with cutting length is attributed to an increase in flank wear. According to Ref. [22], when a cutting tool is subjected to a wear experiment, the flank wear will change with cutting length. The rate of flank wear is high at the beginning of the process, causing a sharp increase in the cutting forces components. After that, the wear is quite stable in the stable state region, resulting in very predictable cutting force components.

Also, it should be noted that the thrust force (Ft) is also influenced by the formation of BUE. The presence of a BUE can cause an increase in edge radius, as shown previously in Fig. 4-7 and a consequent increase of the contact area. Thus, higher thrust forces are acquired at a 60 m/min cutting speed compared to higher cutting speeds (Fig. 4-14a) [44].

`

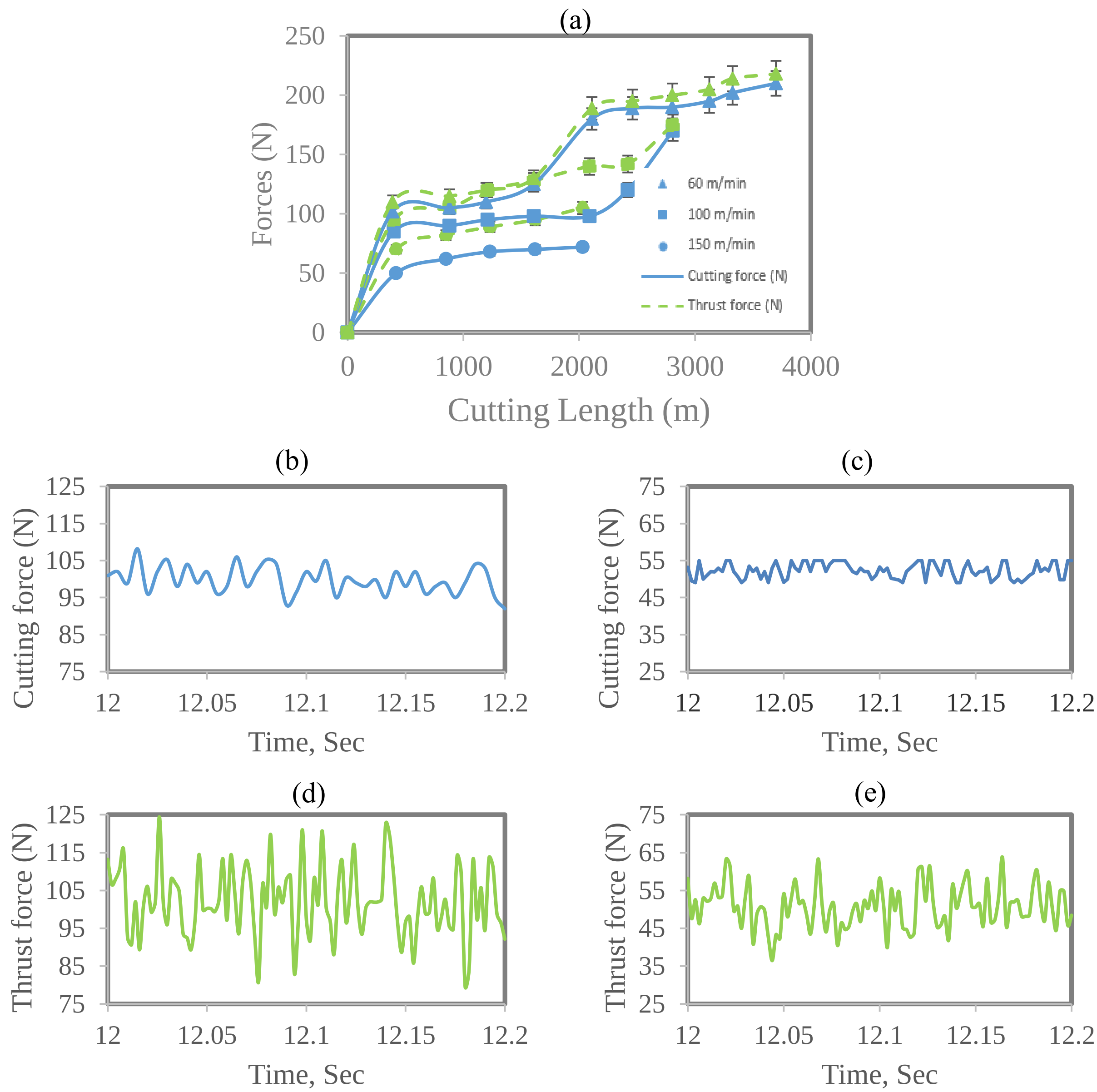

Figure 4-14 (a) Relation between cutting force components and contact length for different cutting speeds, (b) and (c) cutting forces variations collected at 60 m/min and 150 m/min, respectively, and (d) and (e) thrust force variations collected at 60 m/min and150 m/min, respectively

Additionally, it is worth stating that BUE formation agrees with the extensive cutting and thrust force values. Fig. 4-14(b-e) shows the variations of cutting force components

`

collected after cutting 400 m. As shown, significant changes of the cutting and thrust force values are observed at vc=60 m/min (Fig. 4-14b, d), which demonstrates that intensive friction conditions were obtained as a result of high BUE formation (low cutting speed). This phenomenon is less prominent at a higher cutting speed (low BUE), see Fig. 4-14c, e: The variations of cutting force components are smaller.

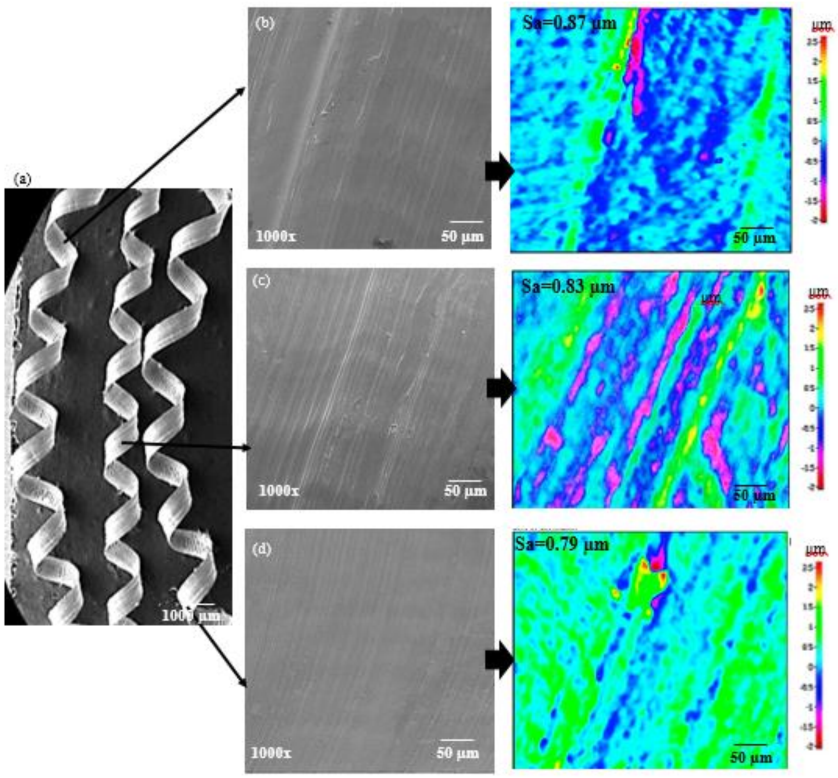

Figure 4-15(a) General macrograph aspect of the chips, and chip undersurface obtained at (b) 60 m/min, (c) 100 m/min, and (d) 150 m/min

4.3.3.2 Chip characteristics

Figure 4-15 presents the chip types and morphologies produced at various cutting speeds. Although the chips have similar curling at different cutting speeds (Figure 4-15(a)), the chip undersurface is rougher at low cutting speeds (Figure 4-15(b)) compared to the other speeds (Figure 4-15 (c, d)). The intensive friction conditions in the cutting zone obtained

`

at 60 m/min (Figure 4-15(b)) can be due to the considerable tool-chip contact area causing unstable BUE formation. The BUE formed at higher cutting speeds is lower and more stable because of the less severe friction conditions in the tool-chip interface (Figure 4-15(c, d)).

Commonly, chip characteristics also help understand frictional conditions at the tool-chip interface [70]. Figure 4-16 shows the measurements of maximum and minimum chip thickness, as well as the shear angle at different cutting speeds, and their values are reported in Table 4-4. Analysis of chip characteristics presents more favorable conclusions at a lower BUE - chip thickness and shear angle are better at 150 m/min (low BUE) than 60 m/min (high BUE). These measurements confirm that BUE size can significantly affect the friction behavior in the cutting zone.

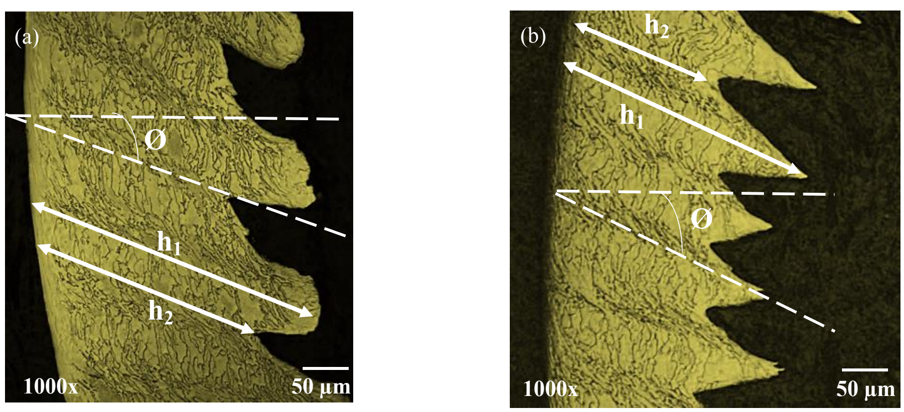

Figure 4-16 Chip microstructure obtained at (a) 60 m/min and (b) 150 m/min

`

Table 4-4 Chip characteristics obtained at different cutting speeds

Cutting speed (m/min)	Maximum chip thickness (mm)	Minimum chip thickness (mm)	Chip thickness ratio	Shear angle (°)
60	0.225	0.178	0.75	35.75
100	0.212	0.168	0.71	37.01
150	0.205	0.150	0.68	43.06

4.3.3.3 Machined material characteristics

SDSS is known by its high strain hardening effect during the machining process, which in turn may negatively affect the machining performance of stainless steels, causing severe chipping and tool failure. In this research, two sets of microhardness tests were used to inspect the influence of both cutting speed and BUE formation on induced work hardening of the workpiece. First, concise cutting tests (where no significant tool wear was observed) were implemented to investigate only the impact of various cutting speeds on the surface work hardening. In Figure 4-17(a), microhardness measurements of the workpiece after the machining test are shown. In general, it can be concluded that microhardness values increase alongside the cutting speed. This is because an increase in the cutting temperature (Figure 4-9) during the machining process causes a significant rise in the machined surface temperature. These changes in temperature contribute to a surge in plastic formation, resulting in a higher microhardness value.

To estimate the impact of BUE on the induced microhardness of the workpiece sublayer, it was necessary to keep all the cutting conditions constant. For this reason, the microhardness profile was measured at cutting speed (60 m/min) and a constant tool wear (around 0.13 mm) and in two different cases with high and low BUE (Figure 4-17(b)). The results in Figure 4-17(b) illustrate a noticeable decrease in the strain hardening of the machined surface with high BUE compared to the one with low BUE. These results confirmed that BUE formation could have a beneficial effect on strain hardening of the workpiece which in turn may considerably improve SDSS machining performance. These conclusions agree with the results obtained in section 3.1.

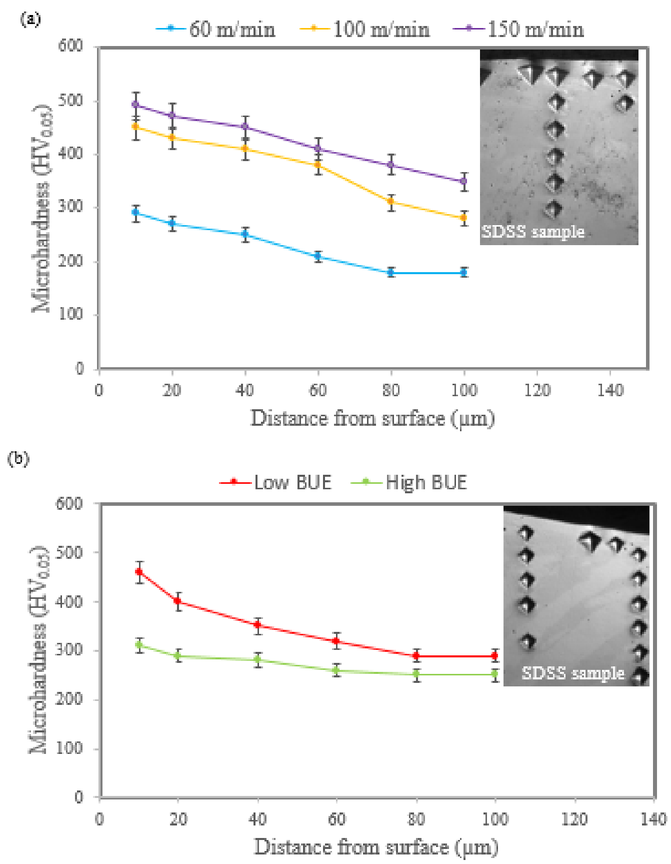

Figure 4-17 Microhardness profile of the machined surface after machining (a) with different cutting speed and (b) high and low BUE

The machined workpiece surfaces were investigated by the Alicona microscope at the beginning of cut where no significant wear can be observed. Here, the average surface roughness (Ra) of the workpiece was analysed at a cut-off value of 80 µm. Figure 4-18(a)

`

illustrates real 3D workpiece topologies obtained at different cutting speeds. From the surface roughness values, it can be reported that the lowest surface roughness is present at the most significant BUE height and cutting forces (lower cutting speed). A possible reason for the considerable enhancement of the workpiece's surface quality is that BUE acts like a burnishing tool, reducing the irregularity of the surface. In general, it can be indicated from Figure 4-18(b) that the machined surface obtained at 60 m/min (highest BUE) is the smoothest, and no defects can be observed compared to the lower BUE (high cutting speeds). A similar conclusion was made by Gómez-Parra et al. [35].

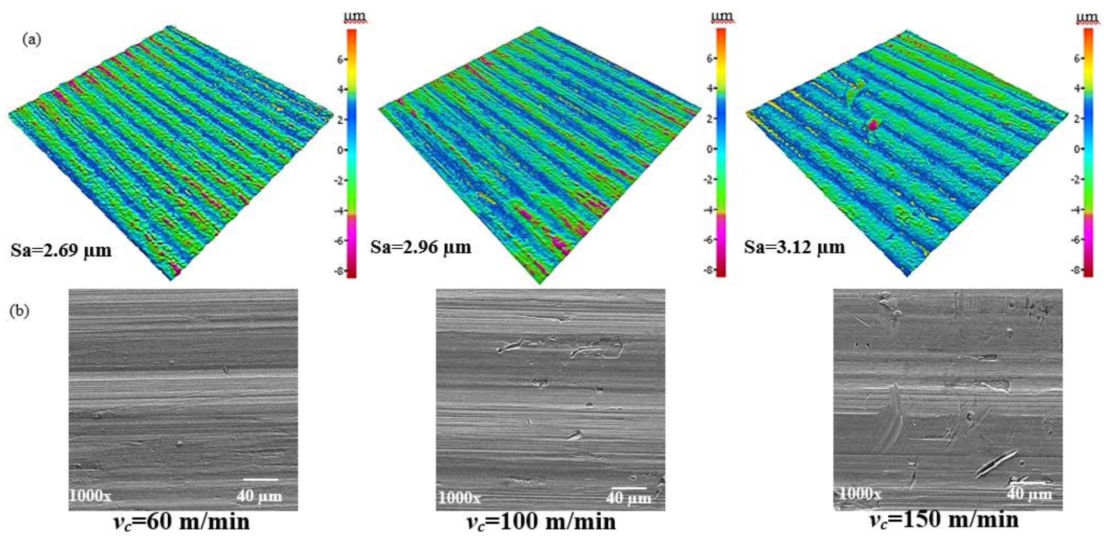

Figure 4-18 (a) Three dimensional and (b) SEM images of the machined surface obtained at different cutting speeds, associated with surface roughness values

4.4 Conclusions

The BUE formation phenomenon was investigated with uncoated cemented carbide tools during the machining of SDSS-UNS S32750 stainless steel. This research aims to analyze in detail BUE morphologies obtained at different cutting speeds. In addition, the

`

connection between BUE formation, tool wear, and machining outputs was examined. The following conclusions can be made from the results presented in this research;

1. Low BUE formation during SDSS machining can be attributed to the strain difference between the austenite and ferrite phases. The most significant strain difference was related to the highest BUE size during the formation process. At high cutting speeds, the austenite strain values were quite similar to the ferrite strain values, resulting in the reduction of plastic strain recovery and consequently, BUE dimensions.
2. Analysis of BUE patterns over the cutting tools reveal that the BUE consists of shear lamellae at different cutting speeds. However, the structure obtained at the higher speed is thinner than the one at the lower cutting speed. This is caused by high strains and temperatures generated at a higher cutting speed.
3. Examination of the BUE's protective effect at various cutting speeds reveals an enhancement of tool life at low cutting speeds, where only low flank wear is observed compared to various wear types (flank wear, chipping) found at high cutting speeds. These results highlight the beneficial impact of BUE in terms of increasing tool life and lowering tool breakage probability.
4. The effect of different cutting speeds on BUE formation is characterized by several friction behaviors in the cutting zone. The tool-chip interface exhibits more beneficial friction conditions, which result in diverse BUE patterns forming at various cutting speeds. This phenomenon affects workpiece surface integrity, and a

`

consequent improvement in surface finish and noticeable reduction in the workpiece work hardening layer are observed.

Acknowledgments

This research was supported by Natural Sciences and Engineering Research Council of Canada (NSERC) under the CANRIMT Strategic Research Network Grant NETGP 479639-15.

References

1. AlMotasem AT, Posselt M, Bergström J. Nanoindentation and nanoscratching of a ferrite/austenite iron bicrystal: an atomistic study. Tribol Int 2018; 127:231–9. https://doi.org/10.1016/J.TRIBOINT.2018.06.017.
2. Corrêa JG, Schroeter RB, Machado ÁR. Tool life and wear mechanism analysis of carbide tools used in the machining of martensitic and super martensitic stainless steels. Tribol Int 2017; 105:102–17. https://doi.org/10.1016/J.TRIBOINT.2016.09. 035.
3. Wang B, Liu Z. Evaluation on fracture locus of serrated chip generation with stress triaxiality in high speed machining of Ti6Al4V. Mater Des 2016;98:68–78. https:// doi.org/10.1016/j.matdes.2016.03.012.
4. Ahmed YS, Alam MS, Arif AD, Veldhuis SC. Use of acoustic emission and cutting force signals to monitor built-up edge formation in stainless steel turning. Int J Adv Manuf Technol 2019; 49:779–84. https://doi.org/10.1007/s00170-019-03607-3.
5. Trent EM, Wright PK. Metal cutting. fourth ed. Butterworth: Heinemann; 2000.

`

6. SONG X, HE W, IHARA T. Predicting periodic evolution of BUE formation mechanisms during machining ductile material using damage mechanics. Mech Eng J 2016;3. https://doi.org/10.1299/mej.15-00534. 15-00534-15-00534.
7. Bagherzadeh A, Budak E. Investigation of machinability in turning of difficult-to-cut materials using a new cryogenic cooling approach. Tribol Int 2018; 119:510–20. https://doi.org/10.1016/J.TRIBOINT.2017.11.033.
8. Liang X, Liu Z. Tool wear behaviors and corresponding machined surface topography during high-speed machining of Ti-6Al-4V with fine grain tools. Tribol Int 2018; 121:321–32. https://doi.org/10.1016/J.TRIBOINT.2018.01.057.
9. Ahmed YS, Fox-Rabinovich G, Paiva JM, Wagg T, Veldhuis SC. Effect of built-up edge formation during stable state of wear in AISI 304 stainless steel on machining performance and surface integrity of the machined part. Materials 2017;10. https:// doi.org/10.3390/ma10111230.
10. Oliaei SNB, Karpat Y. Built-up edge effects on process outputs of titanium alloy micro milling. Precis Eng 2017; 49:305–15. https://doi.org/10.1016/j.precisioneng. 2017.02.019.
11. Sivaiah P, Chakradhar D. Performance improvement of cryogenic turning process during machining of 17-4 PH stainless steel using multi objective optimization techniques. Meas J Int Confed 2019; 136:326–36. https://doi.org/10.1016/j. measurement.2018.12.094.
12. Wika KK, Litwa P, Hitchens C. Impact of supercritical carbon dioxide cooling with Minimum Quantity Lubrication on tool wear and surface integrity in the milling of AISI 304L stainless steel. Wear 2019;426–427:1691–701. https://doi.org/10.1016/ j. wear.2019.01.103.

`

13. Medeossi F, Sorgato M, Bruschi S, Savio E. Novel method for burrs quantitative evaluation in micro-milling. Precis Eng 2018; 54:379–87. https://doi.org/10.1016/ j. precisioneng.2018.07.007.
14. Nomani J, Pramanik A, Hilditch T, Little fair G. Stagnation zone during the turning of Duplex SAF 2205 stainless steels alloy. Mater Manuf Process 2017; 32:1486–9. https://doi.org/10.1080/10426914.2017.1279289.
15. Kumar CS, Patel SK. Application of surface modification techniques during hard turning: present work and future prospects. Int J Refract Metals ard Mater 2018; 76:112–27. https://doi.org/10.1016/j.ijrmhm.2018.06.003.
16. Niknam SA, Kouam J, Songmene V, Balazinski M. Dry and semi-dry turning of titanium metal matrix composites (Ti-MMCs). Procedia CIRP 2018; 77:62–5. https:// doi.org/10.1016/j.procir.2018.08.215.
17. Kümmel J, Gibmeier J, Müller E, Schneider R, Schulze V, Wanner A. Detailed analysis of microstructure of intentionally formed built-up edges for improving wear behaviour in dry metal cutting process of steel. Wear 2014; 311:21–30. https://doi.org/10.1016/j.wear.2013.12.012.
18. Andersson A. Built-up edge formation in stainless steel milling. Degree project in materials science and engineering. Stockholm: Swedan; 2017.
19. Klocke F, Lortz W, Trauth D. Analysis of the dynamic chip formation process in turning. Int J Mech Sci 2018; 135:313–24. https://doi.org/10.1016/j.ijmecsci.2017. 11.035.
20. Medina-Clavijo B, Saez-de-Buruaga M, Motz C, Soler D, Chuvilin A, Arrazola PJ. Microstructural aspects of the transition between two regimes in orthogonal cutting of

`

AISI 1045 steel. J Mater Process Technol 2018; 260:87–96. https://doi.org/10.1016/j.jmatprotec.2018.05.016.

21. Bilgin MB. Investigating the effects of cutting parameters on the built-up-layer and built-up-edge formation during the machining of AISI 310 austenitic stainless Steels. Mater Tehnol 2015; 49:779–84. https://doi.org/10.17222/mit.2014.253.
22. Trent EM. Metal cutting and the tribology of seizure: II movement of work material over the tool in metal cutting. Wear 1988; 128:47–64. https://doi.org/10.1016/ 0043-1648(88)90252-9.
23. Atlati S, Haddag B, Nouari M, Moufki A. Effect of the local friction and contact nature on the Built-Up Edge formation process in machining ductile metals. Tribol Int 2015; 90:217–27. https://doi.org/10.1016/j.triboint.2015.04.024.
24. Nomani J, Pramanik A, Hilditch T, Littlefair G. Investigation on the behavior of austenite and ferrite phases at stagnation region in the turning of duplex stainless steel alloys. Metall Mater Trans A Phys Met Mater Sci 2016; 47:3165–77. https://doi.org/10.1007/s11661-016-3472-0.
25. ISO 3685–Tool Life Testing with Single-Point Turning Tools, 2nd ed.; International Organization for Standardization: Geneva, Switzerland, 1993. (Revised in 2017).
26. Wälder G, Fulliquet D, Foukia N, Jaquenod F, Lauria M, Rozsnyo R, et al. Smart wire EDM machine. Procedia CIRP 2018; 68:109–14. https://doi.org/10.1016/j.procir.2017.12.032.
27. Shaw MC. The theory of metal cutting. In: Tobias SA, editor. Proc. Twenty-fifth int. Mach. Tool des. Res. Conf. London: Macmillan Education UK; 1985. p. 33–6. https://doi.org/10.1007/978-1-349-07529-4_3.

`

28. Blunt L (Liam), Jiang X. Advanced techniques for assessment surface topography: development of a basis for 3D surface texture standards "surfstand" Kogan Page Science. 2003.
29. Kamruzzaman M, Rahman SS, Ashraf MZI, Dhar NR. Modeling of chip–tool inter- face temperature using response surface methodology and artificial neural network in HPC-assisted turning and tool life investigation. Int J Adv Manuf Technol 2017; 90:1547–68.
30. Mia M, Dhar NR. Effect of high pressure coolant jet on cutting temperature, tool wear and surface finish in turning hardened (Hrc 48) steel. J Mech Eng 2015; 45:1. https://doi.org/10.3329/jme.v45i1.24376.
31. Dhanabalakrishnan KP, Ganeshkumar S, Thirunavukkarasu V. Analysis of tool wear patterns in finishing turning of inconel 718 with zirconium coated tool insert. Int J Appl Eng Res 2015; 10:18560–9.
32. Ahmed YS, Veldhuis SC. Effects of High pressure coolant on machining temperature and machinability of AISI 304 stainless steel. CSME Int Congr 2018. https://doi. org/10.25071/10315/35369.
33. Ikuta A, Shinozaki K, Masuda H, Yamane Y, Kuroki H, Fukaya Y. Consideration of the adhesion mechanism of Ti alloys using a cemented carbide tool during the cutting process. J Mater Process Technol 2002; 127:251–5. https://doi.org/10. 1016/S0924-0136(02)00152-8.
34. Armendia M, Osborne P, Garay A, Belloso J, Turner S, Arrazola P-J. Influence of Heat treatment on the machinability of titanium alloys. Mater Manuf Process 2012; 27:457–61. https://doi.org/10.1080/10426914.2011.585499.

`

35. Gómez-Parra A, Álvarez-Alcón M, Salguero J, Batista M, Marcos M. Analysis of the evolution of the Built-Up Edge and Built-Up Layer formation mechanisms in the dry turning of aeronautical aluminium alloys. Wear 2013; 302:1209–18. https://doi. org/10.1016/J.WEAR.2012.12.001.
36. Diniz AE, Machado ÁR, Corrêa JG. Tool wear mechanisms in the machining of steels and stainless steels. Int J Adv Manuf Technol 2016; 87:3157–68. https://doi.org/10. 1007/s00170-016-8704-3.
37. Childs THC. Developments in simulating built up edge formation in steel Tribology International 137 (2019) 212–227 machining. Procedia CIRP 2012; 1:78–83. https://doi.org/10.1016/j.procir.2012. 04.012.
38. Xavior MA. Evaluating the machinability of AISI 304 stainless steel using alumina inserts. J Achiev Mater Manuf Eng 2012; 55:841–7.
39. Wan ZP, Zhu YE, Liu HW, Tang Y. Microstructure evolution of adiabatic shear bands and mechanisms of saw-tooth chip formation in machining Ti6Al4V. Mater Sci Eng, A 2012;531:155–63. https://doi.org/10.1016/j.msea.2011.10.050.
40. ASTM International. ASTM E 112-96(2004) standard test methods for determining average grain size. Astm 2004:1–26. https://doi.org/10.1520/E0112-96R04.
41. Nomani J. Built-up edge mechanisms in the machining of duplex stainless steels Thesis. Deakin University; 2014.
42. Yang G, Chen LQ, Wang JH. Influences of texture of FCC metals on their mechanical properties. J Kunming Univ Sci Technol 2012; 5:24–7.

`

43. Brinksmeier E, Preuss W, Riemer O, Rentsch R. Cutting forces, tool wear and surface finish in high speed diamond machining. Precis Eng 2017; 49:293–304. https://doi.org/10.1016/j.precisioneng.2017.02.018.

44. Kaynak Y, Gharibi A, Yılmaz U, Köklü U, Aslantaş K. A comparison of flood cooling, minimum quantity lubrication and high pressure coolant on machining and surface integrity of titanium Ti-5553 alloy. J Manuf Process 2018; 34:503–12. https://doi.org/10.1016/j.jmapro.2018.06.003.

45. Seid Ahmed Y, Paiva J, Covelli D, Veldhuis S. Investigation of coated cutting tool performance during machining of super duplex stainless steels through 3D wear evaluations. Coatings 2017; 7:127. https://doi.org/10.3390/coatings7080127.

`

Chapter 5: Effect of Built-Up Edge Formation during Stable State of Wear in AISI 304 Stainless Steel on Machining Performance and Surface Integrity of the Machined Part

Yassmin Seid Ahmed [1, 2, *], German Fox-Rabinovich[1], Jose Mario Paiva [1, 3], Danielle Covelli [4], and Stephen Clarence Veldhuis [1]

[1] McMaster Manufacturing Research Institute (MMRI), Department of Mechanical Engineering, McMaster University, 1280 Main Street West, Hamilton, ON L8S4L7, Canada; gfox@mcmaster.ca (G. F); paivajj@mcmaster.ca (J.M.P.); covelld@mcmaster.ca (D.C.); veldhu@mcmaster.ca (S.C.V.)

[2] Production Engineering Department, Alexandria University, Alexandria, 21544, Egypt

[3] Department of Mechanical and Materials Science, Catholic University of Santa Catarina, Rua Visconde de Taunay, 427-Centro, Joinville-SC 89203-005, Brazil

[4] Biointerfaces Institute, McMaster University, ETB 422, 1280 Main Street West, Hamilton, ON L8S 0A3, Canada; dcovelli172@gmail.com

* **Correspondence:** seidahmy@mcmaster.ca; Tel.: +1-365-888-1186

`

This paper is published in Materials Journal. Volume 10, pp 1230–1245. https://doi.org/10.3390/ma10111230. This paper is republished here with permission.

Abstract

During machining of stainless steels at low cutting speeds, workpiece material tends to adhere to the cutting tool at the tool-chip interface, forming built-up edge (BUE). BUE has a great importance in machining processes; it can significantly modify the phenomenon in the cutting zone, directly affecting the workpiece surface integrity, cutting tool forces, and chip formation. AISI 304 stainless steel has a high tendency to form an unstable BUE, leading to deterioration of the surface quality. Therefore, it is necessary to understand the nature of the surface integrity induced during machining operations. Although many reports have been published on the effect of tool wear during machining of AISI 304 stainless steel on surface integrity, studies on the influence of the BUE phenomenon in the stable state of wear have not been investigated so far. The main goal of the present work is to investigate the close link between the BUE formation, surface integrity and cutting forces in the stable sate of wear for uncoated cutting tool during the cutting tests of AISI 304 stainless steel. The cutting parameters were chosen to induce BUE formation during machining. X-ray diffraction (XRD) method was used for measuring superficial residual stresses of the machined surface through the stable state of wear in the cutting and feed directions. In addition, surface roughness of the machined surface was investigated using the Alicona microscope and SEM was used to reveal the surface distortions created during the cutting process, combined with chip undersurface analyses. The investigated BUE formation during the stable state of wear showed that the BUE can cause a significant

improvement in the surface integrity and cutting forces. Moreover, it can be used to compensate for tool wear through changing the tool geometry, leading to the protection of the cutting tool from wear.

Keywords

stable state of wear; built-up edge; tool wear; surface integrity; cutting forces; AISI 304 stainless steel

5.1 Introduction

Austenitic stainless steels are widely used in chemical industries and nuclear power industries because they have a good combination of high mechanical strength and corrosion resistance. However, the residual stresses induced by machining operations can affect their ability to withstand loading conditions such as stress concentration, corrosion, cracking, and fatigue [1, 2]. Austenitic stainless steels are considered difficult-to-machine materials because of their low thermal conductivity and high strain hardening rate during cutting [3]. Their low thermal conductivity leads to heat concentration in the cutting zone that results in high localized temperatures. In addition, their high work hardening leads to high adhesion of the workpiece material to the cutting tool, resulting in unstable chip and BUE formation [4].

A BUE consists of highly deformed material layers, which are bonded to the tool surface and can lead to change the tool geometry and the mechanics of the process [5]. BUE is not permanently situated on the cutting edge, but periodically becomes detached, sometimes adhering to the machined surface, and sometimes to the chip [6]. The stability of a BUE as a structure is low and

`

the breakage of it can cause cracks and damages on the tool surface. At the same time, a thin and stable BUE can be used to protect the tool from wear by reducing the friction between the cutting tool and workpiece [7]. The demand of high quality products during the production has its attention in the workpiece surface properties, especially in the surface finish and the residual stress of the machined surfaces, due to its effects in the acting of the components and reliability [8, 9]. Fatigue, creep, and stress cracking leads to product failure. Therefore, it is of extreme importance to characterize the influence of the BUE formation in surface integrity [10]. Furthermore, the high residual stress can cause deformations, accelerate phase transformations and corrosion processes and it is one of the crucial factors in the superficial quality determination. Machining of austenitic stainless steels with BUE formation is a very complex tribological phenomenon [11]. To understand the effect of BUE formation on machining forces and surface integrity, it was necessary to study its effect in the stable state of wear (steady state zone) to isolate the effect of tool wear and ensure that all the conditions are the same.

Surface integrity of a machined workpiece can be described by three main parameters: the residual stresses, the surface roughness, and the work hardening in the surface zone [12]. The residual stress is defined as the stress that exists in an elastic body after all the external loads are removed [13]. Machining generally involves a large amount of plastic deformation with extremely high strain and strain rate [8]. The residual stress in the surface layer originates from three effects: mechanical effect, which leads to severe plastic deformation, thermal effect, which causes thermal plastic flow, and phase transformation. In most machining processes, the temperature does not exceed the phase transformation point, so the phase transformation can be isolated [14]. High mechanical properties and severe work hardening of austenitic stainless steels

`

during the chip formation process, combined with low thermal conductivity, generate high cutting forces along with high localized interfacial temperatures and adhesion in the cutting zone, which are the main reasons for high level of residual stresses [15–20]. XRD method of residual stress determination measures the angles at which the maximum diffracted intensity takes place when a crystalline sample is subjected to x-rays [21]. The residual stresses in the surface layer are an important factor in determining the performance and fatigue life of components. Reducing residual stresses determines mainly dimensional changes in the shape and mutual position of surfaces that can change the functional conditions of the assembly to which the workpiece belongs [22]. XRD can also provide detailed information about lattice parameters of single crystals, phase, and texture. Analysis of XRD peak profiles indicated that full-width at half-maximum (FWHM) is sensitive to the variation in stress–strain accumulation in the material [20].

Few studies on surface integrity induced in the machining of AISI 304 stainless steel have been performed. Xavior et al. [23] reported that high work-hardening rate, high built-up edge tendency, and low thermal conductivity of AISI 304 stainless steel are responsible for the poor surface finish and high tool wear. Moreover, Selvam et al. [24] observed that the BUE is continually growing during machining AISI 304 and digging into the workpiece and when built-up edge reaches a critical size, it breaks and welds on the machined surface, leading to increase surface roughness. Arunachalam et al. [25] reported that high tensile residual stress values were obtained, as a result of BUE deposition on the machined surface. The authors noted also that these BUE fragments deteriorated the surface integrity under loading conditions by their effect on the fatigue crack growth. Nagawaka et al. [26] found that the cutting stresses were greater than those in the longitudinal direction and the thickness on the tensile layer was found to be 150 µm.

`

Wiesner et al. [27] reported that stresses decrease in-depth direction becoming zero at 300 μm from the surface and the tensile residual stresses were found to penetrate deeper into the workpiece when the cutting speed decreases. The authors also concluded that the mechanical effect not only produces compressive residual stresses but can also contribute to tensile residual stresses. It is also stated that the strong work hardening of the work material and a considerable increase in the microstructural defects close to the machined surface can also contribute to tensile residual stresses. Jang et al. [8] reported that the residual stresses in the circumferential direction are tensile (close to + 600 MPa) and are greater than the compressive residual stresses predominant in the longitudinal direction. The circumferential residual stresses increase slightly with the cutting speed and decrease dramatically with the depth of cut.

A small number of papers are available concerning the interaction of worn cutting tools on the residual stress state in the machined surface of stainless steel [8, 28]. However, a detailed analysis of residual stress depth profiles in the regime of built-up edge formation in the stable state of wear has not been carried out yet. The main objective of this study is to investigate the close link between the BUE formation process and surface integrity when machining austenitic stainless steel AISI 304. To allow evaluation and optimization of the effects of BUE formation on the machined surface, hoop and axial components of residual stresses, cutting forces and chip formation in the stable state of wear have been investigated. These investigations are supported by Alicona microscope, SEM, EDS and XRD analyses.

`

5.2. Experimental Procedures

5.2.1 Work material, Cutting Tool, and Cutting Parameters

In this research, a round bar (120 mm diameter by 500 mm length) of an austenitic stainless steel AISI 304 was investigated during turning (finishing operation). The chemical composition and mechanical properties of the material are shown in Table 5-1. To reveal the workpiece microstructure, a sample of the AISI 304 was prepared, polished and etched with Glycergia solution (1 mL Glycerol + 20 mL hydrochloric acid (HCl) + 20 mL HNO3). The microstructure of the AISI 304 workpiece was characterized using a Nikon ECLIPSE IV 100 microscope (Nikon Canada Inc., Mississauga, ON, Canada) equipped with UC30 camera, see Figure 5-1.

Table 5-1 Chemical composition and mechanical properties of AISI 304 [29]

Elements	**Chemical Composition %**	**Proof Strength (0.2% yield) MPa**	**Tensile Strength MPa**	**Elongation%**	**Hardness HRC**
C	0.08	215	505	70	70
Si	0.75				
Mn	2.0				
P	0.045				
S	0.03				
Cr	20.0				
Ni	0.50				
N	0.10				

`

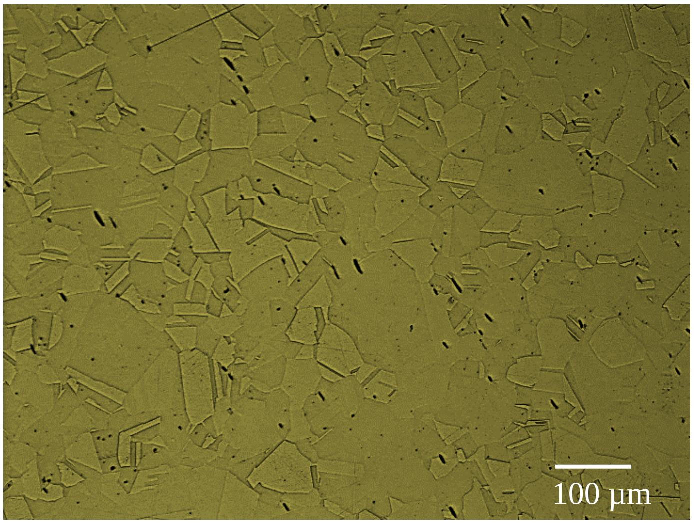

Figure 5-1 The microstructure of AISI 304 with an austenitic structure

The turning process was performed using an OKUMA CNC Crown L1060 lathe (OKUMA, Charlotte, NC, USA) with 15 kW of power and an OKUMA OSP-U10L controller. The cutting tool (Manufacturer: Kennametal) used for the experiments was an uncoated cemented carbide insert with WC/6%Co, which promotes BUE formation due to adhesion tendency to stainless steels. The designation of the insert is ISO CNGG432FS with the following geometry characteristics: back rake angle, $\lambda0 = 5°$; clearance angle, $\alpha0 = 7°$; wedge angle, β=78°; edge radius, r=10.5 µm and nose radius, $R\varepsilon = 0.8$ mm. The turning tests were conducted for finishing the operation with a cutting speed of 60 m/min, feed rate of 0.1 mm/rev, and depth of cut of 0.5 mm. The cutting speed vc= 60 m/min was selected to ensure BUE formation. Higher cutting velocities (vc> 60 m/min) lead to less provoked BUE formation, whereas lower cutting velocities(vc< 60 m/min) result in wear rates, which are too low for reasonable wear tests. The cutting tests were performed under wet conditions to reduce friction and heat generation during the cutting process. The cutting fluid was applied at a flow rate of 11 L/min via a nozzle positioned directly above the cutting tool and directed toward the tooltip. The cutting fluid chosen was semi-synthetic coolant-CommCool ™ 8800,

`

manufactured by the Wallover Company (Harrow, ON, Canada), at a concentration of 7%, typically used with stainless steel alloys.

5.2.2 Experimental Machine Techniques

The tool flank wear was measured using a KEYENCE – VHX 5000 digital microscope (Keyence Corp., Osaka, Japan), equipped with a CCD camera and image analyzer software. The tool life criterion was set to flank wear of 0.3 mm according to the recommendation of the ISO 3685 Standard [30]. During the tests, the cutting tools were analyzed by SEM, using a Vega 3-TESCAN (Vega 3-TESCAN, Brno, Czech Republic), coupled to EDS. The new and worn insert were also analyzed using an Alicona Infinite Focus G5 microscope (Alicona Manufacturing Inc., Bartlett, IL, USA), which works by focus variation, to generate real 3D surface images. This microscope allows for the capture of images with a lateral resolution down to 400 nm and a vertical resolution down to 10 nm. In order to measure the BUE volume of a cutting edge through steady state zone, first a 3D image of a new edge of the original insert was obtained and then the edge was measured a second time after cutting. The software used the 3D image of the new edge as a reference and compared it with a 3D image of a worn edge.

To evaluate the influence of BUE formation in the steady state zone on surface roughness, the surface roughness of the machined workpiece was measured across the tool feed direction by means of an Alicona Infinite Focus-with the Profile roughness module. The procedures of surface roughness measurements were performed according to EN ISO standard 25178 [31]. Roughness measurements were taken with a cut-off wavelength of 800 µm, a vertical resolution of 100 nm and a lateral resolution of 2 µm. Accuracy for roughness measurement of the

`

microscope in terms of uncertainty was U = 25nm at Ra =100nm. The surface roughness used in this study is the arithmetic mean surface roughness value (Ra), which is generally used in the industry. This evaluation was conducted three times and the average reading was considered.

Throughout the steady state region of tool wear, small pieces of the machined workpiece were cut using a water jet to evaluate any changes in machining induced residual stresses, which might be affected by BUE formation. X-ray stress data was collected using the Bruker D8 DISCOVER with DAVINCI.DESIGN diffractometer (Bruker, Burlington, ON, Canada), equipped with Cobalt Sealed Tube Source (λavg= 1.79026 Å) and Power settings: 35kV, 45mA. Residual stresses were analyzed in Diffrac.Leptos version 7.8 (Bruker, Burlington, ON, Canada), and the parameters used for analysis are summarized in Table 5-2. The residual stresses are measured on the machined surface and the sub-surface, in the direction of primary motion (along the cutting direction, R_c) and the direction of feed motion (along the feed direction, R_f) as shown in Figure 5-2.

Table 5-2 Parameters for X-ray residual stress analysis

Young`s modulus (GPa)	Poisson ratio	Radiation	Bragg Angle (2Φ)	Filter	X ray elastic constant ½ S_2 [MPa^{-1}]	X ray elastic constant s_1[MPa^{-1}]
193	0.275	kα	118	Cr	7.036 10^{-6}	-1.597 10^{-6}

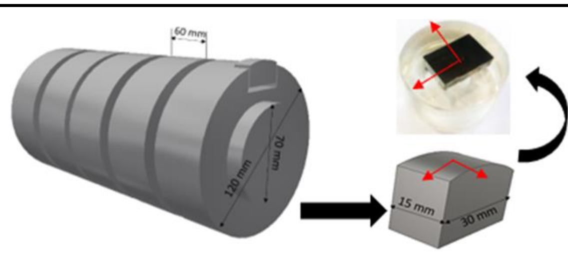

Figure 5-2 Method of sample preparation for XRD analysis

`

To determine the in-depth residual stress profiles, successive layers of material with a step of 20 μm were removed by electro etching to avoid the reintroduction of additional residuals stresses [1]. In addition, in-depth peak half width (FWHM) in feed and cutting direction was determined to estimate material work hardening like microhardness [14]. 2D frames were collected with DIFFRAC. Measurement Centre Version 3.0 software (Bruker, Madison, WI, USA) integrated to 1D using DIFFRAC.EVA Version 4.0 (Bruker, Madison, WI, USA), and displayed and analyzed in Topas Version 4.2 (Bruker, Madison, WI, USA). Moreover, the machined workpiece was investigated during steady state zone using SEM to reveal the surface distortion created by BUE formation.

During the machining tests, the cutting force measurements were performed with a 3D component tool holder Kistler dynamometer type 9121 (Kistler Instrument Corp., Amherst, NY, USA) with a data acquisition system. The signals of the forces from the dynamometer were transmitted to a Kistler 5010 type amplifier and then recorded on a computer using LABVIEW version 14.0 software (National Instruments, Austin, USA). The acquisition rate was 1000 data points per second, the scale was 20 MU/volt and sensitivity was 3.85 mV/MU.

5.3 Results and discussion

5.3.1 Investigation of the BUE in the steady state zone

As discussed previously, the focus of this research is to understand the effect of BUE formation on surface integrity and cutting forces. To understand this idea in more detail, a wear performance of the uncoated cemented carbide cutting tool during machining AISI 304 stainless

`

steel associated with progressive SEM images of BUE formation is presented in Figure 5-3. It can be shown that the BUE formation is unstable, and it gradually increases layer by layer and when it has reached a certain size, it tears off. This causes cracks and damages on the tool surface and eventually results in a cutting edge break out [7].

The BUE increases the contact between the workpiece and cutting tool and it engages the material being deformed in the same way as a punch [5]. Therefore, a large force is required to deform a material and cut the workpiece, and this force may to separate the BUE from the tool. When the BUE is not strongly attached to the tool, the friction force fractures it, and it is removed by the chip. After a fracture, a new BUE is produced in the same place and the same order of events is repeated. The BUE continuously appears and disappears as long as the cutting forces increase on the tool [6]. The lack of a constant height of the BUE is characteristic of this unstable state. Therefore, the BUE changes critically the friction conditions at the tool–chip and tool-workpiece interfaces, affecting thus surface integrity of the workpiece and tool wear behavior.

We have seen similar behavior in the steady state zone, as shown in Figure 5-3. The BUE is not stable at all: the built-up forms, accumulates, and eventually breaks off, akin to an avalanche [7], and then a new BUE is formed again. The instability of BUE may cause cracks and damage on the tool surface and eventually leads to a cutting edge break-out [11], as it is shown in failure region (Figure 5-3) where a large-sized built up is broken and it tears off the tool edge and results in a catastrophic failure of the cutting tool. The BUE is compressed from three sides, by the chip, the tool and the component being machined. These three forces balance each other and the BUE is held on the tool. The BUE is pressed against the tool so strongly that it sticks to it, forming a

`

strong junction that is capable of removing chips. Under excessive pressure, the BUE becomes so work hardened that it cut the material from which it has been produced instead of the tool and in this way, it prevents the tool from wear [6].

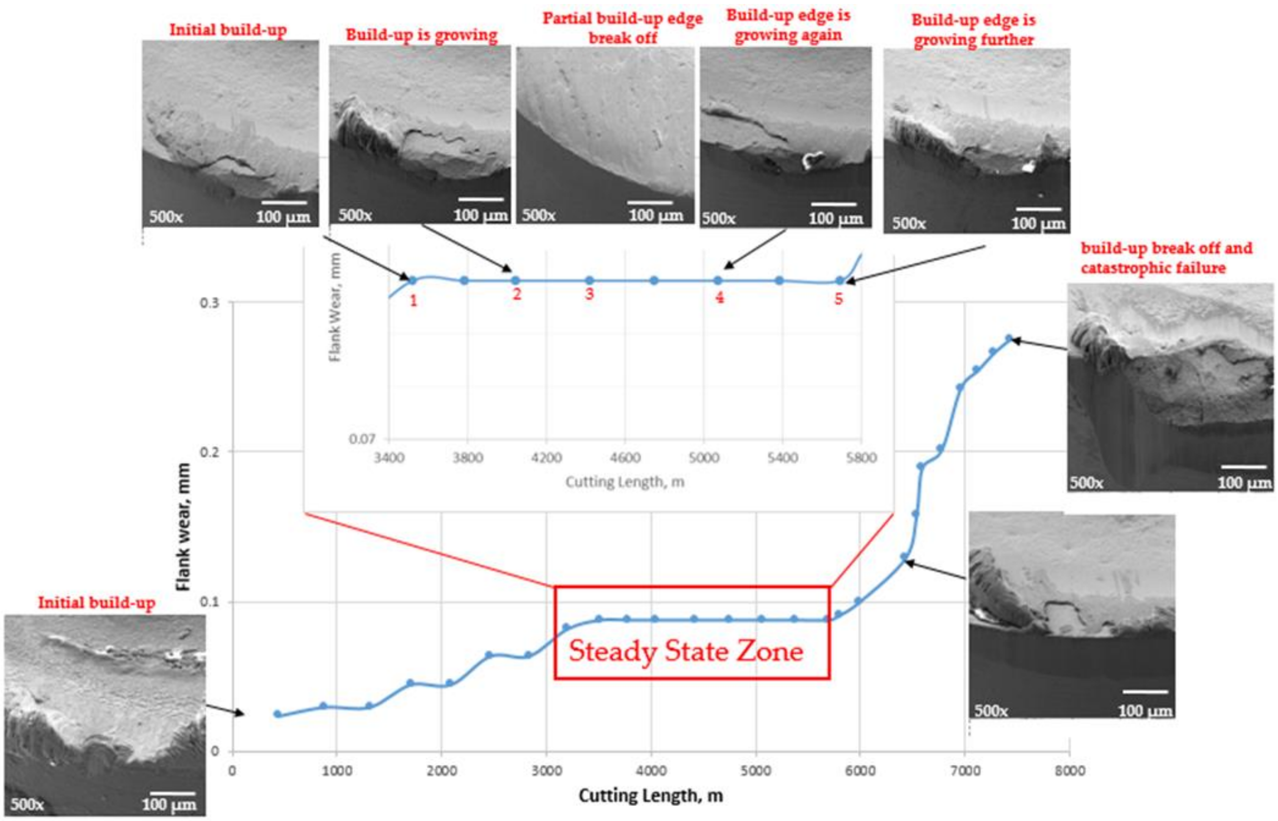

Figure 5-3 Relation between flank wear and cutting length for the uncoated carbide insert during machining AISI 304 stainless steel, combined with progressive SEM studies showing the BUE formation

Figure 5-4(a) shows the real 3D images of cutting tool profiles obtained with the Alicona microscope where the shapes of BUE at different cutting lengths through the steady state zone can be seen in orange and the associated values of BUE volume are shown in Figure 5-4(b). To understand more about how the BUE is formed through the steady state zone, it was necessary to measure its average height during cutting. The average height of BUE in the steady state zone

`

was measured using the KEYENCE microscope and plotted in Figure 5-5. It is seen that gradually BUE is formed gradually for a while and when it reaches a certain magnitude, pushed by the chip along the rake face, the edge is partially uncovered, and new BUE begins to form.

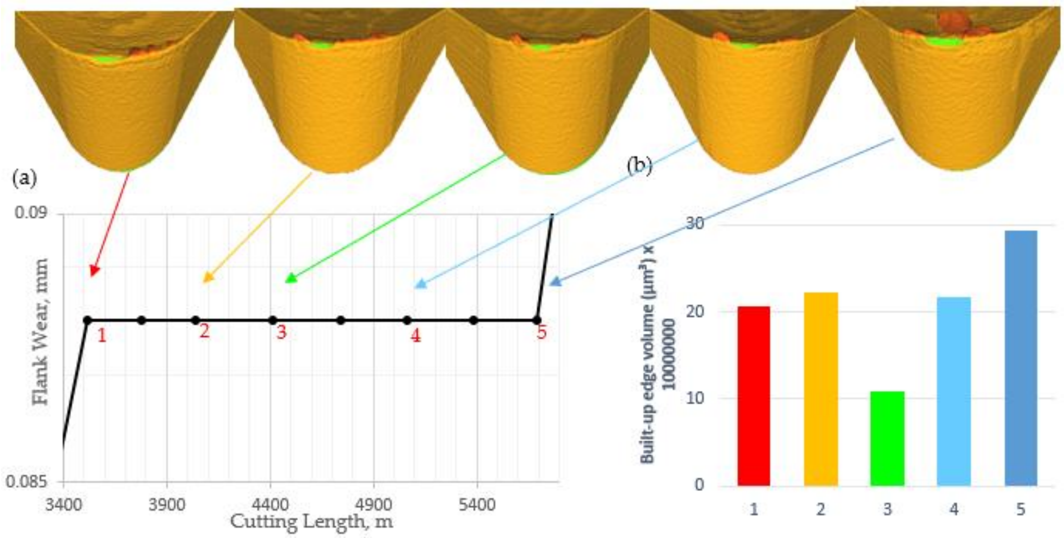

Figure 5-4(a) Alicona 3D images of the cutting tool during steady state zone showing BUE propagation, combined with (b) BUE volume

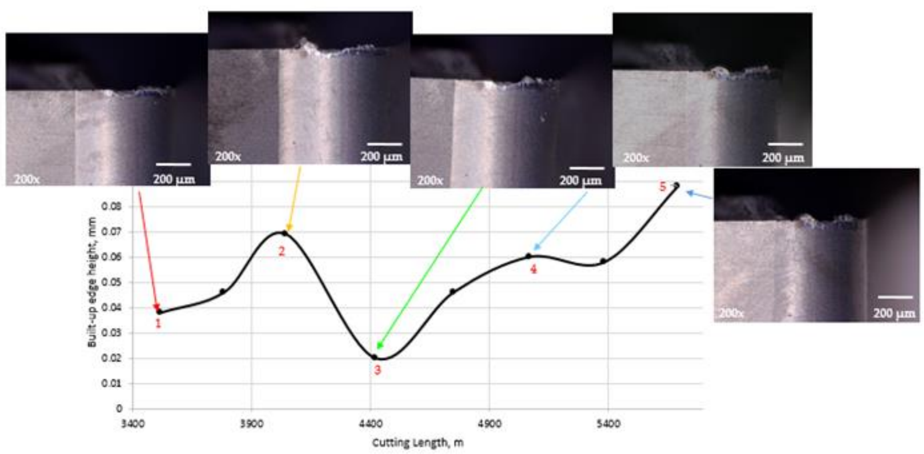

Figure 5-5 Relation between BUE height and cutting length for uncoated insert during steady state zone. Additionally, the flank surface presented for some points in the steady state zone

`

In order to investigate the chemical composition of the tool and BUE, an EDS analysis was performed and the results are shown in Figure 5-6. An SEM image of the BUE region in the steady state zone (at cutting length=4043 m) can be seen in Figure 5-6(a). EDS of the BUE region was performed and the spectrum illustrated in Figure 5-6(b). The presence of elements that are not part of the composition of the tool, such as Iron, Chromium, and Nickel were found, which indicates the tendency of workpiece material to cause intensive adhesion. EDS analysis of the tool surface shown in Figure 5-6(c) reveals a tungsten signal that comes from the cemented carbide substrate. The chemical composition of BUE region and the tool are given in Table 5-3. A color map of Iron and Chromium elements on the BUE region and tool surface are shown in Figure 5-6(d) (Fe in red and Cr in green). The EDS analysis was performed on the cutting tool for all the cutting lengths in the steady state zone and similar results were observed. The influence of BUE on machining forces and surface quality is investigated in the next sections.

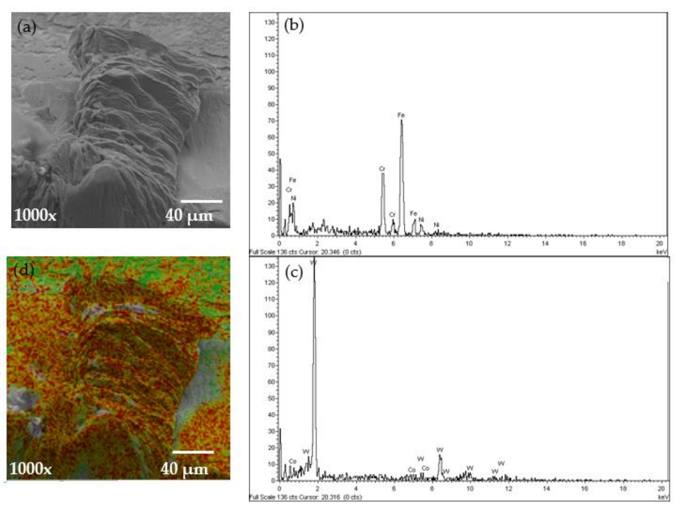

Figure 5-6 (a) SEM image of BUE region, (b) EDS spectrum analysis of the BUE zone on the rake face, (c) EDS spectrum analysis of the tool surface and (d) color map of the Fe and Cr elements on the BUE region

`

Table 5-3 EDS analysis of surface on the tool

Analysis of BUE	Analysis of insert surface
Fe%70.90	W% 94.87
Cr%29.10	Co% 5.13

5.3.2 Effect of BUE formation on machined surface and chip undersurface

One of the main factors contributing to natural surface roughness is the occurrence of the BUE. In the steady state zone, the BUE is continually building up and breaking down, which may lead to the fractured particles being carried away on the surface of the chip and the workpiece surface. Thus, it would be expected that the larger BUE, the rougher would be the surface produced. However, another phenomenon is observed here: Figure 5-7 shows the surface roughness and BUE values in the steady state zone where it is observed that the roughness increased when BUE increases and vice versa. After 4420 m cutting length, the opposite phenomenon is observed: roughness decreased with increasing the BUE and then after 5069 m surface roughness increased with increasing BUE. To understand the main reasons for the two opposite phenomena, SEM tests were conducted on the machined surfaces and the chip undersurface. The results show in general that the machined surface presented different types of defects, such as tearing, micro-pits, grooves, and scratches. It must be highlighted that these defects were less significant when the tool presented lower BUE, see points 1 and 4 in Table 5-4.

`

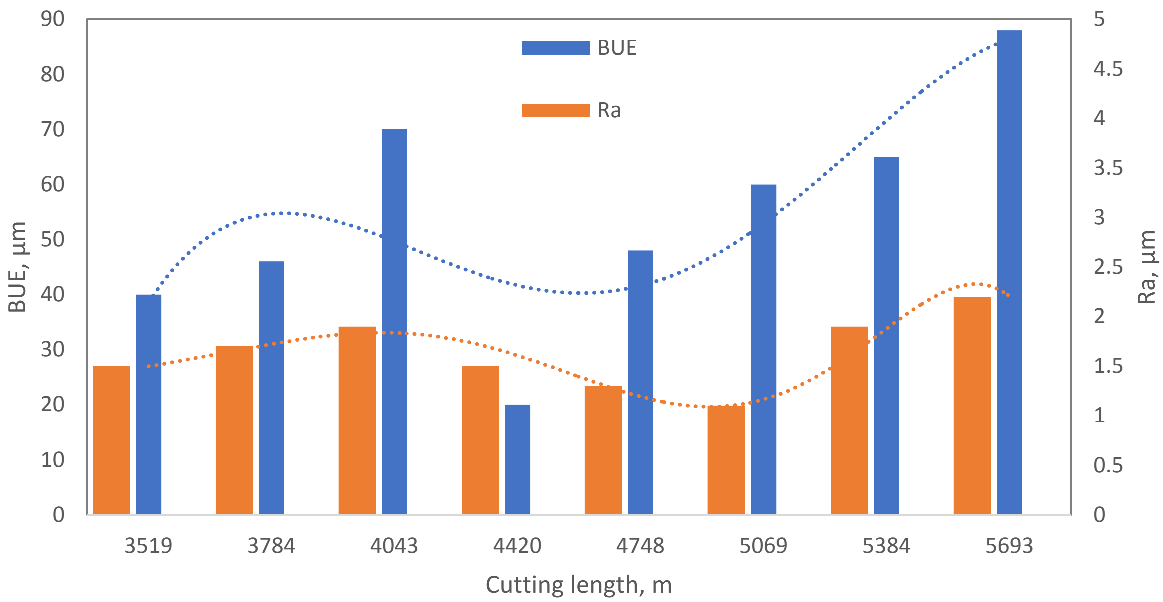

Figure 5-7 Relation between surface roughness and cutting length during steady state zone

Table 5-4 Machined surface and chip undersurface of five selected points in the steady state zone

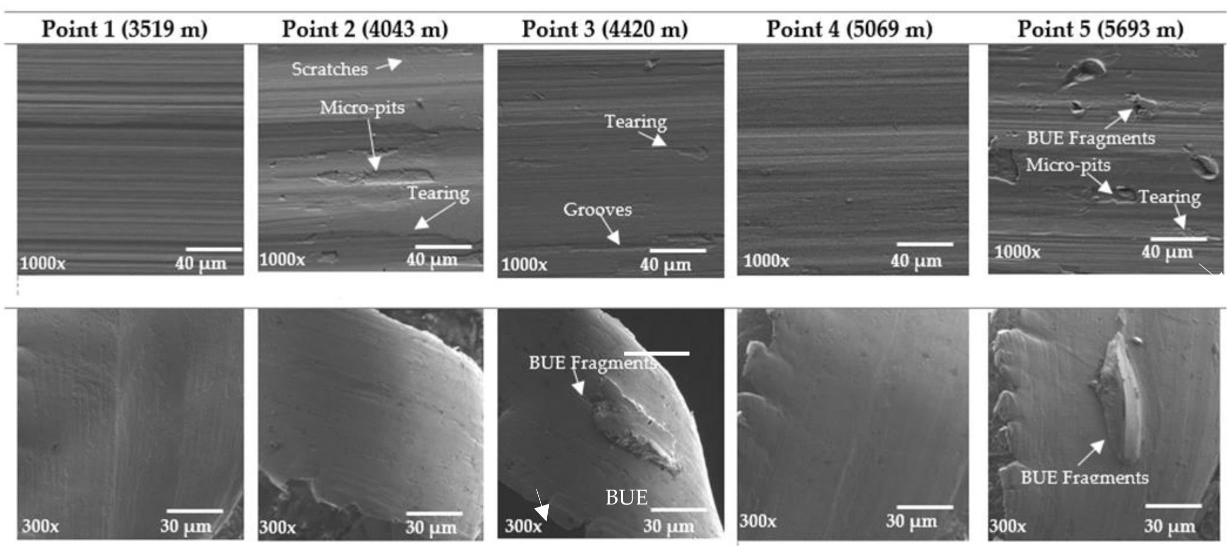

BUE is an unstable structure; during cutting the highly strain hardened fragments of BUE were torn off, may adhere to the workpiece and/or chips surface, leading to increase surface roughness. A number of different phenomena are occurring simultaneously within the steady state zone.

`

1. At the beginning of the steady state zone (from point 1 to point 2), BUE is continuously growing and engaging the machined surface, leading to the production of deep grooves, lowering the quality of surface finish, see point 2 in Table 5-4. When the BUE reaches a certain size, it tears off and new BUE is formed.

2. Before a new BUE is formed, the previous one is removed by the chip to the back of the tool rake face (Point 3 in Table 5-4), leading to improved surface finish.

3. Then, BUE is growing again and adheres strongly to the tool edge. Here, as shown in Point 4 in Table 5-4, the adhesion layer prevents sliding at the interface, protects the workpiece surface from scratching and improves the surface finish.

4. Finally, the friction force reaches a certain magnitude, overcomes the adhesion of the BUE to the tool, and plucks it off the tool. The nose of the BUE is broken off and presses into the cut surface, while the remainder is carried away by the chip. Point 5 in Table 5-4 shows some bright spots on both of the workpiece and the chip. This confirms the proposition of Kuzentsov [6] that the bright spots on the machined surface are caused by the reminders of the fractured BUE [1].

5.3.3 Effect of BUE formation on residual stresses and peak half width

As discussed before, the residual stresses induced are very important parameters that should be considered in the design of mechanical parts. The stresses will be tensile or compressive depending on the balance between the mechanical and thermal loads [32]. Therefore, it is necessary to understand how the BUE affects induced residual stresses. In this section the BUE formation can be related to a gradual evolution of the friction conditions at the tool–chip interface during the chip formation process in the steady state zone, which leads to the different results for residual stress distribution (Figure 5-8). As observed, all the values of surface residual

`

stresses are tensile, meaning that the thermal effect is more significant than the mechanical effect, and their magnitude varied, depending on the height of BUE. As it is shown in Figure 8, tensile residual stresses decreased with increasing of BUE, which can be attributed to the high cutting temperature, leading to softening of the material, and eventually, a decrease in the residual stresses [1]. Figure 5-8 also shows that the values of hoop stresses were higher, ranging from 240 to 550 MPa, than those of axial stresses, varying between 270 and 450 MPa. The high level of tensile residual stress both in the hoop and axial directions is due to high mechanical properties and severe work hardening of austenitic stainless steel, combined with low thermal conductivity.

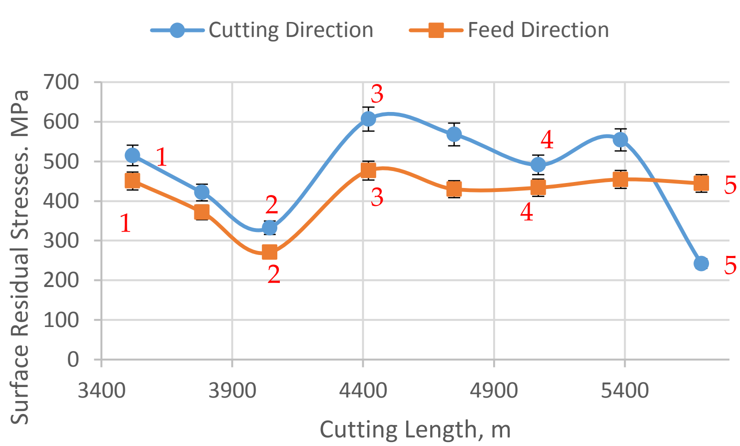

Figure 5-8 Relation between surface residual stresses and cutting length during steady state zone in cutting and feed directions

Residual stress profiles measured in the cutting and feed directions, respectively, are shown in Figure 5-9. It can be seen that tensile residual stresses at the near surface drop to compressive residual stresses within a shallow layer until a maximum compressive peak value is reached, and after that residual stresses are stabilized at a level corresponding to the state of the material before machining. Also, it is observed from residual stress profiles in the cutting direction that

`

the maximum residual stress and its depth are approximately the same for all the selected points of steady state because all the points have the same flank wear (stable state of wear).

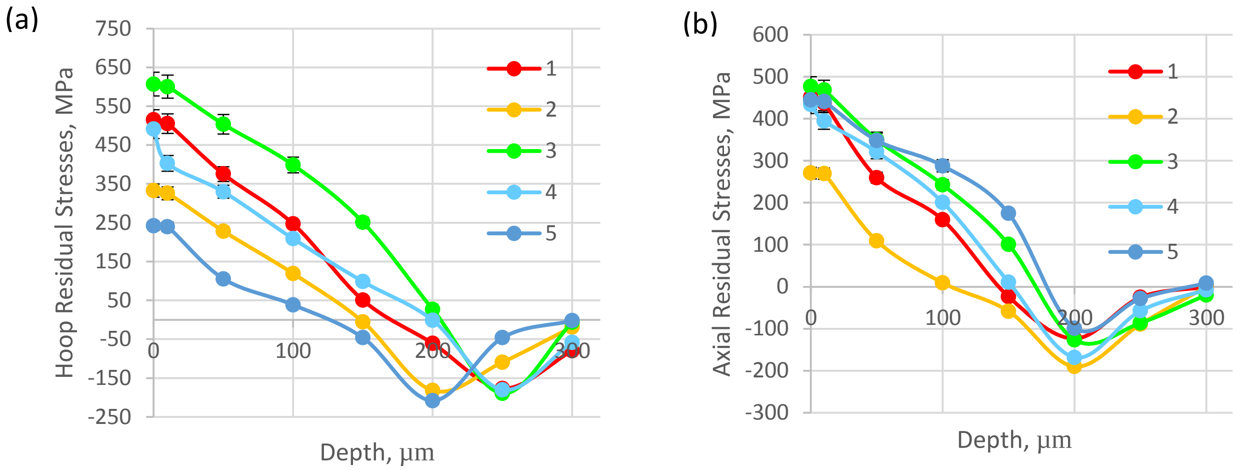

Figure 5-9 In-depth residual stresses profiles for five selected points in the steady state zone in (a) cutting direction and (b) feed direction

The work hardening and defect density gradient beneath the machined surface were evaluated using X-ray peak half width measurement. The peak half width is determined by the distribution of the randomly oriented lattice plane distances. Figure 5-10(a) shows the distribution of peak half width in the steady state zone, the results obtained on the same points as in Figure 5-9. As seen, the peak half width is influenced considerably by the BUE height. The peak half width is reduced when the BUE height increases because of high cutting temperature, which leads to the softening of the machined surface and, consequently, reduced peak half width.

Figure 5-10(b) shows the in depth evolution of the peak half width in feed and cutting directions for one of the samples in the steady state zone (Point 1). As shown, the highest value of about 1.3° is measured directly at the surface, and this value decreases continuously to 1° for the unaffected workpiece. The depth at which the peak half width stabilizes corresponds to the thickness of the work hardening layer due to machining [6]. For the all specimens, this layer was

`

found to be around 250 µm. Peak half width profile was performed on all the selected points of the steady state zone and similar results were observed.

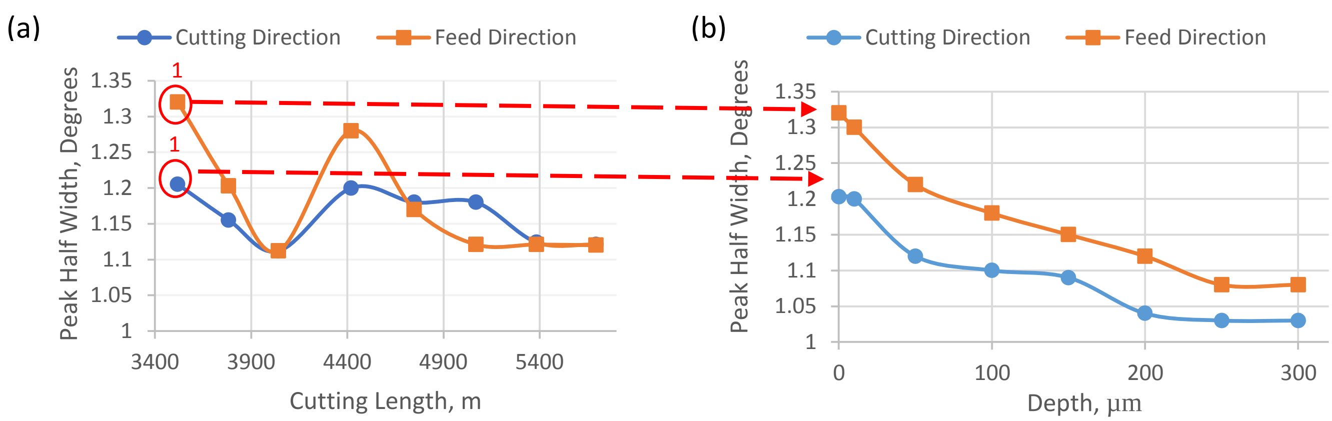

Figure 5-10 (a) Relation between Peak Half width and cutting length during steady state zone and (b) In depth peak half width profiles in cutting and feed directions for the first point of steady state zone

5.3.4 Effect of BUE formation on cutting forces and chip formation

To better understand the correlation between the BUE formation and the resulting residual stresses, it was decided to measure the cutting force components while machining the workpiece for the previous discussed residual stress tests. The cutting forces play a significant role in the formation of the residual stresses, although the influence is lower than that of cutting temperature [1]. Figure 5-11(a) shows the mean values of the cutting forces in the steady state zone. As shown, as a result of unstable BUE, the cutting force varies greatly, increasing instantly when a BUE is torn off, and decreasing as a new BUE is formed (Figure 5-5). An increase or decrease in cutting forces may depend on wedge angle; when a BUE increases, the wedge angle is reduced, resulting in a reduction of the work of cutting, cutting temperature and, consequently, cutting force and chip formation [6]. Moreover, the SEM image in Figure 5-11(a) shows that the chips formed by the cutting tool with low BUE are curlier than the chips from high BUE, which means that the contact length between the tool and the chip is shorter. Reduced contact length is beneficial in lowering the friction between the chip and the tool [33].

It is also observed that the cutting force oscillations are connected with the formation and disappearance of BUE: the oscillations are gradually reduced when the BUE is more stable, see Figure 5-11(b**).** Figure 5-11(c) shows SEM images of chip undersurfaces for the two selected points in the steady state zone (Points 3 and 5), they show that the chips formed with large BUE are rougher than those formed with low BUE. As the BUE grows, it becomes unstable and parts of it get removed while cutting. The removed portions of BUE adhere partly to the chip undersurface and partly to the machined surface. This causes the chip undersurface to be rough, and friction at the chip-tool interface increases, leading to a reduction in the chip speeds during the chip flow and an increase in the area of contact between tool and chip on the rake face surface [34].

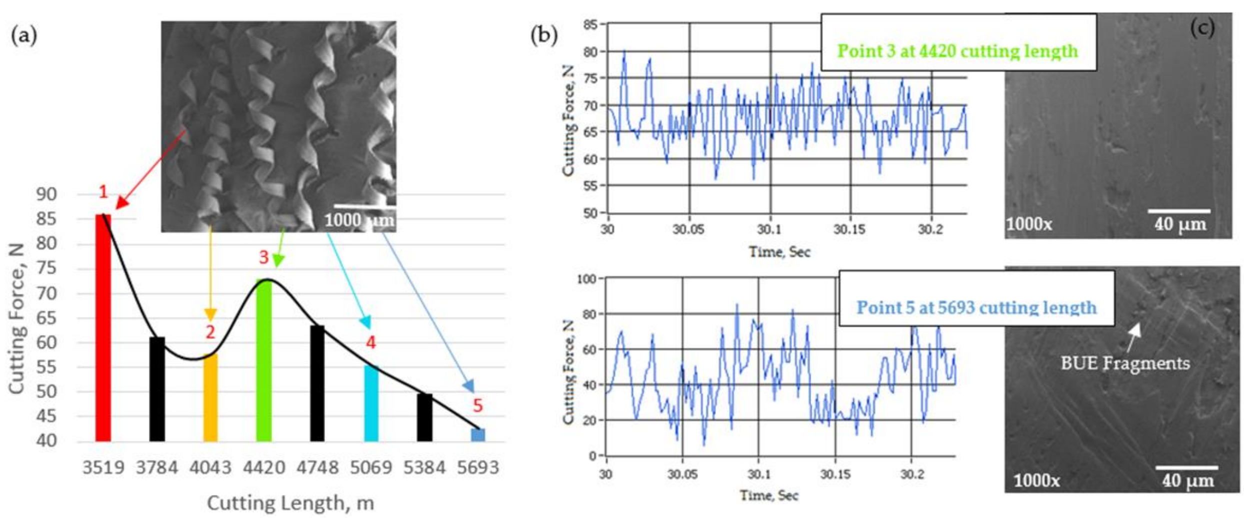

Figure 5-11 (a) Relation between cutting force and cutting length during steady state zone combined with SEM image of chip formation, (b) Cutting force variations and (c) Chip undersurface for two selected points in Figure 5-11(a)

`

5.4 Conclusions

The influence of BUE was investigated in wet machining of the austenitic stainless steel- type AISI 304 with the uncoated cemented carbide tool (WC-Co). Specifically, the effect of the variation of BUE height in the steady state zone on process outputs was studied. Surface roughness, residual stresses, cutting forces were examined in order to evaluate the BUE formation. The following conclusions can be drawn from this research:

1. BUE formation is an unstable process; it gradually increases layer by layer and when it has reached a certain size, it tears off. This causes cracks and damage on the tool surface, leading to a cutting edge break out. However, sometimes the BUE prevents sliding at the interface, protecting the tool from wear.

2. BUE growth is responsible for a decrease in surface roughness of the machined surface as the BUE is an unstable structure, and when it is broken off, some of the BUE particles detach from the surface and reduce surface finish. However, in some situations, broken BUE was removed by chips, leading to improved machined surface finish.

3. Tensile residual stresses were found on the surface of the machined workpiece; these stresses were decreasing when the BUE height increased, as the machined surface was softened as a result of high cutting temperature, eventually decreasing the residual stresses. Residual stresses were measured in both feed and cutting directions and it was found that that the hoop residual stresses are larger than the axial component ones, and the maximum compressive stresses and their depth are the same because tool wear remains the same in the steady state zone.

4. The peak half width reduced when the BUE height increased because of high cutting temperature, which leads to the softening of the machined surface, causing a reduction in peak

`

half width. Its value was the highest on the surface and then decreased continuously for the unaffected workpiece, whereas the thickness of the work hardening layer was found to be 250 µm.

5. The cutting force varied greatly, increasing when a BUE was torn off, and decreasing as a new BUE was formed. When a BUE increased, the wedge angle was reduced, resulting in a reduction in cutting force. It was also reported that the cutting force oscillations were gradually reduced when the BUE is more stable.

Finally, it is important to emphasize that the BUE formation always follows the same scenario, it forms, accumulates, and breaks off and then a new BUE is formed again. However, its form and intensity change under the same cutting conditions. This study is useful to investigate the beneficial effect of BUE on tool life and understand how the BUE affects surface integrity and cutting forces.

Acknowledgments

The authors would like to gratefully acknowledge the financial supported from the Natural Sciences and Engineering Research Council of Canada's (NSERC) Strategic Canadian Network for Research and Innovation in Machining Technology (CANRIMT).

Author Contributions

Yassmin Seid Ahmed performed the cutting experiments, performed XRD, metallographic, SEM, and Alicona studies, and wrote the paper, German Fox-Rabinovich designed cutting experiments, Jose Mario Paiva reviewed and edited the paper, Terry Wagg cut the samples using

`

water jet machine and Stephen Clarence Veldhuis is the supervisor of the research team. All authors have read and approved the final manuscript.

References

1. Fernández-Abia, A.T.; Barreiro, J.; Fernández-Larrinoa, J.; López de Lacalle; L. N., Fernández-Valdivielso; A., Perreira; O.M. Behaviour of PVD coatings in the turning of austenitic stainless steels, Procedia Engineering 2013, 63, 133–141.

2. Outeiro, J. C.; Dias, A.M.; Lebrum, J.L.; Astakhov, V.P. Machining residual stresses in AISI 316L steel and Their correlation with the cutting parameters. Machining Science and Technology- Manufacturing Technology 2002, 6, 251–270.

3. Leppert, T.; Peng, R.L. Residual stresses in surface layer after dry and MQL turning of AISI 316L steel, Prod. Eng. Res. Devel. 2012, 6, 367–374.

4. Diniz, A. E.; Marcondes, F.C.; Coppini, N. L. The performance evaluation of ceramic and carbide cutting tools in machining of stainless steels. Tecnologia da Usinagem dos Materiais, [Technology of machining of materials], 5th edn; Artliber Editora: São Paulo, 2006.

5. Atlati, S.; Haddag, B.; Nouari, M.; Moufki, A. Effect of local friction and contact nature on the Built-Up Edge formation process in machining ductile metals. Tribology International 2015, 90, 217–227.

6. Kuznetsov, V.D. Metal Transfer and Build up in Friction and Cutting; pergamon press Ltd. Gostekhizdat: Moscow, 1966.

`

7. Fox-Rabinovich, G.S.; Paiva, J.M; Gershman, I.; Aramesh, M.; Cavelli, D.; Yamamoto, K.; Dosbaeva, G.; Veldhuis, S.C. Control of self-organized criticality through adaptive behavior of nano-structured thin film coatings. Entropy 2016, 18, 290.
8. Jang, D. Y.; Watkins, T. R.; Kozaczek, K. J.; Hubbard, C. R.; Cavin, O. B. Surface residual stresses in machined austenitic stainless steel. Wear 1996, 194, 168–173.
9. Saoubi, R. M.; Outeiro, J. C.; Changeux, B.; Lebrun, J. L; Dias, A. M. Residual stress analysis in orthogonal machining of standard and resulfurized AISI 316L steels. Journal of materials processing technology 1999, 96, 225–233.
10. Sauvage, X.; Le Breton, J. M.; Guillet, A.; Meyer, A.; Teillet, J. Phase transformation in surface layers of machined steels investigated by X-ray diffraction and Mössbauer spectrometry. Materials Science and Engineering 2003, 362, 181–186.
11. Kulkarni, A. P.; Joshi, G.G; Sargade, V.G. Dry turning of AISI 304 austenitic stainless steel using AlTiCrN coated insert produced by HPPMS technique, Procedia Engineering 2013, 64, 737–746.
12. Takago, S., Gotoh, M., Sasaki, T. Hirose, Y. The residual stress measurements of TiCN PVD films, International for Diffraction Data. Adv X-ray Anal 2002, 45, 365–370.
13. Valiorgue, F., Rech, J., Hamdi, H., Gilles, P., Belg, J., 3D modeling of residual stresses induced in finish turning of an AISI304L stainless steel, International Journal of Machine Tools & Manufacture 2012, 53, 77–90.
14. Vashist, M.; Paul, S. Correlation between full width at half maximum (FWHM) of XRD peak with residual stress on ground surfaces. Journal Philosophical Magazine 2012, 92, Issue 33.

`

15. Saoubi R.M.; Outeiro J.C.; Chandrasekaran H.; Dillon O.W.; Jawahir I.S. A review of surface integrity in machining and its impact on functional performance and life of machined products. Int J Sustain Manuf. 2008, 1, 203–236.
16. Jeelani S.; Bailey J.A. Residual stress distribution in machining annealed 18% nickel maraging steel. J Eng Mater technol. 1986, 108, 2, 93–98.
17. Henriksen, E.K. Residual stresses in machined surfaces, Transactions of the ASME 1951, 73, 69–76.
18. Johnson, K.L., Contact Mechanics; Cambridge University Press: England, 1987, ISBN 9780521347969.
19. Fitzpatrick, M.E.; Fry, A.T.; Holdway, P.; Kandil, F.A.; Shackleton, J.; Suominen, L. Determination of Residual Stress by X-Ray Diffraction, National Physical Laboratory 2002, Teddington, Middlesex, UK.
20. Outeiro, J.C.; Pina, J.C.; Saoubi, R.; Pusavec, F.; Jawahir, I.S. Analysis of residual stresses induced by dry turning of difficult to- machine materials. Ann CIRP 2008, 57, 77–80.
21. Capello, E. Residual stresses in turning part I: influence of process parameters, Journal of Materials Processing Technology 2005, 160, 221–228.
22. Deng, X.; Shet, C. Residual stresses and strains in orthogonal metal cutting, International Journal of Machine Tool and Technology 2007, 43, 573–587.
23. Xavior, M. A. and Adithan, M. Determining the influence of cutting fluids on tool wear and surface roughness during turning of AISI 304 austenitic stainless steel. J. Mater. Process. Technol. 2009, 209, 900–909.
24. Selvam, M. S. and Radhakrishnan, V. Characteristics of a surface machined with a single point tool. Tribology 1973, 6, 93–96.

`

25. Arunachalam, R. M.; Mannan, M. A.; Spowage, M. A. Surface integrity when machining age hardened Inconel 718 with coated carbide cutting tools, Int. J. Mach. Tools Manuf. 2004, 44, 1481–1491.
26. Nagawaka, Y.; Usami, K.; Minato, A.; Tamamura, T; Sasaki, R.; Naruse, A. Effects of surface finish on residual stress distribution and stress corrosion cracking susceptibility of Type 304 Austenitic Stainless Steel in A Boiling 42% Mgcl/2 Solution. ICM3 1979, 2, 603–610.
27. Wiesner, C. 3D modeling of residual stresses induced in finish turning of an AISI 304L stainless steel. Metallurgical and Materials Transactions 1992, 23, 989–996.
28. Liu, C.R.; Barash, M.M. Variables governing patterns of mechanical residual stress in a machined surface. Journal of Engineering for Industry 1982, 104, 257 –264.
29. ISO 15510-Stainless Steels-Chemical composition: Annex C: classification of grades, c.1: stainless steels; International Organization for Standardization: Geneva, Switzerland, 2014.
30. ISO 3685–Tool Life Testing with Single-Point Turning Tools, 2nd ed.; International Organization for Standardization: Geneva, Switzerland, 1993. (Revised in 2017).
31. ISO 25178-2 Geometrical Product Specifications (GPS) –Surface Texture: Areal Part 2: Terms, Definitions and Surface Texture Parameters; International Organization for Standardization: Geneva, Switzerland, 2012.
32. Ulutan, D.; Ozel, T. Machining induced surface integrity in titanium and nickel alloys: A review. International Journal of Machine Tools & Manufacture 2011, 51, 250–280.
33. Natash, A.R.; Ghani, J.A.; Syariff, J.; Haron, C.H.C.; Hadi, M.A. Comparison of Dry and Cryogenic Machining on Chip Formation and Coefficient of Friction in Turning AISI 4340 Alloy Steel. Applied Mechanics and Materials 2014, 554, 7–11.

`

34. Seid Ahmed, Y.; Paiva, J.M.; Covelli, D.; Veldhuis, S.C. Investigation of Coated Cutting Tool Performance during Machining of Super Duplex Stainless Steels through 3D Wear Evaluations. Coatings 2017, 7(8), 127.

`

Chapter 6: Effect of laser micro- scale textured tools on tool-chip interface performance and surface integrity during turning of austenitic stainless steel

Yassmin Seid Ahmed [*, 1, 2], Jose Mario Paiva[1], A.F.M. Arif[1], Fred L. Amorim[3], Torres FL[3], S.C. Veldhuis[1]

[1] McMaster Manufacturing Research Institute (MMRI), Department of Mechanical Engineering, McMaster University, 1280 Main Street West, Hamilton, ON L8S4L7, Canada; paivajj@mcmaster.ca (J.M.P.); arifa10@mcmaster.ca (A.A.); Fred.amorim@pucpr.br (F.M.); ricardo.torres@pucpr.br (R.T.); veldhu@mcmaster.ca (S.C.V.)

[2] Production Engineering Department, Alexandria University, Alexandria, 21544, Egypt

[*] **Correspondence**: seidahmy@mcmaster.ca; Tel.: +1-365-888-1186

This paper is accepted in Applied Surface Science, Elsevier in January 2020.

Abstract

Demand for stainless steels is rapidly increasing, especially in the oil and gas industries. Stainless steel offers a number of key advantages such as high tensile strength, toughness, and excellent corrosion resistance. However, stainless steel machining still poses some serious difficulties. At low cutting speeds, workpiece material and chips tend to adhere to the cutting tool surface, forming a built-up edge (BUE). Unstable BUE can cause tool failure and deterioration of the workpiece surface quality. However, stable BUE formation can protect the cutting tool from further wear, improving the productivity of AISI 304 stainless steel machining. In this work, a femtosecond laser was used to apply different shaped textures on the rake face of the cutting tool (square, parallel, perpendicular) to understand the effect of different texture shapes and orientations on tool-chip interface performance, BUE stabilization and process efficiency, when turning AISI 304 austenitic stainless steel with a (WC + 6%Co) cemented carbide cutting tool. It was found that: the maximum reductions of 58%, 100%, and 24% in the respective cutting force, feed force, and coefficient of friction were obtained with the square textured tool; BUE formation was lower and more stable with square textured tools, reducing flank wear by 41-78% and enhancing surface finish by 54-68% in comparison to the untextured tool; the thickness and hardness values of the heat-affected zone were lower in the workpiece machined by the tools with the square textured pattern.

Keywords

Built-up edge, Laser texturing, Friction, Machining, AISI 304 stainless steel

6.1 Introduction

Austenitic stainless steel-type 304 is commonly used in different applications due to its notable anti-corrosion properties, excellent mechanical strength, and high toughness [1]. However, this material is known for its poor thermal conductivity, high work hardening rate, as well as poor tribological performance due to high friction coefficient, high cutting temperature and formation of a strong built-up edge (BUE) [2]. Any combination of these factors can reduce tool life and increase tool costs. The BUE consists of highly deformed material that promptly adheres to the

`

cutting tool during cutting, altering the cutting edge geometry [3]. The unstable state of BUE during the machining process can hamper the surface quality and reduce tool life [4]. When the BUE reaches a specific size, it breaks off completely, damaging the tool surface. BUE particles can adhere to the workpiece material, reducing the surface finish [5]. However, the BUE can sometimes inhibit sliding at the tool-chip interface, thereby preventing further wear on the cutting tool [5, 6]. As such, it was important to introduce a new approach of controlling the BUE formation and reducing the friction at the tool-chip interface during the cutting process to guarantee higher productivity and ensure high quality in the machined part [7].

In view of these problems, several methods were proposed to alleviate the tool wear and increase tool life, such as the use of new tool materials [8], tool geometries [9], tool coatings [10] and new lubrication methods such as high pressure coolant (HPC) [11]. However, the use of new tool materials is limited by their inherent characteristics, such as low impact toughness [12]. Modifications of tool geometries can also affect the strength of the cutting tools [13]. Moreover, the development of new coating materials usually requires a very long time to pass from the research to application stages [14]. In addition, many of the devices used to apply lubricants are expensive and difficult to operate [15]. Surface texturing of the cutting tool can be an efficient solution to address these issues [16, 17].

Surface texturing was used in different industrial applications to enhance the anti-adhesion, anti-wear properties of the tool, as well as to provide better lubrication, thus enhancing machining capability [18, 19]. In this regard, it was considered that the best cutting performance can be achieved through the use of surface textures combined with lubricants. In cutting tools, the sticking areas at the tool-chip interface exert extreme pressures and temperatures on the tool

`

[15], since it is very difficult for the cutting fluid to permeate into the contact zones. The textures on the cutting tool rake face can be used as micro channels or pools to transport or supply lubricant, reducing the temperature in the cutting zone [20]. Micro-texturing on the cutting tool surface can also reduce the tool-chip interface length, increase the heat transfer area, and entrap wear debris [21, 22]. For these reasons, surface texturing of a cutting tool can be a feasible method of enhancing the machining performance of stainless steel.

Recently published studies are concerned with improving the performance of cutting tools by creating textures on their cutting surface using femtosecond laser techniques. Micro-scale texturing on the cutting tool has been used for reducing cutting forces and friction at the tool-chip interface and consequently reducing adhesion or BUE formation, which benefits tool life and overall surface finish. Vasumathy and Meena [23] developed micro-textures on a carbide tool and the authors found that cutting forces and wear performance are better than those obtained by untextured tools during the machining of austenitic stainless steel. They concluded that a net reduction of 10-15% in cutting forces and machining energy consumption could be achieved by this process, compared to untextured tools. Arulkirubakaran et al. [24, 25] created different micro-textures on the cutting tools and the authors reported 20% reduction in the mean friction coefficient along with a 30% reduction in the contact length of the chip on the tool. Similar observations were made by Zhang et al. [26] for AISI 316 L stainless steel cutting. Kümmel et al. [27] also found that micro-grooved tools improved the antiadhesion properties and machined surface finish during the cutting of AISI 1045. They reported that textures formed on the cutting tool surface stabilize BUE formation over the course of the machining process, leading to a better surface finish. Jesudass Thomas and Kalaichelvan [28] observed an improvement in the machined surface quality during turning of Aluminium (AA 6351) and mild

`

steel (EN3B) with the use of a textured tool. The enhancement in surface finish was attributed to lower adhesion tendency during the machining process where a 23% and 16% reduction in surface roughness was noticed following the machining of a mild steel and aluminium alloy. Texture orientation also played an important role in machining performance [27, 29, 30]. Grguraš and Pušavec [29] observed that the wear performance of parallel micro-grooved tools was higher, but Kawasegi et al. [31] and Xing et al. [32] concluded that perpendicular micro-grooved tools gave lower cutting forces. Kümmel et al. [27] also compared the effects of dimple and groove textures on the tool rake face and reported that the use of micro-grooves is better than dimples at inhibiting BUE formation. Nonlinear texture patterns were also studied by [33] and based on their observations they concluded that the elliptical grooves reduced both cutting forces and temperature. From the above discussion, it becomes clear that micro-textures can enhance machining performance, but an exact method of finding the optimum textures 'shape and orientation is yet to be found.

Considering past research, an in-depth investigation of tool-chip interfaces was conducted to understand the effect of different texture shapes and orientations on machining performance and process efficiency. The textured and untextured cutting tools were inspected and compared at different cutting lengths and cutting speeds during the cutting test. This research addresses the following points: (i) a comprehensive study of the influence of rake face textures (square, parallel and perpendicular) on the tool-chip interface performance; (ii) an-depth investigation of BUE formation during the continuous turning process to understand the underlying reasons for the BUE stabilization; and (iii) an assessment of the deformation characteristics and mechanical state of the machined workpiece subsurface layers following machining with textured and untextured tools at different cutting speeds.

`

6.2 Material and methods

6.2.1 Tool and workpiece material

Uncoated cemented carbide with 6% Co was used as the cutting tool material. Table 6-1 shows the mechanical properties of uncoated carbide. The workpiece material was AISI 304 austenitic stainless steel with a diameter of 150 mm and a length of 300 mm. Before machining a 2 mm depth was removed from the surface to eliminate workpiece inhomogeneities. The chemical composition, mechanical properties and the microstructure of the workpiece used in the experiments are presented in Table 6-2.

Table 6-1 Mechanical properties of uncoated cemented carbide tool

Density (g/cm3)	**Hardness (GPa)**	**Flexural strength (Mpa)**	**Fracture toughness (MPa $m^{1/2}$)**	**Thermal conductivity (W/mK)**	**Thermal expansion coefficient ($10^{-6/}$K)**
14.6	16.0	2300	14.8	75.4	4.51

Table 6-2 Chemical composition, material properties and microstructure of AISI 304 stainless steel

Element	**Weight %**	**Proof Strength (MPa)**	**Tensile Strength (MPa)**	**Elongation (%)**	**Modulus of Elasticity (GPa)**	**Shear Modulus (GPa)**	**Hardness (HRC)**
C	0.08	215	505	70	200	86	70
Si	0.75						

`

Mn	2.0	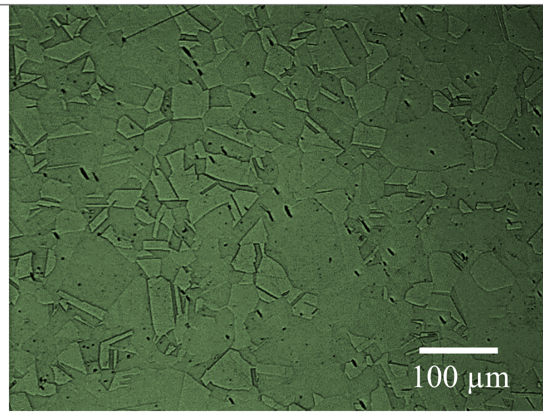
P	0.045	
S	0.03	
Cr	20.0	
Ni	0.50	
N	0.10	

6.2.2 Textured tools preparation

6.2.2.1 Fabrication of micro-textures

Different micro-textures were shaped by a femtosecond laser on polished cemented carbide tools. The femtosecond laser system was Ti: sapphire model "PRO 400" from Femtolasers Produktions GmbH, amplified by a "Femtopower Double 10 kHz" system. The output laser beam was polarized, with an emission centered at 800 nm, pulse length of 30 fs, maximum energy per pulse of 200 µJ and a repetition rate of 10 kHz. The laser beam was injected into the workstation model during machining. The motions were programmed using Mastercam 2018 - Mill software with post-processing connected to the laser system. A doublet lens with a focal length of 20 mm was used to focus the laser beam and the calculated focal point diameter was around 3.6 µm. The experimental setup, as well as the main parameters of the laser system, are presented in Table 6-3.

Table 6-3 Experimental setup and machining parameters used for laser system

Laser system parameters		Experimental setup
Pulse length	30 fs	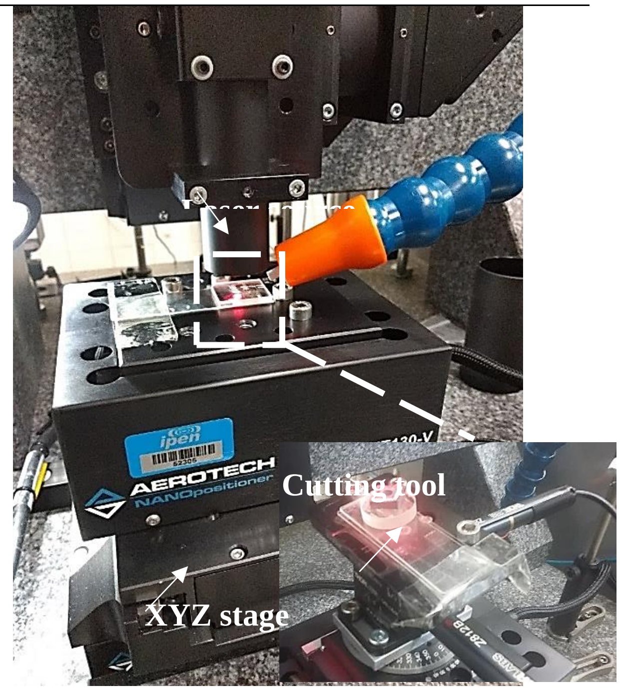
Energy/pulse	200 µJ	
Repetition rate	10 KHz	
Focal length	20 mm	
Focal dimeter	3.6 µm	
Beam positioning	Linear stages	
Polarization state	Linear	

6.2.2.2 Selection of the texturing area of textured tools

Micro texturing of the cutting tool was fabricated by a femtosecond laser, where micro-textures in the form of parallel, perpendicular, and square patterns were created on the rake face of the cutting tool, as shown in Figure 6-1(a). Before making the surface textures on the cutting tools, a turning experiment was carried out with an untextured cutting tool to obtain the maximum affected rake face area for a cutting length of 50 m at vc = 60 m/min. Figure 6-1(b) shows the rake face of the untextured cutting tool, where the adhesion and chipping region is clearly identifiable (approximately in the area of 700 x 700 µm²). The region on the cutting tools that was selected to undergo texturing, comprises the potential wear zone at a distance from the cutting edge such that the strength of the tool was not significantly affected (Figure 6-1(c)). The femtosecond laser was employed to produce surface texturing over an area of 700x 700 µm² on

`

the tool rake face, at a distance of 50 μm from the main cutting edges of the cutting tools (Figure 6-1(c)). The texture dimensions were selected according to the literature [33, 34]: width of 5 μm, pitch of 20 μm and depth of 2 μm. Following laser surface texturing, the cutting tools were polished with sandpaper to remove any edges at the textures. An untextured cutting tool was also used to establish the benchmark performance for comparison purposes.

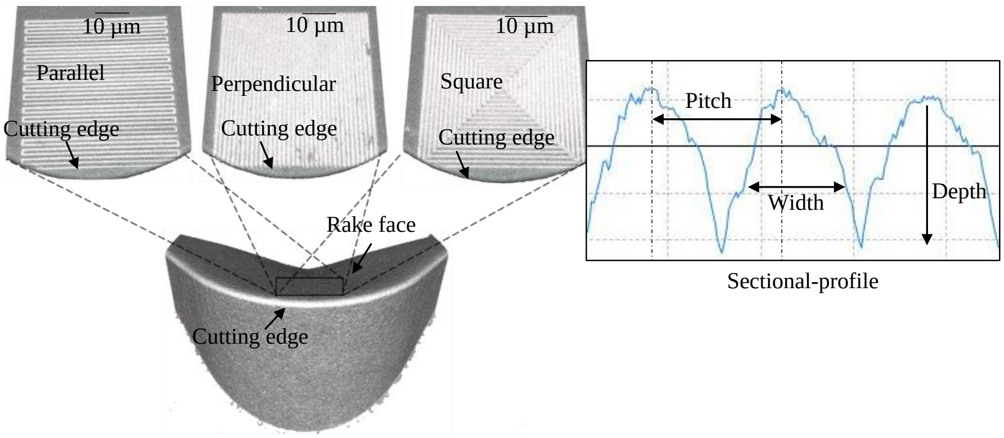

(a)

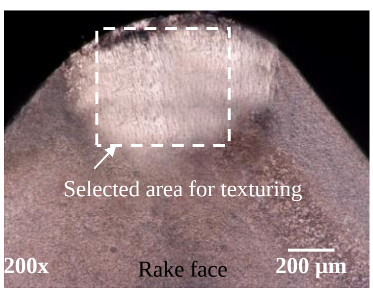

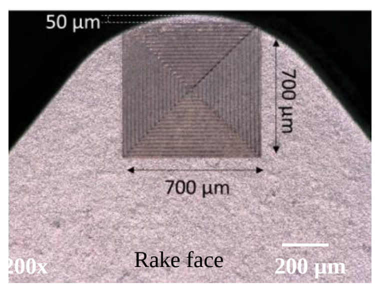

(b) (c)

Figure 6-1(a) Different shapes of textures and an example of sectional-profile of textures, (b) rake face region for mechanical micro-texturing, and (c) fabricated rake face mechanical micro-textured cutting tool

Figure 6-2(a) shows the SEM images of different micro-textured cutting tool shapes and the atomic force microscope (AFM) three-dimensional (3D) topography of the enlarged micro-textured area as well as their depth profile, Figure 6-2 (b, c). Figures 6-2 (a, b) show that micro-textures on the rake face of the different cutting tools were very smooth and there were few

`

residual deposits of melted material. A square microtexture area of 700×700 μm^2 was produced and located 50 μm from the main cutting edge of the cutting tools. In the depth profile shown in Figure 6-2(c), the generated grooves have the following dimensions: width of 5 ± 0.2 μm, 20 ± 0.3 μm pitch and depth of 1.5±1 μm. The variation in depth was greater than that of width and pitch due to the presence of carbide particles in the cutting tool, which alters the laser intensity during the fabrication process. The morphology of the cutting tool surfaces was evaluated by AFM. The cutting tools` arithmetical mean height (Sa) values obtained in the 3D model within a scan size of 21 × 21 μm^2 are presented in Figure 6-3. The Sa of the untextured tool was 55 nm, whereas the respective Sa of the textured tools was 95 nm, 85 nm, and 100 nm for the parallel, perpendicular, and square textures. As shown, the surface roughness of the textured tools was higher than the untextured tool which was due to the micro-scale textures applied to the tool.

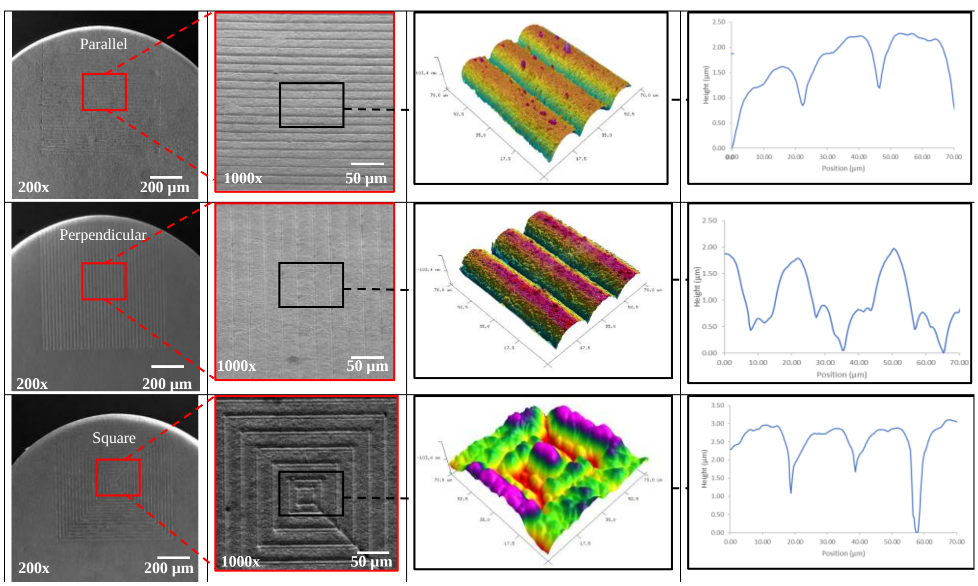

Figure 6-2 (a) SEM images of textured tools before machining, (b) the three-dimensional atomic force microscope image and (c) the corresponding two-dimensional profile of different textured tools with 5 ± 0.2 µm in width, 20 ± 0.3 µm in pitch, and 1.5±1 µm in depth.

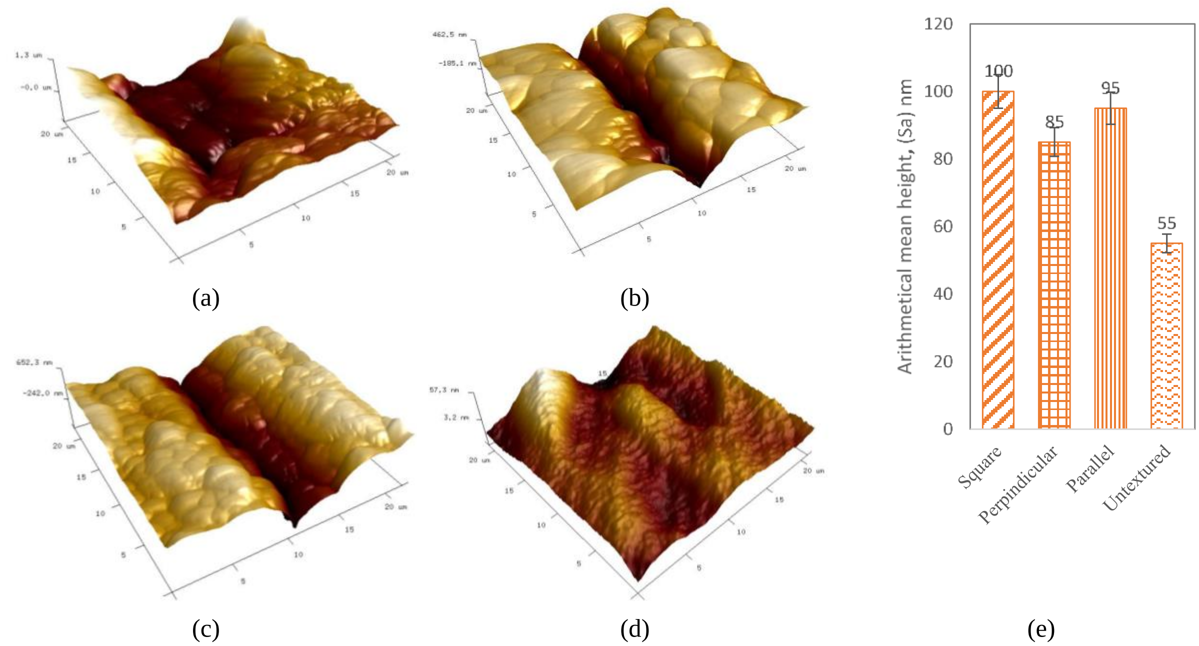

Figure 6-3 Atomic force microscope images of surface topography of (a) square, (b) perpendicular (c) parallel, (d) untextured tools, and (e) the corresponding average surface roughness values

6.2.3 Testing and characterizations

Cutting experiments involving both untextured and textured carbide tools were conducted on a Nakamura-Tome Sc-450a CNC machine, equipped with a piezoelectric dynamometer (Kistler-type 9121) to measure machining forces components. A constant depth of cut (0.5 mm), feed rate (0.1 mm/rev) and four cutting speeds (60, 100, 120, and 150) were performed under wet conditions throughout the machining tests. A 6% semi-synthetic coolant with a flow rate of 2.7 L/min was used during the cutting process. Table 6-4 summarizes the machining parameters, as well as the tool geometry data.

Table 6-4 Tool geometry and cutting parameters used in cutting experiments

Tool geometry	
Rake angle (°)	7
Clearance angle (°)	5
Wedge angle (°)	78
Nose radius (mm)	0.8
Edge radius (μm)	28
Cutting parameters	
Cutting speeds (m/min)	60, 100, 120, 150
Feed rate (mm/rev)	0.1
Depth of cut (mm)	0.5

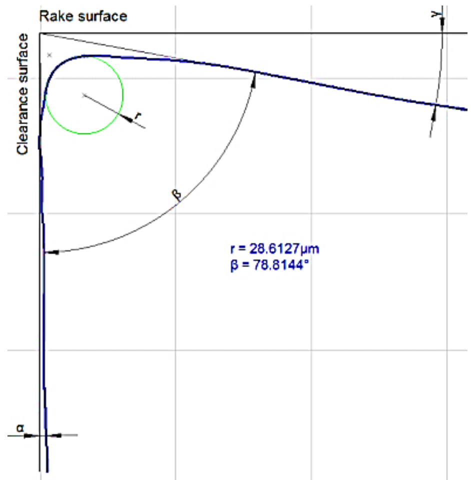

Several levels of characterization were performed in this work. An optical microscope (VHX-2000, Keyence) was used to measure the flank wear width (VB_B) of the cutting tool, with an average flank wear value of 300 μm serving as the end of tool life criterion. The wear modes of the cutting tools were analyzed using a scanning electron microscope (SEM Vega 3-TESCAN), equipped with an energy dispersive spectrometer analysis system (EDS). Five measurements of each sample were performed at a minimum to ensure the reliability of results. White light interferometer (Alicona infinite focus G5 microscope) and atomic force microscope (AFM TOSCATM 400) were used to investigate the topographies of the different textured and untextured tools. Detailed examination of the interface between the BUE and different textures was conducted by a focused ion beam microscope (FIB Zeiss NVision 40). Measurements were

`

taken of the chip up curl radius produced by different textured and untextured tools under different cutting speeds. The chip`s free (top) surface, undersurface (bottom), and cross-section were also analyzed using the backscatter electron microscope (BSE/SEM) to investigate the chip formation and understand the friction behavior between the contact bodies.

To investigate the influence of the tool state on surface integrity, the average surface roughness (Ra) of the machined workpiece surface was measured using an Alicona microscope with a roughness profile module [35]. In addition, electron backscatter diffraction (EBSD) measurements were performed on polished cross-sections of the machined samples. The polishing steps were performed according to [6]. An EBSD study was conducted by an SEM (JEOL 6610LV) microscope, and the EBSD orientation mapping, as well as representative pole figures were respectively analyzed by Tango-Maps and Mambo-Pole figure software. Finally, a nano-indentation tester (Anton Paar NHT3-indentation platform) was used to measure the nanohardness profiles of the workpiece layers were generated by a nano-indentation tester. The measurements were performed at a load of 50 mN and indentation depth of 30 μm.

6.3 Results and discussion

6.3.1 Cutting force components and average friction coefficients

To assess the friction conditions on the tool-chip interface of various untextured and textured tools, the cutting force components were investigated. Figure 6-4(a) shows the average of each tool’s cutting force at different cutting speeds obtained from three cutting experiments. A downward trend in the cutting force can be observed for both the untextured and textured tools with the increase of cutting speed. At greater cutting speeds, the higher temperature can fully soften the workpiece material [11]. In this case, the deterioration of the workpiece's strength is more rapid than that of the tool material, which facilitates material removal. This is why the cutting forces gradually decrease with increasing cutting speed. Additionally, the textured tools have lower cutting forces at all cutting speeds than the untextured tools. The cutting forces in the tools with perpendicular, parallel and square textured areas were approximately 14%, 20%, and 31% less than those of the untextured tools. This reduction in the cutting forces can be due to the decrease of the contact length (Figure 6-4(b)) achieved by the micro-textures created on the sliding surfaces. As can be seen in Figure 6-4(b), the tool–chip contact length was decreased by 30.2%, 50.5%, 65.1% in the perpendicular, parallel and square textured tools compared to the untextured one.

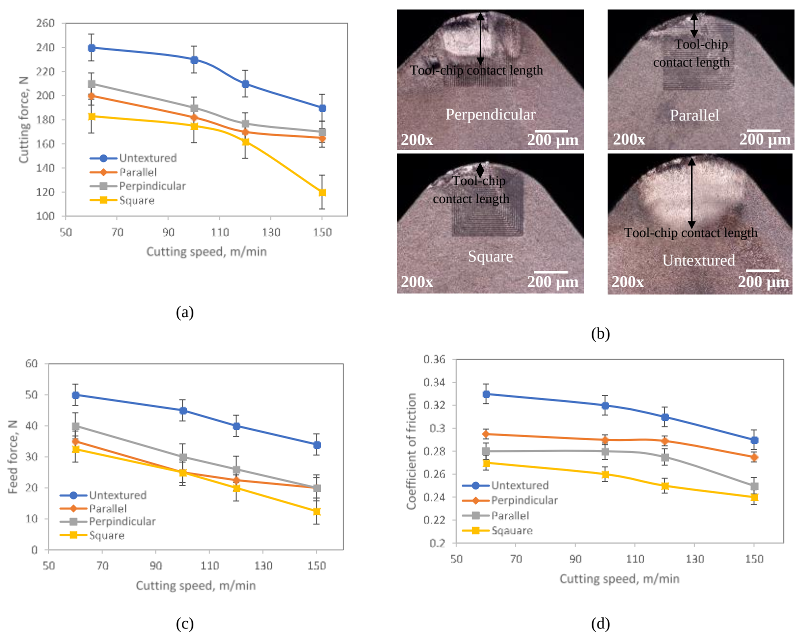

Figure 6-4(a) cutting force variation with cutting speeds, (b) tool-chip contact length, (c) feed force variation with cutting speeds, and (d) coefficient of friction with cutting speeds for different textured and untextured tools

`

It can be observed in Figure 6-4(c) that the average feed force of all tools decreased with the growth in cutting velocity, which was a similar trend for the cutting force. The feed force of the untextured tool was greater than that of the textured tools. The feed force of the square textured tool had the lowest value among all the cutting tools at all cutting speeds. The feed force of the square textured tool showed the highest (53-100%) reduction in feed force compared to the untextured tools.

The average coefficient of friction (COF) at the tool-chip interface was derived from the cutting and feed force values [15], according to Equation 1.

$$\mu = \frac{F_f + F_c tan\alpha}{F_c - F_f tan\alpha} \tag{1}$$

Where α, F_c, and F_f are the rake face, cutting force, and feed force, respectively.

Figure 6-4(d) presents the average COF values obtained with untextured and textured tools at different cutting speeds. It should be noted that the average COF of the cutting tools showed a tendency of decreasing with the growth of cutting speed. In addition, the untextured tools always had the highest average friction coefficient followed by the tools with the perpendicular, parallel and square textures when used at the same cutting speeds. Compared to the untextured tools, the average COF of the square textured tool was decreased by 20-24%. This confirms that the square textured tool was able to reduce the contact length and improve the friction behaviors, which may lead to lower tool wear and enhanced chip formation.

To confirm the improved cutting efficiency of the textured tools, the tool wear and chip morphology will be discussed in detail in the following section.

`

6.3.2 Wear examination of textured tools

6.3.2.1 Tool wear morphology

Figure 6-5(a) presents the wear morphology of the untextured tool's rake face after a cutting length of 1000 m at a cutting speed of 60 m/min. Considerable wear was present on the untextured tool rake face. Due to the high pressure and temperature in the cutting zone, the chips can adhere to the cutting tool and then detach with the cutting tool. The continuity of this process will increase tool wear, thereby causing the tool to fail. In Figure 6-5a (A), a severe area of chipping emerges on the rake face due to the high intensity of workpiece adhesion on the cutting tool, Figure 6-5a (B). The EDS element analysis of the marked area C on the tool rake face (Figure 6-5a (C)), reveals the high content of Fe and Cr, indicating the severe adhesion of workpiece material to the tool.

Figure 6-5b shows the rake face morphology of the perpendicular textured tool at the same stage of machining. In Figure 6-5b (A), a smaller chipping area was observed on the main cutting edge compared to the untextured tool. A consistent adhesion layer was also present in the worn area of the textured tool rake face (Figure 6-5b (A)). The EDS composition analysis (Figure 6-5b (C)) of the highlighted region C showed that the percentage of Fe was lower than that on the untextured tool. Thus, it can be concluded that the perpendicular textured tool has better machining performance than the untextured one.

`

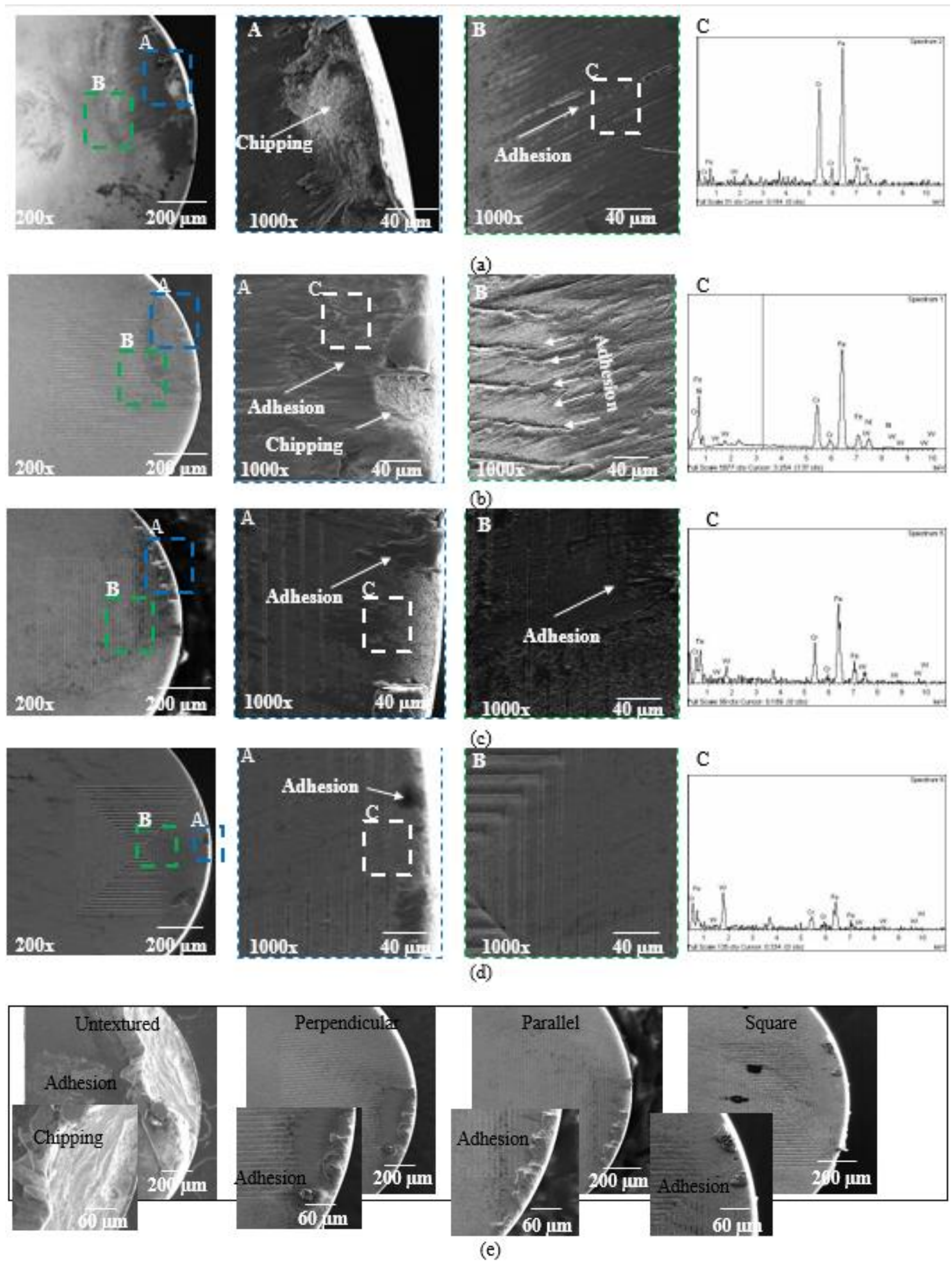

Figure 6-5 SEM images of (a) untextured, (b) perpendicular, (c) parallel, (d) and square textured tools after cutting length of 1000 m at cutting speed of 60 m/min and (e) SEM images of untextured and textured tools at cutting speed of 150 m/min

`

A similar observation was also conducted for the parallel textured tool, as shown in Figure 6-5(c). The intensity of wear in the parallel textured tool (Figure 6-5(c)) was lower than in the perpendicular textured tool (Figure 6-5(b)), showing that a parallel textured tool can provide a better anti-adhesion property. Figure 6-5c (A, B) presents the wear morphology of the tool rake face. No chipping was noticeable on the main cutting edge. An adhesion area was still present near the cutting edge, which was lower than in the perpendicular textured tool (Figure 6-5(b)). In addition, the chemical compositions of the region C shown in (Figure 6-5c (C) indicates that both the components of the workpiece material and the cutting tool material were present in the worn area. To some extent, this indicates that the direction of the applied textures affects the intensity of adhesion wear.

Figure 6-5(d) depicts the morphology of the square textured tool rake face. Figure 6-5d (A, B) shows that the wear rate of the tool was quite small, the surface of the tool rake face was smoother than that of the other tools. The EDS chemical composition in Figure 6-5d (C) indicates high amounts of W and low amounts of Fe present on the highlighted area C, which shows lower adhesion of the material to the tool rake face. Consequently, it can be concluded that the square textured tool featured lower adhesion compared to the other textured tools.

To understand the effect of cutting speed on adhesion in different textured and untextured tools, the rake face of the cutting tools was investigated at a higher cutting speed (150 m/min), Figure 6-5(e). Severe chipping occurred only with the untextured tool, confirming the better tool performance of the textured tools. Minor adhesion was present on the surfaces of all cutting tools compared to that occurring at low cutting speeds. This can be attributed to the lower tool-chip

`

contact length at the higher cutting speed, which reduces the adhesion of the material to the cutting tool [36]. However, the adhesion of the workpiece material on the square textured tools was significantly less than that on the untextured tool.

The superior machining performance of the square textured tool may be due to the formation of a stable adhesion layer on the tool-chip interface throughout the cutting process, which could provide better wear resistance compared to an untextured tool [27]. To confirm this hypothesis, the wear behavior and BUE stability during machining with square textured and untextured tools was investigated and summarized in detail below.

6.3.2.2 Flank wear resistance and mechanism of antiadhesion behavior

Figure 6-6 shows the average flank wear intensity vs. cutting length for the square textured and untextured tools at two different cutting speeds. At both speeds, the average flank wear present in the square textured tool was less than that of the untextured tool and improved by 41-78%. Severe chipping was only observed on the untextured tool at both cutting speeds. No chipping was noticeable on the square textured tools.

`

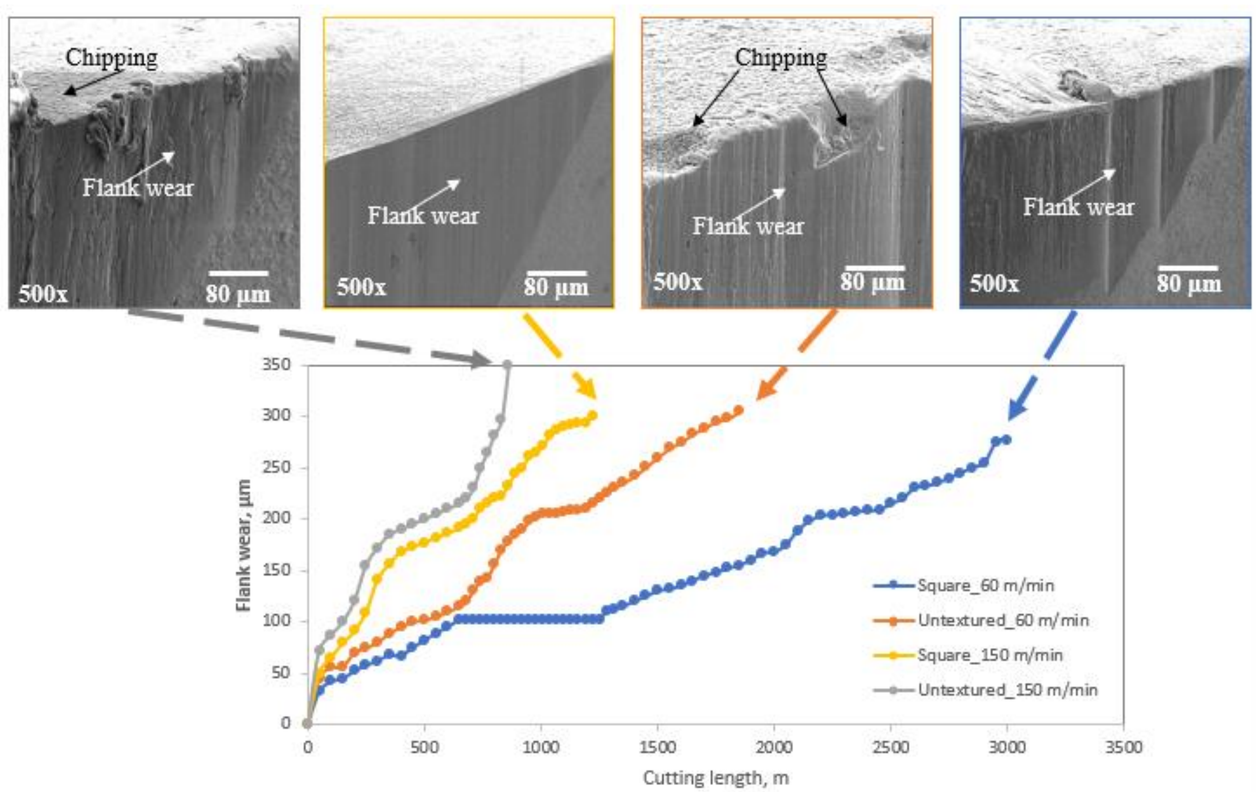

Figure 6-6 Relation between flank wear and cutting length for square textured and untextured tools under cutting speeds of 60 m/min and 150 m/min, associated with SEM images of the cutting tools at the end of tool life

One possible reason for this tool wear improvement in the square textured tool was the enhanced stability of the BUE formation during the cutting test, Figure 6-7. Figure 6-7(a) presents a three dimensional (3D) progressive study of the square textured and untextured tools at low (60 m/min) and high cutting speeds (150 m/min). It was shown from the 3D images that the BUE selectively forms all over the tool with varying levels of coverage. It is worth noting that the BUE formation diminishes with the increase of cutting speed.

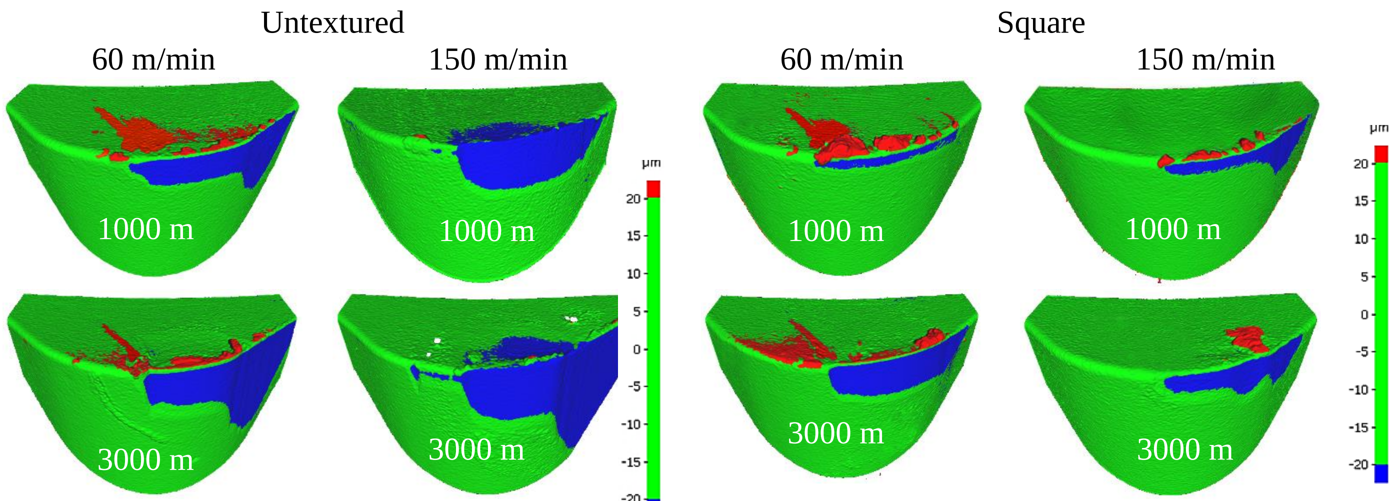

(a)

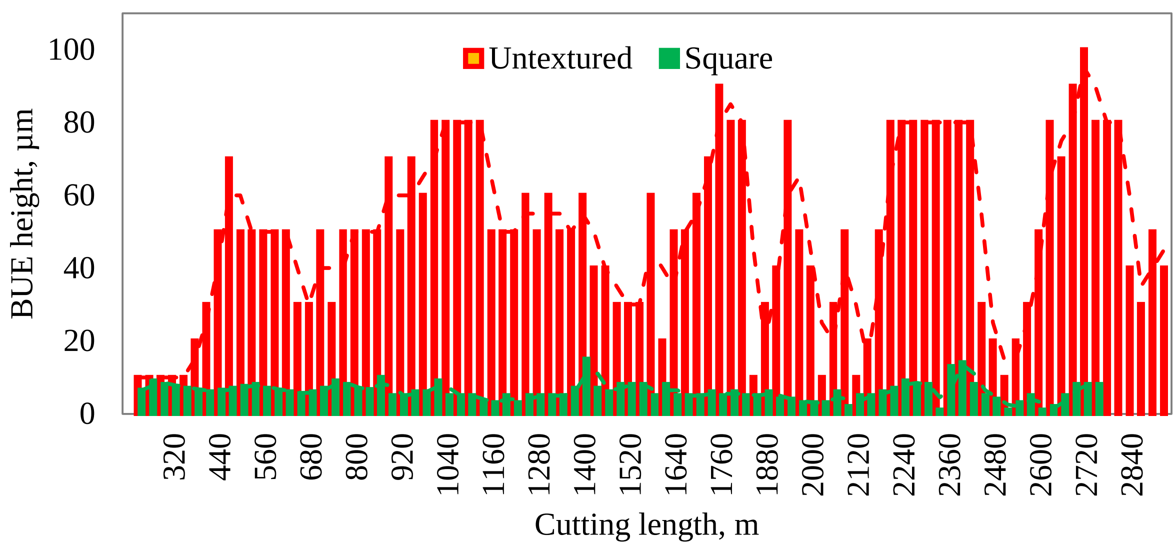

(b)

Figure 6-7 (a) 3D progressive study of untextured and square textured tool for cutting speeds of 60 m/min and 150 m/min, and (b) BUE height variation with cutting length at cutting speed of 60 m/min for untextured and square textured cutting tools

`

As an example, Figure 6-7(b) shows the BUE height variation for square textured and untextured cutting tools obtained at a speed of 60 m/min and different cutting lengths. The variation of BUE height in the square textured tool was minor (Δh=11 μm) compared to that in the untextured cutting tool (Δh=90 μm). This confirmed that more stable BUE formed on the square textured tool. To assess the mechanism that accounts for the superior antiadhesion behavior of the square textured tool, the interface between the adhered material and both untextured and textured areas on the cutting tool were examined using a focused ion beam microscope (FIB), Figure 6-8(a). The same analysis was conducted on the perpendicular textured tool which was the worst-performing tool.

Figure 6-8a (A) presents a FIB cross-section of the square textured tool. The texture to which the workpiece material had adhered was selected (Figure 6-8a (B)) to examine the interaction between the BUE and the cutting tool. In Figure 6-8a (C), small cracks can be observed beneath the BUE and within the cutting tool (see black arrows). The adhered workpiece material in the texture was bonded strongly to the cutting tool, as shown in Figure 6-8a (D). Due to the chip flow (see white arrows), the BUE was preferentially interlocked on the undersurface of the cemented carbide, where the chip flow was restrained. Conversely, the adhered workpiece material in the untextured area had a weaker bond with the cemented carbide, as shown in Figure 6-8a (E, F), demonstrating the ability of the texture to interlock with the BUE during chip flow. Hence, Figure 6-8(a) indicates that mechanical interlocking played the most important role in reducing the adhesion of BUE on the square textured cutting tool.

`

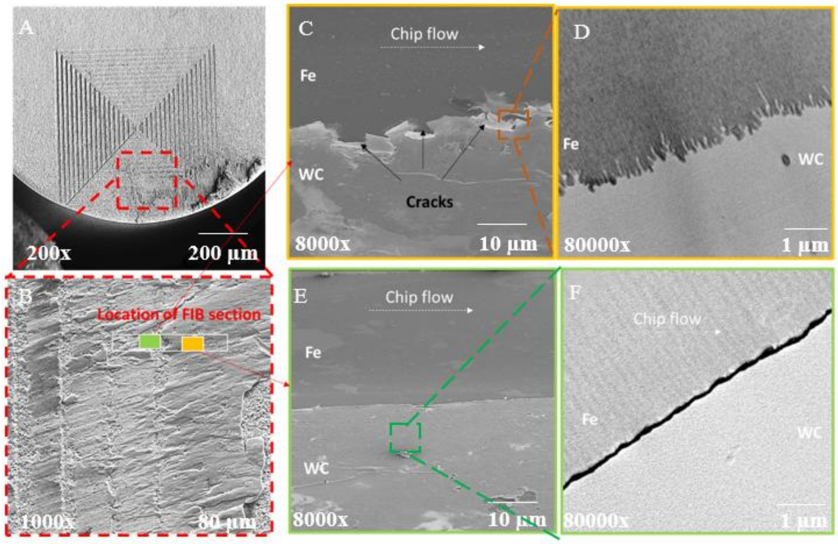

(a)

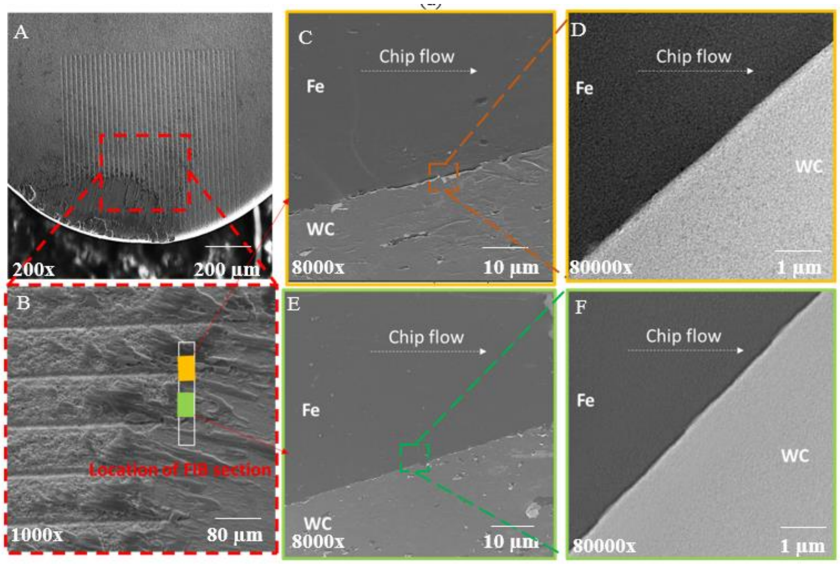

(b)

Figure 6-8 Illustration of FIB-examinations of (a) square texture and (b) plain on the rake face with adhering workpiece material. (A) an overview of the rake face, (B) the location for FIB cross section, (C) surface bottom, and (D) region of worn surface

`

On the other hand, the perpendicular textures led to a destabilization of BUE on the rake face. In Figure 6-8b (A) the perpendicular texture produced by FIB is described and in Figure 6-8b (B) the texture with adhesion was selected for investigation. As shown in Figure 6-8b (C, D), the BUE was not interlocked with the perpendicular grooves on the textured surface of the tool (no cracks can be observed), which confirmed that the perpendicular textures were not able to bond with the BUE, contributing to its destabilization. Also, as shown in Figure 6-8a (E, F), the adhered workpiece material in the untextured area formed a weaker bond with the cemented carbide.

6.3.2.3 Effect of texture design on material adhesion and chip flow

The angle of chip flow regarding the orientation of the textured layer was derived from the worn cutting tools and described in Figure 6-9. The respective angle between the chip flow and texture orientation for perpendicular and parallel textures are 30° and 60°. In square textures, the angle can be 30° or 60° depending on the position of the chip flow, as shown in Figure 6-9(c). Micro textures play a significant role in the chip formation. They act as micro cutters that reduce the contact between the chip-tool interface. This will result in highly localized pressure which can increase the resistance force to the chip flow [23]. The resistance force (F_{per}) is given by Equation 2.

$$F_{per} = F sin\theta \tag{2}$$

Where F is the force along the chip direction and θ is the angle between the texture direction and the chip flow. It was noticed in this study that the orientation of the texture affects F_{per}. The maximum F_{per} was obtained for the square textured tool (as shown in Figure 6-9), which means that F_{per} inhibits chip flow, reducing the cutting force on the tool. Thus, the larger F_{per} improved the efficient function provided by the texture, thereby reducing the cutting force (Figure 6-4(a)) coefficient of friction (Figure 6-4(d)) and adhesion (Figures 6-7 and 6-8) on the square textured tool.

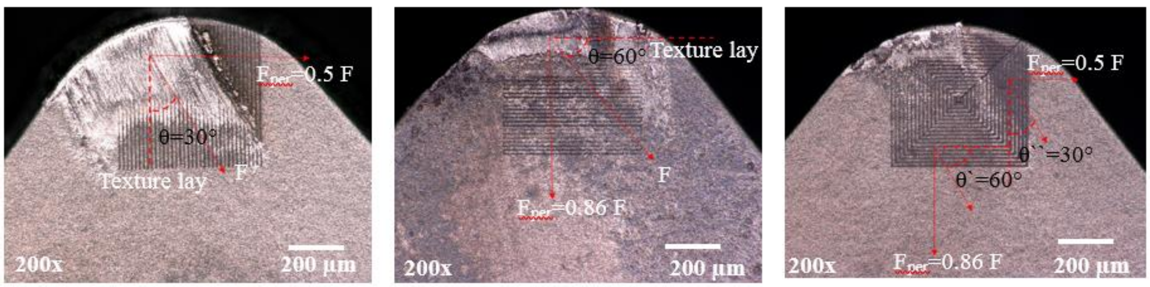

(a) (b) (c)

Figure 6-9 Angle between chip flow and (a) perpendicular, (b) parallel, and (c) square textured tools

6.3.3 Chip formation

6.3.3.1 Chip up curl radius

The morphology and formation of the chips produced by the surface textured tools during the turning experiments were investigated in depth. Table 6-5 shows the different chips obtained at cutting speeds of 60 m/min and 150 m/min by various textured and untextured tools. The friction at the tool-chip interface has a significant effect on producing different types of chips. Greater contact at the tool-chip interface produced a larger chip up curl radius. When the resultant force at the shear plane was equal to the resultant force at the ~~rake tool~~ rake face, it generated a bending moment that caused the chip to curl. In general, a reduction in friction will enhance this moment and the curvature of the chip [15].

Table 6-5 Chip up curl radius under different cutting conditions

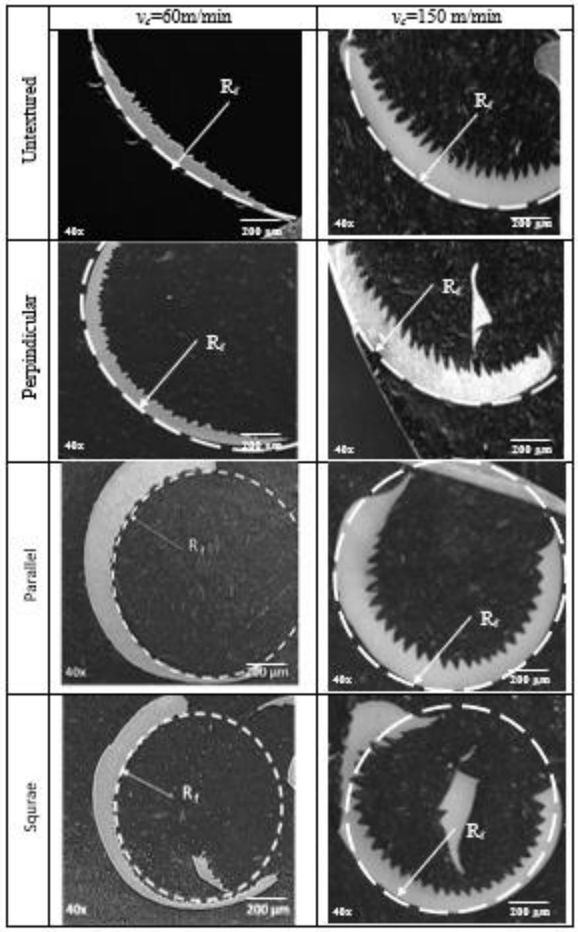

As shown in Table 6-5, the untextured tool produced continuous chips with a larger chip up curl radius, especially at a cutting speed of 60 m/min since the friction at the tool-chip interface was greater than that of the textured tools. However, the chip up curl radius was observed to be lower in the textured tool due to the smaller tool-chip contact length and lower friction. This result agreed with the calculated mean coefficient of friction in Figure 6-4(d). Also, the texture edge of the textured tools acted as a chip breaker, increasing the bending moment on the chip, consequently reducing the chip up curl radius.

`

Meanwhile, when the cutting speed increased up to 150 m/min (Table 6-5), the diameter of the snarled chips was slightly smaller for both untextured and textured tools. This was due to the reduced chip thickness at the higher cutting speeds, which facilitated chip deformation and increased the bending force [37]. Also, it is possible to see from Table 6-5 that there is a clear difference in the chip up curl radius among the different textured tools. The chips generated by the square textured tools had a smaller up curl radius, due to the significant reduction of contact length (Figure 6-4(b)).

6.3.3.2 Chip morphology

Figure 6-10 (a-c) shows the chip-free surfaces, chip undersurfaces and chip cross-sections produced by the untextured and textured tools at a lower cutting speed of 60 m/min, respectively. In general, the chips present in Figure 6-10(a) are continuous. Figure 6-10 a (B-D) shows that the chip-free surface generated by the textured tools has a lamellar structure compared with Fig. 6-10a (A) which showed a lower amount of lamellar structures on the chip-free surface of the untextured tool. Due to the thermo-plastic flow instability, some micro-defects could appear in the shear plane, causing layer by layer slipping and consequently the formation of a lamellar structure [14]. The minimum amount of lamellar structures obtained by the untextured tool was attributed to the high friction at the tool-chip interface. This caused a rise in the cutting temperature, which increased the ductility of the workpiece and restrained the shear instability [38].

`

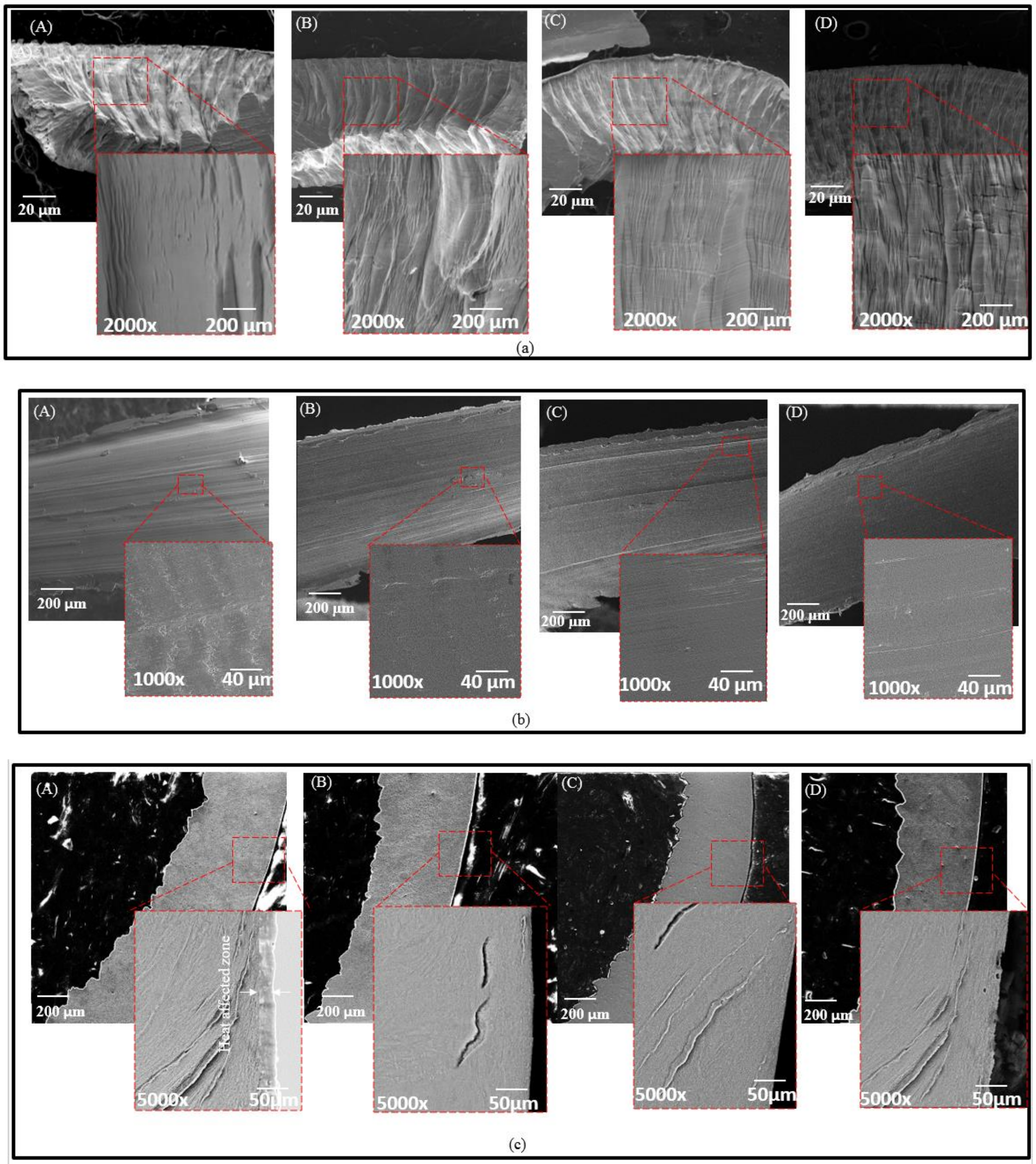

Figure 6-10 Back scatter electron (BSE) images of (a) chip free surfaces, (b) chip undersurfaces and (c) chip cross-sections obtained with (A) untextured, (B) perpendicular, (c) parallel, and (D) square textured tools

Compared to the undersurface of the chip produced by the textured tool (Figure 6-10b (C-D)), damage caused by abrasion can be observed on the underside of the chip obtained by the

`

untextured tool observed in Figure 6-10b (A), due to high tool-chip friction [28]. In addition, the chip cross-sections showed the secondary shear deformation area with a continuous heat-affected zone (HAZ) in the chip generated by the untextured tool (Figure 6-10c (A)). In contrast, no HAZ can be observed on the chip produced by the textured tool (Figure 6-10c (B-D)). As the chips are formed by the untextured tool, the high tool-chip contact length intensified the chip material plastic deformation [38].

Figure 6-11 (a, b) shows the change of the chip-free surface generated by the square textured (Figure 6-11(a)) and untextured tool (Figure 6-11(b)) at three different cutting speeds (60, 100, and 150 m/min). The figures reveal identical lamellar structures created on the segmented chips as those on the continuous chip free-surface (Figure 6-10(a)). It is also noted that the sliding surface machined by the textured and untextured tools becomes smoother as the cutting speed increases. This is due to the increase in the temperature and shear strain rate with the growth of cutting speed, limiting the time period in which the layer by layer slipping could occur [15]. In addition, the thickness of the lamellar structures produced by the untextured tool (Figure 6-11(b)) appeared to be smaller than that produced by the square textured tool (Figure 6-11(a)) at the same cutting speed. This occurred due to the high friction generated by the untextured tool, as previously discussed in section 3.2.1 and Figure 6-4(b), leading to an increase in cutting temperatures and consequently reduced lamellar thickness [15]. To understand the influence of textured tools on segmented chip formation at different cutting speeds, the chip segmentation frequency and percentage of segmentation were studied in Figure 6-11 (c, d).

`

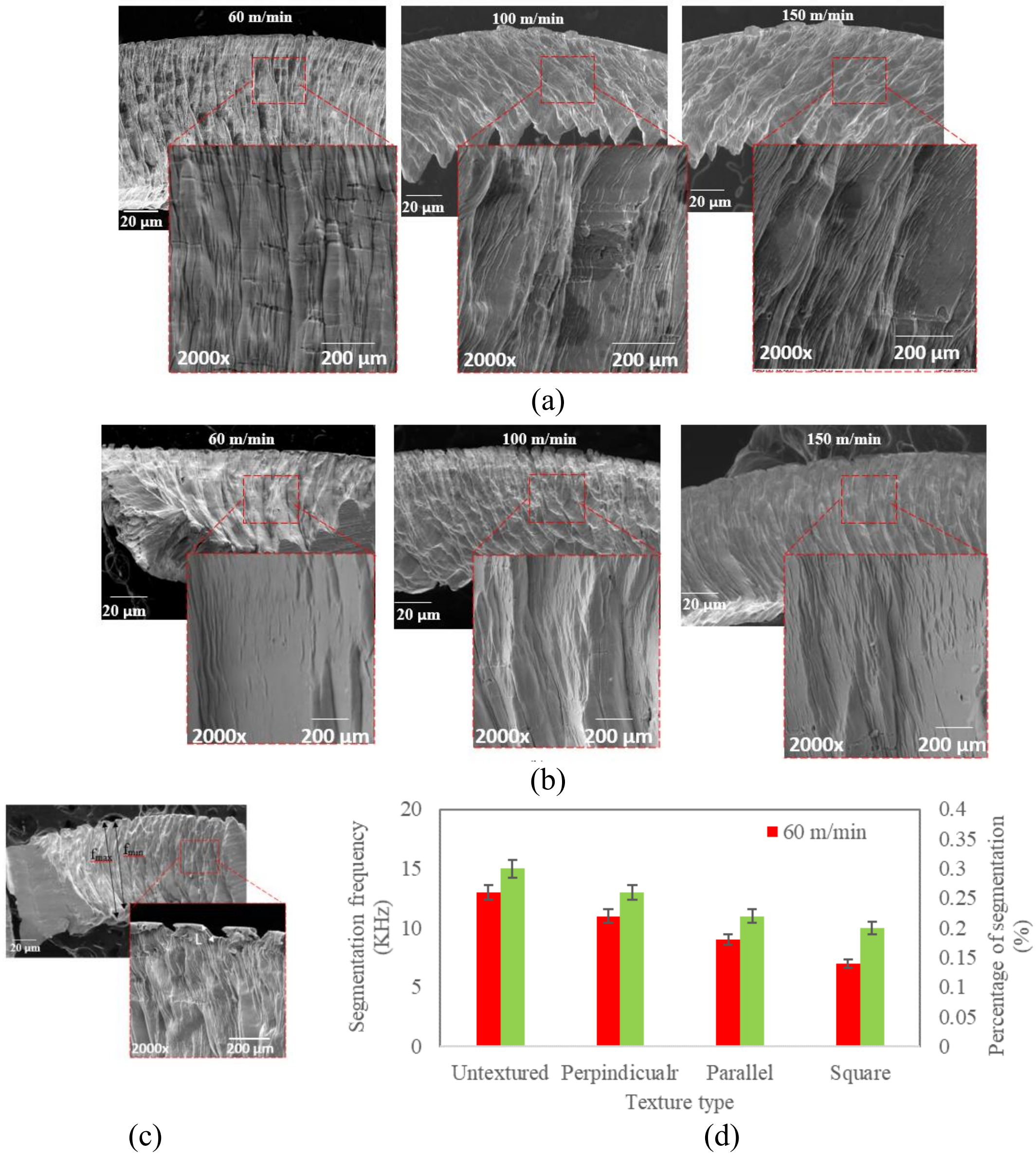

Figure 6-11 (a, b) BSE images of the chip free surface obtained with the (a) square textured and (b) untextured tools, (c) an example of the geometrical feature of segmented chips, and (d) variation of segmentation frequency and percentage of segmentation for different textured and untextured tools at various cutting speed

`

Chips segmentation frequency (f_c) and percentage of segmentation (G_s) can be derived from Equations 3 and 4 [39].

$$f_c = \frac{v}{L} \tag{3}$$

$$G_s = \frac{f_{max} - f_{min}}{f_{max}} \tag{4}$$

Where v is the cutting speed, L is the undeformed chip length, f_{max} is the maximum chip thickness and f_{min} is the minimum chip thickness. An example of a geometrical feature of the segmented chips is described in Figure 6-11(c) and plotted in Figure 6-11(d). In Figure 6-11(d), the chip segmentation frequency and degree of segmentation become lower in the textured tools compared to the untextured tool. This describes the reduction in cutting forces due to lower vibrations generated by the lower frequency associated with chip segmentation [39].

6.3.4 Influence of cutting tool state on Surface integrity

6.3.4.1 Topography and surface roughness of the machined surface

To evaluate the surface quality produced by the different cutting tools, the workpiece surface topographies machined with untextured and textured tools were studied. Detailed surface topography and average surface roughness are shown in Figure 6-12. A small area of 100×100 μm^2 was selected in the middle of the machined surface to analyze the topography of the surface. In Figure 6-12(a), the average surface roughness values tend to decrease for the textured tools, especially for the square texturing. As can be seen, the square textured tool improves the surface finish by 54-68% when compared to the untextured tool.

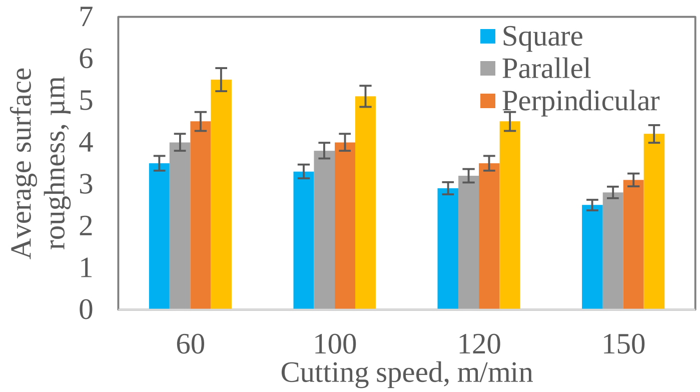

(a)

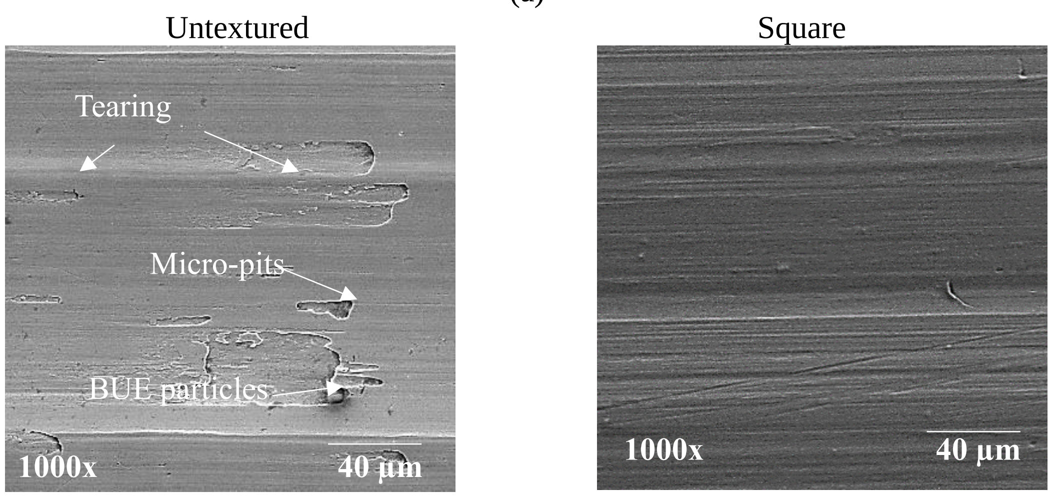

(b)

Figure 6-12 (a) Average surface roughness obtained at different cutting speeds for different textured and untextured tools and (b) SEM images of the machined surface obtained by square textured and untextured tool

These results are consistent with the BUE formation observations in Figure 6-6(b), which showed a stable BUE in the square textured inserts and an unstable one for the untextured tools. The instability of the untextured tool's BUE caused the fractured particles to be carried away from the machined surface, reducing the quality of the surface finish. Conversely, the stable BUE of the square texture tool enhanced the machined surface finish. It was also noticed that as cutting speed

`

increased, the value of surface roughness decreased for all untextured and textured tools. At a low cutting speed, the sliding velocity of the chips decreased which leads to creating a large unstable BUE, which produced a rough surface finish [40]. At a higher cutting speed, the BUE was diminished, chip fracture decreased, the surface finish improved, and the machining time was reduced.

Figure 6-12(b) shows SEM images of the machined workpiece collected at the beginning of the turning process for square textured and untextured tools. It can be observed that the machined surface produced by the untextured tool feature cracks and distortions. As a result of the unstable BUE formation (Figure 6-7(b)), the BUE particles are adhered to the machined surface, causing distortions on the surface [41]. However, the machined surface with the square textured tool also does not show even minimal surface cracking. Only very fine feed marks are present on the surface due to the small and stable BUE that formed on the square texture tool (Figure 6-7(b)).

6.3.4.2 Microstructure and mechanical state of the machined subsurface

Figure 6-13 shows the optical images of the machined workpiece subsurface obtained with the untextured tools (a, b) and square textured (c, d) at cutting speeds of 60 m/min (a, c) and 150 m/min (b, d). A clear heat-affected zone (HAZ) of varying thicknesses can be observed when using the untextured tools ∼40 μm (untextured at 60 m/min (Figure 6-13(a)) and ∼10 μm (untextured at 150 m/min (Figure 6-13(b)). The HAZ were generally minimal when using the square textured tools at both 60 m/min and 150 m/min (Figure 6-13 (c, d)). This was attributed to the lower and stable BUE formation that generates less tensile residual stress and fewer changes in the surface microstructure as compared to the untextured tool [42].

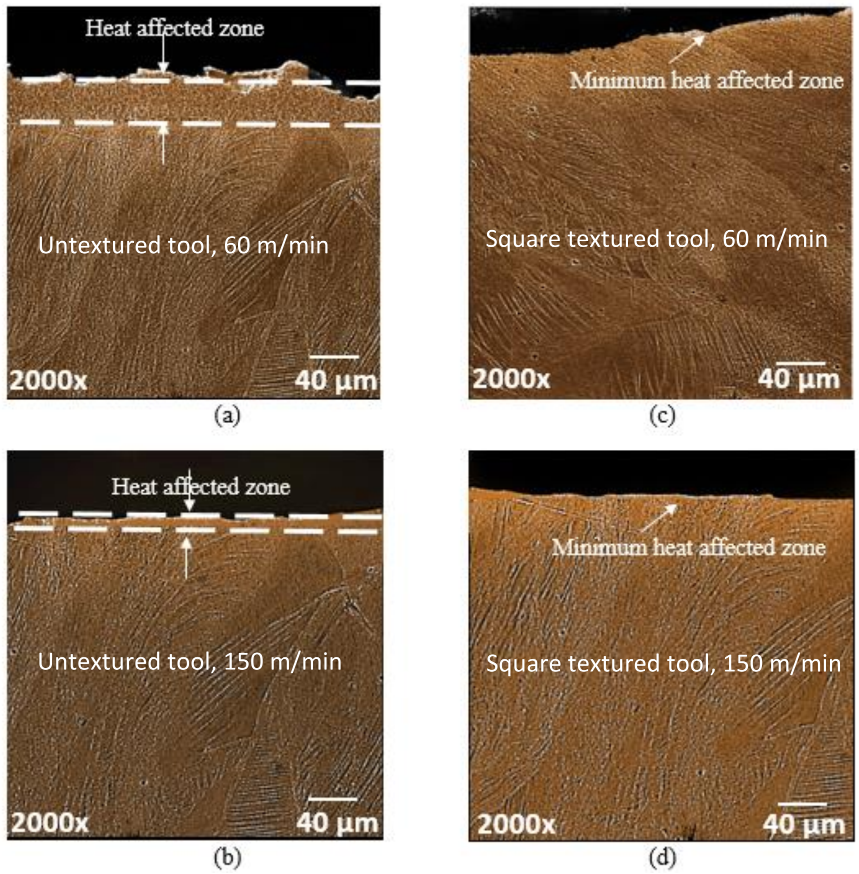

Figure 6-13 Optical images of machined workpiece subsurface obtained with (a, b) untextured and (c, d) square textured tools at cutting speed of (a, c) 60 m/min and (b, d) 150 m/min

When BUE formation is large and more unstable, the temperature at the machined surface is higher during machining. Due to the high temperature, thermal expansion was then greater at the machined surface, thus the surface layers became compressed. The surface layer shrank in size as it cooled, which then generated tensile residual stresses in the surface layers [22], thereby increasing the HAZ formation (Figure 6-13 (a, b)). However, the BUE formation reduced with an increase in cutting speed, (Figure 6-7(a)) generating less tensile stress in the workpiece surface.

`

Since the thickness of the white layer depended on the tensile residual stress, a smaller white layer can be seen in the workpiece which was produced by the untextured tool (Figure 6-13(b)) and the square textured tool (Figure 6-13(d)) at a high cutting speed of 150 m/min [43].

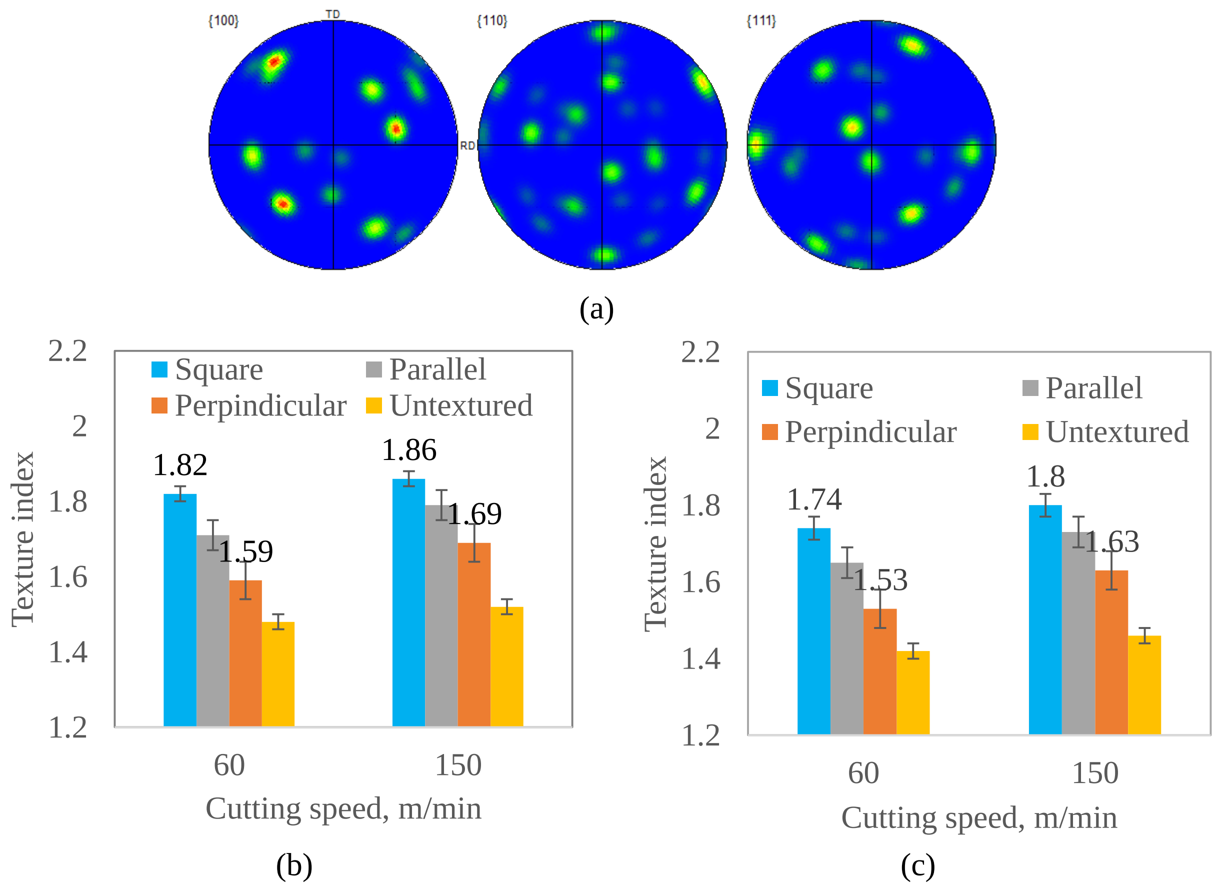

Figure 6-14 (a) Typical pole figures obtained from EBSD analysis of the subsurface layers (square textured tool, new tool, vc = 60 m/min) and (b, c) texture index of the machined workpiece surfaces computed from pole figure analysis obtained with (b) new and (c) worn tools

Figure 6-14(a) shows pole figures generated from EBSD analysis of the machined workpiece subsurface. The texture index derived from the orientation distribution function (ODF) of (111),

`

(001), (011) pole figures are shown in Figure 6-14(b, c). Results show that cutting speed only has a minor effect on this parameter when comparing workpiece surfaces produced by different textured and untextured tools, see Figure 6-14(b). However, a distinct reduction in the intensity of the deformation texture was consistently observed in the machined surfaces produced by the worn cutting tools, as shown in Figure 6-14(c). This was attributed to the higher recrystallization and smaller grains of the HAZ obtained when using the worn tools [43].

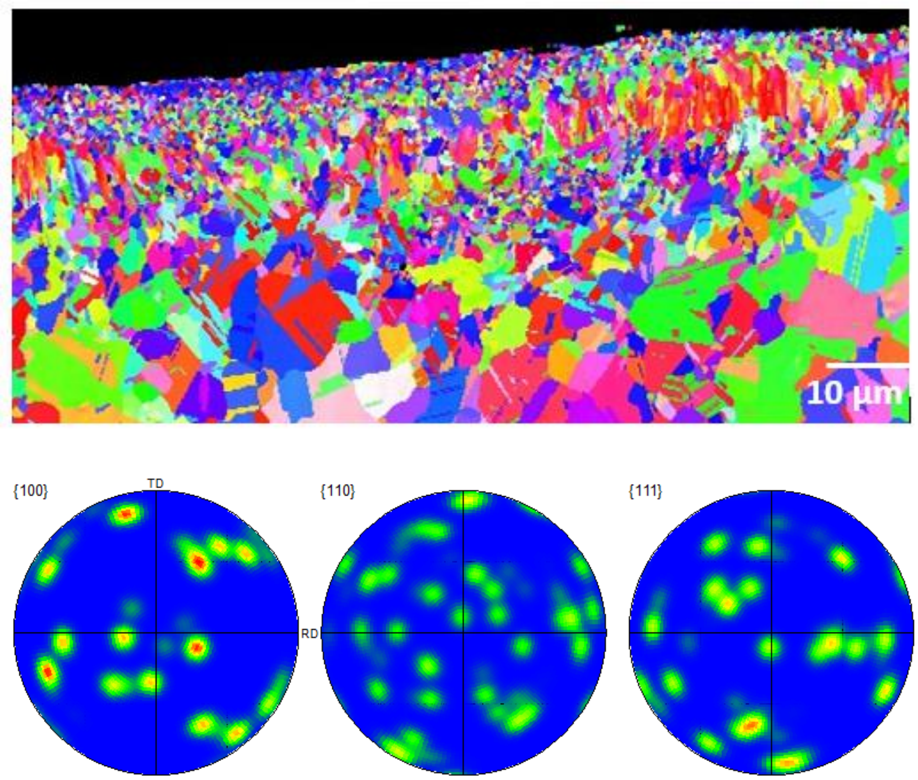

Figure 6-15 Detailed EBSD orientation map and pole figure maps of the heat affected zone of the machined workpiece subsurface obtained with an untextured tool at 60 m/min

`

Further EBSD analysis of the HAZ on the workpiece produced with the untextured tool at a cutting speed of 60 m/min was made possible because of its larger thickness (~40 μm) compared to the other tools. The analyses are displayed in Figure 6-15 where the orientation map and pole figures of the HAZ are shown. In this figure, very fine grains are observed in the HAZ with a grain size of 90 nm. The pole figures indicate the presence of a retained shear-induced deformation texture, typical of face-centered cubic material. This agrees with pole figures obtained in AISI 304 austenitic stainless steel [44].

6.3.4.3 Nano-hardness distribution of the machined subsurface

To conclude the investigations outlined in this study, the nano-hardness distribution of the machined workpiece subsurface was evaluated. Figure 6-16 presents the nano-hardness distribution of the machined surface obtained with textured and untextured tools at two cutting speeds of varying magnitude. The bulk hardness of all workpieces was above 5 GPa. Also, the nano-hardness of the machined surface was found to be higher when machining at the higher cutting speed of 150 m/min. A higher cutting speed was found to generate intensive plastic deformation and consequently increased the nanoscale surface hardness [45].

Furthermore, the results of the textured tools at both cutting speeds show little variation in these distributions, especially when using the square textured tool. However, a distinct zone of increased nano-hardness can be observed in the machined surface obtained with the untextured tool. This was somewhat expected when correlating the nano-hardness distribution under the machined surface with the depths of the HAZ in Figure 6-13 where the thickness of HAZ was larger compared to those obtained when using the square textured tools.

`

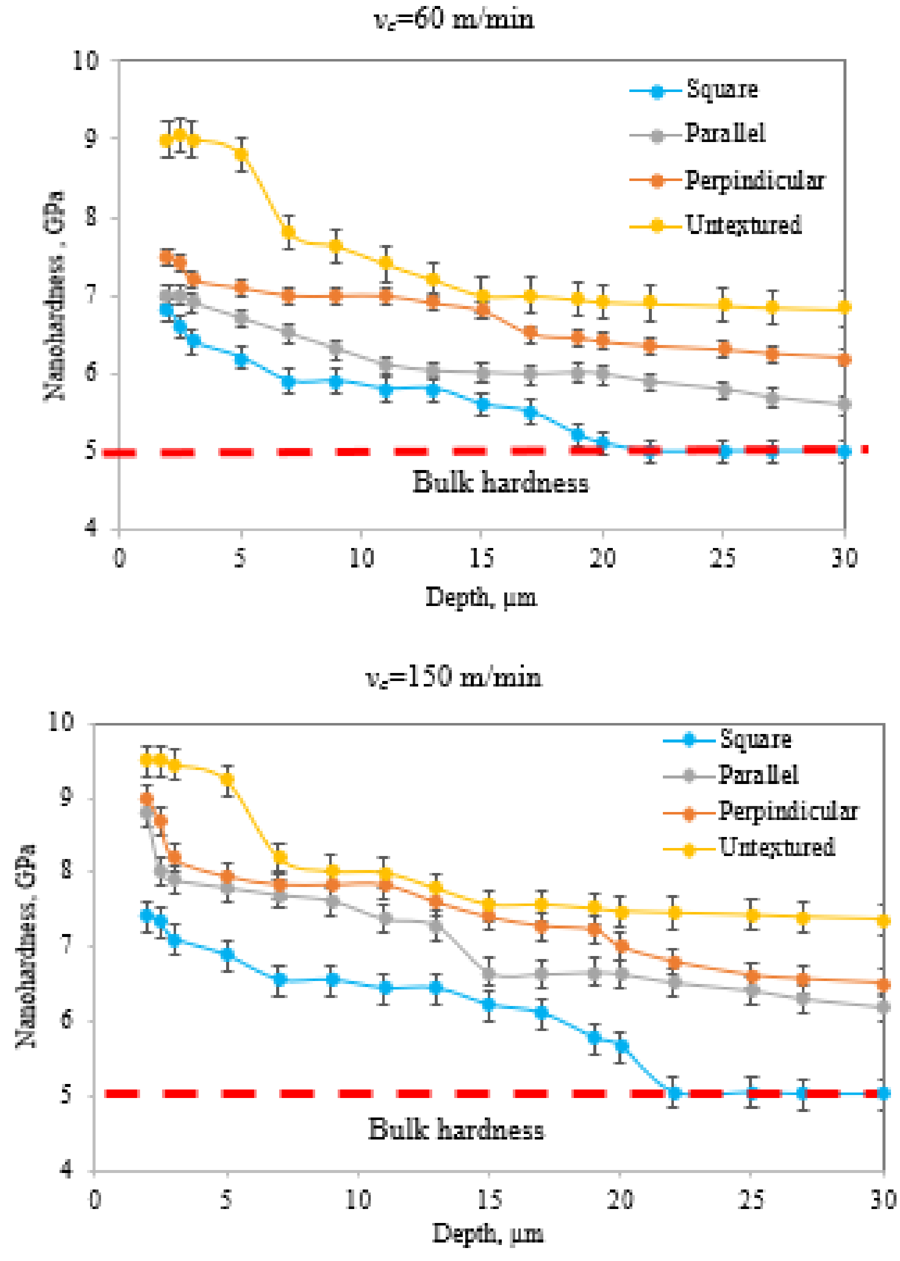

Figure 6-16 Nanohardness distribution of the machined subsurface obtained with different textured and untextured tools at cutting speeds of 60 m/min and 150 m/min

`

Conclusions

An in-depth investigation of the tool-chip interface performance was carried out in the current paper to understand the effect of three different texture shapes (square, parallel, and perpendicular) on the machining performance and process efficiency during the machining of AISI 304 austenitic stainless steel. The key findings of this study are as follows:

1. Surface textured tools helped to reduce the cutting forces, thrust forces and coefficient of friction. The maximum reductions of 58%, 100%, and 24% in the respective cutting force, thrust force, and coefficient of friction were obtained with the square textured tool.
2. Square texturing was capable of stabilizing the BUE formation during the cutting process. FIB examinations of the square textured rake face showed a superior mechanical interlock between the BUE and the textured surface tool. This helped enhance the stability of BUE formation, consequently reducing the machined surface roughness while providing better wear protection as compared to other tools. Square texturing reduced flank wear by 41-78% and improved surface finish by 54-68% in comparison to the untextured tool.
3. The texture orientation had a significant effect on chip flow and adhesion. The greatest improvement to chip flow (F_{per}) was obtained with square texturing, reducing the cutting forces and controlling the adhesion properties.

`

4. The chip undersurface morphology obtained by the square textured tool was found to be superior to that of the untextured tool, indicating a smaller tool-chip contact length and consequently lower friction at the tool-chip interface.
5. The thickness and nano-hardness values of the heat-affected zone were lower in the workpiece machined by the square textured tools. This is due to the formation of a smaller and more stable BUE, which generates lower tensile residual stresses and workpiece surface microstructure changes as compared to the use of the untextured tool.

Future work will focus on performing a sliding friction test to evaluate the extent of friction reduction obtained using different microtextured surfaces. Accordingly, the best texture design on the cutting tool will be selected upon which to deposit a tungsten disulfide (WS_2) coating. Machining experiments will then be carried out on the WS_2 coated textured, uncoated textured and untextured cutting tools to compare their performance.

Acknowledgment

This research was supported by Natural Sciences and Engineering Research Council of Canada (NSERC) under the CANRIMT Strategic Research Network Grant NETGP 479639-15.

References

1. S. Bruschi, L. Pezzato, A. Ghiotti, M. Dabalà, R. Bertolini, Effectiveness of using

`

low-temperature coolants in machining to enhance durability of AISI 316L stainless steel for reusable biomedical devices, J. Manuf. Process. 39 (2019) 295–304. https://doi.org/10.1016/j.jmapro.2019.02.003.

2. J. Nomani, A. Pramanik, T. Hilditch, G. Littlefair, Stagnation zone during the turning of Duplex SAF 2205 stainless steels alloy, Mater. Manuf. Process. 32 (2017) 1486–1489. https://doi.org/10.1080/10426914.2017.1279289.
3. B. Medina-Clavijo, M. Saez-de-Buruaga, C. Motz, D. Soler, A. Chuvilin, P.J. Arrazola, Microstructural aspects of the transition between two regimes in orthogonal cutting of AISI 1045 steel, J. Mater. Process. Technol. 260 (2018) 87–96. https://doi.org/10.1016/j.jmatprotec.2018.05.016.
4. S.N.B. Oliaei, Y. Karpat, Built-up edge effects on process outputs of titanium alloy micro milling, Precis. Eng. 49 (2017) 305–315. https://doi.org/10.1016/j.precisioneng.2017.02.019.
5. J. Kümmel, J. Gibmeier, E. Müller, R. Schneider, V. Schulze, A. Wanner, Detailed analysis of microstructure of intentionally formed built-up edges for improving wear behaviour in dry metal cutting process of steel, Wear. 311 (2014) 21–30. https://doi.org/10.1016/j.wear.2013.12.012.
6. Y.S. Ahmed, J.M. Paiva, B. Bose, S.C. Veldhuis, New observations on built-up edge structures for improving machining performance during the cutting of superduplex stainless steel, Tribol. Int. 137 (2019) 212–227. https://doi.org/10.1016/j.triboint.2019.04.039.
7. X. SONG, W. HE, T. IHARA, Predicting periodic evolution of BUE formation

`

mechanisms during machining ductile material using damage mechanics, Mech. Eng. J. 3 (2016) 15-00534-15–00534. https://doi.org/10.1299/mej.15-00534.

8. K. Ramasubramanian, N. Arunachalam, M.S. Ramachandra Rao, Wear performance of nano-engineered boron doped graded layer CVD diamond coated cutting tool for machining of Al-SiC MMC, Wear. 426–427 (2019) 1536–1547. https://doi.org/10.1016/j.wear.2018.12.004.
9. C. Nath, T. Kurfess, Obstruction-type Chip Breakers for Controllable Chips and Improved Cooling/Lubrication During Drilling – A Feasibility Study, Procedia Manuf. 5 (2016) 375–385. https://doi.org/10.1016/j.promfg.2016.08.032.
10. K. Ramasubramanian, N. Arunachalam, M.S.R. Rao, A Study on CVD Diamond Coated Cutting Tools Wear Performance using Vibration and Acoustic Emission Signals, Procedia CIRP. 72 (2018) 1415–1420. https://doi.org/10.1016/j.procir.2018.03.032.
11. M. Mia, N.R. Dhar, Effect of High Pressure Coolant Jet on Cutting Temperature, Tool Wear and Surface Finish in Turning Hardened (Hrc 48) Steel, J. Mech. Eng. 45 (2015) 1. https://doi.org/10.3329/jme.v45i1.24376.
12. H. Çalişkan, C. Kurbanoğlu, P. Panjan, D. Kramar, Investigation of the performance of carbide cutting tools with hard coatings in hard milling based on the response surface methodology, Int. J. Adv. Manuf. Technol. 66 (2013) 883–893. https://doi.org/10.1007/s00170-012-4374-y.
13. E. Uhlmann, S. Henze, K. Brömmelhoff, Influence of the built-up edge on the stress state in the chip formation zone during orthogonal cutting of AISI1045,

`

Procedia CIRP. 31 (2015) 310–315. https://doi.org/10.1016/j.procir.2015.03.101.

14. M.C. Shaw, The Theory of Metal Cutting, in: S.A. Tobias (Ed.), Proc. Twenty-Fifth Int. Mach. Tool Des. Res. Conf., Macmillan Education UK, London, 2005: pp. 33–36. https://doi.org/10.1007/978-1-349-07529-4_3.
15. Y. Seid Ahmed, J.M. Paiva, S.C. Veldhuis, Characterization and prediction of chip formation dynamics in machining austenitic stainless steel through supply of a high-pressure coolant, Int. J. Adv. Manuf. Technol. 102 (2019) 1671–1688. https://doi.org/10.1007/s00170-018-03277-7.
16. D. Neves, A.E. Diniz, M.S.F. Lima, Microstructural analyses and wear behavior of the cemented carbide tools after laser surface treatment and PVD coating, Appl. Surf. Sci. 282 (2013) 680–688. https://doi.org/10.1016/j.apsusc.2013.06.033.
17. K. Zhang, J. Deng, Y. Xing, S. Li, H. Gao, Effect of microscale texture on cutting performance of WC/Co-based TiAlN coated tools under different lubrication conditions, Appl. Surf. Sci. 326 (2015) 107–118. https://doi.org/10.1016/j.apsusc.2014.11.059.
18. S. Amini, H.N. Hosseinabadi, S.A. Sajjady, Experimental study on effect of micro textured surfaces generated by ultrasonic vibration assisted face turning on friction and wear performance, Appl. Surf. Sci. 390 (2016) 633–648. https://doi.org/10.1016/j.apsusc.2016.07.064.
19. N. Li, Y. Chen, D. Kong, S. Tan, Experimental investigation with respect to the performance of deep submillimeter-scaled textured tools in dry turning titanium alloy Ti-6Al-4V, Appl. Surf. Sci. 403 (2017) 187–199.

`

https://doi.org/10.1016/j.apsusc.2017.01.166.

20. K. Zhang, J. Deng, J.Sun, C. Jiang, Y. Liue, S. chen, Effect of micro/nano-scale textures on anti-adhesive wear properties of WC/Co-based TiAlN coated tools in AISI 316 austenitic stainless steel cutting, Appl. Surf. Sci. 355 (2015) 602–614. https://doi.org/10.1016/J.APSUSC.2015.07.132.
21. A. Pratap, K. Patra, A.A. Dyakonov, On-machine texturing of PCD micro-tools for dry micro-slot grinding of BK7 glass, Precis. Eng. 55 (2019) 491–502. https://doi.org/10.1016/j.precisioneng.2018.11.004.
22. S.K. Rajbongshi, D.K. Sarma, Performance parameters studies in machining of AISI D2 steel with dot-textured, groove-textured & non-textured cutting tool at the flank face, Int. J. Refract. Met. Hard Mater. 83 (2019) 104970. https://doi.org/10.1016/j.ijrmhm.2019.104970.
23. D. Vasumathy, A. Meena, Influence of micro scale textured tools on tribological properties at tool-chip interface in turning AISI 316 austenitic stainless steel, Wear. 376–377 (2017) 1747–1758. https://doi.org/10.1016/j.wear.2017.01.024.
24. D. Arulkirubakaran, V. Senthilkumar, S. Dinesh, C. Velmurugan, N. Manikandan, R. Raju, Effect of Textured Tools on Machining of Ti-6Al-4V Alloy under Lubricant Condition, Mater. Today Proc. 5 (2018) 14230–14236. https://doi.org/10.1016/J.MATPR.2018.03.003.
25. D. Arulkirubakaran, V. Senthilkumar, V.L. Chilamwar, P. Senthil, Performance of surface textured tools during machining of Al-Cu/TiB2 composite, Measurement. 137 (2019) 636–646. https://doi.org/10.1016/J.MEASUREMENT.2019.02.013.

`

26. Y.L. Zhang, X.G. Zhang, G. Matsoukas, Numerical study of surface texturing for improving tribological properties of ultra-high molecular weight polyethylene, Biosurface and Biotribology. 1 (2015) 270–277. https://doi.org/10.1016/j.bsbt.2015.11.003.
27. J. Kümmel, D. Braun, J. Gibmeier, J. Schneider, C. Greiner, V. Schulze, A. Wanner, Study on micro texturing of uncoated cemented carbide cutting tools for wear improvement and built-up edge stabilisation, J. Mater. Process. Technol. 215 (2015) 62–70. https://doi.org/10.1016/j.jmatprotec.2014.07.032.
28. S. Jesudass Thomas, K. Kalaichelvan, Comparative study of the effect of surface texturing on cutting tool in dry cutting, Mater. Manuf. Process. 33 (2018) 683–694. https://doi.org/10.1080/10426914.2017.1376070.
29. D. Grguraš, F. Pušavec, Influence of rake face texturing on machining performance of carbide tools, Procedia CIRP. 81 (2019) 904–907. https://doi.org/10.1016/J.PROCIR.2019.03.224.
30. X.L. Xing, Y.F. Zhou, S.Y. Gao, J.B. Wang, Y.L. Yang, Q.X. Yang, Nano-twin in surface modified bainite induced by laser surface modification, Mater. Lett. 165 (2016) 79–82. https://doi.org/10.1016/J.MATLET.2015.11.084.
31. N. Kawasegi, T. Kawashima, N. Morita, K. Nishimura, M. Yamaguchi, N. Takano, Effect of texture shape on machining performance of textured diamond cutting tool, Precis. Eng. 60 (2019) 21–27. https://doi.org/10.1016/J.PRECISIONENG.2019.07.007.
32. Y. Xing, J. Deng, Z. Wu, F. Wu, High friction and low wear properties of laser-

`

textured ceramic surface under dry friction, Opt. Laser Technol. 93 (2017) 24–32. https://doi.org/10.1016/J.OPTLASTEC.2017.01.032.

33. Q. Wang, B. Jiang, A. Tang, C. He, D. Zhang, J. Song, T. Yang, G. Huang, F. Pan, Formation of the elliptical texture and its effect on the mechanical properties and stretch formability of dilute Mg-Sn-Y sheet by Zn addition, Mater. Sci. Eng. A. 746 (2019) 259–275. https://doi.org/10.1016/J.MSEA.2019.01.040.
34. [S. Niketh, G.L. Samuel, Surface texturing for tribology enhancement and its application on drill tool for the sustainable machining of titanium alloy, J. Clean. Prod. 167 (2017) 253–270. https://doi.org/10.1016/J.JCLEPRO.2017.08.178.
35. Blunt L (Liam), Jiang X. Advanced techniques for assessment surface topography : development of a basis for 3D surface texture standards "surfstand" Kogan Page Science. 2003..
36. V.D. Kuznetsov, Metal Transfer and Build-Up in Friction and Cutting, Met. Transf. Build-Up Frict. Cut. (1966) 304–347. https://doi.org/10.1016/B978-1-4832-3216-4.50010-2.
37. M. Kamruzzaman, S.S. Rahman, M.Z.I. Ashraf, N.R. Dhar, Modeling of chip–tool interface temperature using response surface methodology and artificial neural network in HPC-assisted turning and tool life investigation, Int. J. Adv. Manuf. Technol. 90 (2017) 1547–1568. https://doi.org/10.1007/s00170-016-9467-6.
38. W. Bai, R. Sun, A. Roy, V.V. Silberschmidt, Improved analytical prediction of chip formation in orthogonal cutting of titanium alloy Ti6Al4V, Int. J. Mech. Sci. 133 (2017) 357–367. https://doi.org/10.1016/j.ijmecsci.2017.08.054.

`

39. Q. Yang, Y. Wu, D. Liu, L. Chen, D. Lou, Z. Zhai, Z. Liu, Characteristics of serrated chip formation in high-speed machining of metallic materials, Int. J. Adv. Manuf. Technol. 86 (2016) 1201–1206. https://doi.org/10.1007/s00170-015-8265-x.
40. Y.S. Ahmed, G. Fox-Rabinovich, J.M. Paiva, T. Wagg, S.C. Veldhuis, Effect of built-up edge formation during stable state of wear in AISI 304 stainless steel on machining performance and surface integrity of the machined part, Materials (Basel). 10 (2017) 1–15. https://doi.org/10.3390/ma10111230.
41. E.M. Trent, Metal cutting and the tribology of seizure: II movement of work material over the tool in metal cutting, Wear. 128 (1988) 47–64. https://doi.org/10.1016/0043-1648(88)90252-9.
42. Z. Wang, V. Kovvuri, A. Araujo, M. Bacci, W.N.P. Hung, S.T.S. Bukkapatnam, Built-up-edge effects on surface deterioration in micromilling processes, J. Manuf. Process. 24 (2016) 321–327. https://doi.org/10.1016/j.jmapro.2016.03.016.
43. M. Brown, P. Crawforth, R. M'Saoubi, T. Larsson, B. Wynne, A. Mantle, H. Ghadbeigi, Quantitative characterization of machining-induced white layers in Ti–6Al–4V, Mater. Sci. Eng. A. 764 (2019) 138220. https://doi.org/10.1016/j.msea.2019.138220.
44. J. Fu, J. Sun, X. Cen, X. Zhang, F. Li, Y. Wu, Growth behavior and orientation relationships in AISI 304 stainless steel during directional solidification, Mater. Charact. 139 (2018) 241–248. https://doi.org/10.1016/J.MATCHAR.2018.03.015.
45. A.T. AlMotasem, M. Posselt, J. Bergström, Nanoindentation and nanoscratching

`

of a ferrite/austenite iron bi-crystal: An atomistic study, Tribol. Int. 127 (2018) 231–239. https://doi.org/10.1016/J.TRIBOINT.2018.06.017.

`

Chapter 7: Conclusions and Future Work

This chapter outlines the general conclusions of the research reported in this thesis as well as research contributions and recommendations for future work.

7.1 General Conclusions

Stainless steels are currently used for various applications due to their combination of high mechanical strength, corrosion resistance and low thermal conductivity. However, stainless steel machining is characterized by rapid tool wear and poor surface quality. This thesis seeks to provide a comprehensive overview of machining performance during stainless steel machining. The wear mechanisms and tribological performance of uncoated and coated carbide tools were investigated during the turning of stainless steel under wet conditions. Tool wear was evaluated during the cutting tests to identify the dominant wear mechanisms. At low cutting speeds, workpiece material and chips tend to adhere to the cutting tool surface, forming a built-up edge (BUE). The BUE consists of extremely deformed material that firmly sticks to the tool-chip interface throughout the cutting test, affecting tool life and surface integrity. The role of high pressure coolant (HPC) on tribological performance was evaluated by a study of tool life, BUE formation chip characteristics, segmentation and free surface area. BUE structures obtained at different cutting speeds were examined in detail to characterize BUE formation during the machining test. Various BUE adhesion patterns were analyzed via electron backscatter

`

diffraction (EBSD) and nano-indentation methods. Then, to maintain high productivity and quality of the machined part, different textures were generated on the uncoated WC/Co tool rake face using LST to control the BUE stability and reduce friction at the tool-chip interface.

This thesis work seeks to enhance the machinability of stainless steel through the control of friction and adhesion mechanisms during the machining process. The general conclusions from this thesis are outlined below:

- An in-depth study of machining performance during stainless steel machining showed that the predominant wear mechanisms were adhesion and chipping for all of the investigated tools. This was attributed to the formation of an unstable BUE which causes cracks and damage on the tool surface eventually leading to cutting-edge chipping.
- A substantial tool life improvement was achieved using HPC: tool life was extended by 26% and 36% compared to wet and dry conditions, respectively. The tribological performance was also improved. A lower chip thickness and higher shear angle were obtained as a result of using HPC, in addition to a 10% decrease in the coefficient of friction and a 30% reduction in the tool chip contact length as compared to wet machining. Although the use of HPC was shown to extend tool life and improve the overall tribological performance, it could not achieve control of BUE stability, since a high variation of BUE height was observed during the

`

machining of stainless steel. Thus, the use of HPC did not result in an improvement of the workpiece surface quality.

- Investigation of the role of adhesion mechanisms on tool failure and surface integrity demonstrated the protective effect of a BUE at low cutting speeds that enhanced tool life. At low speeds, only low flank wear was observed compared to various wear types found at high cutting speeds. The BUE formed at lower cutting speeds covered a greater area of the rake face compared to that at the higher cutting speed, which protected the cutting tool from wear by reducing the friction at the tool-chip interface. These results highlighted the beneficial impact of having a stable BUE in terms of increasing tool life and lowering the probability of tool breakage.
- BUE formation also had a great effect on surface integrity. An unstable BUE was responsible for the increase in surface roughness of the machined surface. In addition, tensile residual stresses on the machined surface decreased with the growth of BUE height, which was attributed to the high cutting temperature softening the material, thereby causing the residual stresses to decrease.
- Control of BUE formation during stainless steel machining was shown to be necessary to maintain high productivity and quality of the machined part. Different texture shapes were applied on the rake face of the cutting tool with LST to mitigate BUE adhesion on the cutting tool. The results showed that square texturing stabilized the BUE formation during the cutting process. This, in turn,

`

reduced the machined surface roughness and provided superior wear protection when compared to other tools. Square texturing reduced flank wear by 41-78% and increased surface finish by 54-68% when compared to the use of an untextured tool. In addition, surface textured tools helped reduce the cutting forces, thrust forces and the coefficient of friction. The maximum reductions of 58%, 100%, and 24% in the respective cutting force, thrust force, and coefficient of friction were obtained with the square textured tool. Furthermore, the thickness and hardness values of the heat-affected zone were lower in the workpiece machined by the square textured tools.

7.2 Research Contributions

The main contributions of this thesis include achieving control of the adhesion mechanism and reducing friction during stainless steel machining. These contributions can be summarized as follows:

1. An in-depth investigation of machining behavior during stainless steel machining was performed. A description of tool wear mechanisms and tribological performance of different coated and uncoated tools was provided.
2. The chip forming mechanism and chip breakability of stainless steel were studied under the supply of HPC. The experiments were conducted under different cooling conditions: dry machining, conventional coolant supply and two HPC pressures. The chip formation mechanism was evaluated in terms of chip

`

characteristics, segmentation and free surface. Furthermore, a 3D model of chip curling was used to evaluate the effect of HPC supply on chip geometry during metal cutting.

3. The BUE structures were studied in detail under different cutting conditions to investigate the beneficial and detrimental effect of BUE on tool failure and surface integrity. In addition, the BUE mechanisms were analyzed by means of an in-depth investigation of microcrack formation and EBSD analysis.
4. A femtosecond laser was used to apply different shaped textures on the rake face of the cutting tool (square, parallel, perpendicular). An in-depth investigation of tool-chip interfaces was then conducted to understand the effect of different texture shapes and orientations on machining performance and process efficiency. The textured and untextured cutting tools were inspected and compared at different cutting lengths and cutting speeds during the cutting test. This investigation can be summarized by the following points:

   (i) A comprehensive study of the influence of rake face textures on the tool-chip interface performance.

   (ii) An in-depth investigation of BUE formation during the continuous turning process to understand the underlying reasons for its stabilization.

   (iii) An assessment of the deformation characteristics and mechanical state of the machined workpiece subsurface layers following machining with textured and untextured tools at different cutting speeds.

`

7. The results presented in this thesis can be implemented in industrial practice to control BUE stability and reduce friction during stainless steel machining. In this manner, tool life can be potentially enhanced by 41-78% and surface quality by 54-68%.

7.3 Recommendations for Future Research

The following research topics are suggested for future studies:

- A sliding friction test should be performed to evaluate the degree of friction reduction obtained using different microtextured surfaces. Accordingly, the best cutting tool texture design can then be combined with the advantages of using a tungsten disulfide (WS_2) coating. Machining experiments will then need to be carried out on the WS_2 coated textured, uncoated textured and untextured cutting tools to compare performance.
- The machining tests with surface textured tools were performed at a limited range of cutting speeds (60, 100, 120 and 150 m/min), a constant feed rate (0.1 mm/rev) and depth of cut (0.5 mm). In the future, a wider range of feed rates and depths of cut should be considered. In addition, micro texturing was applied on uncoated carbide tools - future work should be extended to consider coated tools as well.
- A correlation between different texture parameters such as width, pitch, depth and machining conditions may be determined following extensive research and could

`

be used to build a database of conditions for which texturing may prove to be beneficial.

- The principle of surface texturing can be extended to smaller length scales, i.e. the nanoscale, and their effect on the adhesion and friction can be explored during cutting tests. Furthermore, since this thesis was limited to negative surface texturing, future investigations might concern testing similar hypotheses on positive surface texturing.

`

Appendix A: Effect of HPC on tool life, BUE formation, and cutting forces

Preface

The effect of high pressure coolant jets directed into the tool–chip interface, during turning with uncoated carbide tools is investigated in this appendix and compared with dry and conventional coolant conditions. During the turning of AISI 304 stainless steel, the cutting forces, tool wear, BUE formation, and machined surface finish were analyzed as a function of the coolant supply pressure.

Chapter 3 analyses the chip forming mechanism and chip breakability of stainless steel with a supply of HPC. This appendix consists of an unpublished section on the effect of HPC on tool life, BUE formation, cutting forces and machined surface roughness which were not covered in Chapter 3.

A.1 Cutting forces

To better understand the correlation between BUE formation and the resulting cutting forces, cutting force components were measured while machining the workpiece. The cutting forces are almost always used to assess the chip formation process of engineering materials. Although direct measurement of the cutting forces helps to determine the power requirement for cutting the work material, it is also useful to evaluate the entire

`

cutting process [1]. The main cutting forces for the dry, conventional coolant and two HPC conditions are depicted in Figure A-1 (a).

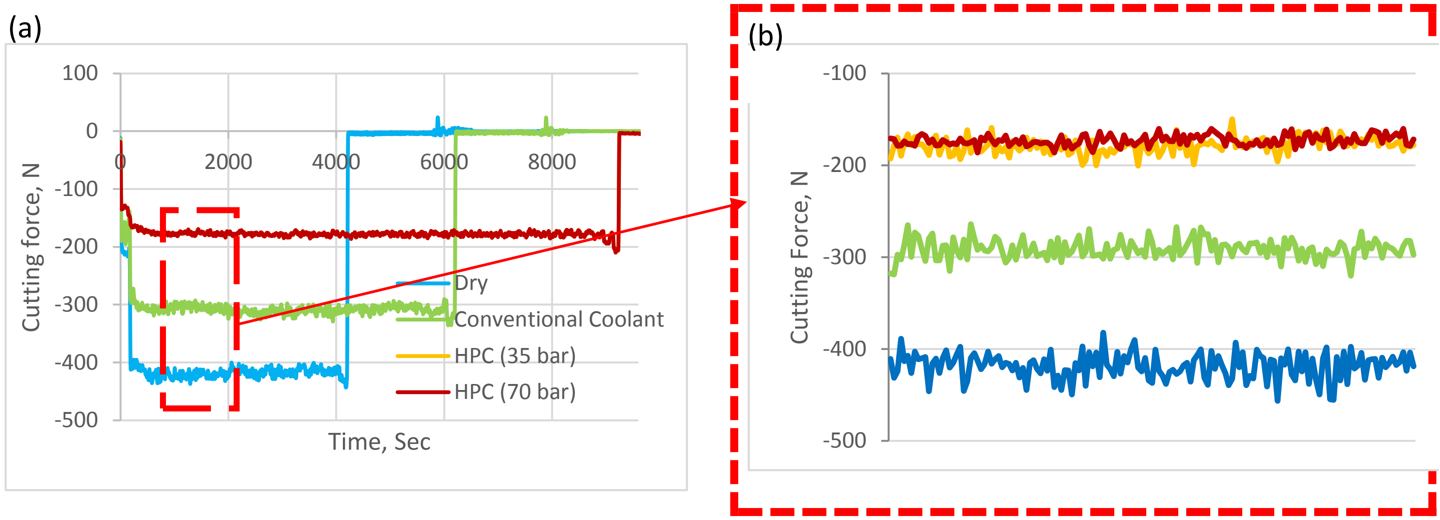

Figure A-1(a) Relation between cutting force and time at optimum cutting conditions and (b) associated cutting force variations for different cooling conditions

The main cutting forces are higher under the use of dry and conventional coolant than under HPC. No difference in cutting forces was observed at the two HPC pressures. The reduction in the cutting force under HPC conditions was attributed to several factors. The HPC jet strikes the chip at a point very close to the cutting edge of the insert, removing a serrated portion of the chip and thereby reducing its width [2]. Consequently, the tool chip contact area on the rake face was diminished, which leads to a reduction in BUE formation due to less friction being present between the insert and the chip, which eventually reduced the cutting force as well [3]. Another reason is that HPC is capable of reaching deeper into the cutting interface to deliver more efficient cooling and lubrication. Thus, the coolant water wedge created at the tool-chip interface reduced the tool-chip

`

contact length and cutting forces, which can also potentially benefit friction conditions and BUE control [4].

A comparative study of the dynamic cutting forces during machining under dry, conventional, and HPC conditions is shown in Figure A-1 (b). The cutting force fluctuates between high and low values. This fluctuation becomes more prominent with the formation of BUE. If the inserts exhibit a high BUE intensity, the cutting force jumps to a very high value before dropping off under the use of dry and conventional coolant [5]. However, no sudden increase of cutting force was observed under HPC conditions and its magnitude was lower than under conventional coolants and dry conditions throughout the entire duration of machining.

A.2 Tool Life

Figure A-2 shows the progression of average flank wear with machining time associated with SEM images of the cutting tools at the end of tool life. The volume of wear is lowest in HPC and the highest in the dry condition. Based on the tool rejection criteria defined by ISO standard 3685, the tool life under dry cutting and when a conventional coolant was used were 8.8 min and 9.5 min respectively, whereas in HPC, it was 12 min. Therefore, HPC prolonged tool life by 26% and 36% compared to respective conventional and dry conditions. This performance improvement can be attributed to the highly pressurized jet displacing the chips, which reduced friction and BUE formation [6,

`

7]. In addition, the HPC jet left behind a thin lubricating film that also contributed to wear reduction.

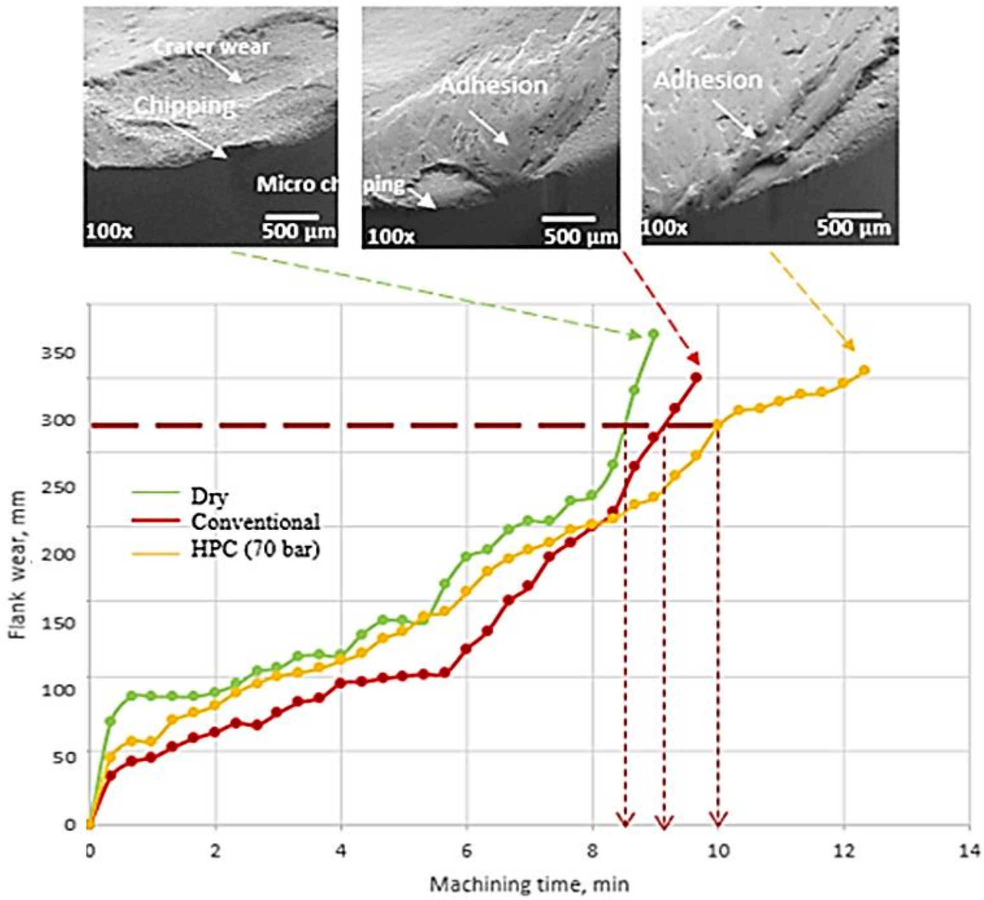

Figure A-2 Relation between flank wear and machining time during machining AISI 304. Additionally, SEM image for cooling condition is presented at the end of tool life (v = 60 m/min, a = 0.5mm, f = 0.1 mm/r)

A.3 BUE formation

The tool wear morphologies under the different coolant pressure conditions are shown in Figure A-3. Tool wear was alleviated, and adhesion reduced with increasing coolant pressure. The coolant liquids could not reach the cutting edge due to the relatively low coolant pressure as compared to the high contact pressure in the cutting zone so its impact on BUE formation was minimal. However, the coolant with the high energy jet can reduce the chip contact area with the tool surface, thus reducing the seizure effect and the cutting temperature [3]. Therefore, high pressure coolant was found to be effective at minimizing adhesive wear and other thermo-related wear mechanisms.

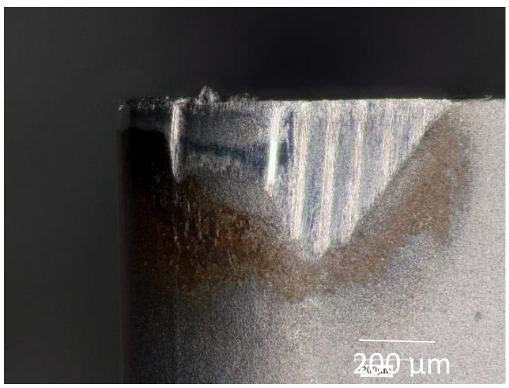

Flank face under dry condition

Rake face under dry condition

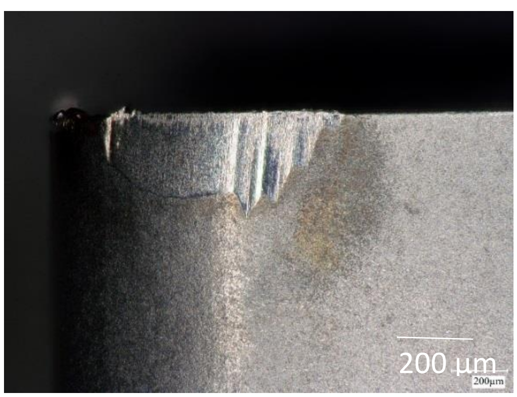

Flank face under wet condition

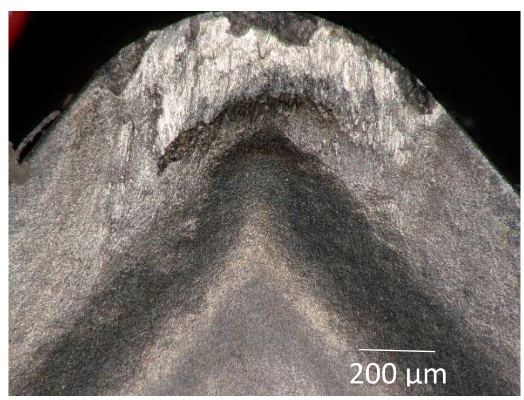

Rake face under wet condition

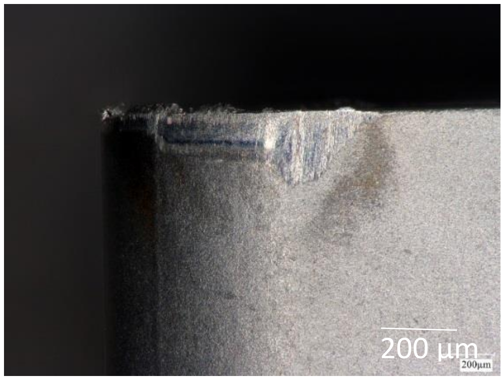

Flank face under HPC (35 bar)

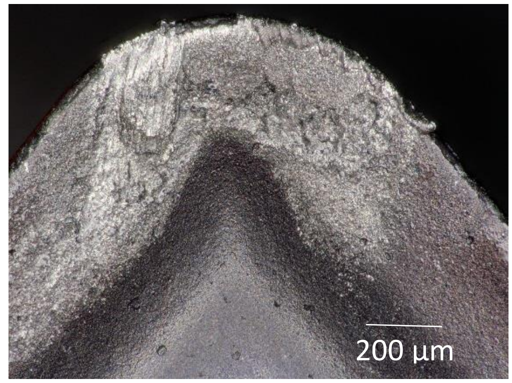

Rake face under HPC (35 bar)

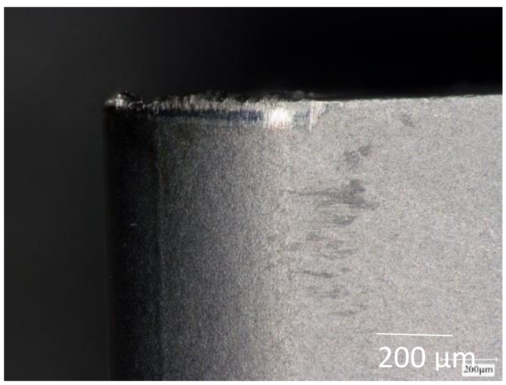

Flank face under HPC (70 bar)

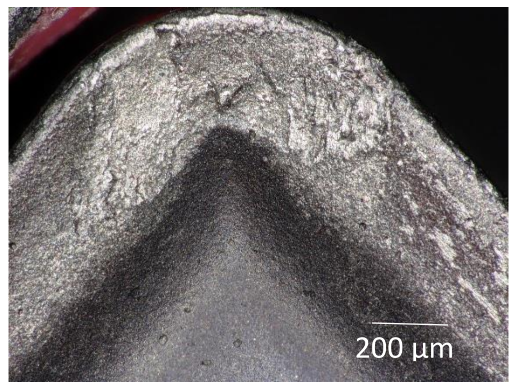

Rake face under HPC (70 bar)

Figure A-3 Tool wear morphologies under different cooling conditions

(v = 60 m/min, a_p = 0.5mm, f = 0.1 mm/r)

To understand the effect of HPC on BUE stabilization, the average BUE height was measured during the cutting process and plotted in Figure A-4. Although BUE formation was lower under HPC conditions, it remained unstable during the machining process: the variation of BUE height under HPC and dry conditions was the same (Δh=15μm). This confirmed that HPC was not capable of stabilizing the BUE formation during the machining process.

`

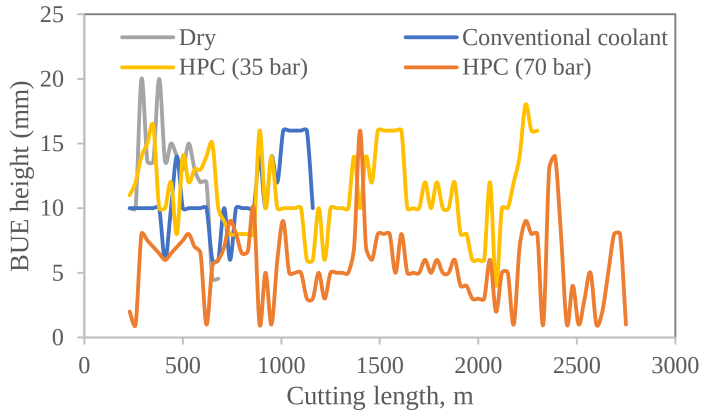

Figure A-4 BUE height variations obtained with different cooling conditions (v = 60 m/min, a = 0.5mm, f = 0.1 mm/r)

A.4 Machined surface roughness

To evaluate the surface quality produced by the different cooling conditions, a measurement of the average surface roughness is presented in Figure A-5. As can be seen, no significant improvement can be observed in average surface roughness obtained with HPC. This was attributed to the instability of BUE formation during stainless steel machining.

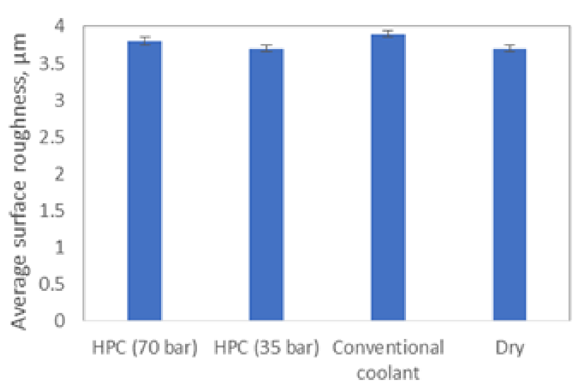

Figure A-5 Average surface roughness obtained at different cooling conditions

`

A.5 Remarks

The effects of various coolants such as dry, conventional coolant and two different HPC pressures on cutting forces, tool life, BUE formation and machined surface quality were discussed. The resulting observations are the following:

1. The main cutting forces were higher under dry and conventional coolant than with the use of HPC. No sudden increase in cutting force was observed under HPC conditions over the course of machining due to low BUE formation.
2. HPC managed to prolong tool life by 26% and 36% compared to conventional and dry conditions. This performance improvement was attributed to the highly pressurized jet displacing the chips, which reduced friction and BUE formation.
3. HPC was not capable of stabilizing the BUE formation during the machining process. As a result, no significant improvement was observed in the machined surface roughness.

References

1. Y. Amini, M. Mokhtari, M. Haghshenasfard, and M. Barzegar Gerdroodbary, “Heat transfer of swirling impinging jets ejected from Nozzles with twisted tapes utilizing CFD technique,” Case Stud. Therm. Eng., vol. 6, pp. 104–115, 2015.
2. M. Mia and N. R. Dhar, “Effect of High Pressure Coolant Jet on Cutting Temperature, Tool Wear and Surface Finish in Turning Hardened (Hrc 48) Steel,” J. Mech. Eng., vol. 45, no. 1, p. 1, 2015.

`

3. Y. Kaynak, A. Gharibi, and M. Ozkutuk, “Experimental and numerical study of chip formation in orthogonal cutting of Ti-5553 alloy: the influence of cryogenic, MQL, and high pressure coolant supply,” Int. J. Adv. Manuf. Technol., vol. 94, no. 1–4, pp. 1411–1428, 2018.
4. U. T. Guidance, “an Analysis of Strain in Chip Breaking Using Slip-Line Field Theory With Adhesion Friction At Chip / Tool Interface an Analysis of Strain in Chip Breaking Using Slip-Line Field Theory With Adhesion Friction At Chip / Tool Interface,” no. July, 2005.
5. O. Çolak, “Investigation on machining performance of Inconel 718 under high pressure cooling conditions,” Stroj. Vestnik/Journal Mech. Eng., vol. 58, no. 11, pp. 683–690, 2012.
6. M. Ahmed, “ Optimisation of Tool Wear and Cutting Forces on the basis of different Cutting Parameters ,” no. 1, pp. 613–626, 2017.
7. M. Kamruzzaman and N. R. Dhar, “The Effect of Applying High-Pressure Coolant (Hpc) Jet In Machining Of 42crmo4 Steel By Uncoated Carbide Inserts,” *Jorunal Mech. Eng.*, vol. 39, no. 2, pp. 71–77, 2008.

`

Appendix B: Effect of laser micro- scale textured tools on the tool-chip interface performance during stainless steel machining under a dry condition

Preface

Chapter 8 discusses the influence of different rake faces on the tool-chip interface performance during wet machining of stainless steels. Appendix B consists of an unpublished section on the effect of laser micro-scale textured tools on tool-chip interface performance during stainless steel machining under dry conditions. All cutting experiments were performed using the same tools, workpiece materials and machines, under the same parameters except no cutting coolant was used.

B.1 Flank wear resistance

The average flank wear vs. cutting length for different textured and untextured tools at a cutting speed of 60 m/min, feed rate of 0.1 mm/rev and depth of cut of 0.5 mm is displayed in Figure B-1. It could be observed that each of the three textured cutting tools featured superior flank wear resistance compared with the untextured tool. Square and parallel textured tools were shown to reduce flank wear to a greater degree compared with

`

perpendicular textured and untextured tools. The average flank wear present in the square textured tool was the lowest and improved by 47% compared with the use of the untextured tool. However, it is worth noting that the square textured tool had the poorest wear resistance at a cutting distance below 160 m. But as the cutting distance exceeded 200 m, its cutting performance was observed to be superior to that of the other tools.

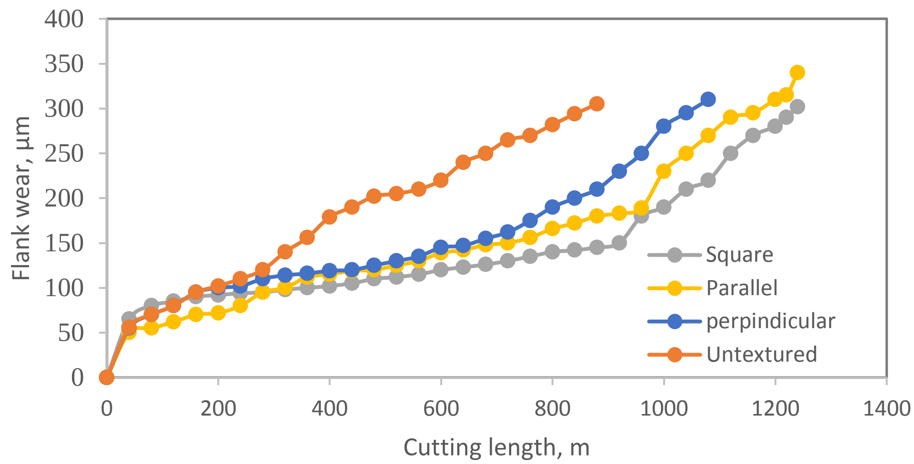

Figure B-1 Relation between flank wear and cutting length for different textured and untextured tools at a cutting speed of 60 m/min

B.2 Tool wear morphology

To evaluate the anti-adhesive properties of the textured tools under dry cutting conditions, dry cutting experiments were conducted at a cutting speed of 60 m/min. Figure B-2 shows the SEM images of the rake face after a cutting length of 1000m. Adhesion of workpiece material (Fig. B-2 (b)) to the untextured tool was observed to be more intense during dry cutting than wet cutting (Fig. B-2(a)). In addition, the decrease in the adhesion of the untextured tool near the cutting edge can be attributed to the cutting temperature near the

`

cutting edge exceeding the recrystallization temperature of stainless steel under the dry cutting condition [1]. Additionally, a more severe chipping area on the cutting edge can be observed under the dry condition compared to the wet condition (Fig. B-2(b)).

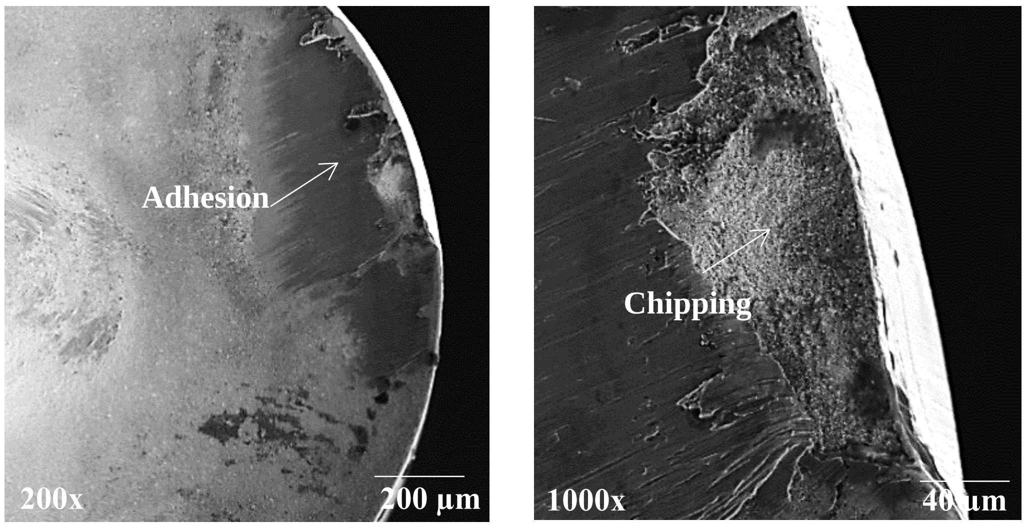

(a) Wet condition

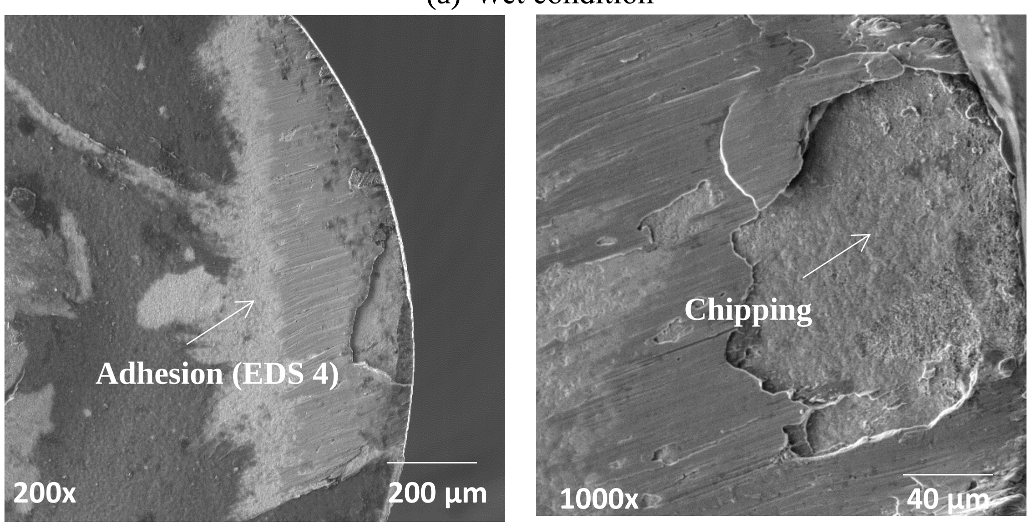

(b) Dry condition

Figure B-2 SEM images of untextured tools after cutting length of 1000 m at cutting speed of 60 m/min.

`

Figure B-3 (a-c) shows the rake face morphology of different textured tools at the same machining stage. As shown, a smaller chipping area can be observed on the main cutting edge of the textured tools compared to the untextured tool (Figure B-2 (b)). It can be therefore concluded that the application of micro-textures on the rake face could enhance the machining performance of a tool. An adhesion layer was also present on the worn area of the rake face of the textured tools. EDS composition analysis (see EDS (1-3) In Table B-1) shows that the percentage of Fe was lower in the textured tool (EDS 4 in Table B-1). Therefore, it can be concluded that the textured tools have better machining performance than the untextured tool even under dry conditions.

(a)

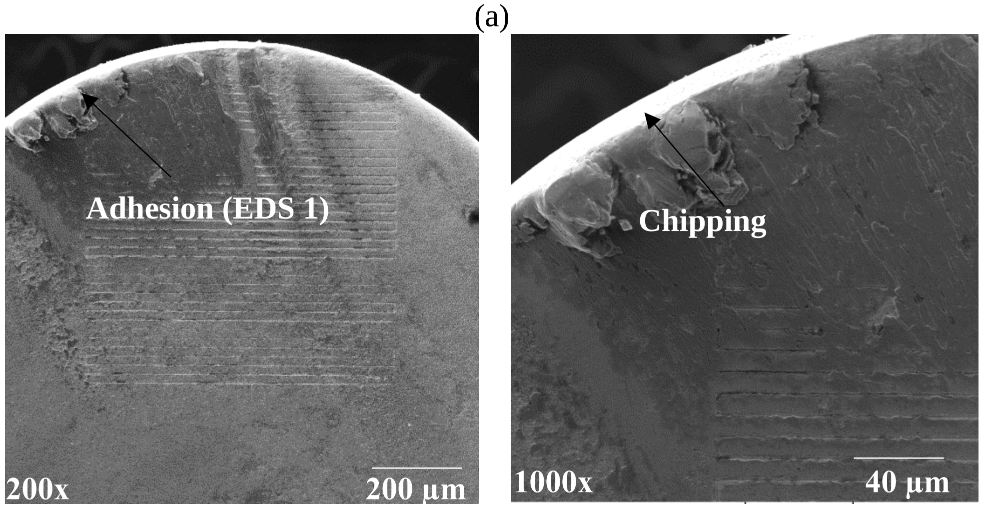

`

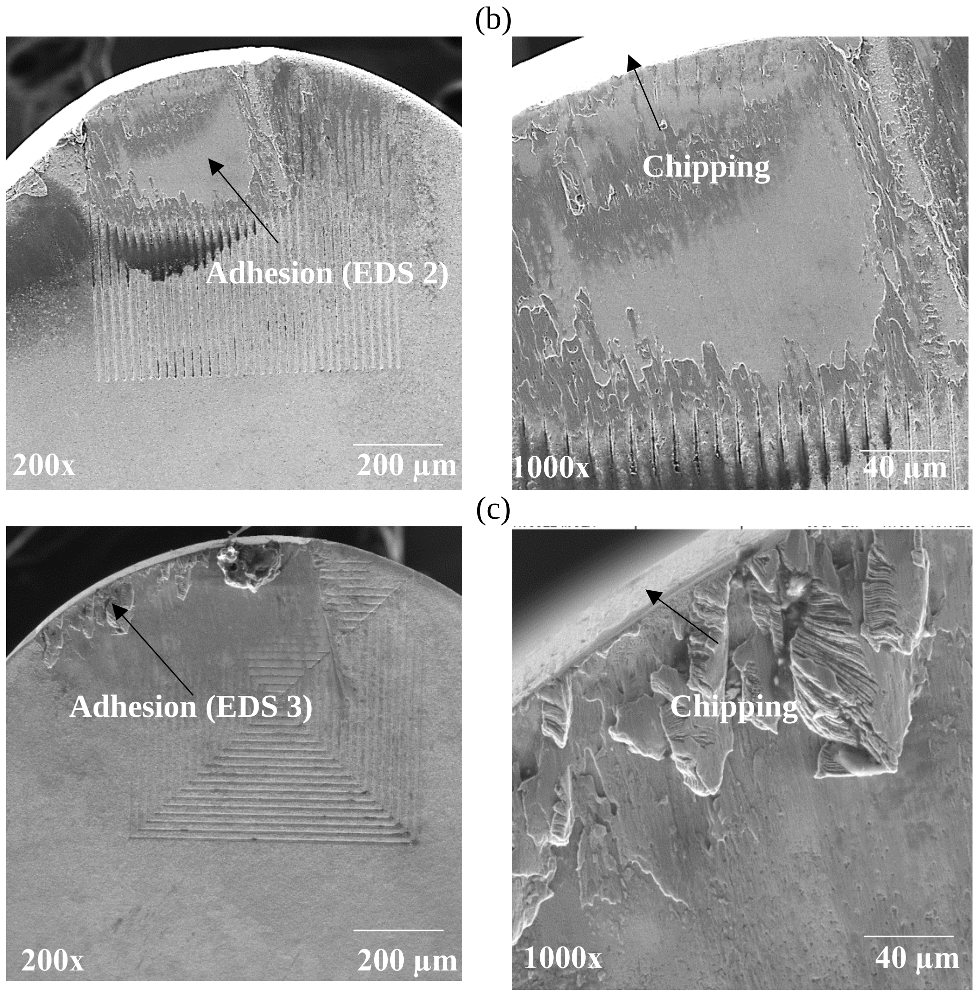

Figure B-3 SEM images of (a) parallel, (b) perpendicular and (c) square textured tools after cutting length of 1000 m at cutting speed of 60 m/min

Table B-1 EDS analysis related to Figures B-2 and B-3

EDS	Fe	Cr	W
1	66.5	28.9	0.8
2	72.3	25.3	1.2
3	69.2	24.4	4.5
4	80.22	12.33	5.6

To understand the effect of cutting speed on adhesion under different textured and untextured tools, the rake face of the cutting tools was investigated at a higher cutting speed (150 m/min), as shown in Figure B-4. The results show that severe chipping occurs on all cutting tools. Less adhesion could be observed on the surfaces of each cutting tool at the higher cutting speeds than at lower ones (Figure B-3). This may be due to the reduction in the tool-chip contact length achieved at a higher cutting speed [2].

(a)

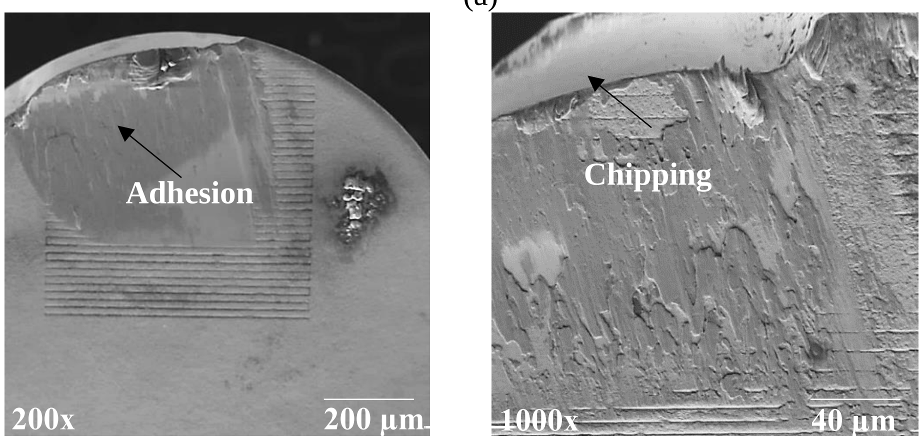

(b)

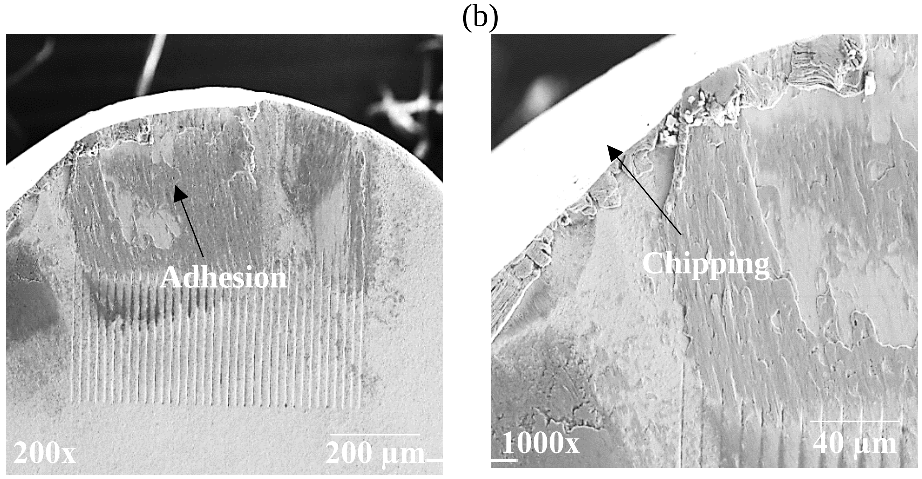

(c)

`

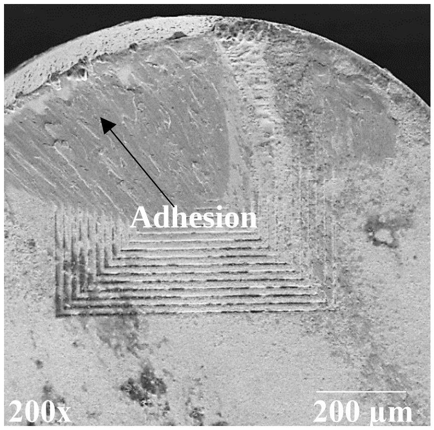

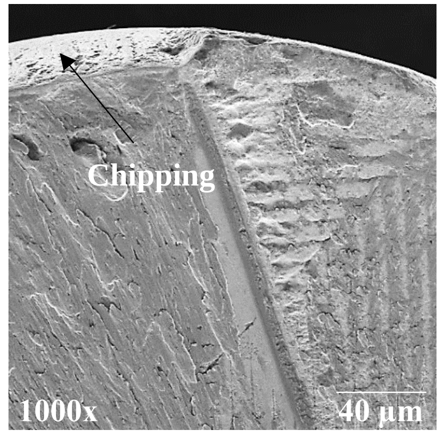

Figure B-4 SEM images of (a) parallel, (b) perpendicular and (c) square textured tools after cutting length of 1000 m at cutting speed of 150 m/min

B.3 Remarks

The effects of the three different texture shapes (square, parallel, and perpendicular) on the tool wear morphology and flank wear resistance were investigated during the dry turning of AISI 304 austenitic stainless steel. The following are the key conclusions of this study:

1. Surface textured tools improved wear protection. The average flank wear of the square textured tool was 47% and 78% lower than that of the untextured tool in the respective dry and wet conditions.
2. Adhesion of workpiece material to the untextured tool was more intense during dry cutting than wet cutting. Also, a larger area of severe chipping on the cutting edge was observed under the dry condition compared with the wet condition. Furthermore, less adhesion was observed on the surfaces of each cutting tool at the higher cutting speeds than at that lower ones.

`

References

1. J. Kümmel, J. Gibmeier, E. Müller, R. Schneider, V. Schulze, A. Wanner, Detailed analysis of microstructure of intentionally formed built-up edges for improving wear behaviour in dry metal cutting process of steel, Wear. 311 (2014) 21–30. https://doi.org/10.1016/j.wear.2013.12.012.
2. X. SONG, W. HE, T. IHARA, Predicting periodic evolution of BUE formation mechanisms during machining ductile material using damage mechanics, Mech. Eng. J. 3 (2016) 15-00534-15–00534. https://doi.org/10.1299/mej.15-00534.